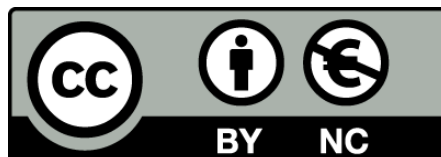




Structure and nature of gamma-ray binaries by means of VLBI observations

Francisco Javier Moldón Vara



Aquesta tesi doctoral està subjecta a la llicència **Reconeixement- NoComercial 3.0. Espanya de Creative Commons.**

Esta tesis doctoral está sujeta a la licencia **Reconocimiento - NoComercial 3.0. España de Creative Commons.**

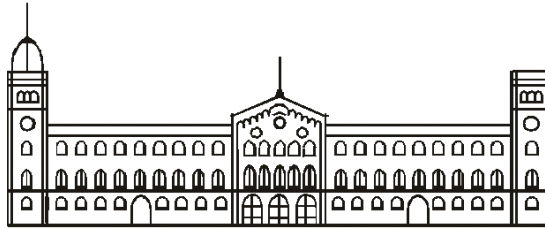
This doctoral thesis is licensed under the **Creative Commons Attribution-NonCommercial 3.0. Spain License.**

Structure and nature of gamma-ray binaries by means of VLBI observations



Francisco Javier Moldón Vara

Ph.D. Thesis, July 2012



UNIVERSITAT DE BARCELONA

DEPARTAMENT D'ASTRONOMIA I METEOROLOGIA

Structure and nature of gamma-ray binaries by means of VLBI observations

Francisco Javier Moldón Vara

PH.D. THESIS IN PHYSICS

BARCELONA (SPAIN)

JULY 2012

PROGRAMA DE DOCTORAT DE FÍSICA

Memòria presentada per **Francisco Javier Moldón Vara**
per optar al grau de Doctor en Física

Aquesta Tesi Doctoral ha estat dirigida per

Dr. Marc Ribó i Gomis

Universitat de Barcelona

Dr. Josep M. Paredes i Poy

Universitat de Barcelona



We don't stop playing because we grow old;
we grow old because we stop playing.

George Bernard Shaw

*Quienes se sientan subyugados por la invencibilidad
del espíritu humano y la incesante eficacia
del método científico como herramienta útil
para desentrañar las complejidades del universo,
encontrarán muy vivificador e incitante
el veloz progreso de la ciencia.*

Introducción a la ciencia. (Isaac Asimov)

Agradecimientos / Agraïments / Acknowledgments

I want to thank all the people who supported and helped me, either directly or indirectly, to prepare this work, either if they are mentioned below or not.

En primer lloc voldria agrair profundament a tot el conjunt del grup d'Astrofísica d'altres energies del Departament d'Astronomia i Meteorologia de la Universitat de Barcelona. Aquest grup és especialment competent tant científica com humanament, que són dues qualitats imprescindibles per a portar a terme qualsevol tipus d'investigació.

Moltes gràcies al doctor Marc Ribó, que m'ha guiat sempre en tot el que m'he proposat, ha obert camins nous per explorar, sempre amb rigor, completesa i certesa de que el que fem ho fem bé. Gran part d'aquesta tesi està basada en idees seves originals, i per tant vull agrair especialment el seu treball i suport per tirar endavant tot el que hem fet per aquesta tesi, i molts altres treballs paral·lels. També agrair que hagi sabut crear un ambient de treball ideal, facilitant fer ciència i a més convertint aquest treball en una tasca apassionant.

Al professor Josep Maria Paredes, que com a líder d'aquest mateix grup ha sabut orientar tots els nostres camins, sempre amb idees noves i amb una contagiosa curiositat per descobrir. La seva gran experiència ha fet possible trobar allò que faltava i obrir nous camins. També ha contribuït a crear un ambient immillorable.

Al doctor Valentí Bosch-Ramon, que quan jo començava tu marxaves, i ara que acabo tu tornes. M'agradaria haver tingut més temps per tenir projectes comuns, però per sort encara queda molt per fer! Al doctor Pol Bordas per acompanyar-me en els primers anys de la meva tesi. Al doctor Víctor Zabalza, company de despatx durant molt de temps, amb qui he compartit la passió per la fotografia, el gust per fer pa, i l'eficiència de python. Gràcies al Pere Munar, company de despatx durant l'últim any, amb qui he compartit bons moments, dubtes, tant dins com fora la Universitat, i amb el que he "conreat" la millor terrassa del DAM. Gràcies a Albert Cañellas, amb qui vaig compartir un període interessant, ampliant també el meu interès històric i polític.

También agradecer a los demás integrantes del grupo, agradecer a Benito Marcote, que va por el buen camino de radio+python, al doctor Simone Migliari con el que han empezado a surgir nuevos proyectos comunes, a parte de las observaciones con estudiantes, y a los demás integrantes del grupo con los que yo he coincidido: Kazushi Iwasawa, Yolanda Sestayo, Roberta Zanin y Xavier Paredes.

I want to thank doctor Simon Johnston, for all the past, present, and future works we have in common. Thank you for sharing with us your work since the first moment we met, which really opened a new world of science to do. Thank you Walter Brisen for helping me to use the very powerful techniques related with pulsars and their astrometry. Also, thank you for the good moments during my stay in Socorro. I also want to thank Vivek Dhawan the warm welcome when I arrived in Socorro and for sharing your research interests.

Acknowledgments

Gràcies al doctor Josep Martí, que lidera un grup molt interessant amb una investigació paral·lela a la que fem al DAM, perquè quan ambdues línies es creuen es tornen molt enriquidores.

I want to thank Zsolt Paragi for his kind hospitality and interest during my different short stays at JIVE, for his enthusiastic help, suggestions and lessons. I also want to thank the people at the Max-Planck-Institut für Radioastronomie who showed me the basic notions of how to use the correlator and how it works.

I also thank the other researches with which I have collaborated in the last years, A. Deller, M. Cadolle, M. Kramer, A. G. Lyne, and B. W. Stappers.

Las estancias dentro de la colaboración MAGIC son mucho más que estancias, son vivencias. Tras cuatro *shifts* de varias semanas cada uno durante los últimos años, se convive con mucha gente, que sin duda forman parte de esta Tesis. Es una gran experiencia pasar las largas noches en la cumbre de esa magnífica isla con momentos de calma y momentos de estrés para que aquello que no acabábamos de comprender acaben funcionando. Quiero agradecer en especial a Valeria Scapin, con la que he compartido dos *shifts*, y a Villi Scalzotto, ambos habéis convertido esa bonita y solitaria montaña en algo más parecido a un hogar. Valeria, qué grandes tus pasteles y tus comidas! To the rest of the *shifters*, many people, thank you for sharing those moments.

Me gustaría agradecer a Eduardo Ros por acoger mi estancia en el Max-Planck-Institut für Radioastronomie en Bonn, por mostrarme algunos de los “trucos” avanzados de VLBI y por su acogida. I’m very glad to have known a lot of interesting people during my stay in Bonn. I specially want to thank Yoon Kyung (you are great!), Mar Mezcuca, Felipe Navarrete, Seungkyung Oh, Brenda Miranda, and everybody I met there during my different visits. Thank you very much for the barbecues, the visits to Fiddler’s, and to the beautiful parks.

During my stays in Socorro(!) I meet very nice people that make my life there very nice. Special thanks to Kristina Nyland for taking care of so many things and for showing me so many places from New Mexico, from North to South. Also I want to thank Crystal Anderson for her hospitality and Katey Alatalo for the good moments. I want to thank all the nice people I met in the NRAO, who make that isolated place so interesting.

Finally, I want to thank the people of the ATNF in Australia for making my stay at the other side of the World interesting. Of course to Simon Johnston for kindly hosting me. Special thanks to Tui Britton for her hospitality and friendship. I was very glad to play ping-pong every day after lunch, so thanks to all players! I want to thank all the non-astronomers from Robert Menzies College for sharing with me their experiences during my firsts days there. Me gustaría mandar un saludo a Ángel López y a Vicente Maestro, a los que a pesar de conocer justo al final de mi estancia, me hicieron pasar muy buenos momentos, y a descubrir que se pueden encontrar churros en Sidney!. Thanks to the ATNF staff for helping with many residence changes and accommodation.

I want to thank everybody I have met at the different conferences and meetings around the world, for sharing so many interesting moments and pictures.

Es importante agradecer a aquellos que han compartido conmigo la experiencia de doctorado, no necesariamente la investigación, pero sí todo lo demás. Gracias a todos los compañeros del DAM que me han apoyado y/o ayudado en el transcurso de todos estos años, compartiendo comidas, dificultades y alegrías. Muchas gracias a Laura Darriba por estar siempre ahí, por alimentarnos, por enseñarnos que hay muchos más cereales de los que pensábamos, y por mostrarnos lo que es la lucha constante, ánimos con todo y sigue adelante! Un saludo a Jordi Viñas, que a pesar de los malos momentos siempre ha estado ahí como un gran amigo, y la de tiempo que hemos perdido (o invertido!) haciendo el tonto. A Sinue Serra, que nos dejó para ir a una vida mejor (espero que tu proyecto con Google vaya bien!), me alegro mucho de haberte tenido cerca todo este tiempo. Espero que disfrutes de tu pequeño y que le enseñes a ser especial, como ya sabes hacer. Un saludo a Ricard Matas, por su compañerismo desde la carrera hasta el último día de tesis. Tras mucho esfuerzo has conseguido seguir tu camino, así que enhorabuena.

Un saludo a Neus Àgueda, por su sencillez, a Carme Toribio, por sus estudios, a Pere Munar, por su amistad, a Rosa Rodríguez, por sus organizaciones, a Josep Maria Masqué, por su desprendimiento, y a Víctor Zabalza por su compañerismo. Un saludo también a Maria Monguió, Pau Frau, Benito Marcote, Héctor Gil, Álvaro Sánchez, Gemma Busquet y Felipe Alvés. A todos ellos por estar ahí cada día para comer, que ya es mucho! Un saludo también para otros compañeros Adolfo, Santi, Carrasco y los demás.

Como compañero de despacho durante muchos años, también quiero agradecer a Octavi Fors por los ratos compartidos. También quiero agradecer a Francesca Figueras por guiarme en mis primeros momentos en el departamento, por su entusiasmo y pasión por la ciencia.

También del DAM, quiero agradecer el trabajo incansable de JR, que ha ayudado enormemente con todos los trámites burocráticos, dudas y necesidades que han surgido en el departamento. Pronto te darán un premio por tu gran contribución a la ciencia, después de tantas tesis!

Aunque ya empieza a quedar algo lejos, no quiero dejar de agradecer a los compañeros de la carrera por compartir los primeros años de mi preparación como científico. Ellos contribuyeron en algún momento a hacer posible que acabara aquí, escribiendo estas líneas. En especial agradecer a Imma Martínez, que aunque ahora esté lejos, siempre ha estado cerca. También agradecer a Rosa Colom por acompañarme en los últimos años de carrera y los primeros del doctorado.

También saludar a los amigos de toda la vida, gente de Gavà que veo más o menos a menudo. En especial agradecer a Carlos Pinteño por haber estado ahí y haber escuchado mis problemas, tuvieran o no que ver con ciencia. También un saludo para Oriol Lamiel,

Acknowledgments

al que cada vez veo menos, aunque siempre nos quedará el bus. Aunque todo esto les pille un poco lejos, también agradecer a los colegas que de vez en cuando algo aún nos vemos, Kever, Trentor, Jona, Mota, Christian, un saludo!

Quiero agradecer a todas aquellas personas que alguna vez han contribuido a cualquier tipo de mejora del software libre en general, y de los paquetes científicos de Python en particular. Es increíble y emocionante poder participar en algo tan grande y desinteresado, y con tanto potencial, posibilidades y sorpresas como Python, algo que enriquece como científico y como persona. Quiero agradecer a Google su capacidad de unir y transportar ideas, y por su inestimable ayuda para encontrar información. M'agradaria també agrair al Goku per la seva honestitat i per salvar al món en tantes ocasions!

Una tesis doctoral es algo grande, y además intenso y complejo. Más allá de las técnicas, las búsquedas, los datos, los modelos y los resultados, hay algo más importante, y es la estabilidad necesaria para llevarlo todo adelante. La base de ello ha sido, sin ningún tipo de duda, el apoyo de mi familia. Todo esto no hubiese sido posible sin todo el apoyo, incondicional y constante, de mis padres, Martín Moldón y Petra Vara, que han hecho posible algo como esta tesis doctoral. Quiero agradecer a mi hermano mayor, Alberto Moldón, por ser guía y ejemplo durante toda mi vida, por descubrirme ya desde muy pequeño el placer de descubrir. Un abrazo para mi tío Pedro, que me ha enseñado muchas cosas de esta vida, en particular que lo bueno puede ser malo y que lo malo puede ser bueno. Sin duda alguna agradezco también a mis abuelos, que aunque veo extremadamente poco, muchísimo menos de lo que se merecen o lo que me gustaría. Ellos han puesto ahí los apellidos y el alma para sacar adelante una vida dura, y me siento orgulloso de decir que gracias a ellos esta tesis ha sido posible. Y sin olvidar que han hecho posible la dieta del chorizo! Al resto de mis tíos (que son muchos!) y primos (que aún son más), gracias por estar ahí.

Sin más decir que una tesis doctoral es algo grande, extenso pero concentrado, que va más allá de la ciencia y el descubrimiento, y que nada de esto hubiese sido posible sin toda la gente que he conocido a lo largo de mi vida. Gracias a todo aquel que alguna vez aportó su granito de arena en todo el proceso.

Agradezco el soporte económico recibido a través de la beca FPI del Ministerio de ciencia e innovación BES-2008-004564, así como sus estancias que me han permitido hacer ciencia tanto en la Universitat de Barcelona como en otros países e instituciones.

The Very Long Baseline Array is operated by the USA National Radio Astronomy Observatory, which is a facility of the USA National Science Foundation operated under co-operative agreement by Associated Universities, Inc.

The NRAO is a facility of the National Science Foundation operated under cooperative agreement by Associated Universities, Inc.

The European VLBI Network (<http://www.evlbi.org/>) is a joint facility of European, Chinese, South African, and other radio astronomy institutes funded by their national research councils.

This work made use of the Swinburne University of Technology software correlator, developed as part of the Australian Major National Research Facilities Programme and operated under licence.

This research has made use of SAO/NASA's Astrophysics Data System.

This research has made use of the SIMBAD database, operated at CDS, Strasbourg, France.

We acknowledge support by the Spanish Ministerio de Ciencia e Innovación (MICINN) under grants AYA2010-21782-C03-01 and FPA2010-22056-C06-02.

Contents

Resumen de la tesis	xi
1 Introduction	1
1.1 High-energy gamma-ray Astrophysics	1
1.2 Binary systems with gamma-ray emission	2
1.2.1 X-ray binaries	3
1.2.2 Gamma-ray binaries	4
1.3 Possible Scenarios	6
1.4 Radio emission from gamma-ray emitting binaries	8
1.4.1 Radio emission from microquasars	9
1.4.2 Radio emission from colliding wind binary systems	10
1.5 Overview of the thesis	11
2 Synthesis imaging with VLBI	15
2.1 Introduction	15
2.2 Radio telescopes and synthesis imaging	15
2.3 Calibration and imaging	22
2.4 VLBI arrays	27
3 Discovery of extended emission from PSR B1259–63	31
3.1 Introduction	31
3.2 The gamma-ray binary PSR B1259–63	32
3.3 Observations with the LBA and data reduction	34
3.4 The radio structure of PSR B1259–63	36
3.5 Kinematical interpretation of the radio outflow	39
3.6 Discussion and conclusions	40
3.7 Work in progress	43
4 The changing milliarcsecond radio morphology of LS 5039	47
4.1 Introduction	47
4.2 The binary system LS 5039	48
4.3 VLBA observations of LS 5039	50
4.4 Data reduction	51

CONTENTS

4.5	Results	52
4.5.1	Flux density with the VLA	52
4.5.2	Morphology with the VLBA	52
4.5.3	Astrometry of the peak of the emission	55
4.6	Interpretation of the changing morphology	56
4.7	Conclusions	58
5	Periodic morphological changes in the radio structure of LS 5039	59
5.1	Introduction	59
5.2	A multi-epoch VLBA campaign on LS 5039	60
5.3	Data reduction	63
5.3.1	Ionospheric correction	63
5.3.2	Amplitude and phase calibration	65
5.3.3	Phase referencing imaging	66
5.3.4	Self-calibration	67
5.4	Analysis and results	67
5.4.1	Relative astrometry of the peak of the emission	67
5.4.2	Morphology	70
5.5	Compilation of VLBI observations	75
5.5.1	Morphology at larger scales	77
5.6	A model of the outflow of relativistic particles	77
5.7	Discussion and conclusions	85
6	On the origin of LS 5039 and PSR J1825-1446	89
6.1	Introduction	89
6.2	Compact objects in the field of G016.8-01.1	91
6.2.1	The proper motion of the gamma-ray binary LS 5039	91
6.2.2	The nearby isolated pulsar PSR J1825-1446	93
6.3	Astrometry and proper motion of PSR J1825-1446	95
6.3.1	Radio VLBI observations	95
6.3.2	Archival astrometry of PSR J1825-1446	97
6.3.3	Proper motion of PSR J1825-1446	101
6.4	Astrometry and proper motion of LS 5039	101
6.4.1	VLA-PT observation	102
6.4.2	VLBA astrometric project	102
6.4.3	EVN observations	103
6.4.4	Archival data of LS 5039	104
6.4.5	Uncertainties in the position of LS 5039	107
6.4.6	Proper motion of LS 5039	108
6.5	Galactic space velocity	113
6.6	The origin of LS 5039 and PSR J1825-1446	118

6.7	Discussion and conclusions	123
7	VLBI observations of LS I +61 303 within a MAGIC multiwavelength campaign	127
7.1	Introduction	127
7.1.1	Previous VLBI observations of LS I +61 303	128
7.1.2	The September 2007 multiwavelength campaign	129
7.2	Observations and data reduction	130
7.3	Analysis and results I: astrometry	134
7.3.1	Standard phase referencing	134
7.3.2	Connecting the astrometry at 8.4 and 2.3 GHz	136
7.4	Analysis and results II: morphology	143
7.4.1	Morphology at 8.4 GHz	143
7.4.2	Morphology at 2.3 GHz	144
7.5	Discussion and conclusions	147
8	Study of new gamma-ray binary candidates	151
8.1	Introduction	151
8.2	The gamma-ray binary candidate HESS J0632+057	152
8.2.1	Introduction	152
8.2.2	Observations and data reduction	154
8.2.3	Revealing the extended emission of HESS J0632+057	156
8.2.4	Discussion	157
8.3	The gamma-ray binary candidate AGL J2241+4454	161
8.3.1	Introduction	161
8.3.2	The candidate counterpart to the HE source AGL J2241+4454	162
8.3.3	VLBI observations of MWC 656	164
8.3.4	Results and discussion	166
9	Concluding remarks	171
9.1	Summary of the results	171
9.2	Concluding remarks	174
A	Orbital elements in binary systems and constraints to the mass of the compact object	177
A.1	Orbital elements in binary systems	177
A.2	Degeneracy between the mass of the compact object and the orbit inclination	179
B	Free-free absorption in LS I +61 303	183
	References	187

Resumen de la Tesis

Estructura y naturaleza de binarias de rayos gamma mediante observaciones VLBI

Introducción

El trabajo de investigación presentado en esta tesis se basa en el estudio de sistemas binarios que presentan emisión de rayos gamma mediante técnicas de interferometría radio. Las binarias de rayos gamma son sistemas exóticos, formados por una estrella joven y masiva, entorno a la cual orbita un objeto compacto, que puede ser un agujero negro o bien un púlsar joven no acretante. La órbita de estos sistemas es muy excéntrica y/o tiene un periodo orbital muy corto, por lo que en ciertos momentos de la órbita la gran proximidad entre los dos elementos facilita su interacción, que da como resultado la emisión, entre otros rangos energéticos, en rayos gamma. Actualmente sólo se conoce un número reducido de este tipo de sistemas. Sin embargo, la riqueza que proporcionan al campo de la Física en general, y de la Astrofísica en particular los hace únicos, puesto que nos permiten estudiar fenómenos de alta energía en escalas de tiempo cortas, en configuraciones geométricas variables, pero a la vez de forma periódica. En la actualidad, debido en parte al limitado número de sistemas identificados, no se conocen con exactitud sus propiedades ni los fundamentos físicos de su naturaleza.

Estos sistemas binarios, aparte de rayos gamma, presentan emisión en longitudes de onda radio. Esta emisión procede de chorros de partículas relativistas producidas en el sistema, pero que viajan a grandes distancias, del orden de varias unidades astronómicas (AU). El tamaño angular de estos chorros vistos desde la tierra es del orden del milisegundo de arco (mas). Para poder observar estas estructuras es necesario obtener imágenes radio de muy alta resolución angular, que pueden ser conseguidas mediante interferometría de muy larga línea de base (VLBI). En la presente tesis describiremos las técnicas necesarias para conseguir dichas resoluciones, y presentaremos una serie de observaciones de binarias de rayos gamma que tienen como objetivo caracterizar su estructura a pequeña escala.

Metodología

Se han realizado observaciones radio en longitudes de onda centimétricas utilizando varios arreglos de antenas de muy larga línea de base. Para las observaciones se han uti-

lizado diferentes antenas (radiotelescopios) separados por grandes distancias, entre 100 y 10 000 km. Mediante interferometría entre las señales de las antenas, y la técnica conocida como síntesis de imagen, es posible reconstruir la distribución de densidad de flujo en el cielo, y por lo tanto observar radiofuentes con una muy alta resolución angular. Las antenas, situadas en diferentes puntos de la tierra, se sincronizan de manera que observen la misma región del cielo simultáneamente. La simultaneidad se consigue gracias a un programa pre-establecido y al uso de relojes atómicos que coordinan el momento exacto de cada instante de la observación. Estos datos se obtienen en el espacio de Fourier de la imagen del cielo, por lo que su calibración y análisis es complejo. Esto es necesario para obtener imágenes con una resolución angular que depende de la separación máxima entre antenas, en lugar del tamaño de las antenas.

De las seis binarias de rayos gamma conocidas actualmente, cinco de ellas han sido observadas a lo largo de la tesis. Se han preparado campañas observacionales para monitorizar el comportamiento de estos sistemas en diferentes fases orbitales del sistema binario, y se han obtenido datos a diversas frecuencias y resoluciones. En particular se han realizado observaciones con tres instrumentos (arreglos de antenas): el *Very Long Baseline Array* (VLBA), en Estados Unidos, la *European VLBI Network* (EVN), mantenida por una colaboración entre varios países europeos, China y Sudáfrica, y el *Long Baseline Array* (LBA), situado en Australia.

Resumen de resultados

Resumimos brevemente los resultados más significativos obtenidos mediante observaciones VLBI de las siguientes binarias de rayos gamma:

- *PSR B1259–63*. Se ha descubierto emisión extendida y variable con tamaños proyectados de 120 UA. Esta es la primera prueba observacional de que un púlsar joven no acretante orbitando estrellas masivas pueden producir emisión extendida y variable.
- *LS 5039*. Observaciones de este sistema, cuya emisión extendida ya era conocida y se creía persistente, han mostrado que su estructura radio es variable. Mediante el monitoreo de estos cambios a lo largo de un periodo orbital completo (4 días), ha sido posible descubrir que estos cambios, además, son periódicos. Estos resultados han sido utilizados para testear los modelos teóricos propuestos para describir este sistema. Paralelamente se han obtenido medidas precisas de su movimiento propio que han permitido restringir la trayectoria de este sistema en la Galaxia, así como explorar sus posibles orígenes.
- *LS I +61 303*. Este sistema había sido observado en numerosas ocasiones por medio de VLBI, por lo que se conocía la variabilidad orbital de su emisión extendida. Hemos llevado a cabo observaciones radio en el contexto de una campaña multilongitud de onda. Obtuvimos imágenes de la radio fuente en dos frecuencias, que nos

permitieron trazar los cambios morfológicos y astrométricos producidos en 10 días. La similitud de las imágenes respecto a imágenes obtenidas un año antes sugieren que su variabilidad orbital es periódica. El estudio a dos frecuencias muestra que la estructura de la fuente es compatible con la presencia de un chorro de partículas relativistas cuyo eje cruza cerca de la línea de visión del observador. Este hecho puede ser utilizado para testear los modelos mediante simulaciones detalladas del comportamiento de la fuente.

- *HESS J0632+057*. Este sistema fue propuesto como posible binaria de rayos gamma hace tres años. La estrella masiva MWC 148 fue propuesta como contrapartida óptica de esta fuente de rayos gamma. Realizamos observaciones VLBI durante una explosión de rayos X y rayos gamma que tuvo lugar en 2011. La detección de emisión compacta asociada con la estrella MWC 148 permitió asociar unívocamente esta estrella con emisión radio compacta y no-térmica, favoreciendo a su vez la asociación con la fuente gamma. Se realizaron nuevas observaciones 30 días después para monitorizar la evolución de la fuente. La nueva imagen mostró que la fuente también presenta estructura radio extendida. Además, se encontró que el pico de la emisión se produce a distancias de varias UA, y por lo tanto mucho mayores que el sistema binario.
- *AGL J2241+4454*. Finalmente, se llevó a cabo una campaña de observación de la estrella masiva MWC 656, propuesta como contrapartida óptica de la fuente de alta energía AGL J2241+4454. Sin embargo, las observaciones de alta sensibilidad no mostraron contrapartidas radio. Estos resultados muestran que la fuente podría presentar emisión radio transitoria, o bien que la fuente produce chorros de material en rápida expansión, produciendo emisión difusa no observable mediante VLBI.

Conclusiones

En esta tesis se presentan resultados de observaciones VLBI de cinco binarias de rayos gamma. Mediante observaciones con diferentes instrumentos y configuraciones hemos descubierto emisión extendida de dos binarias de rayos gamma, y hemos encontrado cambios estructurales periódicos en otras dos. Estos resultados permiten establecer una base observacional de propiedades comunes de este tipo de sistemas. Este enlace observacional entre sistemas, que por otra parte son muy diferentes entre ellos, posibilitará un detallado estudio teórico de la estructura de estas fuentes, y en particular ayudará a restringir modelos que describen la propagación de estos chorros de partículas relativistas a largas escalas. Por otra parte, las bases comunes permitirán en el futuro identificar otros sistemas similares que presenten las mismas propiedades.

1

Introduction

1.1 High-energy gamma-ray Astrophysics

High-energy gamma-ray Astrophysics has become one of the most interesting and prolific research fields in physics. A huge leap in this field has been possible thanks to the new generation of high-energy detectors observing the sky in the last years. On one hand, satellites like *AGILE*¹ and *Fermi*², in operation since 2007 and 2008, respectively, have provided an accurate view of the whole sky in the energy range from 30 MeV to 300 GeV. They have discovered about one hundred gamma-ray pulsars, some of them millisecond pulsars, studied gamma-ray burst (GRB) in detail, galactic diffuse emission, galactic binary systems, blazars and active galaxies, among other astrophysical objects. Some of their results have implications in fundamental physics, dark matter or cosmic ray acceleration (Abdo et al. 2010a). On the other hand, emission at higher energies, in the range between 100 GeV and several TeV, has been studied by the new generation of Cherenkov telescopes, in particular H.E.S.S.³, the MAGIC Telescopes⁴, and VERITAS⁵, in operation since 2003, 2004, and 2007, respectively. These ground-based telescopes provide unprecedented sensitivity thanks to their large collecting area compared to satellite detectors. This also provides accurate timing capabilities. A wide range of astrophysical sources in different contexts have been studied, like supernovae, pulsars and pulsar wind nebulae,

¹<http://agile.rm.iasf.cnr.it/>

²<http://www-glast.stanford.edu/>

³<http://www.mpi-hd.mpg.de/hfm/HESS/>

⁴<http://magic.mppmu.mpg.de/>

⁵<http://veritas.sao.arizona.edu/>

1. Introduction

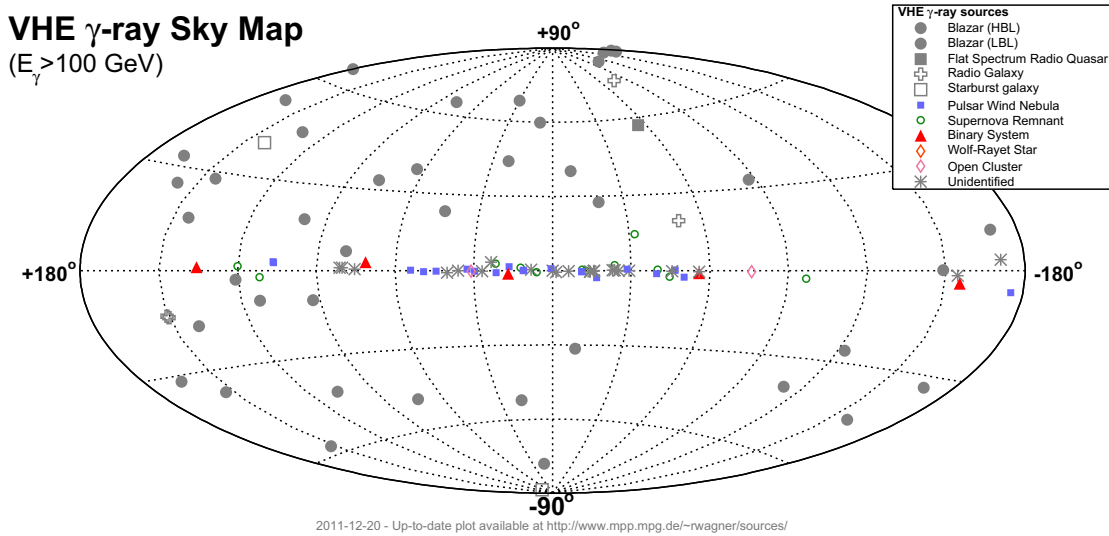


Figure 1.1: VHE gamma-ray sky map as of 2011 December 20 (adapted from <http://www.mppmu.mpg.de/~rwagner/sources/>). 46 extragalactic sources are plotted (grey symbols) together with 61 Galactic sources including pulsar wind nebulae, supernova remnants, binary systems and many unidentified sources.

binary stars, giant molecular clouds, starburst galaxies, clusters of galaxies, and active galaxies (Hinton & Hofmann 2009). In Fig. 1.1 we show the distribution in the sky of the more than 100 sources that have been detected above 100 GeV. The detected high and very-high energy emission can only be caused by non-thermal processes, which imply the presence of particle populations accelerated up to TeV energies. Therefore, astrophysical high-energy sources provide unique physical laboratories to study non-thermal physical systems. In this thesis we focus on the study on the population of galactic binary systems displaying gamma-ray emission known as gamma-ray binaries.

1.2 Binary systems with gamma-ray emission

Some galactic binary systems have been detected in high-energy (HE; > 100 MeV) and/or very-high-energy (VHE; > 100 GeV) gamma rays, showing a broadband spectral energy distribution (SED) from radio to gamma-rays. The definition of gamma-ray binaries as a new population of binary systems can be ambiguous because of our still limited knowledge of these system and the low number of cases known. We will give here a general view of our current knowledge on this topic and a description of what a gamma-ray binary is.

The population of X-ray binaries, with hundreds of known members, are characterised by displaying X-ray emission that dominates the non-thermal broadband spectrum (see the reviews in Fender et al. 2004; Remillard & McClintock 2006, and references therein). The X-ray emission basically depends on the thermal emission from an accretion disc

and/or an optically thin corona or the jet base. These sources present “states” based on the spectral and brightness properties of their X-ray emission (Fabbiano 2006). These states are associated to changes in the configuration of the accretion disc. Those X-ray binaries that display radio emission are known as radio emitting X-ray binaries, and if this emission comes from ejected bipolar relativistic jets they are known as microquasars, in analogy with the extragalactic quasars (Mirabel & Rodríguez 1999). The framework used to describe X-ray binaries was naturally used to describe those binaries presenting predominant gamma-ray emission. However the binaries presenting gamma-ray emission can be divided in two groups based on their behaviour: gamma-ray emitting X-ray binaries and gamma-ray binaries. As an example, in Fig. 1.2 we show the SED of the gamma-ray emitting X-ray binary Cygnus X-3 (top panel) and the gamma-ray binary LS I +61 303 (bottom panel). We describe the main properties of these two populations below.

1.2.1 X-ray binaries

Two X-ray binaries have been detected in gamma-rays thanks to the improvement in sensitivity of the gamma-ray instrumentation. They present a clear signature of the presence of an accretion disc, the characteristics of their broadband emission are determined by their X-ray states, the changes between X-ray states are recurrent but in general unpredictable, and the output of their non-thermal emission is dominated by the X-ray band of the spectrum. In summary, the members of this group share the common features of X-ray binaries and occasionally display gamma-ray emission. Therefore, we will refer to them as gamma-ray emitting X-ray binaries, in analogy with the radio emitting X-ray binaries, which are X-ray binaries that display radio emission. The two gamma-ray emitting X-ray binaries are Cygnus X-1 and Cygnus X-3, whose SED is dominated by the X-ray component from an accretion disc/corona (see Fig. 1.2).

MAGIC observed Cygnus X-1, and evidence ($4.1\text{-}\sigma$ post-trial significance) of TeV emission was found during a short-lived flaring episode (Albert et al. 2007). Sabatini et al. (2010) reported significant transient gamma-ray emission detected by *AGILE* above 100 MeV, although a search of the *Fermi*/LAT data for signs of the *AGILE* flare yielded no significant detection (Hill et al. 2011). Cygnus X-3 displays two X-ray states where transient ejections (soft state) or persistent jets (hard state) are observed. *Fermi*/LAT detected GeV emission during active periods, associated with transitions from/to the soft state (Fermi LAT Collaboration et al. 2009; Corbel et al. 2012). During these active periods, the HE emission displayed orbital periodicity. *AGILE* detected emission peaks during short flares (Tavani et al. 2009; Bulgarelli et al. 2012). No VHE signal has been found so far from data obtained during different X-ray states, including periods when enhanced HE emission was detected (Aleksić et al. 2010). Unsuccessful searches for VHE gamma-ray emission from other X-ray binaries have been conducted: GRS 1915+105 (H.E.S.S. Collaboration et al. 2009), Scorpius X-1 (Aleksić et al. 2011), and SS 433 (Bordas 2009). From now on we will consider this kind of binaries as gamma-ray emitting X-ray binaries.

1. Introduction

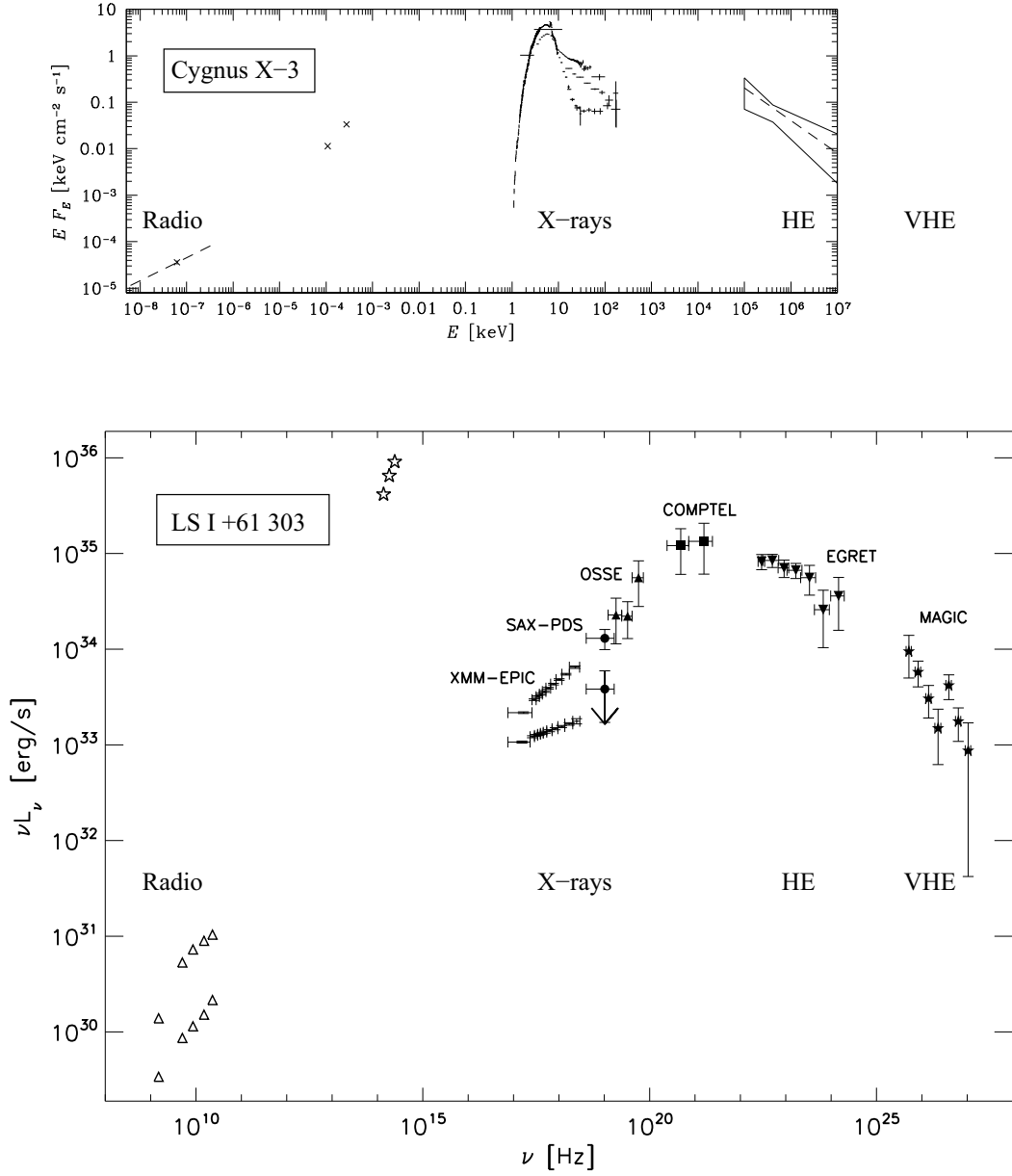


Figure 1.2: Spectral energy distribution (SED) of the gamma-ray emitting X-ray binary Cygnus X-3 (top panel) and the gamma-ray binary LS I +61 303 (bottom panel). Adapted from Zdziarski et al. (2012) and Sidoli et al. (2006), respectively.

1.2.2 Gamma-ray binaries

There is a second group of binary systems displaying gamma-ray emission at HE and/or VHE that presents a different behaviour. In particular, the spectral and brightness properties appear to be synchronised with the orbit of the binary system and they do not show

evidence of the presence of an accretion disc. The latter point has implications in the nature of the systems, as explained below. Also, the non-thermal emission of this second group is dominated by MeV–GeV photons. There are three sources that share these properties, namely PSR B1259–63, LS 5039, and LS I +61 303, and all of them have been clearly detected above TeV energies. In Fig. 1.2) we show an example of the broadband SED of LS I +61 303.

PSR B1259–63 has an orbital period of 3.4 yr, and it has been detected recursively by H.E.S.S. during the last three periastron passages (Aharonian et al. 2009) showing a clear orbital modulation. The source has also been detected by *Fermi*/LAT (Abdo et al. 2011), although only one periastron passage has occurred since the satellite started operations. LS 5039, with a short period of 3.9 days, has been detected at HE (Paredes et al. 2000; Abdo et al. 2009b) and at VHE up to 4 TeV (Aharonian et al. 2005a, 2006). The X-ray emission is periodic and stable (Kishishita et al. 2009), and shows no hints of transient states. Interestingly, LS 5039 displays the most accurate and stable periodicity from X-rays to TeV energies (see e.g. Hadasch et al. 2012). Finally, LS I +61 303 also shows orbital modulation of its X-ray (Paredes et al. 1997), HE (Abdo et al. 2009a), and VHE (Albert et al. 2009) emission, although recent data suggests that the global emission can change on longer time scales (Hadasch et al. 2012). Other binary systems have been proposed to be gamma-ray binaries in the last three years, for instance HESS J0632+057 (Hinton et al. 2009), 1FGL J1018.6–5856 (Fermi LAT Collaboration et al. 2012a), and AGL J2241+4454 (Williams et al. 2010), the first two being recently confirmed.

One clear difference between these two populations is the SED (see Fig. 1.2). We have aligned the panels so that the horizontal scale represents the same energy. The SED of Cygnus X-3 is dominated by the emission at X-rays, which has a clear signature of an accretion disc (thermal component). The source displays HE emission although it has not been detected at VHE (Aleksić et al. 2010). On the other hand, the SED of the gamma-ray binary LS I +61 303 is dominated by the MeV–GeV photons (10^{20} to 10^{23} Hz). The X-ray emission does not show signatures of an accretion disc (the data at higher luminosity in radio and X-rays correspond to the periodic outburst). The source has also been detected at VHE. Interestingly, for Cygnus X-3 the HE flux is ~ 1.5 orders of magnitude lower than the X-ray flux, whereas for LS I +61 303 it is ~ 1.5 orders of magnitude higher. These two examples show the global features of the two populations, although each individual source has its own particular features.

We note that the star η Car, also a binary system, might have been detected at HE (see Abdo et al. 2010b and references therein). It is a colliding wind binary (non-accreting) composed of a very massive variable star and a secondary main-sequence companion. It has suffered important eruptive events in the last centuries, not seen in the other gamma-ray binaries. Also, this source is the only of the considered binary systems that harbours a star as a secondary, instead of a compact object. Although similar physical processes are possibly taking place in this system, given the differences in composition and behaviour

1. Introduction

Table 1.1: Main properties of binary systems (massive star+compact object) with gamma-ray emission. Adapted from Table 1 in Paredes (2011).

Parameters	Cygnus X-1	Cygnus X-3	PSR B1259–63	LS I +61 303	LS 5039
Star	O9.7Iab	WN _e	O9.5Ve	B0Ve	O6.5V((f))
Compact obj.	BH	?	NS	?	?
P_{orb}	5.6 d	0.2 d	1237 d	26.5 d	3.9 d
Periodicity					
Radio	5.6 d	persistent+ outbursts	48 ms 3.4 yr	26.5 d 4.6 yr	persistent
Infrared	5.6 d	–	–	27.0 d	variable
Optical	5.6 d	–	–	26.4 d	variable
X-ray	5.6 d	0.2 d	variable	26.7 d	3.9 d
> 100 MeV	flare ^a	0.2 d ^{a,b}	variable ^{a,b}	26.6 d ^b	3.9 d ^b
> 100 GeV	flare ^d	–	periodic ^c	26.8 d ^d	3.9 d ^c

Notes: we do not include here other systems discovered during the last three years because several properties are unknown or poorly constrained.

Detected by: ^a *AGILE*, ^b *Fermi*, ^c H.E.S.S., ^d *MAGIC*.

with the other gamma-ray binaries, we will not consider this special case in the discussions of this thesis.

In summary, we can see that two phenomenological populations of binaries can be distinguished based on the general behaviour of their X-ray/HE/VHE emission, either associated with an X-ray binary state or showing periodic orbital modulation without state changes. A short summary of the properties described above is shown in Table 1.1. In the next Section we will describe the two general scenarios in which these sources can be understood.

1.3 Possible Scenarios

In the known gamma-ray emitting binaries the optical companion is always a young massive star. The VHE gamma-ray emission produced in these systems can be interpreted as the result of inverse Compton upscattering of stellar UV photons by relativistic electrons, although hadronic models do exist as well. The acceleration of electrons can be explained by two exclusive scenarios: acceleration in the jet of a microquasar powered by accretion (Paredes et al. 2006; Bosch-Ramon et al. 2006 and the review in Bosch-Ramon & Khangulyan 2009), or shocks between the relativistic wind of a young non-accreting pulsar and the wind of the stellar companion (Maraschi & Treves 1981; Tavani & Arons

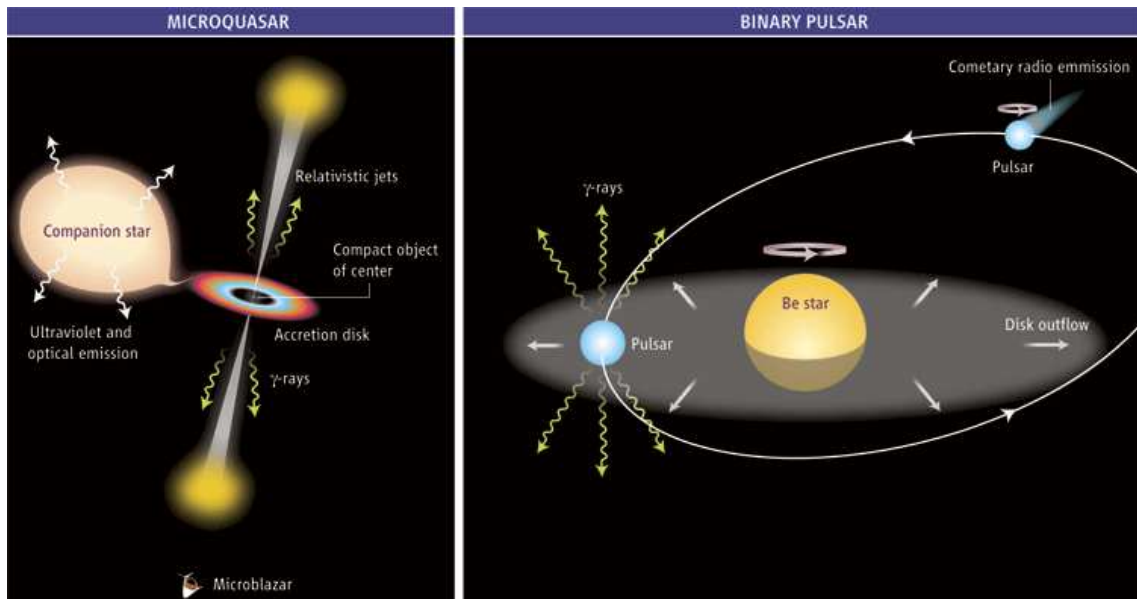


Figure 1.3: Sketch of the two scenarios proposed to understand the gamma-ray emission from binary systems with compact objects. Image from Mirabel (2006).

1997; Dubus 2006; Khangulyan et al. 2007). See a sketch of these scenarios in Fig. 1.3.

Microquasar scenario

The microquasar scenario is based on the presence of an accreting compact object. The gravitational well of this compact object captures material from the companion star that forms an accretion disc that is extremely bright in X-rays. These systems can display bipolar jets of relativistic particles, either persistent or transient, that can be detected in radio or X-rays. Within this scenario, leptonic models predict that the high-energy emission in microquasars is produced by scattering of UV photons of the optical star by the relativistic electrons in the jet. More details are provided in Paredes et al. (2006), Bosch-Ramon et al. (2006) and the review in Bosch-Ramon & Khangulyan (2009). Hadronic models have also been proposed, based on the interaction of wind ions and protons in the jets (Romero et al. 2003). In summary, in this scenario the high-energy emission is powered by accretion.

Young non-accreting pulsar scenario

On the other hand, if the compact object is a young non-accreting pulsar with an intense relativistic wind, the particle acceleration would be produced in the shocks between the relativistic wind of the pulsar and the stellar wind of the massive companion star. We note that this scenario is also known as binary pulsar scenario, or colliding winds scenario. This scenario was first proposed by Maraschi & Treves (1981) to explain the high energy

1. Introduction

emission of LS I +61 303. Several models have been developed since then in Tavani & Arons (1997), Kirk et al. (1999), Dubus (2006), Khangulyan et al. (2007), and Bogovalov et al. (2008, 2012), where the interested reader can find more details. Hadronic models have also been proposed for this scenario (Chernyakova et al. 2006). In summary, in this scenario the high-energy emission is powered by rotational energy of a pulsar.

Relation with the compact object nature

There are two cases in which we can unambiguously associate a source with one of these two scenarios. First, the determination of the mass of the compact object can reveal its nature, either black hole or neutron star. In case the system contains a black hole the non-accreting scenario would be ruled out. Radial velocity observations of spectral lines of the stellar companion are in general not suitable to constrain the mass of the compact object in the known systems because there is a degeneracy between the inclination of the orbit and the mass of the compact object. This is an important issue, and we explain this limitation in more detail in the context of the determination of the orbital elements of a binary system in Appendix A. Despite this degeneracy, an independent determination of the system inclination would yield the mass of the compact object.

A second criterion to discriminate between the two scenarios is the detection of pulsed emission. Such a detection would imply the presence of a pulsar, whose properties can be used to discern between an accreting and a non-accreting pulsar. Non-accreting pulsars display a powerful relativistic wind that avoids the infall of material from the companion. However, direct detection of pulsations may be unfeasible in binary systems with close orbits and powerful massive companions because of free-free absorption (see Dubus 2006). A discussion in the particular case of LS I +61 303 is shown in Appendix B.

1.4 Radio emission from gamma-ray emitting binaries

Gamma-ray emitting binaries are known to display non-thermal synchrotron radio emission. Their flux density is of the order of 0.1–100 milliJansky (mJy)⁶, and usually their spectral index α (where $S_\nu \propto \nu^\alpha$) is negative, being α usually between -0.5 and 0 . Some sources, such as Cygnus X-3, display radio outbursts up to 20 Jy. The radio emission is produced by cooling processes of the relativistic electrons of the outflow, either a collimated jet or an outflow of shocked particles. An electron with energy E_e in a magnetic field B produces synchrotron emission concentrated around a given characteristic frequency

$$\nu_c(\gamma, B) = \frac{3}{4\pi} \frac{q_e B \sin \phi}{m_e c} \frac{E^2}{(m_e c^2)^2}, \quad (1.1)$$

where ϕ is the angle between the electron velocity and the magnetic field, and m_e and q_e stand for the electron mass and charge, respectively, and c is the speed of light (see

⁶The flux density unit Jansky (Jy) is defined as: $1 \text{ Jy} = 10^{-26} \frac{\text{W}}{\text{m}^2 \text{ Hz}} = 10^{-23} \frac{\text{erg}}{\text{s cm}^2 \text{ Hz}}$.

(see Pacholczyk 1970, for a detailed discussion on this topic). Averaging over ϕ (isotropic distribution of velocities), and considering the acceleration of the electron induced by the magnetic field, the energy loss rate due to the synchrotron process can be written as

$$\left. \frac{dE}{dt} \right|_{\text{sync}} = -\frac{4}{3} c \sigma_T \frac{B^2}{8\pi} \frac{E^2}{(m_e c^2)^2} \quad (1.2)$$

where $\sigma_T = 8\pi r_0^2/3$ is the Thomson cross section. The corresponding cooling time of the relativistic electrons is

$$t_{\text{sync}} = \frac{E}{|\dot{E}|} = \frac{3}{4} \frac{8\pi (m_e c^2)^2}{B^2} \frac{1}{c \sigma_T} \frac{1}{E_e} \simeq 4 \times 10^5 \left[\frac{E_e}{\text{GeV}} \right]^{-1} \left[\frac{B}{\text{G}} \right]^{-2} \text{ s}. \quad (1.3)$$

From Equation 1.1 we can see that electrons with energies of 0.5 GeV (Lorentz factors $\gamma = 1000$) produce synchrotron emission at radio frequencies, around 8.6 GHz (~ 4 cm wavelength) for a magnetic field of 1 G. Using Equation 1.3 we can estimate the lifetime of electrons producing radio emission at this frequency, which is ~ 10 days if we ignore adiabatic losses. The bulk velocity of the outflows in gamma-ray emitting binaries, which are also relativistic, allows these electrons to reach long distances. For velocities of $0.05\text{--}0.5c$, electrons can produce emission up to distances of about 40–400 AU (less when considering the adiabatic energy losses). These galactic sources are at distances from Earth of the order of the kpc. Consequently, the radio outflows can easily reach projected angular distances of the order of milliarcseconds (mas), which are directly observable by means of very long baseline interferometry (VLBI) at radio wavelengths.

Although we are considering non-thermal emission, it is common to use the brightness temperature, T_B , of a radio source. T_B is defined as the temperature a black body in thermal equilibrium would be in order to produce the intensity measured from the source. It can be estimated from the detected flux density (S_ν) at a particular frequency (ν) and the angular size of an emitting region (θ) from the relation

$$\left[\frac{T_B}{\text{K}} \right] = 1.76 \times 10^3 \left[\frac{\nu}{\text{GHz}} \right]^{-2} \left[\frac{\theta}{\text{arcsec}} \right]^{-2} \left[\frac{S_\nu}{\text{mJy}} \right] \quad (1.4)$$

1.4.1 Radio emission from microquasars

In the microquasar scenario the radiation at GHz frequencies is interpreted as emission from relativistic jets (collimated ejecta that have opening angles $\lesssim 15^\circ$) emanating symmetrically from the region close to the compact object (Mirabel & Rodríguez 1999). The plasma clouds expand adiabatically while they propagate through space at relativistic bulk velocities. Relativistic Doppler effect enhances the flux density and the apparent transverse velocity of the components of the approaching jet, and produces the inverse effect on the receding jet. The different flux densities of the components provides information on the inclination of the jet with respect to the line of sight of the observer and the bulk



Figure 1.4: This illustration shows the various zones around a pulsar (bright white dot) that is producing a wind of high energy particles as it moves supersonically through the interstellar medium. The image is from NASA/CXC/SAO.

velocity of the jet. These properties can change in case the jet suffers precession or an intense interaction with the medium or the wind of the optical star, specially for binaries with small orbits.

1.4.2 Radio emission from colliding wind binary systems

In the non-accreting pulsar scenario the shocked material is contained by the stellar wind behind the pulsar, producing a bow shaped nebula extending away from the stellar companion (see Dubus 2006 and references therein). The high energy emission might be produced in the region where the wind pressures are balanced, while a tail of accelerated particles forms behind the pulsar. The cooling processes of these accelerated particles along the expanding flow produce the non-thermal broadband emission from radio to X-rays. The global trend of the outflow should be similar to the one expected in isolated pulsars moving through the ISM (see Fig. 1.4) but, as a consequence of the orbital motion of the pulsar around the massive star, the tail of the flow is bent following an approximately elliptical path during the orbital cycle. Detailed hydrodynamical simulations conducted in the last few years have shown that the outflow structure is complex, and might suffer violent instabilities (see Bosch-Ramon et al. 2012, and references therein). In this context, the scenario provides two main predictions about the radio behaviour on mas scales. On one hand, it is expected that the direction of the extended emission changes periodically with the pulsar orbital motion. On the other hand, the peak of the radio emission should trace an ellipse of a few mas because the emission becomes optically thin at distances of ~ 1 mas (Dubus 2006).

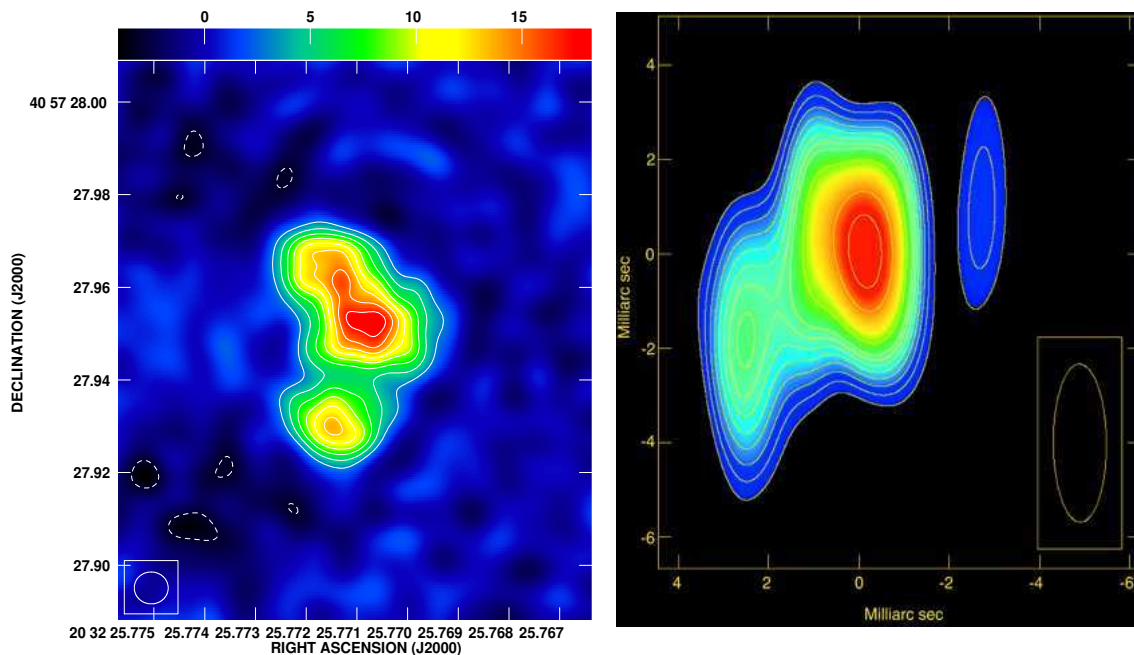


Figure 1.5: The radio emission from the microquasar Cygnus X-3 (left) and from the gamma-ray binary LS 5039 (right) as observed by means of VLBI. A main core and extended emission can be seen as a projection of the outflow of radio emitting particles. Either the microquasar or the non-accreting pulsar scenarios can explain the general morphology of these systems, although an accurate analysis can provide hints of their nature. The images in the left and right panels are adapted from Tudose et al. (2007) and Paredes et al. (2000), respectively.

Despite the different powering source in these two scenarios, the expected morphology, based on the projection on the sky of the outflow of emitting particles, might be very similar in particular cases. See for instance the two images shown in Fig. 1.5, where we can see that the radio emission from Cygnus X-3 (left panel) and from LS 5039 (right panel) are dominated by a bright core and display extended bipolar emission. A detailed analysis of the temporal and morphological properties of the VLBI radio emission from these sources can reveal the evolution of the outflow of accelerated particles, which ultimately reflects the nature of the source itself.

1.5 Overview of the thesis

In this thesis we focus on the study of the radio emission of gamma-ray binaries on mas scales. As quoted above, only six binary systems have been proposed to be gamma-ray binaries, and some of them are currently only candidates. In Table 1.2 we list the main optical and orbital properties of the known gamma-ray binaries. The wide range of different orbital periods and eccentricities provides a diversity of ambient conditions

1. Introduction

in which the physical processes take place. The diversity of systems, together with the repeatability of the conditions within each system, makes gamma-ray binaries excellent physical laboratories in which high energy particle acceleration, diffusion, absorption, and radiation mechanisms can be explored.

However, at the time of beginning this thesis, only two gamma-ray binaries had been observed with VLBI. LS I +61 303 had been extensively observed, showing different and puzzling morphologies (Massi et al. 1993; Peracaula et al. 1998; Paredes et al. 1998; Massi et al. 2001, 2004; Dhawan et al. 2006). For LS 5039, 5 GHz VLBI observations were conducted in the past, always showing a central core and bipolar radio jets (Paredes et al. 2000, 2002). One of the aims of the works presented in this thesis is to increase the VLBI observations on gamma-ray binaries to establish a wider base from which a detailed discussion on the nature of gamma-ray binaries can be undertaken.

In Chapter 2 we give an introduction to synthesis imaging with VLBI, which is the technique used to obtain most part of the observational results obtained through all the thesis.

In Chapter 3 we present observations on PSR B1259–63, one essential gamma-ray binary because it is the only one in which the presence of a pulsar has been confirmed. Consequently, this is a key system, considered as a reference of the properties expected from the non-accreting pulsar scenario, and it is used as a link to understand the other gamma-ray binaries. However, its mas scale structure had not been revealed, in part because of its long period of 3.4 yr. We present observations conducted close to the periastron passage of this eccentric binary system that provide a direct view of the outflow of radio-emitting particles.

In Chapter 4 we present two VLBI observations of LS 5039 obtained at different orbital phases of the binary system, and we interpret the results in the context of the two scenarios presented above. To further explore the radio emission of the source we conducted a VLBI campaign to monitor the structure of LS 5039 during a whole orbital cycle. The results of this campaign are presented and discussed in Chapter 5. We find a clear orbital modulation, and we interpret it by modelling the evolution of the outflow of accelerated particles, which is tested with a compilation of all the high-resolution VLBI observations of the source. On the other hand, VLBI observations provide, apart from the high resolution images, very accurate astrometry, which can be used to obtain the proper motion of a radio source and reveal its origin in the Galaxy. In Chapter 6 we present two astrometric studies, one for LS 5039 and one for a nearby pulsar, aimed to explore the possible origins of these sources.

For LS I +61 303, whose radio structure was already known for very different orbital phases, we conducted observations in the context of a multi-wavelength campaign on behalf of the MAGIC Collaboration, which included radio, optical, X-ray, and VHE gamma-ray observations aimed to understand the source periodic outbursts. Our supporting VLBI observations revealed interesting morphological and astrometric results, which we present

Table 1.2: Orbital properties of the known and candidate gamma-ray binaries (ordered by increasing orbital period). The table is adapted from Casares et al. (2012b). Only two sources had been observed with VLBI before this thesis.

Name	Spectral type	M_{opt} [M_{\odot}]	i [$^{\circ}$]	P_{orb} [day]	e	$a(1 - e)$ [AU]	$a(1 + e)$ [AU]	d [kpc]	Reference	VLBI
LS 5039 ^a	O6.5 V((f))	21–50	> 12	3.91	0.35	0.09	0.19	2.9	(1), (2)	Yes
1FGL J1018.6–5856	O6 V ((f))	~37	–	16.58	–	–	–	~5.4	(3), (4)	No
LS I +61 303 ^b	B0 Ve	10–15	> 10	26.50	0.54	0.19	0.64	1.9	(5), (6), (7), (8)	Yes
AGL J2241+4454 ^c	B3 IVne+sh	6–10	67–80	60.37	0.40	0.38	0.89	~2.6	(9), (10)	No
HESS J0632+057 ^d	B0 Vpe	13–19	47–80	321	0.83	0.40	4.35	~1.4	(11), (12), (10)	No
PSR B1259–63 ^e	O9.5 Ve	31	19–31	1236.79	0.87	0.93	13.44	2.3	(13), (14), (15)	No

References: (1) Casares et al. (2005b); (2) Casares et al. (2012a); (3) Napoli et al. (2011); (4) Fermi LAT Collaboration et al. (2012b); (5) Gregory (2002); (6) Casares et al. (2005a); (7) Aragona et al. (2009); (8) McSwain et al. (2010); (9) Williams et al. (2010); (10) Casares et al. (2012b); (11) Aragona et al. (2010); (12) Bongiorno et al. (2011); (13) Johnston et al. (1994); (14) Wang et al. (2004); (15) Negueruela et al. (2011).

Other names for which the sources are known:

^a HESS J1826–148, 1RXS J182615.1–145034

^b 2CG 135+01, HIP 12469

^c HD 215227, MWC 656

^d HD 259440, MWC 148

^e LS 2883

1. Introduction

in Chapter 7.

We also explored the radio emission on mas scales of new candidates proposed to be gamma-ray binaries. In particular, we conducted target of opportunity observations following an X-ray outburst alert from HESS J0632+057. The observations revealed, for the first time, the radio structure of the source, which we present in Chapter 8. We also conducted a multi-epoch campaign aimed to search for compact radio emission from AGL J2241+4454. In this case, however, the source was not detected, so we discuss the results and compare them with the expected behaviour of the source inferred from the other gamma-ray binaries.

Finally, we summarise the results of this thesis in Chapter 9, where we describe how our view of the radio emission of gamma-ray binaries has changed in the last years.

2

Synthesis imaging with VLBI

2.1 Introduction

The observational results in this thesis are mainly based on radio observations conducted using very long baseline interferometry (VLBI). Here we present a general introduction to the technique without describing in detail all the procedures required to obtain and process the data. The aim of this section is to show the context and the meaning of concepts that are used in the thesis and have some relevance in the interpretation of the data or in the discussion of the results. Radio interferometry by means of very long baselines is a very wide and technical topic that has been extensively described in the literature, where the interested reader can find all the details (e.g. Kraus 1973, Taylor et al. 1999, and Burke & Graham-Smith 2009). A detailed discussion on calibration techniques for VLBI can be found in Moran & Dhawan (1995).

2.2 Radio telescopes and synthesis imaging

The receivers

Observations at cm wavelengths are conducted using radio antennas, or radio telescopes, which are composed of a parabolic reflector that collects electromagnetic waves and a radio receiver that transforms the collected radiation into electrical current. The receiver, or feed, is located at the focal plane of the antenna. As an example of antenna participating in VLBI observations we show the Parkes radio telescope in Fig. 2.1, where the dish and the feed can be seen. There are dedicated feeds optimised for each particular range of frequen-

2. Synthesis imaging with VLBI

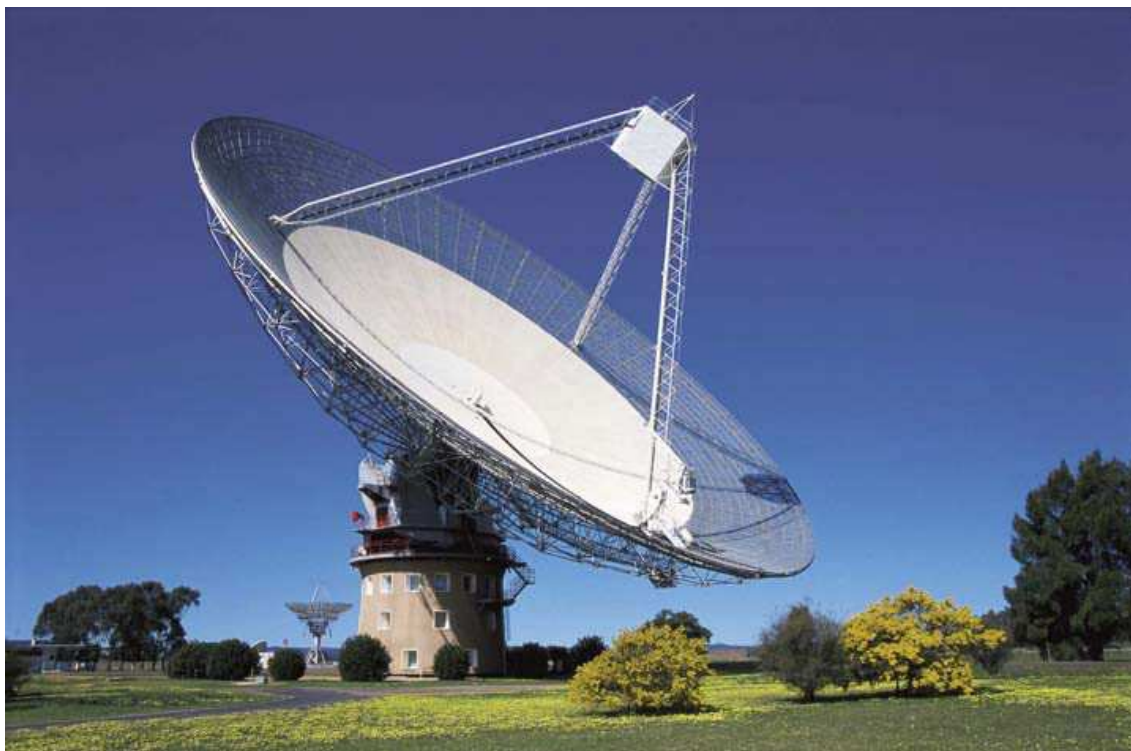


Figure 2.1: The Parkes radio telescope, “The Dish”, is a 64-m diameter radio telescope in New South Wales, Australia.

cies, called bands. The bands have been historically named following the old classification used for radar. The L band covers the 1–2 GHz range, the S band 2–4 GHz, the C band 4–8 GHz, and the X band 8–12 GHz, among others. An electromagnetic wave induces an electrical current at a certain frequency, and consequently the total power collected can be enhanced by adding the signal received at different frequencies. Radio telescopes observe simultaneously at a large number of frequencies by dividing the signal in channels that cover frequency ranges of a few kHz. The antenna feed employs a large number of filters, each tuned to a separate frequency and followed by a separate detector to produce a multichannel, or multifrequency, receiver. Combining several hundreds/thousands separate frequency channels it is possible to obtain total bandwidths of about several MHz, although the new generation of receivers have wide-band feeds providing up to GHz bandwidths. Besides, the incoming electromagnetic wave can be decomposed into two orthogonal polarised components. It is common to decompose the radiation into left- and right-handed circular polarisations. These two components are normally received and recorded separately. In summary, each detector records a single polarisation of an electromagnetic wave and divides the signal into individual frequency channels that are combined to extend the bandwidth and consequently improve the sensitivity of an observation.

Despite the spectral and polarisation capabilities, the receiver is a simple dipole de-

tector that cannot directly reproduce a 2D image of the brightness distribution in the sky because it only records intensity variations on the total power received. When using one station (single dish), images can be obtained by mapping the brightness distribution in different directions. This requires to point the antenna towards as many different directions as pixels needed in the image and, although not very efficient, this procedure is commonly used. Another option is to use focal plane arrays, which are arrays of receivers placed at the focus of the antenna.

At radio wavelengths, the distortions introduced by the atmosphere are less important than at optical wavelengths, and radio telescopes usually work at the diffraction limit. The diffraction limit on the resolution of any telescope is proportional to $\frac{\lambda}{D}$, where λ is the observed wavelength and D is the diameter of the telescope. For a 25-m dish, observations at 5 GHz (6 cm wavelength) provide an angular resolution of 5 arcmin, which is a poor resolution for many scientific cases in radio astronomy.

Synthesis imaging

The resolution of a radio observation can be significantly improved by using aperture synthesis. The principles of interferometry can be used to combine the signals of two or more radio antennas to synthesise a single image with a resolution that depends on the separation of the antennas instead of their diameter. Two antennas observing a source in the sky receive the same signal with a time delay that depends on the positions of the antennas with respect to the source, which produces interference fringes (see Fig. 2.2). When observing a region of the sky, the difference in path lengths from each point of the sky to the elements of the interferometer varies when moving in the direction parallel to the antenna separation. The result is a superposition of the total power from the sky modulated by a sinusoidal oscillation pattern. The measured signal from each pair of antennas thus depends on the detailed nature of the radio brightness distribution in the sky and the separation of the antennas. Therefore, two antennas are only sensitive to one direction in the sky (perpendicular to their projected separation). Combining the signal of several pairs of antennas it is possible to reconstruct the source brightness distribution in the sky.

Although the antennas are usually fixed in a position, the Earth rotation yields different relative positions of each pair of antennas so that a sufficient number of antenna orientations, or patterns in the sky, can be obtained to produce an image of a radio source. For instance, antennas separated 0.1–10 km provide sub-arcsec resolution at cm wavelengths (frequencies of a few GHz). VLBI operates with antennas separated 100–10 000 km, which traditionally have been disconnected from each other. With these antenna separations it is possible to obtain images with very-high angular resolution of the order of milliarcseconds (mas) at cm wavelengths.

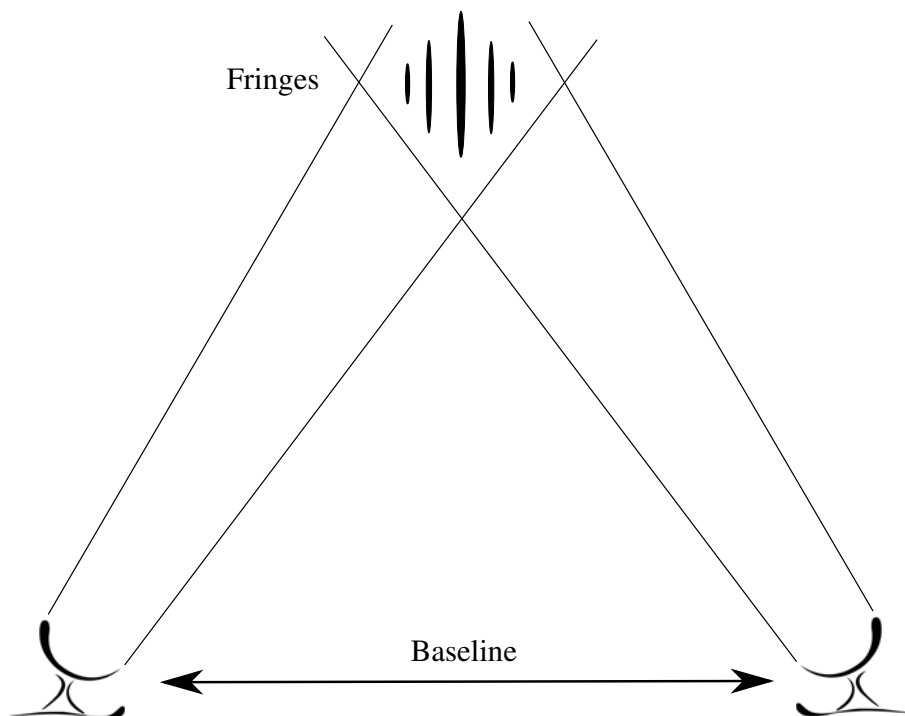


Figure 2.2: Sensitivity pattern fringes from a two-element interferometer.

Correlation and visibilities

We are interested in the product of the time-dependent signals of each pair of antennas. The raw signal from each antenna is recorded at a rate of several million samples per second, and it is normally digitised using two bits to describe each sample. The signal produced in the receiver goes through a local oscillator that reduces the frequency so it can be better manipulated by the system electronics. The total bandwidth is then separated in several subbands, normally called IFs (Intermediate Frequency). The number of subbands is usually about eight, and each of them contains the same number of channels for adjacent, or at least close, frequencies. The signal is ready to be processed by the correlator.

As commented above, there is a delay between the signals received at the feeds of two antennas depending on their geometrical layout, in particular their relative positions or separation, defined as the baseline \vec{B} . Taking into account this time-dependent delay, the signals are cross-correlated, or multiplied in the correlator, which takes into account the power received by the antennas. After the multiplication between two antenna signals the output is averaged in time in order to reduce the data volume. Typical integration times are of one or two seconds. For convenience, the output can be written as a complex number called visibility. The amplitude of the visibility is proportional to the product of the gains of the antennas, whereas the visibility phase contains the information on the baseline length and orientation. The visibility is the output magnitude from the correlator,

and it is the basic element in radio interferometric data. One visibility, which is a complex number, is measured for each pair of antennas, frequency, polarisation, and at each time interval. It can be demonstrated that the visibilities from an interferometric observation are the Fourier transform of the source brightness distribution in the plane of the sky under certain simplifying assumptions (Thompson et al. 1986).

The signal cross-correlation is performed in a main powerful computer, which can be of two different types. Avoiding the technical details, basically the XF correlator first does the multiplication (X) of the signals and then obtains the Fourier transform (F), whereas the FX correlator uses an inverted procedure (see details in Deller et al. 2007). On the other hand, the correlation has been traditionally performed in hardware correlators because of the intensive computational necessities. However, the development of computing equipment in the last decades has allowed the correlation to be performed by software in relatively inexpensive computers, which are suitable for parallel computing and are much easier to maintain and upgrade than a dedicated hardware correlator.

The correlation is conducted in the correlator while the antennas can be located at long distances, even in different continents. For this reason, the VLBI correlation of the data is not performed in real time. The signals of each telescope are recorded in-situ in high-capacity data discs that are later mailed to the central correlation site. The correlation is performed a few days/weeks after the observation. A high precision atomic clock at each antenna makes possible the synchronisation of the signals from different telescopes.

As a summary of the correlation process, the signal has been divided in a number of subbands (IFs), each of them containing different frequency channels, and has been digitised using one or two bits per sample. If the observations were conducted recording the right- (RCP) and the left- (LCP) hand circular polarisations, the correlator can compute four signal multiplications, RR, LL, RL, LR. Different combinations of these correlator products yield the different Stokes parameters. In the observations of this thesis we use the total intensity, defined as $I = (RR + LL)/2$. Every combination of these parameters produces one visibility for each integration time interval. Increasing the number of antennas, the bandwidth, and the number of IFs or polarisations, increases the total data collected, and therefore improves the sensitivity of the observation. The total bit rate from each antenna, computed as the sum of the information recorded, is an estimate of the sensitivity of the observation (besides the size of the antennas). A rule to compute the total data rate in Mbps is to multiply the number of basebands by the samples per second and the bit-sample used. The number of basebands is the number of subbands (IF) at each polarisation. The number of samples, in units of 10^6 samples per second, can be computed as two times the bandwidth of the subband in MHz, for example an 8 MHz subband contributes with 16 Msamples/s. For instance, the standard VLBA¹ mode v6cm-256-8-2-L.set is a configuration setup for observations at 5 GHz (6 cm wavelength) with 8 subbands, 2 bit-sampling and one single polarisation (left-hand).

¹The Very Long Baseline Array

2. Synthesis imaging with VLBI

We have one single polarisation and 8 subbands, therefore there will be 8 IFs. The total data rate is $8 \text{ subbands} \times 16 \text{ Msamples/s/subband} \times 2\text{-bits/sample} = 256 \text{ Mbps}$. The EVN² allows observations with 8 IFs per polarisation, dual polarisation (RR and LL), each subband with a bandwidth of 16 MHz and two bit-sampling. The total data rate is $16 \text{ subbands} \times 32 \text{ Msamples/s/subband} \times 2\text{-bits/sample} = 1024 \text{ Mbps}$. Assuming the same conditions and antennas, the sensitivity provided by the second configuration would be approximately two times better than by the first configuration.

uv coverage

The visibilities obtained from the correlator are usually expressed in the rectilinear coordinate system (u, v, w) . w is defined in the direction towards the observed source, and (u, v) is a plane perpendicular to that direction. These coordinates measure linear distances, and it is convenient to express them in units of the observed wavelength. The u and v coordinates of a visibility correspond to the projected antenna separation as seen from the source, as shown in Fig. 2.3. The figure also shows how the Earth rotation changes the relative position of a pair of antennas with time, yielding different visibilities at different places of the uv plane. Since the true intensity distribution in the sky is real whereas the visibilities are complex, the visibility evaluated at position (u, v) is the complex conjugate of the one at $(-u, -v)$, and therefore a single visibility provides two values in the uv plane. The best possible uv coverage for a particular array is obtained for a full track, which consists of 12 h of continuous observation. The better the coverage of the uv plane is, the more info will be available to obtain the source brightness distribution in the sky. In the left panel of Fig. 2.4 we show the distribution of visibilities for a real VLBA observation of a source at declination -17° during 6 hours. Only one visibility every ~ 4 minutes for one IF is displayed. In the zoomed region in the right panel we show the uv position for different IF subbands. Since uv distances are measured in units of wavelength, the slightly different central frequency of each IF provides uv positions at different radial distances.

Small distances in the uv plane correspond to antennas that are close, and therefore they are sensitive to large angular spacings (low resolution). Large uv distances correspond to separated antennas, which provide highest resolution. The baseline separation B and the observed wavelength λ determine the detectable angular scales through the diffraction limit relation $\theta = 1.22 \frac{\lambda}{B}$, where θ is the angular scale in radians. It is important to note that structures on angular scales significantly larger than the fringe spacing formed by the shortest baseline are not measured. The relation used to compute the angular scale in rad and mas to which a particular baseline in units of $10^6 \lambda$ is sensitive is obtained from

²European VLBI Network

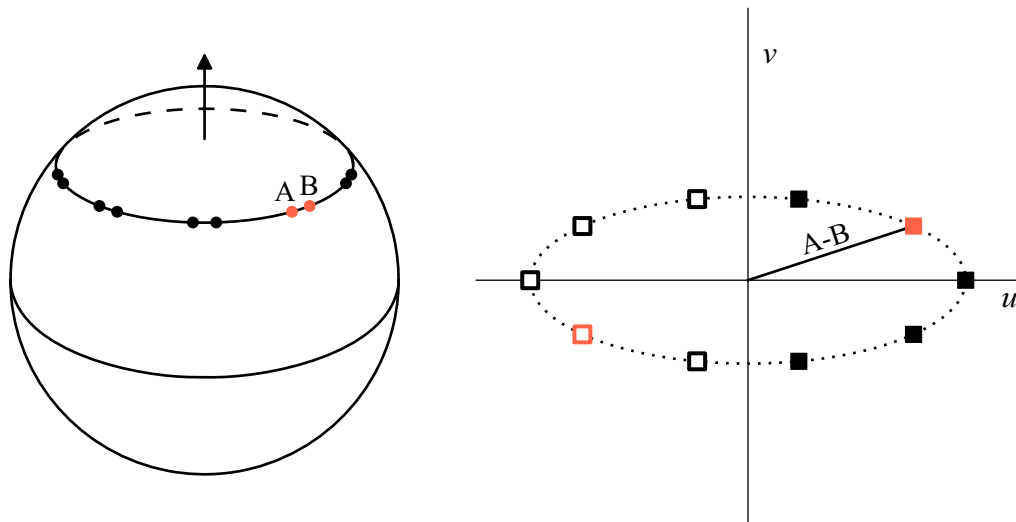


Figure 2.3: *Left*: Sketch of the evolution of a baseline with time. The absolute separation between the two antennas (black circles) remains constant, but their projected distance changes as the Earth rotates. *Right*: The spacing between antennas at each time determines the baseline vector that is projected in the uv plane (filled squares). The empty squares are the symmetric measure of the same visibility, because a visibility evaluated at (u, v) is equivalent to the one at $(-u, -v)$ (see text).

$$\begin{aligned} \left[\frac{\theta}{\text{rad}} \right] &\approx \frac{\lambda}{B} = 10^{-5} \left[\frac{\lambda}{\text{cm}} \right] \left[\frac{B}{\text{km}} \right]^{-1}, \\ \left[\frac{\theta}{\text{mas}} \right] &\approx 206.3 \left[\frac{B}{\text{M}\lambda} \right]^{-1}. \end{aligned} \quad (2.1)$$

If a radio source is intrinsically larger than the maximum fringe spacing mapped by the array, the corresponding flux density of the more extended emission will be lost. This is a common issue for VLBI arrays, in which the shortest baseline is usually of several tens of km, and only the most compact region of radio sources is observable, while the smooth and large structures are not detected. For instance, observations at 5 GHz (6 cm wavelength) with an array with a minimum antenna separation of 100 km ($1.7 \text{ M}\lambda$) would not detect any structure with intrinsic size larger than ~ 0.1 arcsec.

As an example, in Fig. 2.5 we show the same visibility distribution in the uv plane shown in Fig. 2.4, together with the amplitude and phase value of each visibility for a source with a total flux density of 0.35 Jy. At short baselines the visibilities have the amplitude corresponding to the total source flux density, although the amplitude drops for long baselines. This shows that the source has a certain intrinsic size. Antennas separated a distance shorter than that corresponding to the source angular size are sensitive to the whole structure, whereas longer baselines, which trace the small scale features of the

2. Synthesis imaging with VLBI

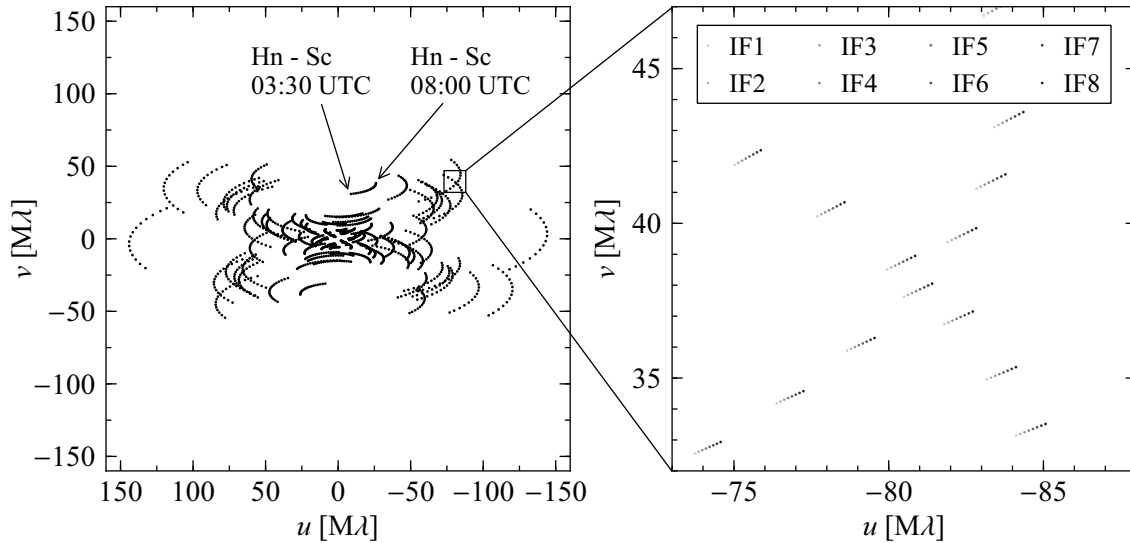


Figure 2.4: *Left*: uv coverage during a 6-h observation with the VLBA on a source with declination -17° . One visibility per scan (every ~ 4 minutes) is shown, and only for one channel, one IF, and one polarisation. The observations were conducted at 6 cm wavelength, which sets the axis scales. We indicate the visibilities provided by the baselines between the VLBA Hn and Sc at the beginning and the end of the observation. A visibility at each (u, v) position is repeated at $(-u, -v)$. *Right*: zoom of a region of the left panel where the 8 IFs are plotted. Each IF is observed at a slightly different frequency, and consequently each antenna separation provides uv positions at slightly different radial distances for each frequency.

source, are not sensitive to all the flux density of the source. For this example, the source has an intrinsic size of ~ 2.8 mas, measured as full width at half maximum (FWHM). Using Equation 2.1 we see that this angular scale corresponds to a uv distance of ~ 75 M λ . We note that the fit of components is usually provided in FWHM, whose relation with a Gaussian component with standard deviation σ is $\text{FWHM} = 2\sqrt{2 \ln 2} \sigma$. Therefore, the source size is described by a Gaussian circle with sigma (radius) of 32 M λ . A useful way of visualising it is by realising that the Fourier transform of a Gaussian is also a Gaussian, and their sizes are related by the relation in equation 2.1.

2.3 Calibration and imaging

Amplitude and phase calibration

The most remarkable aspect of the calibration of VLBI data is that observations are conducted with antennas that are at different places, and therefore fundamental aspects, like the atmosphere conditions or the elevation of the source, are completely different for different parts of the instrument (array). In some cases, the array may contain antennas of

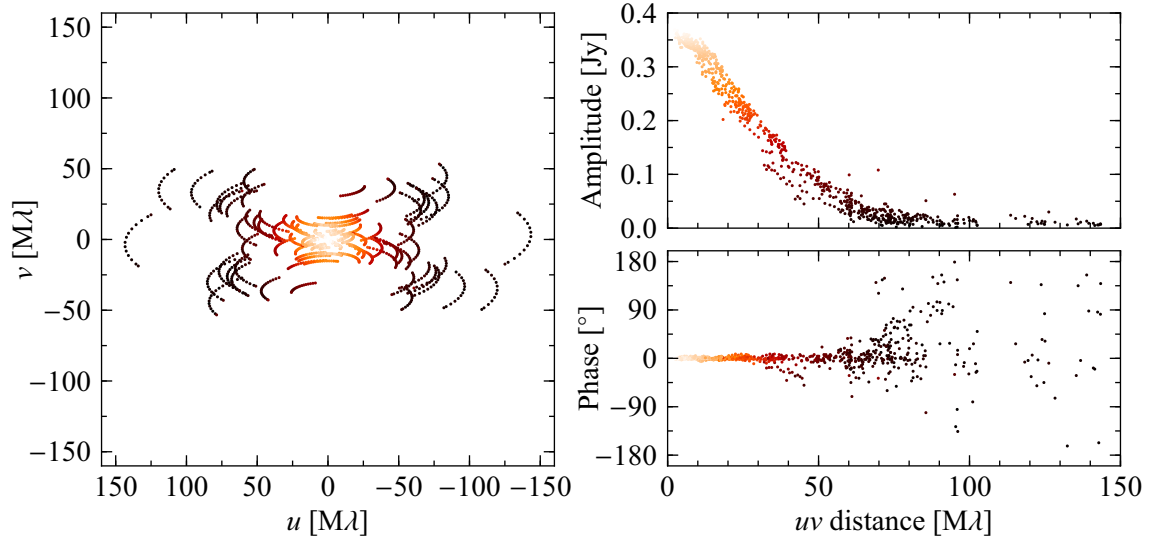


Figure 2.5: Same as Fig. 2.4 but including the amplitude and phase of each visibility. The colour scale indicates the amplitude of the visibilities.

different types and sizes. The amplitude calibration consists of finding the scaling factors that make all the visibility amplitudes between antennas consistent. These scaling factors can be antenna-dependent or baseline dependent (being the latter usually ~ 1). The common approach of observing a bright and persistent source to scale the individual antenna gains to the correct amplitude is not possible in VLBI because these high resolution observations trace the most compact, and therefore intrinsically variable, structure of radio sources. Therefore, it is not possible to find bright and stable flux calibrators that are valid for all baselines. The alternative is to use the system temperature (T_{sys}) of the receiver during the observation. The antenna response for a certain flux density received is corrected by the system equivalent flux density (SEFD), defined as the flux density of a radio source that doubles the T_{sys} . The SEFD is proportional to T_{sys} , in K, over the antenna aperture efficiency, in K/Jy. T_{sys} is measured regularly during the observation and it is converted to real flux density by combining T_{sys} and the gain curve of each telescope.

The interferometric phase is estimated a-priori by the correlator geometrical model, although it cannot account for all the instrumental and atmospheric effects. The phases show a slope as a function of frequency (delay), as well as a change with time (fringe rate). The delay is usually produced by clock errors and is measured in nanoseconds. The fringe delay is basically caused by changing atmospheric conditions. The phases are stable during a short time of the order of minutes, known as the coherence time, which is shorter at high frequencies and in bad weather conditions, and longer at low frequencies and stable weather conditions. Both phase slopes, the delay and the fringe rate, are corrected by a procedure called fringe fitting. This calibration is aimed to set the phases to 0 by

2. Synthesis imaging with VLBI

finding the appropriate phase corrections as a function of time and frequency by fitting simultaneously the phases and their derivatives.

Phase referencing and astrometry

The phase calibration should be good at least for times shorter than approximately the coherence time to provide good data. If the target source is too faint it is not possible to calibrate the phases. In this case, the solution is to observe a nearby bright source, calibrate its phases, and transfer the corrections to the target source. The phase calibrator has to be observed continuously, in time intervals shorter than the coherence time. Normally, the observation scheme consists of several calibrator-target-calibrator cycles of a few minutes. If the calibrator is at long angular distances from the target the sky conditions may be different, which implies that the calibration would not be correct. Angular distances up to $\sim 6^\circ$ are feasible, although systematic errors scale with the source separation (Pradel et al. 2006).

In the calibration process the phases of the calibrator are set to 0, and therefore all astrometric measurements are relative to the phase calibrator position. After the calibration, the phase calibrator will be set by definition at the correlation position, independently of its real position. All the phase corrections (in the end position offsets) are measured from this reference position, and therefore the phase-referencing astrometry is always relative. VLBI calibrators are usually quasars with good absolute positions, determined in the International Celestial Reference Frame (ICRF), which is a realisation of the International Celestial Reference System (ICRS) (Fey et al. 2004).

Imaging and self-calibration

After the data calibration the visibility phases against time and frequency (within and between subbands) are flat for a point-like source at the phase centre and the amplitudes represent a flux density measurement. The visibilities in the uv plane are ready to be transformed to flux density distribution in the sky. This is performed by applying a Fourier transform to the complex visibility data. The image is produced with the resolution given by the dirty beam, or response of the array to a point-like source, which for VLBI usually presents important side lobes. The imaging, or cleaning, process consists of subtracting the dirty beam structure from the brightest region of the dirty image successively, until only a residual noise image is left. The distribution of flux density in the image is stored in a list of clean components, whose sum describes the source flux density distribution. The final image is produced by adding the residual noise image to a convolution of the synthesised beam with the clean components. The synthesised beam is approximated by a 2D Gaussian with the width of the dirty beam, or Half-Power Beam Width (HPBW). This parameter is a convenient and easy way to describe the image resolution.

There are several algorithms to produce images from interferometric data. In this thesis we use the most common one, the CLEAN algorithm (Högbom 1974). In practice

the data are weighted according to their reliability. Each visibility is multiplied by a weight inversely proportional to the noise variance of the visibility. Apart from this, different weighting sampling functions can be used, which have different effects on the synthesised beam size. Weights can be determined by the density of visibilities in different parts of the uv plane, which is divided in a grid of cells. For example, a natural weighting assigns constant weights to all visibilities. The effect of this is that the well-sampled regions of the uv plane (see Fig. 2.4) dominate the deconvolution process. This weighting scheme gives optimum sensitivity, in particular to extended emission, although the resulting synthesised beam is large. Natural weighting provides good sensitivity and lower noise, but worse resolution. On the other hand, the uniform weighting scheme assumes that each uv cell in the plane has the same weight, independently on how many visibilities it contains. Consequently, visibilities in a crowded region of the uv plane are effectively down weighted. The uniform weight along uv cells enhance the influence of the more “isolated” visibilities, which usually correspond to the longest uv distances. The uniform weighting scheme provides better resolution and reduces the sidelobe level but increases the rms image noise. In the particular case of the AIPS³ software package the implementation of the weighting scheme can be controlled by the robustness parameter. This parameter can be set between -5 and 5 , where values above 4 are close to natural weighting and values below -4 correspond to uniform weighting. This parameter can be selected in order to control the resolution and sensitivity of an image.

It is also possible to “taper” the data using a Gaussian weighting function with a particular uv radius. The image is consequently dominated by the baselines with uv distances below the tapering parameter, which provides a larger synthesised beam, lower resolution but also lower noise level and better sensitivity to extended emission.

There are two important issues affecting the cleaning process in VLBI. First, the uv coverage, or how well the uv plane is sampled, is usually poor because of the low number of antennas in VLBI arrays, and consequently the Fourier transform is not ideal. Second, the calibration is never perfect, and residuals in amplitude and phase are found in the final data. These errors spread the signal on the image and lead to artefacts. The signal-to-noise ratio (S/N) of a detection can be significantly improved by performing a self-calibration of the data. It consists of allowing the antenna gains to be free parameters, and fitting them so that the data represents better some a priori known structure of the source. Unfortunately, this means that self-calibration is basically a process to modify the data to fit the source. However, the algorithms used for self-calibration are designed to provide robust results. In particular it is possible to define quantities called closure phases that contain information on the real structure of the source but are free from the systematic errors of individual antennas. A closure phase is the sum of phases around a closed loop of three baselines. These restrictions avoid that the structure information is lost when fitting the phases during self-calibration. The analogue parameter for the amplitude is

³The NRAO Astronomical Image Processing System. <http://www.aips.nrao.edu/>

2. Synthesis imaging with VLBI

the closure amplitude, defined as the product and ratio of four baselines, instead of the sum. This difference is important, as closure amplitudes are not well restricted, and can provide unrealistic amplitude corrections. To assure the robustness of the process the data self-calibration is performed iteratively, alternating phase and amplitude fits with imaging, applying smooth changes that preserve the source structure. Self-calibration is only possible for sources with a high flux density, although this depends on the complexity of the source structure and the quality of the data.

Pulsar gating

When observing a radio pulsar, the detection of the pulsed emission can be improved by correlating the data using the pulsar gating technique, which is possible when the pulsar ephemerides are known (Briskin et al. 2002; Chatterjee et al. 2009). In normal VLBI observations, with integration times of a few seconds, one measures the period-averaged flux density of the observed pulsar, although most of the time the pulsar is not emitting. The instantaneous flux density during the pulsation is usually tens of times higher than the period-averaged value, because the duty cycle (the ratio of the pulse width to the pulse period) is usually below 10%. To optimise radio observations of pulsars one can take advantage of this fact by only correlating the data during on-pulse, and disabling correlation during off-pulse. The total correlated on-source time is considerably reduced (a few minutes for every observed hour), which increases the final image noise (rms) by a factor proportional to one over the square root of the duty cycle ($\Delta\tau_\nu$) at a certain frequency ν . However, the flux (S_ν) increase is approximately proportional to one over the duty cycle, yielding a final signal-to-noise ratio (S/N) improvement:

$$(S/N)_G = \frac{S_{\nu,G}}{rms_G} \simeq \frac{\langle S_\nu \rangle / \Delta\tau_\nu}{\langle rms \rangle / \sqrt{\Delta\tau_\nu}} = (S/N)_0 \frac{1}{\sqrt{\Delta\tau_\nu}}, \quad (2.2)$$

where the subindex G stands for the gated values. This provides a theoretical S/N increase, or gain, proportional to one over the square root of the duty cycle of the pulsar. Typically, the real S/N improves by a factor between 2 and 6 (Briskin et al. 2002), which can make the difference between a non-detection and accurate astrometry. It is important to obtain updated ephemeris of the pulse time of arrivals for each VLBI observation and correlation. The ephemerides are used to configure the opening and closing time “gates” of the correlator. The timing is usually obtained by means of long-term monitoring conducted in single antennas, for example at the Jodrell Bank Observatory or at Parkes (see next Section). Normally, the raw data of a single observation are correlated twice: one is a normal correlation and the other is performed using pulsar gating. With the two correlations it is possible to compare the results obtained with and without the pulsar gating. The same calibration tables applied to the normal data are also applied to the data correlated with pulsar gating. By producing images of the target pulsar using the same parameters it is possible to compare the astrometry obtained with and without pulsar gating. The ratio between S/N with and without gating provides the gain factor.

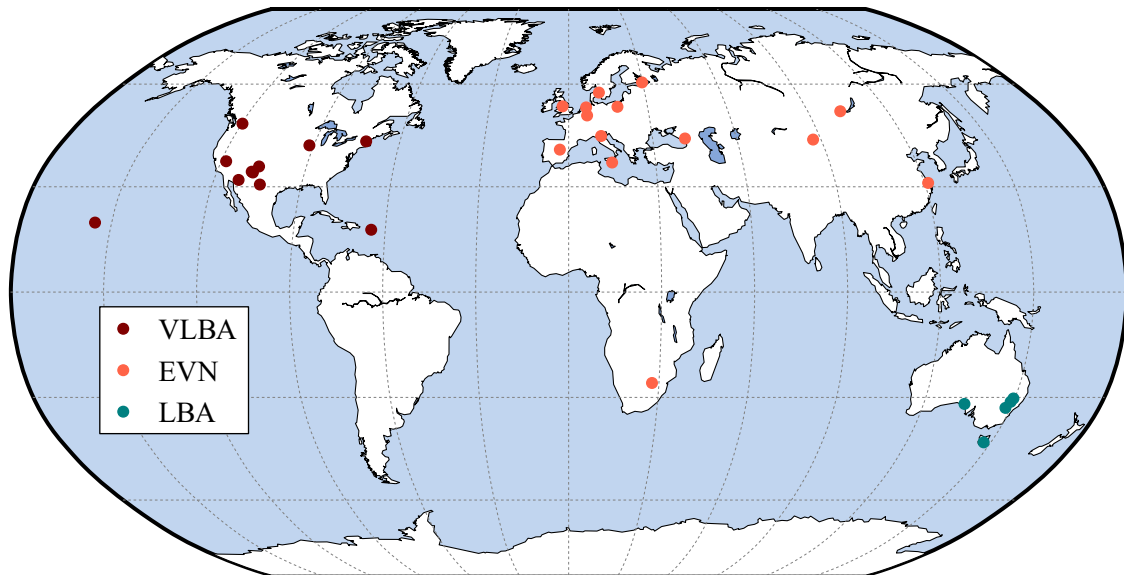


Figure 2.6: World map with the VLBI antennas from the VLBA, the EVN, and the LBA used in this thesis. The Earth longitude and latitude grid is plotted every 30° .

2.4 VLBI arrays

There are different arrays of antennas observing in VLBI mode. We will summarise the most important ones here. In particular, we describe the three VLBI arrays used in this thesis, whose antenna locations are listed in Table 2.1, and are shown in Fig. 2.6.

VLBA

The Very Long Baseline Array (VLBA)⁴ is the world's only dedicated VLBI array. It is managed by the USA National Science Foundation/NRAO. It consists of 10 antennas with a diameter of 25 m located in the USA. It has the capability to conduct observations during all year, and the observations can be scheduled dynamically. This means that observations can be planned without a fixed date, and the different projects are observed following a schedule that can be adapted depending on factors like the weather conditions. The VLBA offers a wide range of frequency bands, between 0.3 and 86 GHz, or 1 m and 0.3 cm, respectively. It is possible to change the observing frequency receiver remotely and in a few seconds/minutes. All the antennas are equal, which facilitates the calibration and operations. However, the main limitations of the array are the small dishes, which provide limited sensitivity, and the relatively narrow bandwidth of 8 MHz for each subband. Another limitation is that it is not possible to correlate the data in real time (eVLBI, see below). The array is currently undergoing a major upgrade with the aim to increase the

⁴<http://www.vlba.nrao.edu>

2. Synthesis imaging with VLBI

Table 2.1: List of the VLBI antennas used in this thesis, classified by array. We show the name, the identification code, the size, and the geographical location of each antenna. Within each array, the antennas are listed in increasing Earth longitude so they can be easily identified in Fig. 2.6.

Name	Code	Size [m]	Longitude [°]	Latitude [°]	Altitude [m]
VLBA					
Saint Croix	Sc	25	64.58363	17.75658	15
Hancock	Hn	25	71.98658	42.93361	296
North Liberty	Nl	25	91.57414	41.77142	222
Fort Davis	Fd	25	103.94482	30.63503	1606
Los Alamos	La	25	106.24560	35.77512	1962
VLA	Y27	27×25	107.61833	34.07881	2114
Pie Town	Pt	25	108.11919	34.30102	2365
Kitt Peak	Kp	25	111.61242	31.95630	1902
Owens Valley	Ov	25	118.27705	37.23165	1196
Brewster	Br	25	119.68328	48.13122	251
Mauna Kea	Mk	25	155.45550	19.80138	3763
EVN					
Sheshan(Shanghai)	Sh	25	-121.19966	31.09916	29
Badary	Bd	32	-102.23392	51.77026	822
Nanshan(Urumqi)	Ur	25	-87.17814	43.47151	2033
Zelenchukskaya	Zc	32	-41.56516	43.78781	1175
Svetloe	Sv	32	-29.78194	60.53234	86
Hartebeesthoek	Hh	26	-27.68539	-25.88975	1416
Torun	Tr	32	-18.56406	53.09546	134
Noto	Nt	32	-14.98905	36.87605	143
Onsala	On	25	-11.92636	57.39584	59
Medicina	Mc	32	-11.64693	44.52049	67
Effelsberg	Ef	100	-6.88361	50.52483	417
Westerbork	Wb	14×25	-6.63333	52.91529	71
Jodrell Bank	Jb	76	2.30858	53.23654	179
Yebes	Ys	40	3.08686	40.52467	989
LBA					
Narrabri (ATCA)	At	6×22	-149.57000	-30.31000	217
Mopra	Mp	22	-149.09964	-31.26782	867
Parkes	Pa	64	-148.26351	-32.99840	415
Hobart	Ho	26	-147.44052	-42.80358	65
Ceduna	Cd	30	-133.80983	-31.86769	165

data rate up to 4 Gbps, increasing the current sensitivity by a factor of ~ 4 .

EVN

The European VLBI Network (EVN)⁵ is operated by national agencies in Europe as well as China and South Africa. The number of antennas is not fixed because it depends on the observing frequency and availability, although in normal observations ~ 12 antennas participate. Also, this number changes along years, as new antennas are included in the array. Most of the antennas have a diameter between 25 and 32 m, although Effelsberg is a 100-m dish, and Westerbork, which is used as a single tied array, is composed of 14 antennas of 25 m. Some observations can include the 305-m antenna of Arecibo (Puerto Rico) if the target source is visible by the antenna. The EVN is the VLBI array with best sensitivity because of the large collection area of its telescopes. Furthermore, it currently provides 16 MHz bandwidths, which improves the sensitivity. Some of the antennas of the EVN regularly conduct eVLBI observations, with a rapid-response correlation in real time at the JIVE⁶ correlator. The data is available a few hours after the observations. The weakness of the array is the fixed observing schedules and the limited available time. The full array is available for observations during three epochs every year, each of them lasting about 3 weeks. Additionally, sessions correlated in real time (e-EVN) are offered approximately once per month, with sessions of 24 h. From the technical point of view, the calibration and response from the array are not as clear or straightforward as in the case of the VLBA, because of the non-uniform antenna properties and aims.

LBA

The Long Baseline Array (LBA)⁷ is currently the only VLBI array in the Southern Hemisphere. The core of the array consists of five antennas: Mopra, Parkes, Hobart, and Ceduna, with diameters between 22 and 64 m, and Narrabri (6 \times 22 phased-up antennas). The 70-m antenna in Tidbinbilla (from the NASA's Deep Space Network) joins the array when available. One-week block schedules are offered several times per year, although additional sessions can be arranged under request. The array provides baselines between 115 and 1700 km. The 26-m antenna in Hartebeesthoek can also join the array. However, the large distance between this antenna and the rest of the array ($> 9\,000$ km) yields an important gap in the uv coverage at long baselines. The array is currently being upgraded for e-VLBI usage, and this mode should be available soon, although currently it is not the default observing mode.

⁵<http://www.evlbi.org>

⁶Joint Institute for VLBI in Europe, <http://www.jive.nl/>

⁷<http://www.atnf.csiro.au/vlbi>

2. Synthesis imaging with VLBI

Other arrays

For completeness, we list here some other VLBI arrays available, although we do not describe them in detail because they are not used in this thesis. The High Sensitivity Array (HSA)⁸ is designed for observations requiring the best possible sensitivity, and it combines the VLBA with the following large antennas: VLA (in phase-array mode), the GBT, Arecibo, and Effelsberg. Global VLBI is used when combining antennas from the VLBA (or the HSA) with antennas from the EVN. It provides long baselines and excellent sensitivity, although it requires the coordination of all antennas. At higher frequencies the Global MM VLBI array, which observes at mm wavelengths, combines the VLBA with Effelsberg, Onsala, Pico Veleta and Metsahovi. The VLBI Exploration of Radio Astrometry (VERA)⁹ array is a Japanese array of 4 antennas aimed to obtain high precision astrometry of Galactic masers. Finally, the Korean VLBI Network (KVN) is currently under construction, and consists of 3 antennas operating at high frequencies.

All the VLBI arrays are continuously evolving and incorporating the most recent technologies, mainly to the electronics and to the correlator hardware and software. They also aim to provide full eVLBI capabilities in the future. Apart from this, a very important milestone is the addition of antennas to the arrays because this provides better sensitivity and, more importantly, better uv coverage. The EVN plans to include new stations like the one in Sardinia (64 m), or two more Chinese antennas with diameters of 40 and 50 m. The LBA is adding antennas to the array, such as Warkworth (12 m), in New Zealand, and the ASKAP, the Australian pathfinder to SKA. These antennas will provide much better uv coverage and resolution. Also, there are plans to build a new VLBI array in Africa. Remarkably, the SKA is aimed to provide an outstanding sensitivity and long baselines of up to 3000 km. It is also probable that the SKA will operate with other antennas from VLBI arrays.

⁸<http://www.nrao.edu/hsa>

⁹<http://veraserver.mtk.nao.ac.jp/>

3

Discovery of extended emission from PSR B1259–63

3.1 Introduction

The gamma-ray binary PSR B1259–63 is one of the unique Galactic binary systems that periodically displays VHE gamma-ray emission. However, the active periods, close to the periastron passage, only occur once every 3.4 years, and therefore, good observational conditions to explore the source behaviour are scarce. On the other hand, the source is in the Southern Hemisphere, and thus the only VLBI observatory capable of resolving its mas structure is the Long Baseline Array (LBA). In this chapter we present the first VLBI radio images of PSR B1259–63, obtained close to its 2007 periastron passage¹. In Sect. 3.2 we introduce the source properties and context. The high-resolution images at three different orbital phases are presented in Sect. 3.3. The resulting images and astrometry are discussed in Sect. 3.4. In Sect. 3.5 we present a kinematical interpretation of the source morphology that allows us to infer some physical parameters of the source. A global discussion and a summary is presented in Sect. 3.6. Finally, some work in progress and future aims are discussed in Sect. 3.7.

¹Published in Moldón, J., Johnston, S., Ribó M., Paredes, J. M., & Deller, A. T. 2011, ApJL, 732, L10.

3.2 The gamma-ray binary PSR B1259–63

The binary system PSR B1259–63/LS 2883² is formed by a young 48 ms radio pulsar in an eccentric orbit of 3.4 years around a massive main-sequence star (Johnston et al. 1992, 1994). The parameters of the system are shown in Table 3.1. The spectral type of the massive star, O9.5 Ve, and some of the binary parameters have been recently updated by Negueruela et al. (2011), who obtained a distance to the system of 2.3 ± 0.4 kpc. Close to the periastron passage the system displays non-thermal unpulsed emission that has been detected in radio (Johnston et al. 2005), X-rays (Cominsky et al. 1994; Uchiyama et al. 2009; Chernyakova et al. 2009), hard X-rays up to 200 keV (Grove et al. 1995). Recently, Pavlov et al. (2011a) found extended emission in X-rays on scales of 4–15'' from PSR B1259–63. In the range ~ 0.1 –100 GeV strict upper limits were obtained by EGRET close to the 1994 periastron passage (Tavani et al. 1996). During the periastron passage of 2010–2011, the source was detected by *Fermi*/LAT (Tam et al. 2011; Abdo et al. 2011). The source has been detected in very high energy (VHE; 0.1–100 TeV) γ -rays above 380 GeV (Aharonian et al. 2005b, 2009). The VHE emission is variable on orbital time scales, and is interpreted as the result of inverse Compton upscattering of stellar UV photons by relativistic electrons that accelerated in the shock between the relativistic wind of the young non-accreting pulsar and the wind of the stellar companion (see Maraschi & Treves 1981; Tavani & Arons 1997; Kirk et al. 1999; Dubus 2006; Bogovalov et al. 2008, and references therein).

The radio emission from the PSR B1259–63 system is described most recently in Johnston et al. (2005), which includes multiwavelength data from ATCA observations obtained during the periastron passages of 1994, 1997, 2000, and 2004 (hereafter we will refer to the epoch of each periastron passage as τ). The emission has two non-thermal components. The first one is pulsed emission with a flux density of ~ 2 –5 mJy at 2.5 GHz and a nearly flat spectral index, which disappears approximately from 16 days prior to periastron ($\tau-16$) to 15 days after periastron ($\tau+15$). This has been interpreted as an eclipse of the pulsar when it crosses behind the equatorial circumstellar disc present around the massive star (Melatos et al. 1995). The second component is transient unpulsed synchrotron emission that appears at $\tau-20$ days and shows two peaks centred around $\tau-10$ and $\tau+20$ days, with flux densities at 2.5 GHz up to ~ 15 –20 mJy and ~ 30 –50 mJy, respectively. After the post-periastron peak, the flux density of the unpulsed emission decreases continuously, and it has been detected up to $\sim \tau+100$ days. This transient emission remains optically thin during the outbursts.

The broadband transient emission of PSR B1259–63/LS 2883 is produced around periastron, when strong interaction is produced between the stellar and pulsar winds. The shocked material is contained by the stellar wind behind the pulsar, producing a nebula

²Star 2883 in the catalogue of Luminous Stars in the Southern Milky Way (Stephenson & Sanduleak 1971). The use of SS 2883 should be avoided, see Negueruela et al. (2011).

Table 3.1: Parameters of the pulsar PSR B1259–63, the massive star LS 2883, and the binary system. The values in parentheses refer to the uncertainty in the last digit at 1- σ level.

Parameter	Symbol	Value	Reference
Pulsar period	P	47.762506780(2) ms	(1)
Period derivative	\dot{P}	$2.276554(2) \times 10^{-15}$	(1)
Characteristic age	τ_c	3.3×10^5 yr	(2)
Surface magnetic field	B	3.3×10^{11} G	(2)
Spindown luminosity	\dot{E}_{sp}	8×10^{35} erg s $^{-1}$	(3)
Spectral type	–	O9.5 Ve	(4)
Effective temperature	T_{eff}	27 500–34 000 K	(4)
Surface gravity	$\log g$	3.7–4.1	(4)
Radius	R_1	8.1–9.7 R_{\odot}	(4)
Optical luminosity	L_{opt}	2.4×10^{38} erg s $^{-1}$	(4)
Mass	M_1	31 M_{\odot}	(4)
Distance	d	2.3 ± 0.4 kpc	(4)
Mass function	$f(M_2)$	1.53 M_{\odot}	(5)
Terminal wind velocity	v_{∞}	1350 ± 200 km s $^{-1}$	(6)
Orbital period	P_{orb}	1236.72432(2) days	(1)
Reference epoch	T_0	MJD 48124.34911(9)	(1)
Semimajor axis	a_2	7.2 ± 0.4 AU	(4) ^a
Orbit inclination	i	$22^{\circ}2 \pm 1.4$	(4) ^a
Eccentricity	e	0.8698872(9)	(1)
Argument of periastron	ω_2	$138^{\circ}6659(1)$	(1)
Longitude of ascending node	Ω	-40°	See the text
Proper motion (right ascension)	$\mu_{\alpha} \cos \delta$	-1.4 ± 2.7 mas yr $^{-1}$	(7)
Proper motion (declination)	μ_{δ}	-3.2 ± 1.9 mas yr $^{-1}$	(7)

^aDerived from (4).

References: (1) Wang et al. 2004; (2) Wex et al. 1998; (3) Manchester et al. 1995; (4) Negueruela et al. 2011; (5) Johnston et al. 1994; (6) McCollum 1993; (7) Zacharias et al. 2009.

extending away from the stellar companion. Along this adiabatically expanding flow, the accelerated particles produce synchrotron emission from radio to X-rays (Tavani & Arons 1997; Kirk et al. 1999; Dubus 2006; Takata & Taam 2009). The expected morphology depends on the magnetisation parameter of the pulsar wind, σ , defined as the upstream ratio of magnetic to kinetic energy.

These models predict that the radio emission from PSR B1259–63 extends up to several AU, corresponding to several milliarcseconds (mas) at 2.3 kpc, and that its structure should

3. Discovery of extended emission from PSR B1259–63

Table 3.2: Observational parameters for each run of project V234. Periastron passage is at $\tau = \text{MJD } 54307.9710(1)$, from the fourth orbital solution obtained in Wang et al. (2004). θ is the mean true anomaly plus 180° .

Run	MJD	On-source Time	Num. of Antennas	τ +days	ϕ_{orb}	True Anomaly [$^\circ$]	θ [$^\circ$]
A	54309.25	4.65	5	1.3(2)	0.00103(14)	10.8(1.4)	191
B	54329.18	3.75	5	21.2(2)	0.01716(14)	98.7(3)	279
C	54623.47	4.20	4	315.5(2)	0.25511(14)	165.98(1)	346

be variable on orbital time scales. The high-mass binaries LS 5039 and LS I +61 303 have also been detected at VHE, and show a broadband spectral energy distribution (SED) similar to that of PSR B1259–63 (Dubus 2006). Given the similarities in the three systems and the theoretical predictions, radio emission on mas scales is expected also from PSR B1259–63. The motivation of the work presented here is to find an observational link between the three gamma-ray binaries that could shed light in the understanding of this kind of systems.

Here we present the first VLBI radio images of PSR B1259–63, obtained close to its 2007 periastron passage. The high-resolution images at three different orbital phases provide a direct view of the small-scale morphology of the source, which is comparable to those previously observed in LS 5039 and LS I +61 303.

3.3 Observations with the LBA and data reduction

PSR B1259–63 was observed with the Australian Long Baseline Array (LBA) at 2.3 GHz (13 cm) on three epochs: 2007 July 28 (run A), 2007 August 17 (run B), and 2008 June 6 (run C). The LBA observations were performed with five antennas of the array: Parkes, ATCA, Mopra, Hobart (not present in run C) and Ceduna. The observational parameters of each of the ~ 10 hr runs are shown in Table 3.2. The small number of antennas provides a rather poor uv -coverage that makes the data calibration and imaging more difficult than for arrays with more elements, because we have less baseline redundancy. The fourth orbital solution obtained in Wang et al. (2004) was used to obtain the days after the periastron (defined as days after $\tau = \text{MJD } 54307.9710(1)$), the orbital phase, and the true anomaly shown in Table 3.2. A sketch of the orbit, as seen from above, is shown in Fig. 3.1. We mark the pulsar position at the orbital phases of each observed run.

The data were recorded at a bit rate of 512 Mbps per telescope distributed in eight sub-bands (four for each right- and left-handed polarisation) with a bandwidth of 16 MHz, each of them correlated using 64 frequency channels, two-bit sampling, and 2 s of integration time. Hobart and Ceduna recorded at 256 Mbps (only two sub-bands per polarisation).

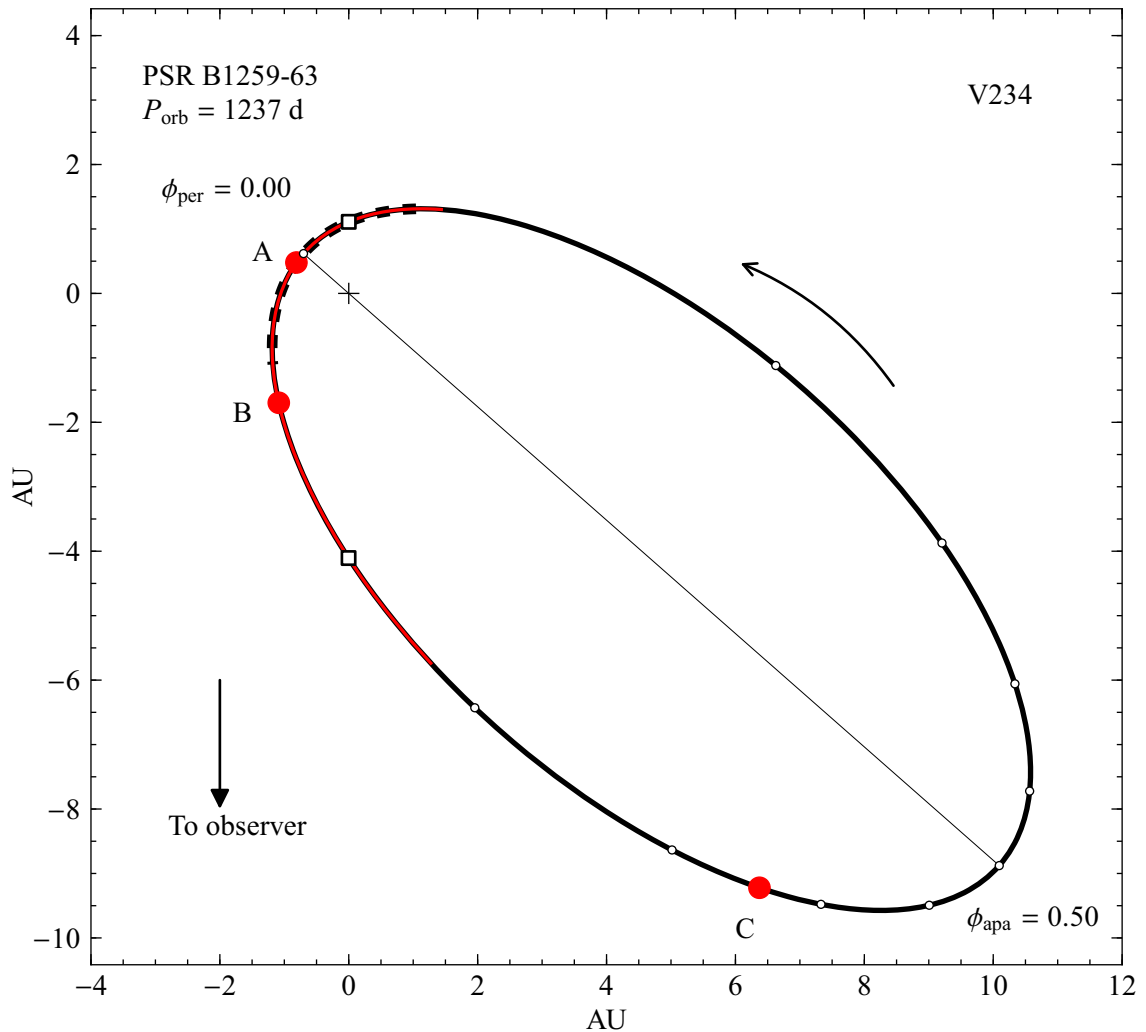


Figure 3.1: Sketch of the orbit of PSR B1259–63 with the position of the pulsar during the three runs of project V234 marked as red circles. The black cross indicates the position of the massive star. The red line approximately indicates the time interval when the transient unpulsed radio emission is detected (Johnston et al. 2005). The dashed line marks the region where pulsations have not been detected. The white dots are plotted every 0.1 orbital phases. The empty squares mark the inferior and superior conjunction of the compact object, which occur at orbital phases 0.04750 and 0.99478, respectively. The orbit was computed using the orbital solution reported in Wang et al. (2004). The orientation of the orbit is arbitrary, and it is seen face-on (see Fig. A.2 on page 180 for examples of other possible projections of the orbit).

The data were correlated at Swinburne University using the DiFX software correlator (Deller et al. 2007) without applying pulsar gating or binning.

3. Discovery of extended emission from PSR B1259–63

The observations were performed using phase referencing on the calibrator J1337–6509 (B1334–649), which has an angular separation of 4° from PSR B1259–63 and was correlated at $\alpha_{J2000.0} = 13^{\text{h}}37^{\text{m}}52^{\text{s}}.4443$ and $\delta_{J2000.0} = -65^{\circ}09'24''.900$. This reference position from the global VLBI solution 2006d_astro³ has an uncertainty of 13 mas. The cycle time was 6 minutes, spending half of the time on the phase calibrator and the target source, alternatively. The total flux density of the phase calibrator was 457 ± 11 , 367 ± 20 , and 491 ± 6 mJy for runs A, B, and C, respectively. The source J0538–4405 (B0537–441) was used as a fringe finder for runs A and B, and J1337–6509 (B1349–439) was used for run C. No astrometric check source was observed during the runs.

The data reduction was performed using AIPS⁴. Total electron content models based on GPS data obtained from the CDDIS data archive⁵ were used to correct phase variations due to the ionosphere. Standard instrumental corrections were applied (parallactic angle, instrumental offsets, and slopes between and within bands and bandpasses). Fringe fitting on the phase calibrator was performed using the AIPS task FRING, and the solutions were applied to the target source. A self-calibrated model of the calibrator was used as an input model for CALIB, which was used to reduce the amplitude instabilities on time scales greater than 10 minutes. The data were averaged in frequency and time, and clean images were produced. For run B only, a single round of phase self-calibration was applied, to mitigate the residual atmospheric phase instabilities, which were more noticeable at this epoch. The final images were produced using a natural weighting scheme (robust 5 within the AIPS task IMAGR). For run B, robust 2 and tapering were applied to avoid the presence of possible unreliable high-resolution features due to sidelobes of the synthesized beam. Self-calibration slightly affects measured properties such as extent and position angle (P.A.), while it preserves the morphology.

3.4 The radio structure of PSR B1259–63

The resulting VLBI images at 2.3 GHz are shown in Fig. 3.2. The image synthesized beams and flux densities are listed in Table 3.3. Extended emission is detected at distances up to 50–55 mas ($120\text{--}130 \pm 20$ AU at 2.3 ± 0.4 kpc) during the two runs shortly after the periastron passage. The emission becomes gradually fainter from the peak toward the northwest, and no individual components have been found. The P.A. of the extended emission with respect to the peak is $\sim -67^{\circ}$ for run A and $\sim -50^{\circ}$ for run B. The emission in run C, 315 days after the periastron passage, is dominated by a point-like source of a few mJy. The resolution and the sensitivity in run C are worse due to the lack of one station. Hints of a faint component towards West can be seen, although one should be cautious with interpretations of extended structure for this run, where the source is

³http://lacerta.gsfc.nasa.gov/vlbi/solutions/2006d/2006d_apr.src

⁴The NRAO Astronomical Image Processing System. <http://www.aips.nrao.edu/>

⁵The Crustal Dynamics Data Information System <http://cddis.nasa.gov/>

3.4. The radio structure of PSR B1259–63

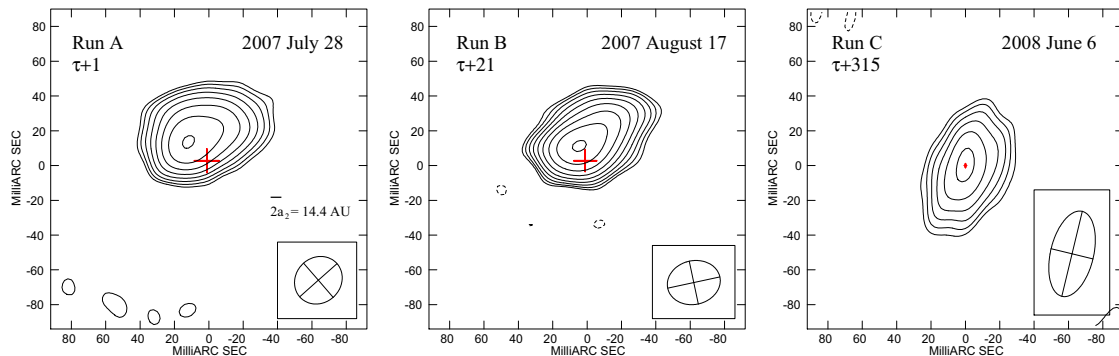


Figure 3.2: LBA images of PSR B1259–63 at 2.3 GHz. North is up and East is to the left. The dates and the days after the periastron passage (τ) are quoted at the top of each panel. The synthesized beam is displayed in the rectangle on the bottom-right corner of each image. The red crosses mark the region where the pulsar should be contained in each run (see the text). As a reference, the size of the major axis of the orbit of PSR B1259–63/LS 2883 is shown in the first panel. For each image, the displayed contours start at $3\text{-}\sigma$ level and increase by factors of $2^{1/2}$; the $1\text{-}\sigma$ rms close to the source in each image from left to right is 0.30, 0.66, and $0.15 \text{ mJy beam}^{-1}$.

Table 3.3: Parameters for the images shown in Fig. 3.2.

Run	S_{total} [mJy]	S_{peak} [mJy beam $^{-1}$]	HPBW $_{\text{size}}$ [mas 2]	HPBW $_{\text{P.A.}}$ [$^{\circ}$]
A	19.9 ± 1.4	10.4 ± 0.2	28.9×26.1	-49
B	46.7 ± 1.0	32.7 ± 0.4	31.0×25.1	-78
C	3.0 ± 0.4	2.8 ± 0.4	50.3×25.1	-14

very faint and the imaging was done with only 4 antennas. The parameters describing the image components are shown in Table 3.4.

Like all VLBI arrays, the absolute flux calibration of the LBA relies on noise calibration injection and so the absolute flux values reported in Table 3.3 should be taken as uncertain at the $\sim 10\%$ level. The flux densities of runs A and B are compatible with previous ATCA observations at the corresponding orbital phases (the ATCA data from the current observations were not correlated as an independent array). The flux density in run C is compatible with the phase-average flux density of the pulsar. This is expected considering the lack of unpulsed emission at $\tau + 150$ and $\tau + 180$ in previous ATCA observations (Johnston et al. 2005).

The phase-referenced observations allow us to obtain relative astrometry between runs. Since no astrometric check source was observed, we do not have real measurements of the

3. Discovery of extended emission from PSR B1259–63

Table 3.4: Size of the extended emission of PSR B1259–63, and astrometry of the peak of the emission. The separation (see the text) is measured from the position of run C.

Run	Size		P.A.	$\Delta\alpha$	$\Delta\delta$	Separation	
	[mas]	[AU]				[mas]	[AU]
A	50	120 ± 20	–67	11.3 ± 0.4	14.0 ± 0.5	$(10-20) \pm 3$	$(24-46) \pm 7$
B	55	132 ± 22	–50	4.2 ± 0.1	11.3 ± 0.1	$(5-14) \pm 3$	$(12-31) \pm 7$
C	<2.8	$<6.7 \pm 1.1$	–	0.0 ± 0.6	0.0 ± 1.1	–	–

astrometric uncertainties, and we will use the formal errors of a Gaussian fit obtained with JMFIT within AIPS. Given the relatively large calibrator–target separation of $\sim 4^\circ$, we expect an additional systematic component to the position error due to the unmodeled ionosphere of 1–5 mas (Brisken et al. 2000). As a reference position for the plots we use the peak position of run C, $\alpha_{J2000.0} = 13^{\text{h}}02^{\text{m}}47^{\text{s}}.6435(1)$ and $\delta_{J2000.0} = -63^\circ 50' 08''.636(1)$, which we consider to represent the pulsar position at MJD 54623.48.

Assuming a mass of the neutron star of $1.4 M_\odot$ and a stellar mass of $31 \pm 5 M_\odot$ (see Table 3.1 for the system parameters), the mass function provides $i = 22.2^\circ$ and the semimajor axis of the pulsar orbit is 7.2 AU, or 3.1 mas for a distance to the system of 2.3 kpc. The red crosses in Fig. 3.2 mark the region where the pulsar should be located in each epoch. Their centres are placed at the position of run C corrected for proper motion at the corresponding epochs (MJD 54309.25 for run A and MJD 54329.18 for run B). Since we do not know the orientation of the orbit in the sky, we plot as error bars the projected orbital separation of the pulsar with respect to run C. The error bars also include the $1-\sigma$ uncertainties on the mass of the star (and hence the distance uncertainty), on the astrometry of run C, and on the offset due to the proper motion. Finally, we have included the astrometry in runs A and B to compute the range of possible separations between the peak of the emission and the pulsar, as shown in Table 3.4. We consider all possible values of the longitude of the ascending node (Ω), which determines the orientation of the orbit in the plane of the sky (see Appendix A for a detailed description of the orbital elements).

We note that in run A the pulsed emission should be completely absorbed, but during run B the flux density from the pulsar can represent up to 10% of the total emission (Johnston et al. 2005). To test if the position of the peak of the extended emission is affected by the presence of the pulsar, we have subtracted from the run B data a 4 mJy point-like source located at 12 mas from the peak of the emission in the direction of the red cross. After this subtraction the peak of the emission is shifted by 0.7 mas, which is much lower than the 7.6 ± 0.5 mas displacement between the peaks of run A and B.

3.5 Kinematical interpretation of the radio outflow

The radio morphology at a given epoch depends on the spatial distribution of synchrotron emitting particles and their emission processes. Given the limitations of our data (only two images, and without accurate astrometry), we have used a simple kinematical model to check if it can trace the extended structures detected.

We have considered the shock between the relativistic pulsar wind and a spherical stellar wind. The shock is produced at the standoff distance, the region where the pulsar and stellar wind pressures balance, as described in Dubus (2006). The evolution of the nebular flow after the shock is described in Kennel & Coroniti (1984). This should be considered as a first approximation to the much more complex hydrodynamic behaviour of a shocked flow in a binary system, as shown in Bogovalov et al. (2008). In the Kennel & Coroniti approximation of a non-turbulent adiabatically expanding flow, the flow speed depends only on the magnetisation parameter σ when assuming $\sigma \ll 1$. This allows us to compute the past trajectory of the flow produced behind the standoff distance, which depends on the components separation along the orbit, the mass loss rate of the star ($0.6 \times 10^{-7} M_{\odot} \text{ yr}^{-1}$ for a typical O9 star; Vink et al. 2000), the terminal wind velocity, v_{∞} , and the spin-down luminosity of the pulsar, \dot{E}_{sp} . With these restrictions, the only free parameters are the longitude of the ascending node, Ω , which describes the orientation of the orbit, and the magnetisation parameter, σ . Projecting the past trajectory of the flow on our VLBI images of runs A and B, we found that the best match with the detected morphologies is obtained for $\Omega \simeq -40^{\circ}$ and a magnetisation parameter of $\sigma \simeq 0.005$, assuming an orbital inclination of $i = 22.2^{\circ}$. The obtained trajectories are shown in Fig. 3.3 for three different values of σ . We note that the uncertainty in the distance to the system (2.3 ± 0.4 kpc) scales the size of the contours, but not the orbit and the trajectories, which are computed in AU. The range of magnetisations in the plots has been chosen to approximately show the effect of keeping $\sigma = 0.005$ and changing either the distance from 1.9 to 2.7 kpc, or Ω from -35 to -45° , or a variation of the product $\dot{M} v_{\infty}$ of two orders of magnitude.

The parameters of the circumstellar equatorial disc of the star are uncertain, but considering $\dot{M}_e = 5 \times 10^{-8} \dot{M} \text{ yr}^{-1}$, (Johnston et al. 1996), and a wind velocity of $\sim 10 \text{ km s}^{-1}$, the product $\dot{M}_e v_{\infty, e}$ is ~ 100 times smaller than the spherical wind contribution. If this equatorial component dominates during certain orbital phases, the flow trajectory would be closer to the orbit than the dashed models in Fig. 3.3 for some specific regions of the more recent part of the trajectory. However, we do not attempt to accurately model this circumstellar disc, as its density, velocity, and crossing time are unknown.

In Figs. 3.4 and 3.5 we show the results of the kinematical model for different values of the longitude of the ascending node and the magnetisation parameter, respectively. We can see that it is not possible to simultaneously fit the two images, although the best values are close to $\Omega \sim -40^{\circ}$ and $\sigma \sim 0.005$.

We note that the astrometric errors can be of the order of ~ 10 AU (see above). We also

3. Discovery of extended emission from PSR B1259–63

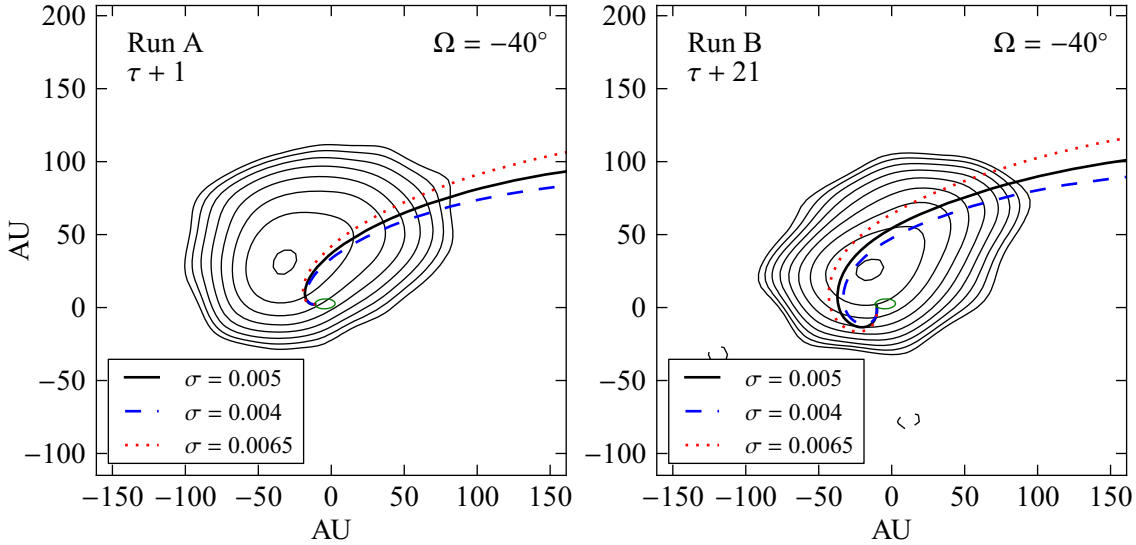


Figure 3.3: Computed trajectory of the nebular flow in the past. The contour plots are the same as in Fig. 3.2 (left and centre). The green ellipse represents the counterclockwise orbit. The longitude of the ascending node, Ω , is set to -40° . The different magnetisations used are displayed in the bottom-left panels. The axes units are AU ($100 \text{ AU} \simeq 43 \text{ mas}$).

emphasise that this simple model cannot account for the complex magnetohydrodynamical turbulence of the real flow and should be considered as a first approximation to constrain σ . Previous studies have assumed a magnetisation parameter σ of around 0.01–0.02 for this pulsar (see Tavani & Arons 1997; Dubus 2006), considerably higher than our best-fit value, although comparable lower values for σ have been suggested for other systems (e.g., the Crab pulsar; Kennel & Coroniti 1984).

3.6 Discussion and conclusions

The results presented here show that the particle accelerator within the binary system PSR B1259–63/LS 2883 can produce a flow of particles emitting synchrotron radiation that can travel several AU. The total projected extent of the nebula is $\sim 50 \text{ mas}$, or $120 \pm 20 \text{ AU}$, and the peak of the emission is clearly displaced from the binary system orbit (see Fig. 3.2 and Table 3.4). Similar morphologies and displacements have been found in the gamma-ray binaries LS 5039 and LS I +61 303, although for smaller sizes and on shorter time scales (Ribó et al. 2008; Moldón et al. 2011d, 2012a; Massi et al. 2004; Dhawan et al. 2006; Albert et al. 2008).

There is an ongoing debate on the nature of the compact object and particle acceleration mechanisms in LS 5039 and LS I +61 303. Although initially suggested to be accreting/ejecting microquasar systems (Paredes et al. 2000; Massi et al. 2004), some au-

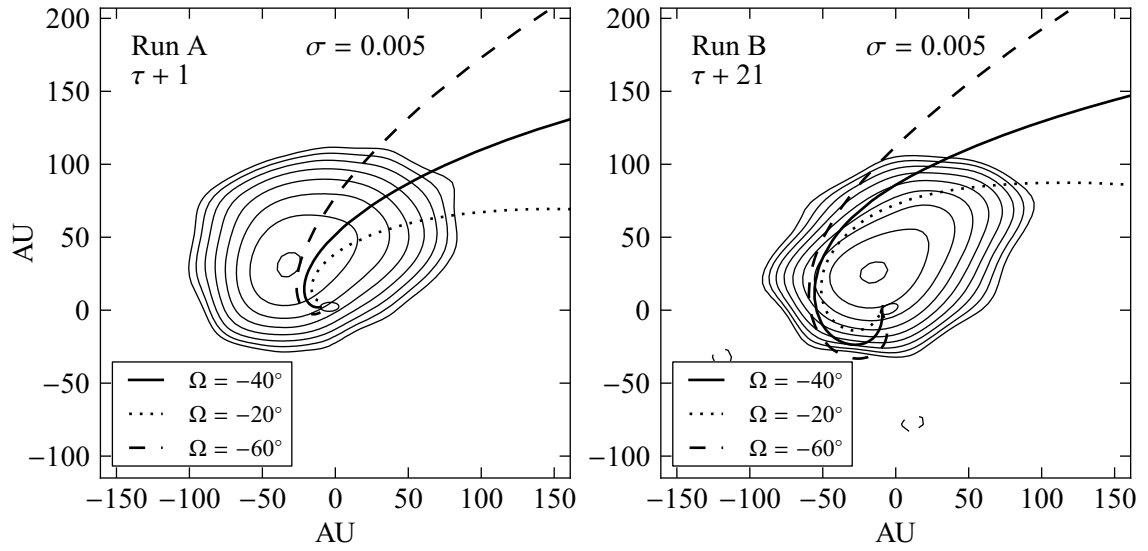


Figure 3.4: Same as in Fig. 3.3 for a fixed σ and different Ω .

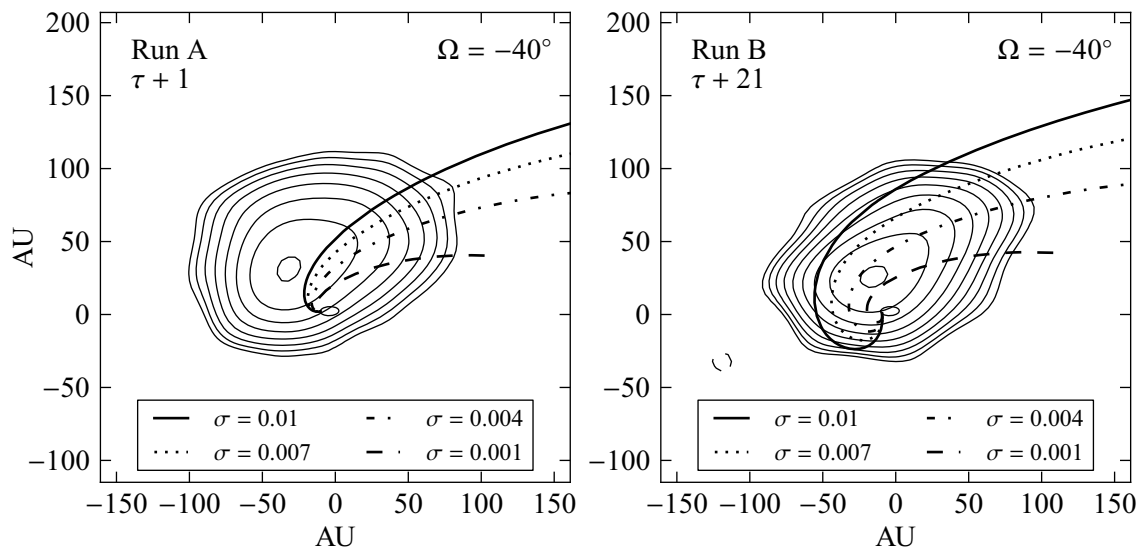


Figure 3.5: Same as in Fig. 3.3 for a fixed Ω and different σ .

3. Discovery of extended emission from PSR B1259–63

thors believe that they contain young non-accreting pulsars (Maraschi & Treves 1981; Dubus 2006; Dhawan et al. 2006; Ribó et al. 2008), which can explain their multiwavelength emission (Sierpowska-Bartosik & Torres 2008; Cerutti et al. 2008; Bogovalov et al. 2008; Zdziarski et al. 2010). However, there are three basic issues that are not well understood for LS 5039 and LS I +61 303, and comparisons with PSR B1259–63/LS 2883 can help to clarify the situation. First, the putative pulsar properties of these two sources are unknown, as no pulsations have been detected for these systems. The lack of pulsations can be explained by the intense stellar wind that produces an extremely high absorption for these small orbits, a 3.9 day orbit with separations between 0.1 and 0.2 AU for LS 5039, and 26.5 days with separations of 0.1–0.7 AU for LS I +61 303 (Casares et al. 2005a,b; Aragona et al. 2009). As a reference, the separation for PSR B1259–63 is in the range 0.9–13.4 AU, and the pulsations disappear for distances below ~ 1.6 AU. For more details on free-free absorption see Appendix B. Second, it is not clear if the massive stellar wind can confine the pulsar wind (Romero et al. 2007). VLBI images, like the ones presented here, can shed light on the shock/outflow conditions and geometry. Third, the observed SED and variability at GeV energies is not well understood (Abdo et al. 2009a,b; Torres & Rea 2011). PSR B1259–63 was detected by *Fermi*/LAT (Abdo et al. 2011) during the periastron passage of 2010–2011, showing a surprising GeV outburst a few weeks after the periastron passage (Takata et al. 2012). In this context, the high-resolution VLBI radio observations presented here establish a common link to test the similarities between the three systems PSR B1259–63 and other gamma-ray binaries displaying resolved radio structures, in particular LS 5039 and LS I +61 303.

In conclusion, our results provide the first observational evidence that non-accreting pulsars orbiting massive stars can produce variable extended radio emission at AU scales. Similar structures are also seen in LS 5039 and LS I +61 303, in which the nature of the compact object is unknown because the detection of pulsations is challenging. The discovery presented here for the young non-accreting pulsar PSR B1259–63 reinforces the link with these two sources and supports the presence of pulsars in these systems as well. LBA observations of PSR B1259–63 during the 2010/2011 periastron passage will allow us to compare the behaviour observed in these sources, which have been extensively monitored during several orbital cycles. We have also shown that the orientation of the orbit and the magnetisation of the pulsar can be inferred from VLBI observations of the source. Several images at different orbital phases covering a wider range of true anomalies will be useful to model the outflow and to understand the orbital changes of the extended emission. Finally, accurate VLBI observations of the pulsed emission during several orbits can provide the pulsar trajectory, from which we can directly obtain the proper motion of the binary system, the inclination and Ω of the orbit, and the distance to the system.

3.7 Work in progress

The periastron passage of PSR B1259–63 during 2007 allowed us to image its morphology on mas scales and to study its variability. After this first detection, the natural step is to arrange a new set of observations aiming to better trace the source morphological changes along the orbit. In order to improve our understanding of the source behaviour we planned a more detailed campaign to cover the following periastron passage. We monitored the orbital variability of the radio nebula of PSR B1259–63 with the LBA (project V434) during the 2010 periastron passage (centred on December 15, 2010). We conducted five observations covering a wide range of true anomalies with a configuration similar to the one used in the observations of the 2007 periastron passage. In Fig. 3.6 we show the orbit of PSR B1259–63 as seen from above. The five red circles indicate the position of the pulsar during the observations of project V434, which correspond to -21 , $+0$, $+29$, $+55$, and $+107$ days after the periastron passage. The corresponding orbital phases are 0.9833, 0.0003, 0.0237, 0.0447, 0.0868, respectively.

In this campaign the data were correlated with pulsar gating, only using the data during the on-pulse or the off-pulse (see Sect. 2.3). This technique will allow us to obtain radio images where we can enhance or eliminate the pulsed emission. This is possible for runs A, C, D, and E. During run B the pulsar was eclipsed and no pulsations could be detected. The pulsar gating observations will allow us to separate the pulsed emission from the transient nebula. Therefore, we will obtain for the first time the position of the pulsar and the nebula simultaneously, providing a direct measurement of the relative position and distance between the pulsar and the emitting flow region. This is important to disentangle the ambiguity of the origin of the flow, which is one of the main limitations for a detailed analysis of the source structure and variability.

In Fig. 3.7 we show a sample of the pulse profile obtained during one of the observations of V434. Using the software from the DiFX correlator in the Curtin Institute of Radio Astronomy, it is possible to obtain the signal received at one particular antenna and distribute it in time bins computed with the pulsar ephemerides. This sample, provided by H. Bignall, was used to determine the opening and closing gates specifically for the final correlation of run D. As we can see, the double peak is relatively wide for this pulsar, making the duty cycle of PSR B1259–63 relatively long, of the order of 60%. Consequently, the gating technique is less efficient for this pulsar than for pulsars with shorter duty cycles.

The results derived from this campaign are still being analysed. The correlation, including the pulsar gating passes, were performed after several iterations with the correlator staff, which prolonged the correlation of the five data runs several months. Preliminary images show that the source behaves very similar at the orbital phases already explored. However, we prefer not to include these preliminary results in the thesis without a complete and detailed analysis of the available data.

3. Discovery of extended emission from PSR B1259–63

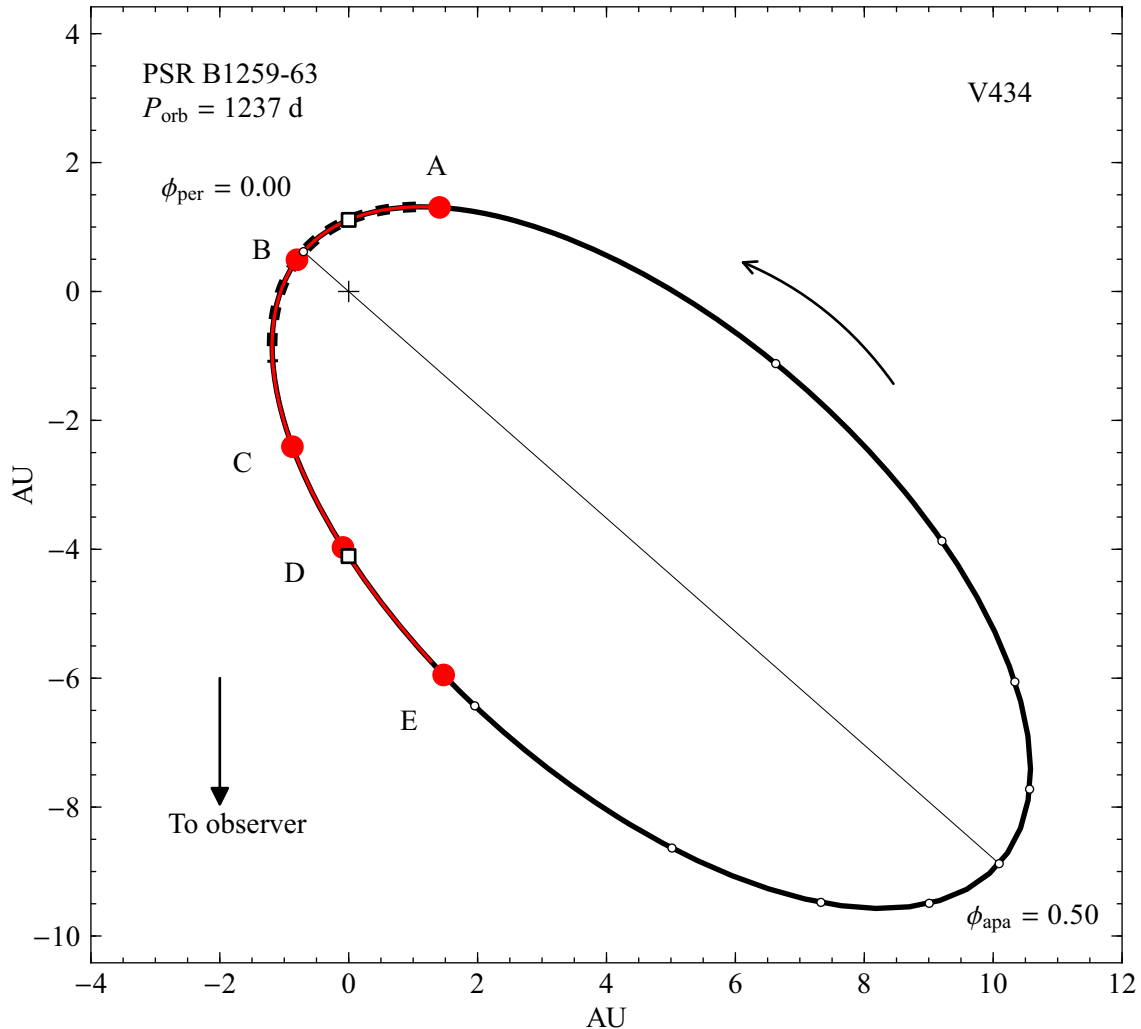


Figure 3.6: Sketch of the orbit of PSR B1259–63 with the position of the pulsar during the five runs of project V434 marked as red circles. The black cross indicates the position of the massive star. The red line approximately indicates the time interval when the transient radio emission is detected (Johnston et al. 2005). The dashed line marks the region where pulsations have not been detected. The white dots are plotted every 0.1 orbital phases. The empty squares mark the inferior and superior conjunction of the compact object, which occur at orbital phases 0.04750 and 0.99478, respectively. The orbit was computed using the orbital solution reported in Wang et al. (2004). The orientation of the orbit is arbitrary, and it is seen face-on (see Fig. A.2 on page 180 for examples of other possible projections of the orbit).

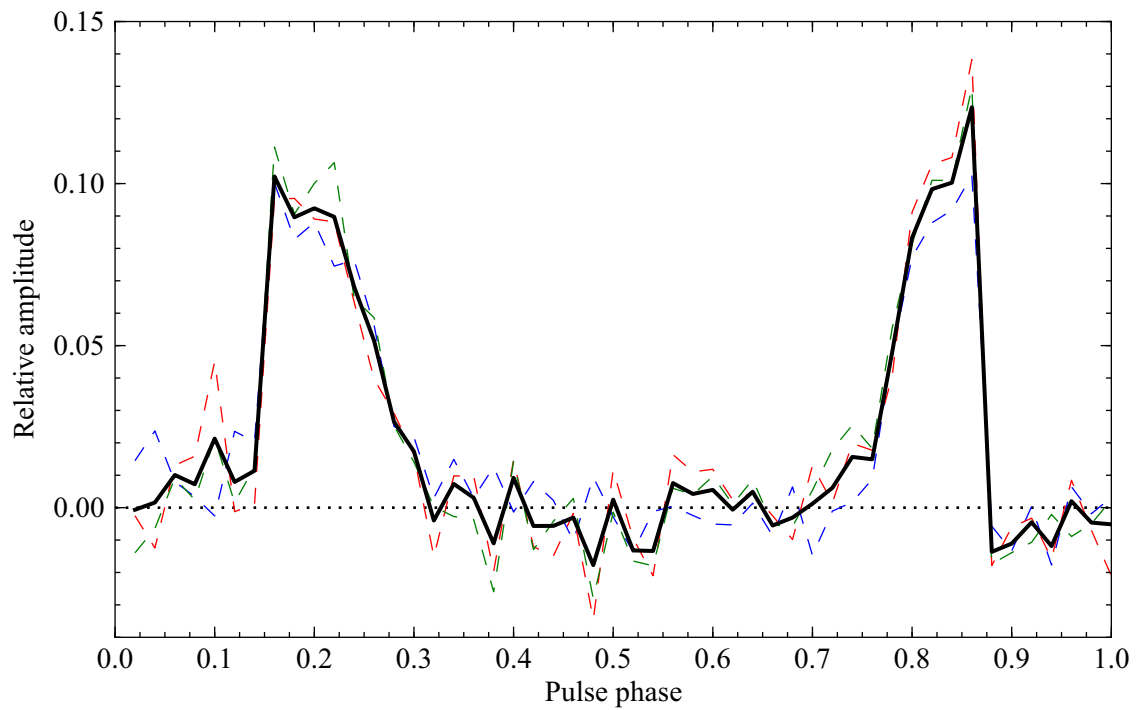


Figure 3.7: Sample of the pulse profile of PSR B1259–63 obtained with Parkes during the fourth epoch of project V434. The dashed lines show the relative amplitude of the pulsed radio signal as a function of the pulsar phase obtained during 5 minutes at three different times within the run. The black line is the average value of the radio amplitude.

4

The changing milliarcsecond radio morphology of LS 5039

4.1 Introduction

LS 5039 is one of the “classical” gamma-ray binaries since its association with an EGRET source by Paredes et al. (2000) and the discovery of bipolar extended emission at AU scales (Paredes et al. 2000, 2002). A peculiarity of this system is that the optical star does not contain a circumstellar equatorial disc, like LS I +61 303 and PSR 1259–63, although it is a beast of $\sim 30 M_{\odot}$ with a powerful thermal energy output of $\sim 10^{39}$ erg s $^{-1}$. Moreover, it is the gamma-ray binary with the smallest orbit and shortest period. The separation between the bright massive star and the compact object during the periastron passage is 0.09 AU, which corresponds to just 1.8 times the stellar radius. The physical conditions of this powerful binary system are extreme, which make it a very interesting source of astrophysical phenomena. In this Chapter we aim to explore the radio emission of LS 5039 on mas scales to complement the image obtained in Paredes et al. (2000) and test the stability of its radio outflow. With this purpose we present and analyse two VLBA observations¹ of LS 5039 obtained at different orbital phases.

¹Published in Ribó, M., Paredes, J. M., Moldón, J., Martí, J., & Massi, M. 2008, A&A, 481, 17.

4.2 The binary system LS 5039

The star number 5039 of the Luminous OB-stars catalogue is an optical bright star with a photometric visual magnitude of 11.3. It is situated in the southern Milky Way, and belongs to the Scutum constellation. The star is classified in the General Catalogue of Variable Stars (GCVS) as V* V479 Sct. LS 5039 is a binary system composed by the homonym bright star LS 5039, of spectral type ON6.5 V((f)), and a compact object of unknown mass (Casares et al. 2005b). The orbital period of the system is 3.9 days and the eccentricity of the orbit is $e \sim 0.35$ (Casares et al. 2005b; Aragona et al. 2009; Sarty et al. 2011). Given the mass function of the binary system the compact object would be a black hole for low inclinations of the orbit, and a neutron star for high inclinations (see the discussion in Casares et al. 2005b and recent constraints in Casares et al. 2012a). No short-period pulsations were found that could demonstrate the presence of a pulsar either in radio (McSwain et al. 2011) or X-rays (Martocchia et al. 2005; Rea et al. 2011). The distance to the system has recently been updated to 2.9 ± 0.8 kpc (Casares et al. 2012a). LS 5039 displays non-thermal, persistent, and periodic gamma-ray emission up to 4 TeV (Paredes et al. 2000; Aharonian et al. 2005a; Abdo et al. 2009b). The X-ray and gamma-ray emission show a periodic modulation of 3.9 days (Bosch-Ramon et al. 2005; Aharonian et al. 2006; Kishishita et al. 2009; Abdo et al. 2009b). The total radio emission of LS 5039 is variable, although no periodicity or strong outbursts have been detected so far (Martí et al. 1998; Ribó et al. 1999, 2002a). The radio emission above 1 GHz is non-thermal, with spectral index of -0.46 (Martí et al. 1998), and inverted at lower frequencies (Godambe et al. 2008; Bhattacharyya et al. 2012, but see Pandey et al. 2007). The synchrotron radio emission appears extended when observed with VLBI on scales of milliarcseconds (mas). The source shows a main core and extended bipolar emission that has been observed in directions with position angles (P.A.) between 120 and 150° and projected angular distances between 1 and 180 mas (3–500 AU) from the core (Paredes et al. 2000, 2002). Finally, Durant et al. (2011) discovered an extended component in X-rays up to $2'$ from LS 5039.

Several theoretical models were developed to explain the multiwavelength behaviour of LS 5039. The very-high-energy gamma-ray emission can be interpreted as the result of inverse Compton upscattering of stellar UV photons by relativistic electrons. The acceleration of electrons can be explained by two exclusive scenarios: acceleration in the jet of a microquasar powered by accretion (Paredes et al. 2006; Bosch-Ramon et al. 2006 and the review in Bosch-Ramon & Khangulyan 2009), or shocks between the relativistic wind of a young non-accreting pulsar and the wind of the stellar companion (Maraschi & Treves 1981; Tavani & Arons 1997; Dubus 2006; Khangulyan et al. 2007). A simple and shockless microquasar scenario is disfavoured by previous VLBI radio observations of LS 5039 (Ribó et al. 2008). Also, no signs of the presence of an accretion disc have been detected so far (although see Barkov & Khangulyan 2012 and Okazaki et al. 2008 for alternative explanations). Sarty et al. (2011) used the stability of the optical photometry of LS 5039

to constrain the orbit inclination to be below 60° and the mass of the compact object above $1.8 M_\odot$. Models based on the young non-accreting pulsar scenario, first proposed for LS 5039 in Martocchia et al. (2005), had provided descriptions of the HE/VHE light curves and the spectral evolution of the source as a function of the orbital phase (see Sierpowska-Bartosik & Torres 2007; Dubus et al. 2008; Khangulyan et al. 2008; Takahashi et al. 2009). Apart from the acceleration of particles in the main shock between winds, additional gamma-ray emission can be produced by the unshocked pulsar wind (Cerutti et al. 2008) and by secondary cascading (Bosch-Ramon et al. 2008; Cerutti et al. 2010). The X-ray light curve and spectrum show orbital variability, although there are no signatures of variable X-ray absorption or X-ray occultations, as discussed in Reig et al. (2003), Martocchia et al. (2005), Bosch-Ramon et al. (2007) and Szostek & Dubus (2011). Zabalza et al. (2011) constrained the spin-down luminosity of the putative pulsar to be $\sim 3\text{--}6 \times 10^{36}$ erg s $^{-1}$.

Very recently, detailed hydrodynamical simulation have been obtained to understand the wind shocks and the flow dynamics in gamma-ray binaries. Two-dimensional hydrodynamic simulations were performed to study the wind-wind collision interaction at scales of the binary system for PSR B1259–63 (Bogovalov et al. 2008, 2012) and for LS I +61 303 (Romero et al. 2007). Also for PSR B1259–63, Okazaki et al. (2011) and Takata et al. (2012) presented 3D simulations of the tidal and wind interactions. Lamberts et al. (2012) considered the general case of colliding wind binaries and described the outflow structure at larger distances. Finally, the flow structure for a case similar to LS 5039 was described in Bosch-Ramon et al. (2012) for scales up to 100 times the orbit size.

From a theoretical point of view, a general discussion on the properties of the radio emission of LS 5039 can be found in Bosch-Ramon et al. (2008). However, only a few predictions on the expected radio morphology have been discussed. Dubus (2006) presented emission maps at different orbital phases for LS 5039 and predicted orbital morphological changes on mas scales, as well as displacements of the peak of the emission of a few mas. Bosch-Ramon & Khangulyan (2011) obtained synthetic maps at radio wavelengths from a model based on secondary particles created from gamma-ray absorption, which may account for a significant fraction of the total radio flux density of the source and also predicts extended radio emission on mas scales.

In this chapter, we report on two high-resolution radio images of LS 5039 in an attempt to disentangle the two possible scenarios using morphological and astrometric information. The observations are described in Sect. 4.3 and the data reduction is discussed in Sect. 4.4. The results, described in Sect. 4.5, are divided in three parts, namely results of the VLA observations as a stand alone observatory, the astrometric results of the VLBA observations, and the description of the self-calibrated images obtained. A discussion on the results and their implications is presented in Sects. 4.6 and 4.7.

4. The changing milliarcsecond radio morphology of LS 5039

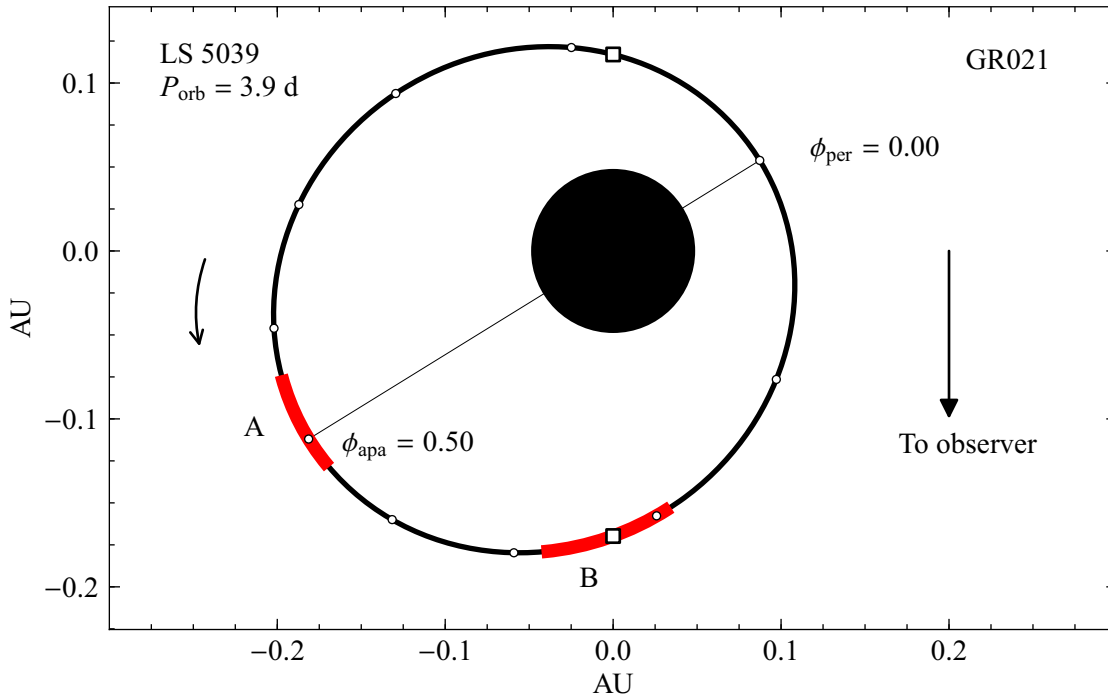


Figure 4.1: Sketch of the orbit of LS 5039 with the position of the compact object during the two runs of project GR021 marked in red. The white dots are plotted every 0.1 orbital phases. The empty squares mark the inferior and superior conjunction of the compact object, which occur at orbital phases 0.770 and 0.080, respectively. The orbit was computed using the orbital solution reported in Casares et al. (2005b). The orbit, size of the star, and the duration of the runs are scaled to the real values. The orientation of the orbit is arbitrary, and it is seen face-on (see Fig. A.2 on page 180 for examples of other possible projections of the orbit).

4.3 VLBA observations of LS 5039

We observed LS 5039 with the National Radio Astronomy Observatory (NRAO) VLBA and the Very Large Array (VLA) at 5 GHz frequency on 2000 June 3 and 8. We used the VLA in its C configuration, both as a connected interferometer and as a phased array. The two observing sessions, hereafter run A and run B, spanned from 4:30 to 12:30 UT on the corresponding dates, and were thus centred on MJD 51698.4 and MJD 51703.4, respectively. The orbital phases of the system were in the range 0.44–0.53 for run A and in the range 0.72–0.81 of the following orbital cycle for run B (using the ephemeris from Casares et al. 2012a). A sketch of the orbit in an arbitrary orientation is shown in Fig. 5.1, where we also mark the position of the compact object during each run.

We performed the observations using the phase-referencing technique, switching between the phase reference calibrator J1825–1718 and LS 5039, separated 2.47° , with

cycling times of 5.5 minutes (2 minutes on J1825–1718 and 3.5 minutes on LS 5039), compatible with the expected coherence time. The fringe finder was 3C 345. The ICRF source J1911–2006, located at 11.9° from LS 5039, was observed every 22 minutes to monitor the performance of the observations. To check the stability of the astrometry we observed the source J1837–1532, located at 3.38° from the phase reference calibrator J1825–1718.

We recorded the data with 2-bit sampling at 256 Mbps, at left-hand circular polarisation. A total bandwidth of 64 MHz was provided by 8 sub-bands. The data were processed at the VLBA correlator in Socorro, using an integration time of 4 s.

The position used hereafter for the phase reference source J1825–1718, obtained by means of dedicated geodetic Very Long Baseline Interferometry (VLBI) observations, is $\alpha_{\text{J2000.0}} = 18^{\text{h}}25^{\text{m}}36^{\text{s}}.53237 \pm 0^{\text{s}}.00021$ (or ± 3.0 mas) and $\delta_{\text{J2000.0}} = -17^\circ 18' 49''.8534 \pm 0''.0045$ (or ± 4.5 mas) in the frame of ICRF-Ext.1 (Craig Walker, private communication). However, this information was not available at the time of correlation, which was performed for a calibrator position shifted by $\Delta\alpha = +57.0$ mas and $\Delta\delta = +21.4$ mas. In the case of LS 5039, due to its proper motion (see Ribó et al. 2002b), the source was found to be $\Delta\alpha = +7.6$ mas and $\Delta\delta = -16.2$ mas away from the correlated phase centre, which was located at $\alpha_{\text{J2000.0}} = 18^{\text{h}}26^{\text{m}}15^{\text{s}}.05600$ and $\delta_{\text{J2000.0}} = -14^\circ 50' 54''.2400$ (Martí et al. 1998).

Regarding the VLA observations, the source 3C 286 was used for flux density calibration, and the source J1825–1718 for phase calibration and to phase up the array.

4.4 Data reduction

We performed the post-correlation data reduction using the Astronomical Image Processing System (AIPS) software package, developed and maintained by NRAO. The phased VLA position had to be corrected by 43 cm, according to later geodetic measurements. The positions of J1825–1718 and LS 5039 were corrected using the task CLCOR. As recommended for phase-referencing experiments, we applied ionospheric and Earth Orientation Parameters corrections to the visibility data using the task CLCOR. A priori visibility amplitude calibration was done using the antenna gains and the system temperatures measured at each station. We then used the fringe finder to calibrate the instrumental phase and delay offsets. The fringe fitting (FRING) of the residual delays and fringe rates was performed for all the radio sources. We found very good solutions for 3C 345, J1911–2006 and J1825–1718. Fringes for 15% and 25% of the baselines were missing for LS 5039 and J1837–1532, respectively. Typical data inspection and flagging were performed. The obtained self-calibrated images of J1911–2006, which show a one-sided jet, are very similar to those present in the VLBA calibrator source catalogue, confirming the reliability of the observations and the initial data reduction.

For each run, we performed standard phase and amplitude calibration and phase self-calibration steps on LS 5039. As a compromise between angular resolution and sensitivity,

4. The changing milliarcsecond radio morphology of LS 5039

we used a weighting scheme with robust 0 to produce the images with the task IMAGR. The obtained image had a synthesised beam of $\sim 6.4 \times 2.2$ mas² in P.A. of $\sim 0^\circ$. Extended emission was visible for both runs. To enhance the small-scale morphology, we produced final images using a convolving beam of 3.4×1.2 mas² in P.A. of 0° (similar to what would be obtained by using robust -2 within AIPS or a uniform weighting scheme within Difmap). This convolving beam is the one we used previously in Paredes et al. (2000), allowing for a straightforward comparison of the images.

To measure the position of LS 5039 in both runs we used the phase-referencing technique, and transferred the phases of the calibrator J1825–1718, fitted with the task FRING, to our target source. The peak flux density of this extragalactic phase-reference calibrator is 118 mJy beam⁻¹ at 5 GHz, enough to provide useful phase information. However, it suffers scattering and becomes resolved with the VLBA, providing relatively noisy phase information on the longest baselines. We inspected and screened the phase delays and delay rates of J1825–1718. Tropospheric corrections were unsuccessful because the observation strategy was not adequate to account for them. Phase-referenced images of the target source with a synthesized beam of $\sim 4.9 \times 1.5$ mas² in P.A. $\sim 0^\circ$ were obtained, and the peak position was measured with the AIPS task JMFIT.

4.5 Results

4.5.1 Flux density with the VLA

The VLA data of LS 5039 were compatible with a point-like source for the obtained synthesized beam of $5.5 \times 3.7''$ in P.A. of $\sim -4^\circ$. We measured the flux density of the source every 30 minutes (see the light curves in Fig. 4.2) and obtained a mean of 29.4 mJy with a standard deviation of $\sigma=1.1$ mJy during the 8 hours of run A, and 28.4 mJy with $\sigma=0.7$ mJy for run B. Therefore, LS 5039 displayed flux density variability below 4% at the $1\text{-}\sigma$ rms level within each 8-hour run. Similar results were obtained within 4-hour halves. This guarantees that we can produce reliable VLBA images for each of the entire observation periods, as well as for 4-hour intervals, provided the morphology does not change within such intervals.

4.5.2 Morphology with the VLBA

We show the final VLBA+phased VLA self-calibrated images in Fig. 4.3. The image obtained for run A displays a central core and bipolar and nearly symmetric extended emission with P.A. $\simeq 116 \pm 2^\circ$, with enhanced emission toward the southeast. The total flux density recovered by the VLBA, obtained with the task TVSTAT within AIPS, is ~ 25 mJy, representing $\sim 85\%$ of the VLA value. The peak flux density of the core is 10.5 mJy beam⁻¹. The image is similar to the one obtained with the same array in 1999 May 8, corresponding to orbital phases 0.13–0.17, which showed a slightly more

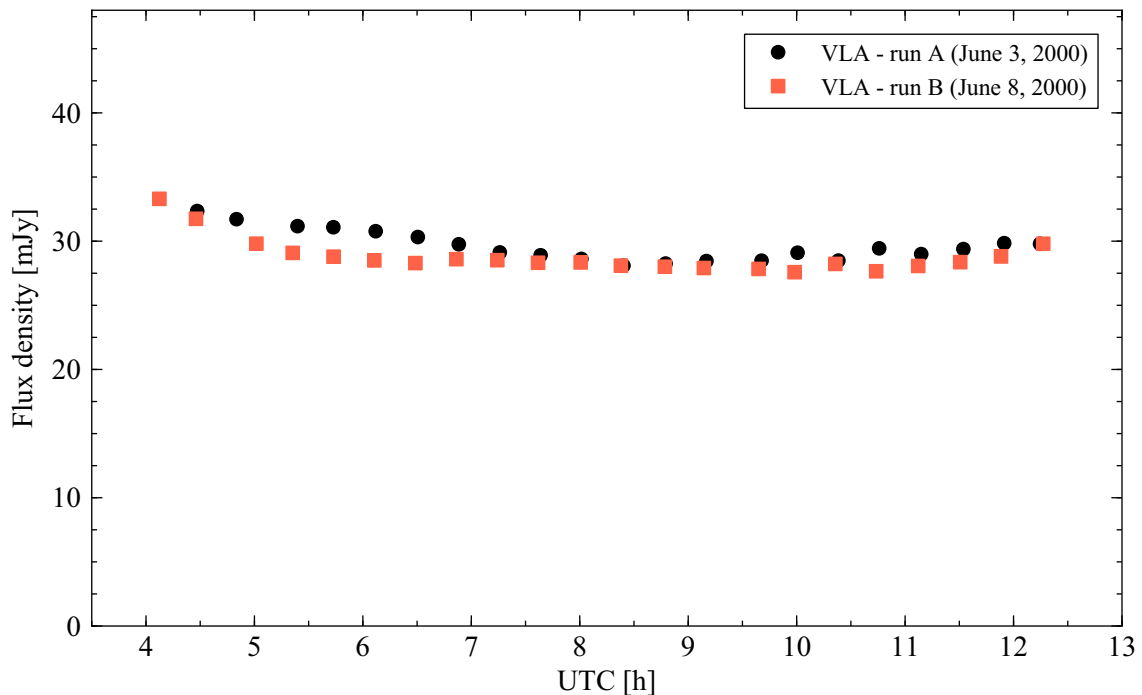


Figure 4.2: Flux density of the self-calibrated VLA observations during the two runs of the VLBA project GR021. The flux density errors of the individual measurements, obtained with JMFIT, are smaller than the symbols.

asymmetric extended emission in P.A. $\sim 125^\circ$, as can be seen in Paredes et al. (2000). In contrast, the image obtained for run B displays a core and bipolar but clearly asymmetric structure, with P.A. $\simeq 128 \pm 2^\circ$ and enhanced emission toward the northwest. The total flux density recovered is ~ 24 mJy, or $\sim 85\%$ of the VLA value. The peak flux density of the core is 10.5 mJy beam $^{-1}$, as in run A.

To characterise the extended emission we used UVFIT and JMFIT within AIPS, as well as model fitting tools within Difmap to check the reliability of the obtained results. The preferred model for run A data consisted of three Gaussian components to account for the core (Core1), the southeast (SE1) and the northwest (NW1) components. A similar model could fit the data for run B, although the southeast (SE2) component is marginally fitted in this case. The fitted parameters are quoted in Table 4.1. As can be seen, the peak flux density of each component is $\sim 50\%$ of its total flux density, although this is partially due to the convolving beam size being smaller than the synthesized beam size. In particular, we stress that the core components are not point-like.

Finally, we splitted the 8 hours of data in each run into 4-hour data sets. For each of them, we performed a similar calibration process as the one described above, and we modelled the final visibilities of the self-calibrated data. We measured no significant morphological differences between the two halves in any of the two runs. In particular,

Table 4.1: Parameters of the Gaussian components fitted to the images for each 8-hour run. Columns 3 and 4 list the peak and integrated flux densities of each component. Columns 5 to 8 list the polar and Cartesian coordinates of the components with respect to the peak position. Columns 9 to 11 list the sizes of the Gaussian major and minor axes and the P.A. of the major axis. The parameters P.A. and P.A._{Axis} are positive from North to the East.

Run	Comp.	Peak S_5 GHz [mJy b ⁻¹]	S_5 GHz [mJy]	r [mas]	P.A. [°]	$\Delta\alpha$ [mas]	$\Delta\delta$ [mas]	Maj. Axis [mas]	Min. Axis [mas]	P.A. _{Axis} [°]
A	Core1	10.54 ± 0.08	20.0 ± 0.2	—	—	—	—	3.69 ± 0.03	2.09 ± 0.02	103 ± 1
	SE1	1.11 ± 0.08	2.6 ± 0.2	3.67 ± 0.08	115.9 ± 1.7	3.30 ± 0.07	-1.60 ± 0.12	4.1 ± 0.3	2.36 ± 0.16	17 ± 5
	NW1	0.88 ± 0.08	1.5 ± 0.2	3.29 ± 0.09	-63 ± 2	-2.92 ± 0.08	1.52 ± 0.14	3.6 ± 0.3	1.99 ± 0.18	3 ± 6
B	Core2	10.45 ± 0.11	17.6 ± 0.3	—	—	—	—	3.71 ± 0.04	1.8 ± 0.2	180 ± 1
	SE2	0.75 ± 0.11	1.8 ± 0.4	2.8 ± 0.2	129 ± 5	2.17 ± 0.13	-1.8 ± 0.3	4.6 ± 0.7	2.1 ± 0.3	1 ± 7
	NW2	2.22 ± 0.11	3.9 ± 0.3	2.94 ± 0.06	-52.2 ± 1.4	-2.32 ± 0.04	1.80 ± 0.09	4.3 ± 0.2	1.68 ± 0.08	174 ± 2

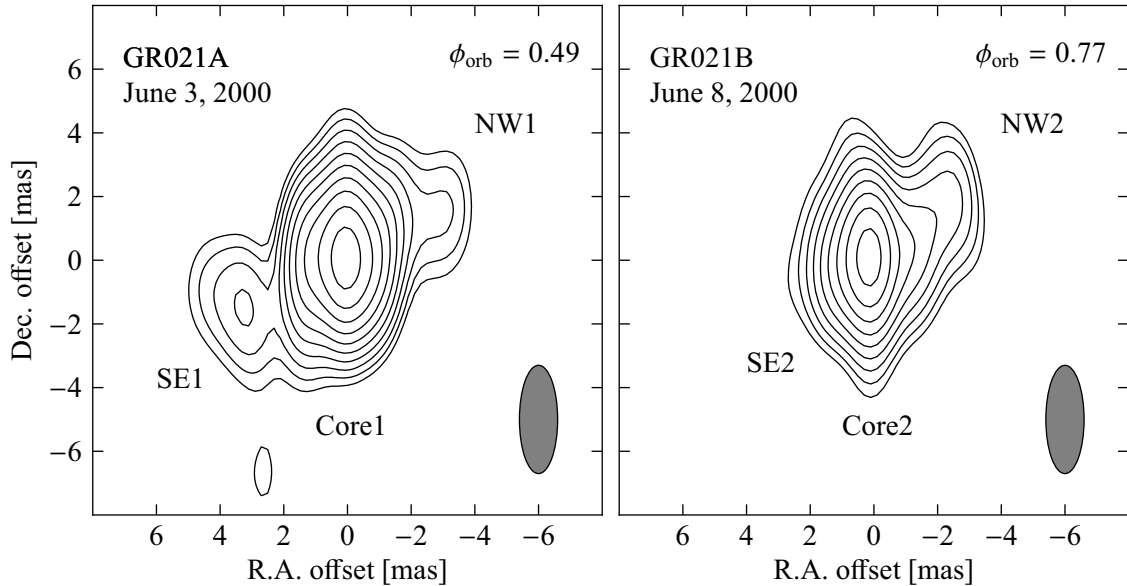


Figure 4.3: VLBA+phased VLA self-calibrated images of LS 5039 at 5 GHz obtained on 2000 June 3 (left) and 8 (right). North is up and East is to the left. Axes units are mas, and the (0,0) position corresponds to the source peak in each image. The convolving beam, plotted in the lower right corner, has a size of 3.4×1.2 mas in P.A. of 0° . The first contour corresponds to 5 times the rms noise of the image (0.08 and 0.11 mJy beam^{-1} for run A and B, respectively), while consecutive ones scale with $2^{1/2}$. The dates and orbital phases are quoted in the images. There is extended radio emission that appears nearly symmetric for run A and clearly asymmetric for run B, with a change of $\sim 10^\circ$ in its position angle. We have labelled the components fitted to the data, the parameters of which are listed in Table 4.1.

the distance between the fitted components Core1 and SE1 is stable in 4 hours within the errors ($\sigma_\alpha^A = 0.31$ mas, $\sigma_\delta^A = 0.62$ mas). This is also the case between Core2 and NW2 components ($\sigma_\alpha^B = 0.55$ mas, $\sigma_\delta^B = 0.25$ mas).

4.5.3 Astrometry of the peak of the emission

The phase-referenced image of LS 5039 obtained for run A, not shown here, displays a compact source with peak flux density of 6.7 mJy beam^{-1} , and faint extended emission toward the southwest (~ 2 mJy beam^{-1} ; the rms is 0.3 mJy beam^{-1}). The measured position of LS 5039 for run A is $\alpha_{J2000.0} = 18^{\text{h}}26^{\text{m}}15^{\text{s}}05653 \pm 0^{\text{s}}00001$ (or ± 0.15 mas), and $\delta_{J2000.0} = -14^\circ 50' 54''.2564 \pm 0''.0015$ (or ± 1.5 mas) (see discussion below). We recall that the reference coordinates are those of J1825–1718 listed in Sect. 4.3, which have systematic uncertainties of ± 3.0 mas and ± 4.5 mas, respectively. For checking purposes we splitted the data in blocks of 4- and 1-hour lengths, made images for each block, and measured the corresponding positions. The peak position of LS 5039 appears to move

4. The changing milliarcsecond radio morphology of LS 5039

$\Delta\alpha = +0.1 \pm 0.1$ mas, $\Delta\delta = +2.8 \pm 0.2$ mas between the two 4-hour blocks, and slightly more in the 1-hour blocks. The observed direction has a P.A. of $1.7 \pm 1.7^\circ$, which is the same as the line joining the positions of the source and the phase-reference calibrator J1825–1718. On the other hand, the expected error for differential astrometry is given by the separation d in degrees from the phase-reference source and the offset Δ of the correlated position of the phase reference calibrator, according to $\Delta \times (d/180^\circ) \times \pi$ (see Walker 1999). Plugging our offset of 60.9 mas and a distance of 2.47° we obtain an error of 2.6 mas, very similar to the observed displacement of LS 5039. A similar procedure using 4-hour blocks for the astrometric check source J1837–1532 ($d = 3.38^\circ$) reveals motion of the peak of this extended source by 3.2 ± 0.4 mas at P.A. = $46 \pm 8^\circ$, as expected. Therefore, these secular motions appear to be purely instrumental. The errors assigned to the coordinates of LS 5039 quoted above are half of the total secular motion measured in 1-hour blocks.

The phase-referenced image of run B, not shown here, reveals a double source in the eastwest direction. The two components have similar peak flux densities of 3.6 ± 0.1 mJy beam⁻¹, much lower than the one of the self-calibrated core, and are separated 2.5 ± 0.1 mas in P.A. of $87 \pm 5^\circ$. Moreover, 4- and 1-hour blocks reveal a fading of the western component and a brightening of the eastern one along the run (as well as a similar secular motion as in run A). This symmetric double structure is in contrast to the asymmetric structure seen in the self-calibrated image shown in Fig. 4.3-right. Tropospheric errors, which affect the phase-referenced image and cannot be accounted for, can easily split Core2 into the observed double source. Therefore, the precise position of the peak of LS 5039 cannot be measured in run B.

4.6 Interpretation of the changing morphology

The observations of LS 5039 reported here, obtained with the VLBA on two runs separated by 5 days, show a changing morphology on mas scales. In both runs there is a core component with a constant flux density within errors, and elongated emission with a P.A. that changes by $12 \pm 3^\circ$ between both runs. The source is nearly symmetric in run A and asymmetric in run B (see Fig. 4.3).

Microquasar scenario

In the microquasar scenario, and assuming ballistic motions of adiabatically expanding plasma clouds without shocks (see Mirabel & Rodríguez 1999), the morphology of run A can be interpreted as a double-sided jet emanating from a central core with the SE1 component as the approaching one. The relative distances of the components to the core would imply a bulk motion with velocity $\beta > 0.05 \pm 0.02$, whereas the flux asymmetry implies $\beta > 0.08 \pm 0.02$ for discrete ejections. The angle θ between the jet and the line of sight is restricted to $< 87^\circ$. These results are similar to those previously found with VLBA

and EVN images (Paredes et al. 2000, 2002). We can compute, for different θ angles, the expected displacement of the SE1 component with respect to Core1 in 4 hours using the measured value for the flux asymmetry of $\beta \cos \theta = 0.08$, and compare it to the upper limits for this displacement quoted at the end of Sect. 4.5.2. This provides a constraint of $\theta < 67^\circ$ at the $3\text{-}\sigma$ level assuming a distance to the source of 2.9 kpc. In contrast, in run B the northwest component appears to be the approaching one emanating from the core. The distances from Core2 to the components NW2 and SE2 are very similar and do not imply any significant relativistic motion. The flux asymmetry implies $\beta > 0.11 \pm 0.03$ and $\theta < 84^\circ$ for discrete ejections. As for run A, our measured upper limits of any displacement in 4 hours imply $\theta < 53^\circ$ at the $3\text{-}\sigma$ level. In conclusion, the lack of proper motions implies that, for the measured flux asymmetries, the SE1 jet should be pointing at $\theta < 67^\circ$, and the NW2 jet at $\theta < 53^\circ$. In this context, jet precession is needed to explain this behaviour. If the precession axis is close to the plane of the sky, as in SS 433 (Blundell & Bowler 2004), the precession cone should have a semi-opening angle $> 45^\circ$ to fulfill the θ limits quoted above. If the precession axis is close to the line of sight, a small precession of a few degrees could explain the images of runs A and B. However, in both cases the P.A. of the jet should vary considerably, in contrast to the small range covered by all observed values on scales of 5–150 mas, between 115 and 140° (Paredes et al. 2000, 2002).

Alternatively, the morphology detected in run B could be the result of a discrete ejection with core suppression where Core2 is the approaching component and NW2 the receding one, while there is no radio emission at the origin of the ejection. In this case, the flux asymmetry implies $\beta > 0.21 \pm 0.01$ and $\theta < 78 \pm 1^\circ$. The measured upper limits of the relative motion of these components in 4 hours provide a strong constraint of $\theta < 14^\circ$ at the 3σ level. Imposing $\beta \cos \theta = 0.21$, the origin of the discrete ejection (i.e., the position of the binary system or the position of Core1 in run A) should be placed at $\Delta\alpha = -1.4$ mas and $\Delta\delta = +1.1$ mas from Core2 in Fig 4.3. Although this would be self-consistent if the precise position of Core2 corresponds to the east component of the phase-referenced image of run B, it could be a chance coincidence produced by tropospheric errors. One should also invoke jet precession on short time scales to explain the change in P.A. of the extended emission. However, large X-ray and radio flux density variations are observed in microquasars displaying discrete ejections (see Fender 2006 and references therein), while the peak and total radio flux densities of LS 5039 are strikingly constant (see also, Ribó et al. 1999; Clark et al. 2001), and there is no evidence of an X-ray flare in 11.5 years of *RXTE*/*ASM* data, although 20-minute miniflares have been detected (Bosch-Ramon et al. 2005).

Non-accreting scenario

In the young non-accreting pulsar scenario, the different morphologies we have detected at different orbital phases could be due to the change of the relative positions between the pulsar and the companion star along the orbit (see Dubus 2006 for details). However,

4. The changing milliarcsecond radio morphology of LS 5039

observations at different orbital phases have always revealed a very similar P.A. for the extended emission, which can only be observed if the binary system is seen nearly edge on. On the other hand, the absence of X-ray eclipses places an upper limit of $i \lesssim 75^\circ$ in this scenario (Dubus 2006). Therefore, these two restrictions imply an inclination angle that should be close to the upper limit of 75° . We note that this is much higher than the inclination angle if the binary system is pseudo-synchronised (Casares et al. 2005b). Also, such a high i would imply a mass of the compact object compatible with a neutron star, and therefore these results provide a coherent framework.

4.7 Conclusions

In conclusion, a simple and shockless microquasar scenario cannot easily explain the observed changes in morphology. On the other hand, an interpretation within the young non-accreting pulsar scenario requires the inclination of the binary system to be very close to the upper limit imposed by the absence of X-ray eclipses. Precise phase-referenced VLBI observations covering a whole orbital cycle are necessary to trace possible periodic displacements of the peak position, expected in the young non-accreting pulsar scenario, and to obtain morphological information along the orbit. These will ultimately reveal the nature of the powering source in this gamma-ray binary.

5

Periodic morphological changes in the radio structure of LS 5039

5.1 Introduction

The bipolar radio morphology of LS 5039 on mas scales discovered in Paredes et al. (2000) was considered as the persistent jet of a microquasar. However, the results presented in Chapter 4 showed that the initial hypothesis was not favoured by the new images that showed a changing morphology (Ribó et al. 2008). The new results brought a new motivation to explore the source in order to characterise the radio morphological changes of LS 5039 and discriminate if they were either repeatable or erratic. The most natural follow up was to observe the source during different orbital phases in similar conditions to measure the flux density distribution and morphology, obtain the P.A. of the extended emission, measure the length and shape of the structure, and trace the relative motion of the radio core with accurate astrometry. The final goal of this project was to unveil the nature of the particle accelerator in LS 5039.

In this Chapter we present the results from a dedicated VLBA campaign that covers a full orbital cycle and provides astrometric and morphological information during five consecutive days. The analysis and results of this Chapter have been submitted for publication to *Astronomy & Astrophysics*¹. The observations and data reduction are presented in Sects. 5.2 and 5.3, including a discussion on the calibration caveats. In Sect. 5.4 we present the obtained astrometry and morphology of the source at different orbital

¹Moldón, J., Ribó, M., Paredes, J. M., 2012a, *A&A*, in press

5. Periodic morphological changes in the radio structure of LS 5039

Table 5.1: Log of VLBA observations of project BR127, conducted at 5 GHz. The orbital phases have an uncertainty of 0.02.

Run	Date (Y-M-D)	MJD	Phase range
A	2007-07-05	54286.15–54286.40	0.00–0.07
B	2007-07-06	54287.15–54287.40	0.26–0.32
C	2007-07-07	54288.15–54288.40	0.51–0.58
D	2007-07-08	54289.15–54289.40	0.77–0.83
E	2007-07-09	54290.15–54290.40	0.03–0.09

phases and analyse the components characterising the extended emission of the source. In Sect. 5.5 we show a compilation of VLBI data on LS 5039 and we describe and compare the morphology at different orbital phases for observations at frequencies between 1.7 and 8.5 GHz taken from 1999 to 2009. In Sect. 5.6 we present a model to check if the measured changes are compatible with a wind-wind collision scenario. The model allows us to estimate the orientation of the orbit on the sky, in particular its inclination, and consequently constrain the mass of the compact object. Finally, we present a summary of the results and the main conclusions of this work in Sect. 5.7.

5.2 A multi-epoch VLBA campaign on LS 5039

We conducted VLBI observations on LS 5039 during five consecutive days to cover an orbit of 3.9 d and an extra day to disentangle between orbital or secular variability. We observed at 5 GHz (6 cm wavelength) with the Very Long Baseline Array (VLBA) of the National Radio Astronomy Observatory (NRAO). The antennas that form the array are Br, Fd, Hn, Kp, La, Mk, Nl, Ov, Pt, and Sc. The VLBA project code is BR127, and the five observations were conducted from July 5 to 9, 2007 (MJD 54286 to 54290). The five runs, hereafter run A–E, spanned from 03:30 to 09:30 UTC and were scheduled in the same way to reduce differences between runs. The corresponding orbital phases were computed using the ephemerides in Casares et al. (2012a), $T_0 = \text{HJD } 2\,453\,478.09(6)$ and $P_{\text{orb}} = 3.90603(8)$, where the values in parentheses refer to the uncertainty in the last digit. The phase of the periastron passage is 0.0. The orbital phase at the centre of each observation was 0.03, 0.29, 0.55, 0.80, and 0.06, respectively, with an uncertainty of 0.02, or approximately 1.9 hours. A log of the observations is shown in Table 5.1. A sketch of the orbit in an arbitrary orientation is shown in Fig. 5.1, where we also mark the position of the compact object during each run.

The data were obtained with single circular left-handed polarisation, with eight sub-bands of 8 MHz, and were correlated with two bits per sample, obtaining a total aggregate

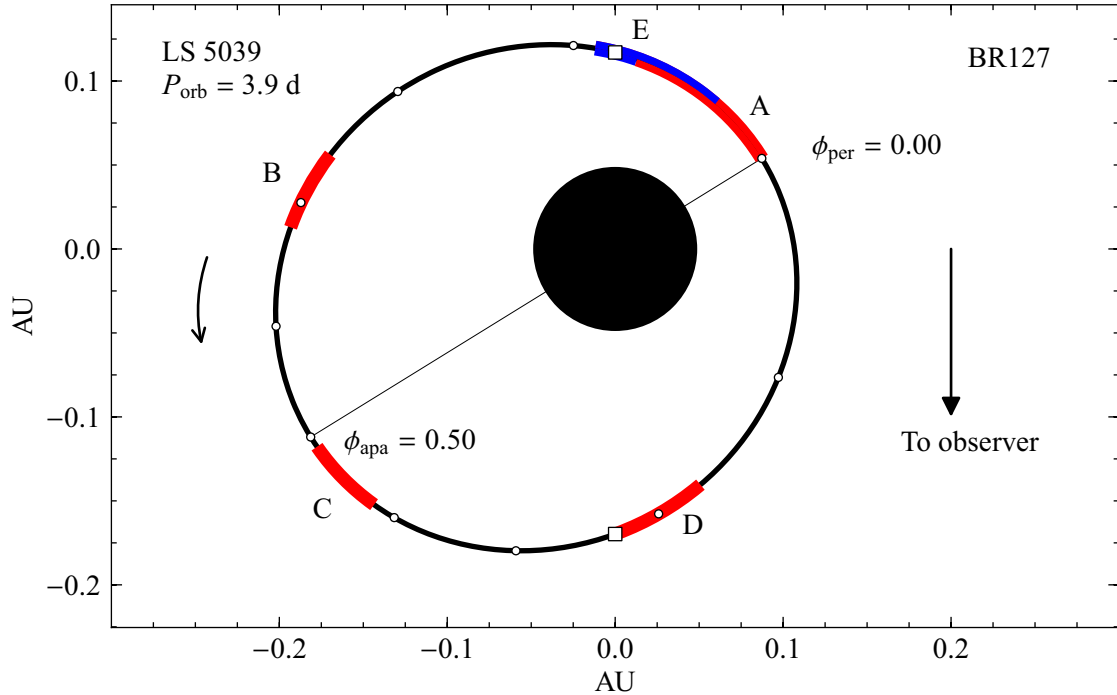


Figure 5.1: Sketch of the orbit of LS 5039 with the position of the compact object during the five runs of project BR127 marked in red and blue. The white dots are plotted every 0.1 orbital phases. The empty squares mark the inferior and superior conjunction of the compact object, which occur at orbital phases 0.770 and 0.080, respectively. The orbit was computed using the orbital solution reported in Casares et al. (2005b). The orbit, size of the star, and the duration of the runs are scaled to the real values. The orientation of the orbit is arbitrary, and it is seen face-on (see Fig. A.2 on page 180 for examples of other possible projections of the orbit).

bit-rate of 256 Mbps. The data were processed at the VLBA hardware correlator in Socorro, which produced the final visibilities with an integration time of 2 seconds.

We conducted the observations using the phase-referencing technique on the phase reference calibrator J1825–1718, located at 2.5° from LS 5039 in a P.A. of -176.4° (see Fig. 5.2). We observed in 4.2-min cycles, spending 2.5 minutes on the target source and 1.7 minutes on J1825–1718. The total scheduled time on the target source was 2.7 hours. As an astrometric check source we used J1818–1108, including one scan of 2.5 minutes every 30 minutes. Finally, we included three 5-minute scans on the fringe finder J1733–1304. The reference position for the observations is the correlation position of the phase reference source J1825–1718 $\alpha_{\text{J2000.0}} = 18^{\text{h}}25^{\text{m}}36^{\text{s}}.53228 \pm 0^{\text{s}}.00009$ (or $\pm 1.3 \text{ mas}$) and $\delta_{\text{J2000.0}} = -17^\circ 18' 49''.848 \pm 0''.002$ (or $\pm 2 \text{ mas}$), taken from Fomalont et al. (2003) via the SCHED database (NASA catalogue 2005f_astrom). LS 5039 is close to the galactic plane, at a galactic latitude of -1.29° . The phase calibrator and the astrometric check

5. Periodic morphological changes in the radio structure of LS 5039

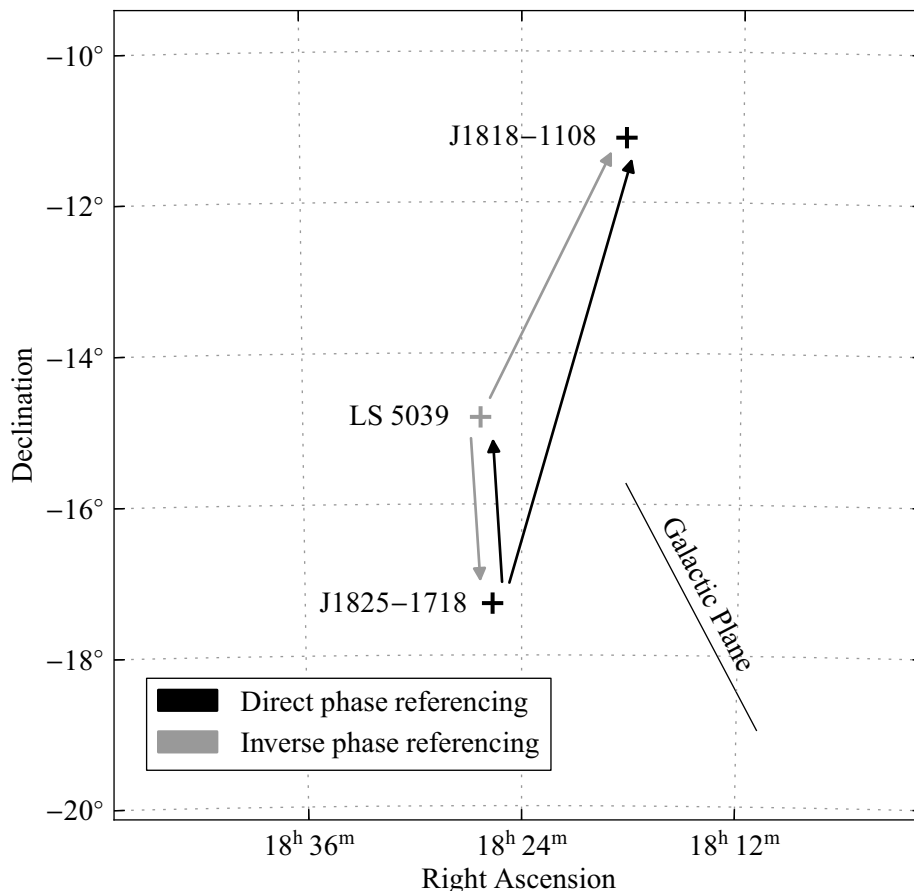


Figure 5.2: Distribution on the sky of LS 5039, the phase calibrator J1825–1718, and the astrometric check source J1818–1108. The dashed line indicates the Galactic Plane. The arrows indicate the two phase calibrations obtained: direct, using J1825–1718 as phase reference; inverse, using LS 5039 as phase reference.

source suffer from galactic scatter broadening (a general discussion on this effect can be found in Fey et al. 1991). The phase calibrator J1825–1718 has a total flux density of 350 mJy at 5 GHz, but the amplitude of the visibilities decreases with the uv distance and the phase calibration fails for baselines longer than ~ 90 – 100 M λ (see Fig. 2.5 on page 23). The compact core has a size of 3 mas. The resolution of the phase-referenced images is therefore limited by the scatter broadening of the phase calibrator. On the other hand, the astrometric check source J1818–1108 is not compact. The self-calibrated images show a main core of 680 mJy and a secondary blob of 180 mJy located at 50 mas westwards from the core. Both components have a size of ~ 8 mas. The visibility amplitudes quickly drop with the uv distance and there is no signal beyond ~ 30 M λ . The distance between J1818–1108 and the phase calibrator is 6.4° in P.A. of 16° (see Fig. 5.2), which makes difficult to transfer the phase solutions for this low elevation source.

5.3 Data reduction

Data reduction was principally performed in AIPS². The Difmap package (Shepherd 1997) was used for imaging and self-calibration. The raw visibilities were loaded into AIPS, and a priori flagging on telescope off-source times because of antenna slewing was applied. We searched for data with instrumental problems and flagged them, as well as all visibilities with antenna elevation below 5° . Initially, we updated the geometrical model of the correlator using the Earth orientation parameters (EOPs). However, the correction implied a change on the final measured positions one order of magnitude below our final uncertainties. Considering the small effect and the problems with this correction in the past (wrong parameters during the correlations between 2003 and 2005³ and a bug in the AIPS task CLCOR from 2009 to 2011), we did not include them in the final data processing. For these observations, the EOPs correction produced a $\sim 10^\circ$ phase offset in the visibilities, which was in any case removed by the phase calibration (see below).

5.3.1 Ionospheric correction

The different ionospheric conditions above VLBI antennas are one of the main contributions to systematic errors for astrometry at low frequencies. The unmodelled phase and delay contribution of the ionosphere modifies randomly the observed phases on time scales of minutes, producing two effects. On one hand, it spreads the signal and broadens the source, producing an overall decrease of the detected signal-to-noise ratio (S/N). On the other hand, it introduces an unknown position offset. This correction is specially important in this case because the sources have low declination, which implies low elevations during the observations, and because the sources are separated mainly in the North-South direction (see Fig. 5.2), where the atmospheric conditions change more significantly.

We used ionospheric total electron content (TEC) models based on GPS data obtained from the CDDIS data archive⁴ to correct the phase variations caused by the ionosphere. These maps provide one TEC measures every two hours on a grid of $5^\circ \times 2.5^\circ$ in terrestrial longitude and latitude, respectively. This is a coarse correction because the ionosphere changes occur on a shorter time scale, although it accounts for significant astrometric offsets. The ionospheric models are produced by different institutes, which estimate the TEC above different locations and provide electron distribution maps (IONEX files) that can be loaded into AIPS to apply the phase corrections. We compared the effects of the phase correction on the visibilities using the models provided by four institutes: the Jet Propulsion Laboratory (JPL), the Center for Orbit Determination in Europe (CODE), the ESOC Ionosphere Monitoring Facility (ESA), and the Universitat Politècnica de Catalunya (UPC). We tested the models by comparing the S/N and the stability of the position of

²The NRAO Astronomical Image Processing System. <http://www.aips.nrao.edu/>

³http://www.vlba.nrao.edu/memos/test/test69memo/eop_problem.html

⁴The Crustal Dynamics Data Information System <http://cddis.nasa.gov/>

5. Periodic morphological changes in the radio structure of LS 5039

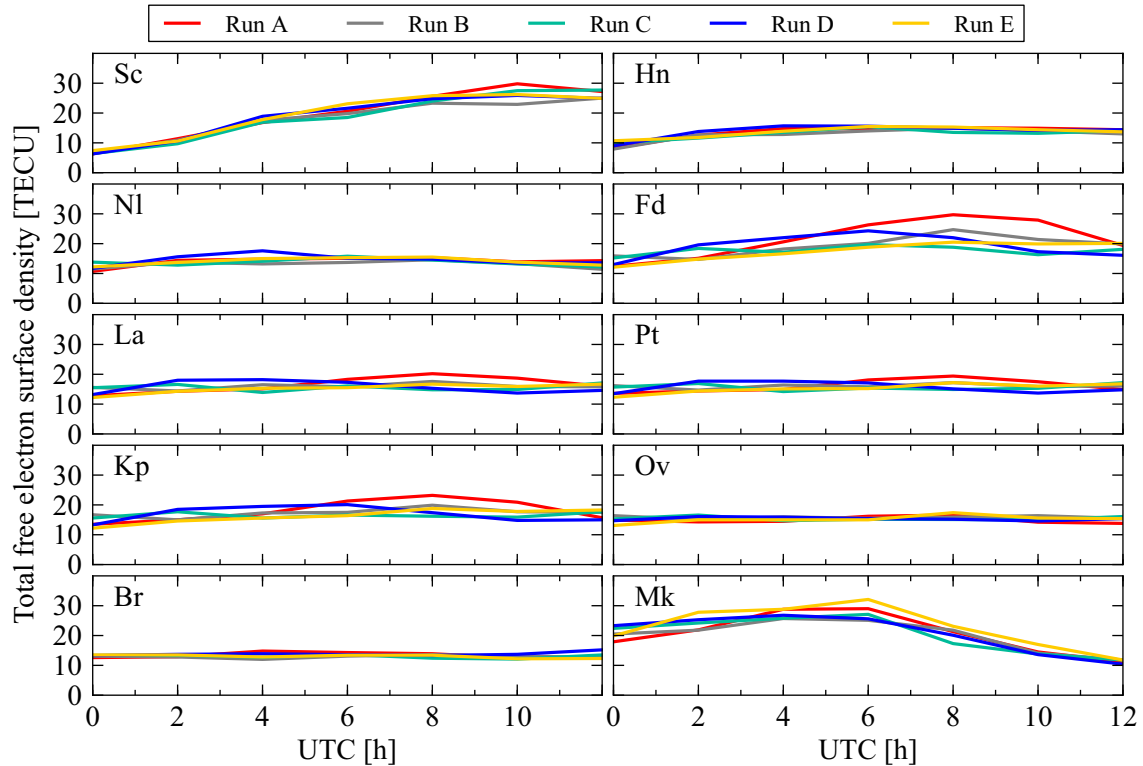


Figure 5.3: Surface density of free electrons above the stations for each observing run. The total electron content is measured in TECU (total electron content units), which corresponds to 10^{16} electrons m^{-2} . The high values in Mk and Sc at the beginning and the end of the observation correspond to the sunset and sunrise, respectively. The plot shows that the ionosphere was less stable for run A, in particular for the stations Fd, La, Pt, and Kp. The observations were conducted between 03:30 and 09:30 UTC.

the peak of the emission of LS 5039 in different short intervals of 1 and 3 hours along the observations. We did not measure appreciable differences in the peak flux density when using the different models. The ionospheric models provide an average position offset of 0.02 and -1.7 mas in right ascension and declination, respectively. The models are very similar, and the dispersion of these corrections are 0.11 and 0.2 mas, respectively. For each run we applied the model that provides offsets closer to the averaged value. The JPL model was used to correct the runs A and C, and the CODE model to correct runs B, D, and E.

We checked the stability of the correction for the observed times by computing the variability of the TEC provided by the GPS maps. In Fig. 5.3 we show the evolution of the TEC from the JPL ionex maps for the five runs. The most variable stations were Sc (at the end of the observation the Sun was already rising) and Mk (the observations started before sunset). Comparing the mean variability of the TEC content for every run

during the central hours of the project (from 4:00 to 8:00 UTC), we found that runs B, D, and E have a relative average variability of 18%, for run C it was 15%, and for run A 22%. This shows that during run A the ionosphere was, in general, more variable. This can in part justify the astrometric problems encountered for this run (see Sect. 5.3.3), being the rest of the weather conditions similar for all runs.

5.3.2 Amplitude and phase calibration

ACCOR was used to fix the amplitudes in the cross correlation spectrum from the VLBA correlator. The amplitude calibration was performed using the antenna gains and the system temperatures measured at each station in real time during the observations, using the APCAL procedure. The parallactic angle correction was automatically applied with VLBAPANG. To correct the instrumental offsets and slopes between and within the different bands we ran FRING on 30 seconds of a scan of the fringe finder 3C 345, setting the phase rates to zero (manual phase-cal). To correct the dependence of the visibility amplitudes with the frequency we used the auto-correlation values from 3C 345 to smooth the bandpass shape of the amplitudes.

An initial fringe fitting was performed using the FRING routine in AIPS, using a point-source model on the phase calibrator J1825–1718. These data were exported to Difmap and self-calibrated. We fitted the visibilities for each run with a circular Gaussian. The mean flux density fitted for the core component was 345 mJy, with a standard deviation between runs of 2.3 mJy (0.67%), while the calibrator structure did not change significantly. Therefore, we combined the five data sets of the calibrator and performed several iterations of imaging and self-calibration to create a master calibrator image. We ran FRING again, but now we removed the source structure contribution to the phase calibration by using the combined image of J1825–1718 as an input model. One solution for each scan for all IFs was searched within a delay and rate search windows of 80 nanoseconds and 20 mHz, respectively. The minimum allowed S/N for solutions was 8, providing 95.8% of good solutions. The 4.2% of the data without solutions mostly correspond to long baselines (above 90 M λ). The solutions for every frequency band were corrected with MBDLY, which fits the phase delay between bands. The final phases were explored and flagged when necessary. Finally, we applied the calibration and flag tables, and we averaged all frequency channels within each IF to obtain three single-source files, one for LS 5039, one for the phase calibrator J1825–1718 and one for the astrometric check source J1818–1108.

We also obtained inverse phase referencing based on LS 5039 because the source can be self-calibrated at 5 GHz. We followed an analogue procedure to fringe-fit the LS 5039 data, although we did not produce a combined data set. The S/N cut was set to 5 because of the faintness of the source. We flagged the data with unstable phases and transferred the solutions from LS 5039 to J1825–1718 and J1818–1108, for which inverse astrometry was obtained. A sketch of the phase referencing schemes is shown in Fig. 5.2.

5.3.3 Phase referencing imaging

To reduce the systematic errors of the phase referencing produced by data taken when the sources were at low elevations, we only used the central hours of the runs. We produced images with time intervals of 30 and 60 minutes and inspected the image quality and the astrometric stability. We also produced images for the individual scans. The data obtained at the beginning and at the end of the observations are not consistent because we measured artificial displacements of the peak of the emission between ~ 0.5 and 3 mas, while the source became elongated in random directions. This behaviour can be explained by the ionosphere affecting the data with low elevation. We note that the effect is more important for run A, which suffered severe displacements of more than 6 mas in the time blocks for the first hour and the last two hours. After inspecting these systematic errors for different time blocks we only used the data in the time intervals when the source was reasonably stable, from 04:40 to 07:40 UT for runs B, C, and D, from 04:30 to 07:00 UT for run A, and from 06:00 to 08:30 UT for run E. Taking into account that the declination of the phase-reference calibrator and the target source are -17.3° and -14.8° , respectively, that the observations were centred at the culmination of the sources, and that the observations were conducted under normal weather conditions (without rain, strong winds or snow), the time ranges used correspond to elevations of most of the antennas above $\sim 25^\circ$. Some antennas contributing to the longest baselines (Mk, Sc, Hn, and Br) were below this value during part of the observations, and the phase calibration was not successful for them during these time intervals, although this can be also caused by the intrinsic calibrator structure.

The phase-referenced data were imaged using task IMAGR with a pixel size of 0.2 mas. We used a weighting scheme with robust 0 as a compromise between angular resolution and sensitivity. Pradel et al. (2006) showed that removing the shorter baselines of the VLBA can decrease the astrometric systematic errors by a 15%. For LS 5039, the source was detected with S/N above 10 when imaging the baselines with uv distances between 15–20 and 100 $M\lambda$. The range of minimum baselines was lowered in those cases in which secondary lobes were more important or when the S/N of the peak emission was too low. The same strategy was used to image the astrometric check source J1818–1108. In this highly resolved source we only used baselines with uv distances between 12 and 40 $M\lambda$.

For the inverse phase referencing, where phases from LS 5039 were transferred to J1825–1718 and J1818–1108, a uv range of 20 to 60 $M\lambda$ was used for J1825–1718 and 12 to 60 $M\lambda$ for the check source. The maximum baseline of the latter is higher than in the direct phase referencing probably because of the smaller angular distance between J1818–1108 and the phase reference source, LS 5039 in this case, (see Fig. 5.2). In both cases we used a pixel size of 0.5 mas.

5.3.4 Self-calibration

In order to perform the self-calibration of the LS 5039 data, we loaded the individual data files into Difmap. We averaged the data with a binning size of 50 seconds. The visibilities with long baselines were down-weighted, using a Gaussian taper at radius of $80 \text{ M}\lambda$. We performed several iterations of cleaning and phase self-calibration. For each of them, phase solutions were found, first for the most compact part of the core by imaging the data with a uniform weighting scheme and then solving for the more extended emission using a natural weighting cleaning. After each cycle, an amplitude self-calibration was obtained, each time with a shorter integration time, up to a minimum of 30 minutes. Finally, two hybrid images were produced for each run, one with natural weight (worse resolution and better sensitivity) and one with uniform weight (better resolution and worse sensitivity). The final images were exported to AIPS. Their rms noise and the total flux density were obtained by fitting the pixel flux density distribution of the image with IMEAN. The extended emission was characterised by fitting two or three Gaussian components to the images using the task JMFIT.

We also fitted Gaussian components to the calibrated uv data sets of LS 5039 (modelfit). This is an iterative process, where the initial values for the fit have to be fixed manually, and the final solution can depend on the starting parameters. Therefore, we note that the model fitting results can be slightly subjective, in particular for this case, where the source structure is not clearly defined by individual components. Despite this caveat, the modelfit provides morphological information directly from the uv data and therefore it is not limited by a synthesised beam because it is independent of the deconvolution procedure used. We obtained the modelfit of the uv data with the task UVFIT in AIPS. As a starting point, we used the solutions from JMFIT obtained from the naturally weighted images. Then we inspected several combinations of number of components and shape restrictions until a robust solution was found. As a parallel check, we performed another modelfit in Difmap to verify the consistency of the results. As both approaches provide similar results, we only present here the solutions obtained with AIPS.

5.4 Analysis and results

5.4.1 Relative astrometry of the peak of the emission

The average position of LS 5039 from the five runs of project BR127 is $\alpha_{\text{J2000.0}} = 18^{\text{h}}26^{\text{m}}15^{\text{s}}06003(3)$ (or $\pm 0.4 \text{ mas}$) and $\delta_{\text{J2000.0}} = -14^{\circ}50'54''3094(6)$ (or $\pm 0.6 \text{ mas}$). This position is measured with respect to the correlation position of J1825–1718, which is listed in Sect. 5.2. The absolute astrometry in this project was used to obtain an accurate proper motion of LS 5039 (?). The astrometric uncertainties cannot be obtained directly from the position fit because of the unknown ionospheric effects, and therefore we used the astrometric check source J1818–1108 to estimate them. The standard deviation of

5. Periodic morphological changes in the radio structure of LS 5039

the peak positions of the check source was 2.3 mas in right ascension and 2.4 mas in declination. These deviations were converted to uncertainties in the determination of the position of LS 5039 by multiplying them by two correction factors that account for the different observing conditions for LS 5039 and J1818–1108, following the general theoretical astrometric precision for an interferometer (Thompson et al. 1986).

$$\sigma = \frac{1}{2\pi} \frac{1}{S/N} \frac{\lambda}{B}, \quad (5.1)$$

where the wavelength (λ) and the maximum baseline (B) can be represented by the synthesised beam size. First, the uncertainty was scaled taking into account the different resolutions of the images. Basically, the data of J1818–1108 were imaged with poorer resolution, only using short baselines (see Sect. 5.3.3). This factor was obtained as a ratio of the synthesised beam size of the LS 5039 observations to the mean size of the J1818–1108 beams. Second, the astrometric precision depends on the S/N of the detection. We scaled the uncertainty by the ratio of individual S/N of LS 5039, which was around 15, to the mean S/N of J1818–1108, which was 7. These two corrections yield a scaling factor applied to the dispersion of J1818–1108 of ~ 0.19 and ~ 0.25 in right ascension and declination, respectively. Finally, the mean uncertainties in the determination of the right ascension and declination of LS 5039 are 0.4 and 0.6 mas, respectively. The same procedure was used for the inverted astrometry.

Another approach to estimate the astrometric uncertainties is to use the expected theoretical systematic uncertainties computed using Eq. 2 in Pradel et al. (2006), although some assumptions considered in the general discussion in that paper are not met in these observations. The minimum theoretical uncertainties for LS 5039 using J1825–1718 as a reference source and assuming mean tropospheric conditions are 0.17 and 0.56 mas in right ascension and declination, respectively, which are compatible with the estimation quoted above. This indicates that the uncertainties in declination seem to be dominated by systematic uncertainties. On the other hand, the minimum theoretical uncertainties for J1818–1108 are 0.43 and 1.42 mas in right ascension and declination, respectively. The real dispersion measured, 2.3 mas in right ascension and 2.4 mas in declination, is significantly larger possibly because the extended nature of the source, the poor uv coverage, and the low S/N. Given these results, we have adopted the more conservative approach described above, although we note that the real uncertainties of the measurement are possibly a non-trivial combination of the systematic and nominal uncertainties.

In Table 5.2 we present the measured astrometry. We show the relative astrometry (with respect to the average position) for the check source J1818–1108 and the synthesised beam of the phase referenced images and the relative astrometry for LS 5039. We also show the inverse astrometry obtained using LS 5039 as a phase reference source. The measured relative offsets of the peak of the emission of LS 5039 using the two methods are plotted in Fig. 5.4. Both approaches provide similar relative astrometry. The peak position of LS 5039 during run A is significantly displaced from the mean value. However,

Table 5.2: Relative astrometry of the five runs of project BR127. The displacements of the check source J1818–1108 are used to determine the astrometric uncertainties (see Sect. 5.4.1). The mean synthesised beam for J1818–1108 in the direct phase referencing is $6.5 \times 3.3 \text{ mas}^2$ at P.A. of 6° , and for the inverse phase referencing it is $6.9 \times 2.7 \text{ mas}^2$ at P.A. of 7° . We show, for LS 5039 and J1825–1718, the beam (HPBW) size and P.A. and the relative displacements measured from the average position. These results are plotted in Fig. 5.4.

Phase referencing from J1825–1718 (direct)					
Run	J1818–1108		LS 5039		
	$\Delta_{\text{R.A.}}$	$\Delta_{\text{Dec.}}$	HPBW	$\Delta_{\text{R.A.}}$	$\Delta_{\text{Dec.}}$
	[mas]	[mas]	[mas ² at $^\circ$]	[mas]	[mas]
A	+4.0	+4.4	3.0×1.2 at -4.3	$+1.3 \pm 0.5$	$+0.4 \pm 0.7$
B	-1.3	-0.6	3.5×1.3 at -0.9	-1.2 ± 0.3	$+1.2 \pm 0.4$
C	+0.1	-2.6	3.2×1.3 at -2.8	-0.2 ± 0.4	-0.8 ± 0.5
D	-2.8	+0.1	3.2×1.3 at -1.9	$+0.2 \pm 0.5$	-0.5 ± 0.6
E	-0.0	-1.2	3.9×1.3 at -5.4	-0.2 ± 0.5	-0.4 ± 0.8
Phase referencing from LS 5039 (inverse)					
Run	J1818–1108		J1825–1718		
	$\Delta_{\text{R.A.}}$	$\Delta_{\text{Dec.}}$	HPBW	$\Delta_{\text{R.A.}}$	$\Delta_{\text{Dec.}}$
	[mas]	[mas]	[mas ² at $^\circ$]	[mas]	[mas]
A	+1.1	+0.3	6.8×2.6 at 6.1	-1.4 ± 0.5	-0.9 ± 1.0
B	+0.7	-1.0	7.2×2.8 at 4.4	$+0.7 \pm 0.5$	-1.2 ± 1.0
C	+0.2	+1.2	6.8×2.7 at 7.8	-0.3 ± 0.4	$+1.3 \pm 0.8$
D	+0.2	+1.5	6.8×2.6 at 2.8	$+0.8 \pm 0.3$	$+0.4 \pm 0.6$
E	-2.2	-2.0	7.1×2.7 at 12.2	$+0.2 \pm 0.4$	$+0.4 \pm 0.8$

in run A, the check source shows a even larger displacement in the same direction (see first row in Table 5.2). This fact, combined with the suspicious behaviour described in Sect. 5.3.3, makes clear that the astrometry of run A suffers from uncorrected ionospheric effects, and therefore we do not consider the peak displacement in run A as reliable. The only significant displacement is found between run B and run C, which corresponds to displacements of $1.0 \pm 0.5 \text{ mas}$ and $-2.0 \pm 0.7 \text{ mas}$ in right ascension and declination, respectively. Therefore, the total displacement between phase 0.29 and phase 0.55 is $2.3 \pm 0.6 \text{ mas}$ in P.A. of 154° , which, considering the limitations of the data, cannot be considered a robust sign of peak displacement.

5. Periodic morphological changes in the radio structure of LS 5039

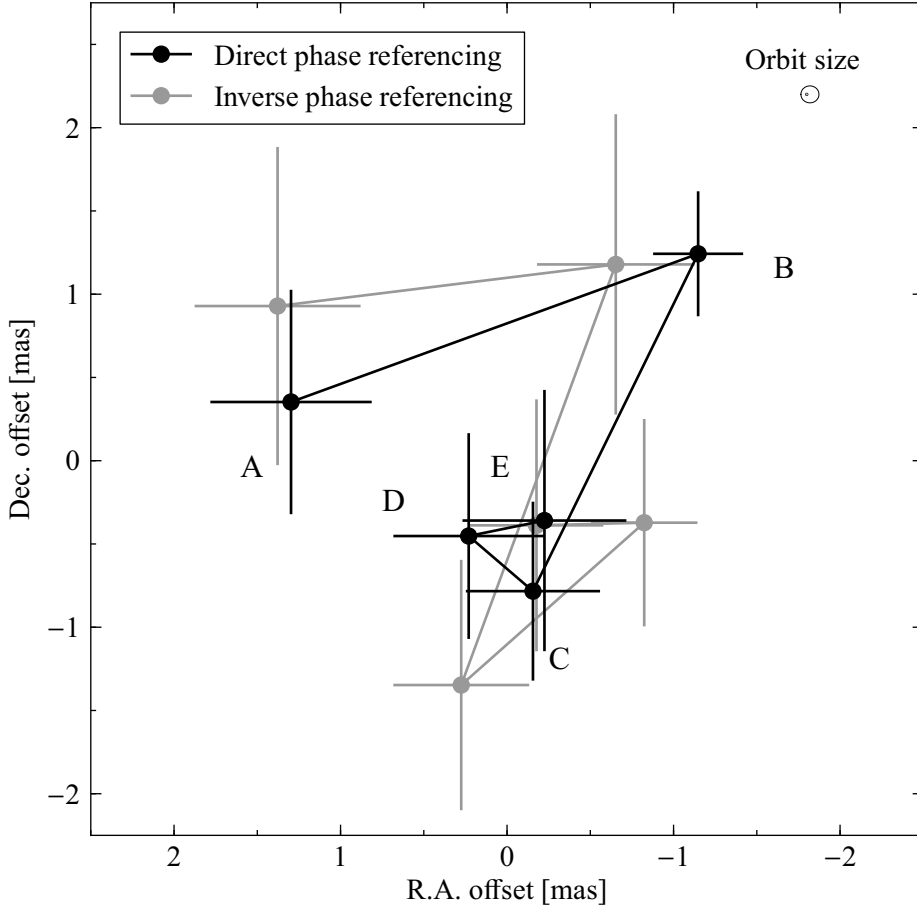


Figure 5.4: Relative offsets of the peak of the emission of LS 5039 during five consecutive days with respect to the average position. For straightforward comparison, we plot the opposite value of the inverse astrometry. The run label is displayed close to each direct measure. The size of the binary system is indicated by the small orbit in the corner, which is plotted face-on and with an arbitrary orientation. The displacements and uncertainties are shown in Table 5.2.

5.4.2 Morphology

The self-calibration of the data improves the S/N of the phase-referenced images while preserving the main features of the extended emission, partially avoiding the problems with the phase calibration caused by the ionosphere, at the expense of losing the astrometric information. In the first two rows of Fig. 5.5 we show the final self-calibrated images for each run, produced with natural and uniform weight, respectively. The five images with natural weight have synthesised beams with sizes about $6.1 \times 2.3 \text{ mas}^2$ and P.A. of -2° and total flux densities of 27.9, 26.1, 24.4, 28.5, and 26.4 mJy, respectively, with a rms noise of the images of $\sim 0.06 \text{ mJy beam}^{-1}$. On the other hand, the images with uniform weight have synthesised beams with sizes around $4.1 \times 1.3 \text{ mas}^2$ and P.A. of -4° . The

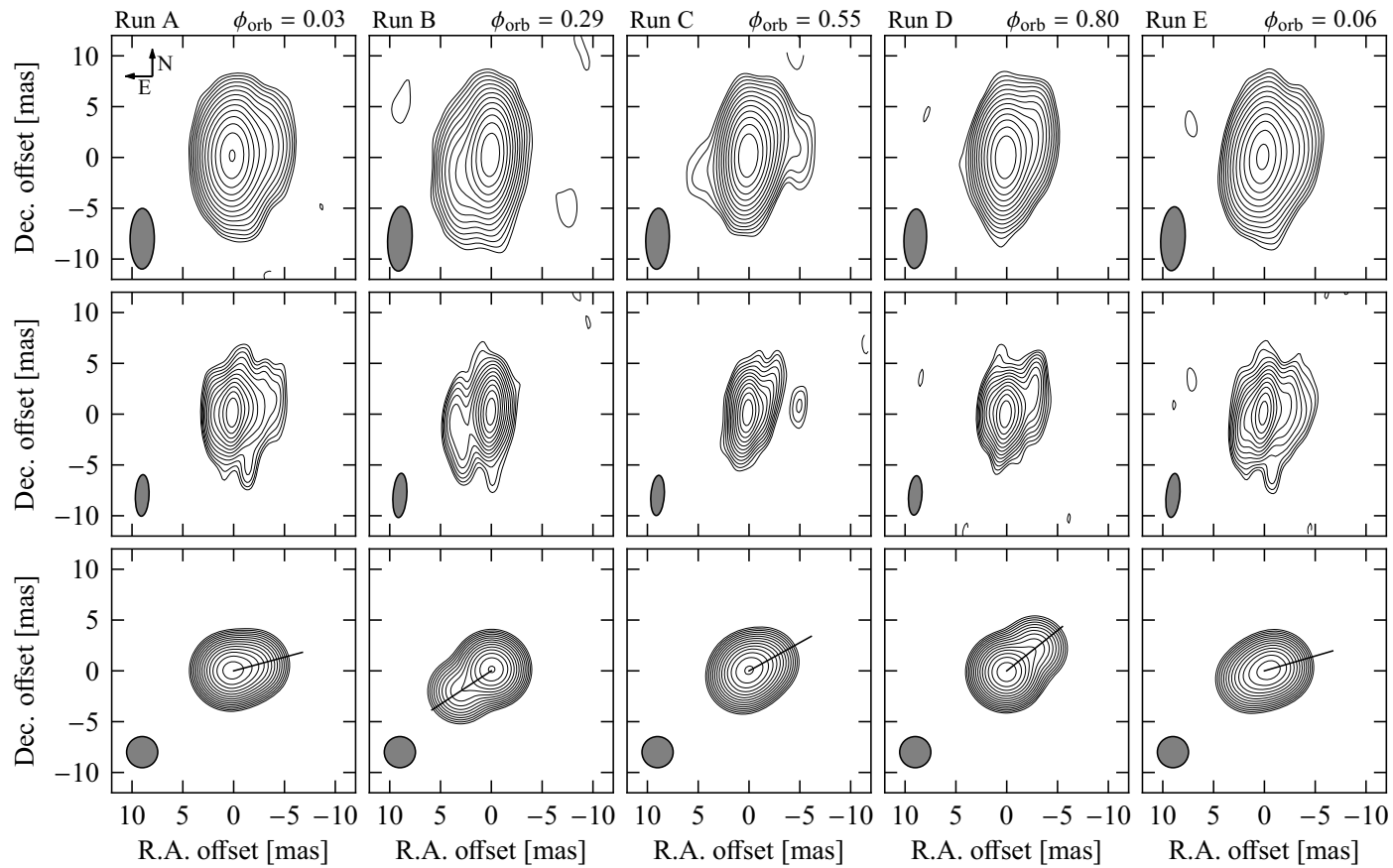


Figure 5.5: VLBA images of LS 5039 at 5 GHz from project BR127, obtained during five consecutive days in July 2007. Each column corresponds to one epoch, for which the first and second rows correspond to the self-calibrated images obtained with a natural and uniform weighting scheme, respectively. The third row shows the uv components fitted to the data convolved with a Gaussian circular beam with an area equal to the average beam of all images. The lines show the direction of the main extended component. The restoring beams are plotted in the bottom-left corner of each panel. Dashed contours are plotted at -3 times the rms noise of each image and solid contours start at 3 times the rms and scale with $2^{1/2}$. The Gaussian components fitted are listed in Table 5.5.

Table 5.3: Gaussian components fitted to the images shown in top row of Fig. 5.5, obtained with natural weighting scheme. Each component is labelled with the corresponding letter of the epoch (A–E). Columns 2 and 3 list the peak and integrated flux density of each component. Columns 4–8 list the position offset and the size fitted to each component. The last two columns list the deconvolved size of the components fitted to the images.

Natural									
Comp.	S_{peak} [mJy b ⁻¹]	S_{tot} [mJy]	$\Delta_{\text{R.A.}}$ [mas]	$\Delta_{\text{Dec.}}$ [mas]	θ_{maj} [mas]	θ_{min} [mas]	$\theta_{\text{P.A.}}$ [°]	Deconvolved size	
								[mas ²]	[°]
A1	9.84 ± 0.06	14.72 ± 0.15	0.36 ± 0.01	0.18 ± 0.02	6.25 ± 0.04	3.41 ± 0.02	177.1 ± 0.4	2.54 × 1.72	111.5
A2	6.27 ± 0.07	6.27 ± 0.07	0.00 ± 0.01	0.00 ± 0.03	5.97 ± 0.01	2.39 ± 0.01	179.6 ± 0.1	Point-like	
A3	3.04 ± 0.06	7.02 ± 0.2	-2.05 ± 0.04	0.17 ± 0.06	7.52 ± 0.15	4.37 ± 0.09	169.5 ± 1.4	4.91 × 3.19	145.5
B1	16.34 ± 0.06	19.55 ± 0.12	-0.03 ± 0.01	0.17 ± 0.01	6.63 ± 0.03	2.76 ± 0.01	177.2 ± 0.2	1.84 × 1.36	2.0
B2	2.99 ± 0.06	4.04 ± 0.13	3.05 ± 0.02	-1.64 ± 0.07	7.64 ± 0.16	2.71 ± 0.06	1.0 ± 0.7	4.27 × 1.03	9.2
C1	13.57 ± 0.06	15.39 ± 0.11	0.03 ± 0.01	-0.03 ± 0.01	6.18 ± 0.03	2.55 ± 0.01	177.2 ± 0.2	1.53 × 1.02	162.6
C2	3.30 ± 0.06	7.18 ± 0.17	-0.75 ± 0.04	0.81 ± 0.05	6.84 ± 0.12	4.41 ± 0.08	161.1 ± 1.5	4.58 × 1.99	119.1
D1	17.48 ± 0.06	23.80 ± 0.13	0.03 ± 0.01	-0.07 ± 0.01	6.06 ± 0.02	2.93 ± 0.01	177.7 ± 0.2	1.90 × 1.55	87.9
D2	2.95 ± 0.06	3.27 ± 0.12	-2.86 ± 0.02	2.06 ± 0.06	6.19 ± 0.13	2.33 ± 0.05	179.9 ± 0.8	2.09 × 0.33	16.3
E1	9.66 ± 0.07	15.75 ± 0.17	0.35 ± 0.01	-0.09 ± 0.02	6.91 ± 0.05	3.56 ± 0.03	170.3 ± 0.4	3.38 × 1.90	132.8
E2	5.70 ± 0.07	5.70 ± 0.07	0.00 ± 0.01	0.00 ± 0.03	6.30 ± 0.01	2.39 ± 0.01	176.8 ± 0.1	Point-like	
E3	2.41 ± 0.07	3.94 ± 0.17	-2.58 ± 0.04	-0.08 ± 0.09	7.45 ± 0.21	3.31 ± 0.10	168.0 ± 1.3	4.30 × 1.61	148.1

Table 5.4: Gaussian components fitted to the images shown in middle row of Fig. 5.5, obtained with uniform weighting scheme. Each component is labelled with the corresponding letter of the epoch (A–E). Columns 2 and 3 list the peak and integrated flux density of each component. Columns 4–8 list the position offset and the size fitted to each component. The last two columns list the deconvolved size of the components fitted to the images.

Uniform									
Comp.	S_{peak} [mJy b ⁻¹]	S_{tot} [mJy]	$\Delta_{\text{R.A.}}$ [mas]	$\Delta_{\text{Dec.}}$ [mas]	θ_{maj} [mas]	θ_{min} [mas]	$\theta_{\text{P.A.}}$ [°]	Deconvolved size	
								[mas ²]	[°]
A1	7.45 ± 0.08	7.45 ± 0.08	0.00 ± 0.01	0.00 ± 0.02	4.09 ± 0.00	1.34 ± 0.00	177.5 ± 0.1	Point-like	
A2	1.67 ± 0.07	9.39 ± 0.44	-1.53 ± 0.08	0.38 ± 0.12	6.72 ± 0.27	4.58 ± 0.19	169 ± 4	5.41×4.28	156.1
A3	5.43 ± 0.07	11.71 ± 0.21	0.41 ± 0.02	0.11 ± 0.02	4.10 ± 0.05	2.88 ± 0.04	168.8 ± 1.5	2.63×0.00	7.8
B1	13.87 ± 0.08	18.38 ± 0.17	-0.05 ± 0.01	0.19 ± 0.01	4.58 ± 0.03	1.71 ± 0.01	176.7 ± 0.2	1.39×1.02	11.2
B2	2.04 ± 0.08	5.00 ± 0.26	2.92 ± 0.04	-1.62 ± 0.11	6.43 ± 0.25	2.25 ± 0.09	1.6 ± 1.3	4.76×1.71	6.5
C1	13.34 ± 0.08	18.45 ± 0.16	0.07 ± 0.01	0.05 ± 0.01	4.29 ± 0.02	1.68 ± 0.01	174.3 ± 0.2	1.66×1.00	161.3
C2	2.26 ± 0.08	3.12 ± 0.16	-1.86 ± 0.02	1.08 ± 0.07	5.16 ± 0.17	1.40 ± 0.05	169.7 ± 0.8	3.36×0.00	161.9
D1	13.14 ± 0.08	22.89 ± 0.19	0.04 ± 0.01	-0.08 ± 0.01	4.13 ± 0.02	2.15 ± 0.01	175.5 ± 0.3	1.70×1.39	86.0
D2	2.32 ± 0.08	4.04 ± 0.19	-2.73 ± 0.02	1.90 ± 0.07	5.17 ± 0.17	1.71 ± 0.06	176.5 ± 1.0	3.42×1.10	177.7
E1	10.68 ± 0.08	10.68 ± 0.08	0.00 ± 0.00	0.00 ± 0.01	4.34 ± 0.01	1.34 ± 0.01	174.4 ± 0.1	Point-like	
E2	2.65 ± 0.07	10.1 ± 0.3	-1.33 ± 0.05	0.29 ± 0.07	5.70 ± 0.16	3.90 ± 0.11	169 ± 3	3.88×3.46	128.8
E3	3.47 ± 0.08	4.90 ± 0.17	1.63 ± 0.02	-0.80 ± 0.05	5.00 ± 0.11	1.64 ± 0.04	173.5 ± 0.7	2.49×0.94	170.6

5. Periodic morphological changes in the radio structure of LS 5039

Table 5.5: Gaussian components fitted to the uv data. Each component is labelled with the corresponding letter of the epoch (A–E). Column 2 lists the integrated flux density of each component. Columns 3–7 list the position offset and the size fitted to each component. These components, convolved with a circular Gaussian beam are shown in the bottom row of Fig. 5.5.

Comp.	Modelfit					
	S_{tot} [mJy]	$\Delta_{\text{R.A.}}$ [mas]	$\Delta_{\text{Dec.}}$ [mas]	θ_{maj} [mas]	θ_{min} [mas]	$\theta_{\text{P.A.}}$ [$^{\circ}$]
A1	12.4 ± 1.0	0.52 ± 0.08	0.03 ± 0.04	2.60 ± 0.10		Circular
A2	8.0 ± 0.5	0.00 ± 0.01	-0.05 ± 0.02	0.0		Point-like
A3	7.4 ± 1.0	-2.00 ± 0.23	0.54 ± 0.08	3.79 ± 0.16		Circular
B1	18.4 ± 0.5	-0.05 ± 0.01	0.16 ± 0.01	1.11 ± 0.01		Circular
B2	4.5 ± 0.5	3.04 ± 0.02	-2.00 ± 0.07	4.2 ± 0.3	1.2 ± 0.1	14.6 ± 2.1
C1	13.1 ± 1.0	-0.02 ± 0.01	0.19 ± 0.02	0.57 ± 0.06		Circular
C2	3.7 ± 0.5	-1.66 ± 0.03	0.92 ± 0.07	0.76 ± 0.09		Circular
C3	4.8 ± 1.0	0.77 ± 0.14	-0.81 ± 0.17	2.09 ± 0.13		Circular
D1	22.6 ± 0.5	0.02 ± 0.01	-0.13 ± 0.01	1.63 ± 0.01		Circular
E2	4.8 ± 0.5	-2.77 ± 0.04	2.20 ± 0.08	1.64 ± 0.09		Circular
E1	5.3 ± 1.0	1.52 ± 0.06	-0.84 ± 0.09	1.57 ± 0.13		Circular
E2	9.3 ± 0.5	-0.00 ± 0.01	-0.06 ± 0.02	0.18 ± 0.15		Circular
E3	10.5 ± 1.0	-1.23 ± 0.13	0.36 ± 0.05	3.66 ± 0.16		Circular

total flux densities in the five images are 27.8, 26.7, 25.4, 28.5, and 27.0, with a rms noise of $0.08 \text{ mJy beam}^{-1}$. The individual components fitted to the images using JMFIT are summarised in Tables 5.3 and 5.4 (natural and uniform weighting scheme, respectively), where we list the flux density, relative position, and size of each component. The last two columns show the deconvolved size of the components, which describes to a certain degree the intrinsic size of the component, deconvolved from the synthesised beam size. In Table 5.5 we list the Gaussian components fitted to the uv data (modelfit), which are not convolved with any beam. Most of the modelfit components are circular instead of elliptical. We plot these components in the last row of Fig. 5.5 convolved with an artificial circular beam with an area equal to the average synthesised beam of the rest of the images. As a guide, we plot a line towards the direction of the main extended component, which corresponds to P.A. of -75 , 123 , -61 , -52 , and -74° , respectively.

All images show a main core component and extended emission with a different P.A. During run A, which was obtained soon after periastron (orbital phase ~ 0), the source is extended westwards, although the core is better described with two components. This double core has an important contribution eastwards, at a distance of $\sim 0.5 \text{ mas}$. For

the image obtained 24 h later, at orbital phase 0.29, a fast morphological change occurs and the main extended component is detected towards South-East. Run C, obtained soon after apastron, displays bipolar extended emission. The emission towards North-West is in fact composed by two components, although only one component could be fitted. The faint component towards South-East could not be fitted to the data and therefore it is not listed in Tables 5.3, 5.4, and 5.5. Run D is well described by a main core and a bright component towards North-West. Finally, the images from run E, also obtained short after the periastron passage, recover the same morphology of run A. This shows that the morphology of LS 5039 is periodic on consecutive orbital cycles.

We also divided each data set in two blocks to check for possible intraday variations. We obtained modelfit solutions and produced images for the divided uv data sets. However, it was not possible to obtain reliable morphological differences because of the very different uv coverage at the beginning and the end of each run.

5.5 Compilation of VLBI observations

To try to confirm the repeatability of the changing morphological structure of LS 5039 found in our five consecutive days campaign (project BR127), we compiled the available archival VLBI data of the source that provide an angular resolution similar to the one explored here. We compiled images from other eleven observations conducted at frequencies between 1.7 and 8.5 GHz between 1999 and 2009. A log of these observations is shown in Table 5.6. The orbital phases were computed with the ephemerides from Casares et al. (2012a) and have uncertainties below 0.022.

There are three observations at 5 GHz (6 cm wavelength) from 1999 and 2000 that correspond to the projects BP051 and GR021A–B, which included the VLBA and the phased VLA array as an additional VLBI station. These results were already presented in Paredes et al. (2000) and Ribó et al. (2008), where the interested reader can find detailed information on the data and the data reduction process.

Between 2004 and 2006, three runs were observed with the VLBA at 8.5 GHz (3.6 cm wavelength) as part of a long-term astrometric project (PI: V. Dhawan). The observational codes are BD087G, BD105A, and BD105G. The data were correlated with a lower sensitivity provided by 128 Mbps, and the final resolution is slightly better than for the other projects thanks to the higher frequency of the observations. We produced three self-calibrated images with natural weight. The obtained synthesised beam and rms noise for each image are shown in Table 5.6. More details on the data reduction can be found in Moldón et al. (2012b). The total flux densities recovered for BD087G, BD105A, and BD105G were 18.6, 17.6, 20.2 mJy, respectively, with uncertainties of ~ 0.1 mJy.

We also present three self-calibrated images from project EF018 (PI: R. Fender), which consists of 3 runs (A–C) at 5.0 GHz obtained with the European VLBI Network (EVN) in 2007. The runs were separated by 2 days. The antennas used were Effelsberg, Wester-

5. Periodic morphological changes in the radio structure of LS 5039

Table 5.6: Log of the VLBI observations of LS 5039. Project codes starting with B correspond to VLBA observations, E to EVN observations, and G to Global (VLBA+EVN) observations.

Project	Epoch Y-M-D	Orbital phase	Freq [GHz]	HPBW [mas ² at °]	rms [mJy b ⁻¹]
BP051	1999-05-08	0.16	5.0	3.4 × 1.2 at 0.4	0.11
ER011	2000-03-01	0.39	5.0	7.6 × 7.0 at -14	0.10
GR021A	2000-06-03	0.49	5.0	3.4 × 1.2 at 0.0	0.08
GR021B	2000-06-08	0.77	5.0	3.4 × 1.2 at 0.0	0.11
BD087G	2004-06-11	0.58	8.5	2.6 × 1.1 at 12.2	0.11
BD105A	2005-06-11	0.02	8.4	2.9 × 1.3 at 7.9	0.09
BD105G	2006-01-29	0.51	8.4	3.4 × 1.2 at 7.3	0.10
EF018A	2007-03-01	0.89	5.0	5.9 × 4.2 at 5.3	0.14
EF018B	2007-03-03	0.40	5.0	6.9 × 4.1 at 7.3	0.04
EF018C	2007-03-05	0.91	5.0	4.5 × 3.6 at 8.1	0.11
BR127A	2007-07-05	0.03	5.0	6.0 × 2.4 at -0.4	0.06
BR127B	2007-07-06	0.29	5.0	6.4 × 2.4 at -3.0	0.06
BR127C	2007-07-07	0.55	5.0	6.0 × 2.3 at -2.2	0.06
BR127D	2007-07-08	0.80	5.0	5.9 × 2.2 at -2.3	0.07
BR127E	2007-07-09	0.06	5.0	6.3 × 2.4 at -3.2	0.07
EM074	2009-03-07	0.46	1.7	26 × 5.8 at 7.3	0.04

bork, Jodrell Bank (Lovell), Onsala, Medicina, Noto, Torun, Nanshan (Urumqi), Sheshan (Shanghai), and Hartebeesthoek. This array provides good sensitivity, although each run lasted only 4 hours and the elevation of the source was lower than in the previous projects. The longest baselines in these observations were from the stations in Nanshan (Urumqi) and Hartebeesthoek, although the uv coverage for those baselines is poor and the final resolution is lower. The total flux densities measured were 26.2, 19.1, and 27.4 mJy, respectively. The lower flux density and noise of epoch EF018B is probably an artefact of the amplitude self-calibration and not a real change in the source flux density.

In Fig. 5.6 we show the self-calibrated images of these projects. The images in the panels are ordered in increasing phase, from left to right and from top to bottom. We distributed them in four groups, which correspond to images with similar orbital phases and that show approximately a similar morphology. For a quick reference, the inset table included in Fig. 5.6 shows the dates of the images in the panels. Although they were obtained with different instruments, frequencies, and at very different epochs, the images

in each group share common morphological trends. Each group can be approximately characterised with the morphology described in Sect. 5.4.2 for the runs BR127A–D.

5.5.1 Morphology at larger scales

We observed LS 5039 at 1.7 GHz (18 cm wavelength) with the EVN in 2009, project code EM074. This is a deep pointed observation of LS 5039, conducted without phase referencing. The total time on source was 5.8 h, and 9 stations participated: Effelsberg, Westerbork, Cambridge (32 m), Jodrell Bank (Lovell), Onsala, Medicina, Noto, Torun, and Urumqi. At this frequency the resolution is lower, although the long East-West baselines provide good resolution in right ascension. We produced a uniform weighting scheme image with a synthesised beam of $26 \times 5.8 \text{ mas}^2$ at P.A. 7° and a rms noise level of $0.04 \text{ mJy beam}^{-1}$. The total flux density of the source was 33.5 mJy at 1.7 GHz. The self-calibrated image is shown in Fig. 5.7. The source shows a morphology more similar to the images in group 2, although it was observed at orbital phase 0.46, which is closer to the ones of group 3. This can be explained by the longer lifetime of electrons emitting synchrotron radiation at lower frequencies.

On the other hand, the self-calibrated image from project ER011 provides lower angular resolution than the images in Fig. 5.6 and it is not reproduced here because it is already published in Paredes et al. (2002). The image was obtained at orbital phase 0.39. The innermost region of the core shows extended emission towards South-East, as it happens in the group 2 images in Fig. 5.6, although additional bipolar diffuse components extend up to $\sim 20 \text{ mas}$ in opposite directions. Paredes et al. (2002) also presented a lower resolution image obtained with MERLIN showing extended emission with P.A. of 150° up to 170 mas . Finally, we note that lower resolution VLA images show some hints of extended emission in the same North-West/South-East direction at angular distances of $\gtrsim 0.1''$ (Martí et al. 1998). This confirms that LS 5039 contains an additional extended and diffuse component that cannot be traced with the high-resolution images described in Sect. 5.4.2 and 5.5.

5.6 A model of the outflow of relativistic particles

In this section we try to reproduce the changing radio morphology of LS 5039 by modelling the emission produced by an outflow of electrons accelerated as a consequence of the interaction of the stellar wind and the wind of the putative young pulsar. We are interested in describing the orientation of the P.A. of the emission up to scales of $\sim 5\text{--}10 \text{ mas}$. The formation and evolution of the outflow is complex, and hydrodynamical simulations are needed to describe in detail the source radio emission (see the discussion in Sect. 5.1). Our aim here is to check if the general scenario of colliding winds is compatible with the main features and the continuous morphological changes found at scales up to 10 mas .

We assume a mass for the companion star of $33 M_\odot$ and an eccentricity of the system of 0.35 (Casares et al. 2012a). The semimajor axis of the orbit for a $1.4 M_\odot$ neutron star

5. Periodic morphological changes in the radio structure of LS 5039

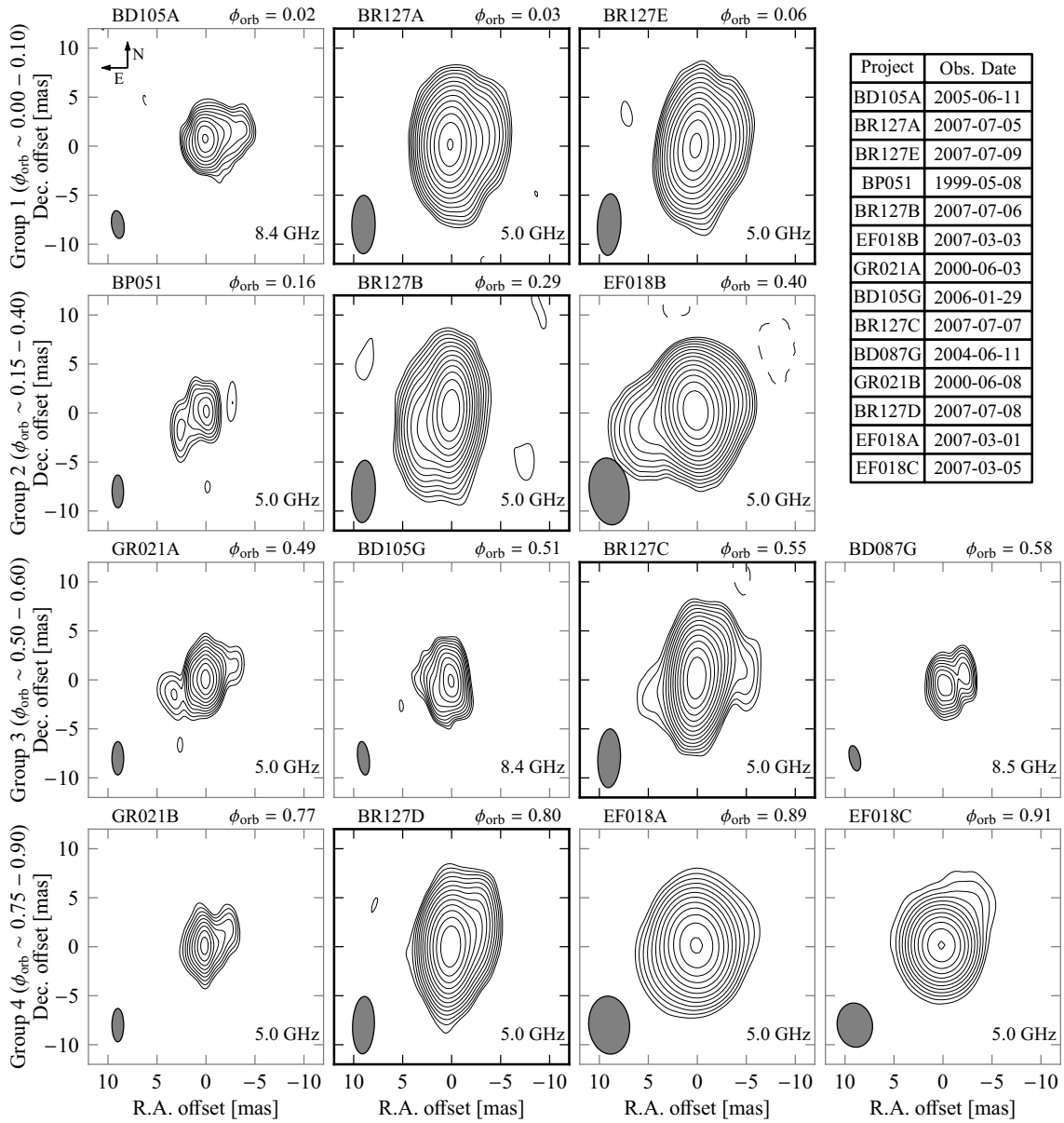


Figure 5.6: VLBI self-calibrated images of LS 5039 at 5.0 and 8.5 GHz (see Table 5.6 for details on the projects). The plotting parameters are the same as in Fig. 5.5. The panel order is in increasing orbital phase from left to right and from top to bottom, and the images have been grouped according to similar morphological features. The project code and orbital phase are quoted on the top part of each panel. The images from project BR127, obtained during the same orbital cycle, have bold axes. Dashed contours are plotted at -3 times the rms noise of each image and solid contours start at 3 times the rms and scale with $2^{1/2}$, except for GR021A-B and BP051, which start at 5σ as in the original publications. The rms noise of each image can be found in Table 5.6.

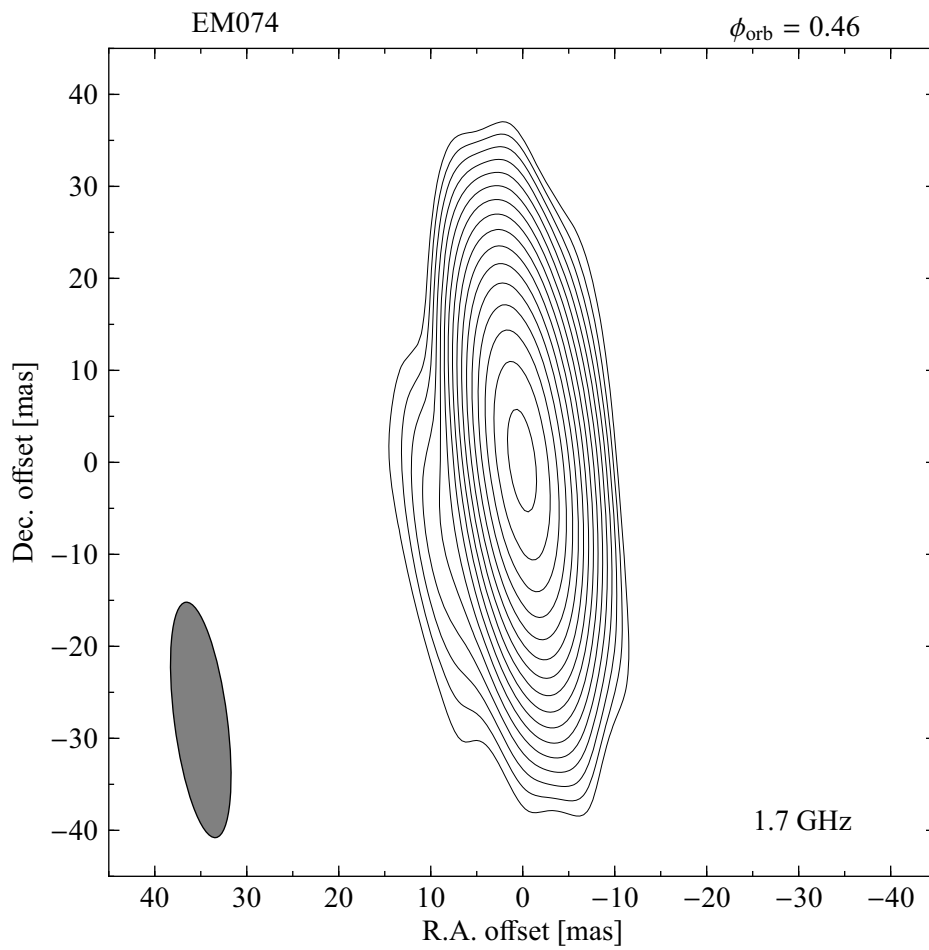


Figure 5.7: Self-calibrated image of LS 5039 at 1.7 GHz obtained with the EVN in 2009. The plot parameters are the same as in Fig. 5.6, although a larger angular scale is shown here.

5. Periodic morphological changes in the radio structure of LS 5039

is approximately $a = 2.4 \times 10^{12}$ cm, or 0.05 mas for a distance to the source of 2.9 kpc (Casares et al. 2012a). The semimajor axis does not change significantly for compact object masses below $5 M_{\odot}$. Bosch-Ramon et al. (2012) identified regions where strong shocks are produced at distances between 5 and $10a$ from the massive star, towards the direction of the pulsar. Here we will assume that the extended radio emission is produced by electrons accelerated at a distance of 10 times the semimajor axis of the orbit, ~ 0.5 mas at 2.9 kpc, and neglect the high-energy processes taking place at shorter distances. We show a sketch of the scenario in the first row of panels of Fig. 5.8, where the grey area indicates the flow of particles accelerated at a distance of $10a$ from the star and are travelling away from it. We consider that the injected electrons follow an energy power law-distribution, $N_e \propto \gamma_e^{-p}$. The global radio spectral index of the source is -0.46 (Martí et al. 1998), and therefore we use an electron index $p = 2$. For simplicity, we assume a constant injection rate of $Q_{\text{inj}} = 10^{35}$ erg s $^{-1}$ (see below) along the orbit, for electron energies of $1 < \gamma_e < 10^4$. Higher electron energies do not significantly contribute to the radio emission at the considered frequencies. On the other hand, a range for the lower electron energy of $\sim 1 - 100$ slightly modifies the most inner part of the emission, but does not significantly affect the larger source structure at 2 – 5 mas. The model is not detailed enough to constrain this value and therefore we assume the minimum energy possible. We note that much higher minimum energies are expected in the primary shock between the stellar and the pulsar wind (Kennel & Coroniti 1984) but we are here considering a secondary shock at larger distances. Zabalza et al. (2011) inferred a spin-down luminosity for the putative pulsar in LS 5039 of $L_{\text{sd}} \sim (3-6) \times 10^{36}$ erg s $^{-1}$, and therefore our injected energy accounts for $\sim 2\%$ of this pulsar spin-down luminosity. The energy spectrum was divided in 200 logarithmic intervals for the computations.

For distances from the massive star larger than $10a$, the evolution of the electron distribution is determined by the radiative losses (synchrotron and inverse Compton in the Thomson regime) and adiabatic cooling. We assume that the particles travel away from the massive star forming an outflow with conical shape (see Fig. 5.8). A conical shape is a coarse estimation, as the ambient pressure and the hydrodynamical instabilities severely modify the flow structure (Bosch-Ramon et al. 2012). We use an opening angle for the cone of 20° , of the same order as the post-shock flow structure seen in Bosch-Ramon et al. (2012) (see also Bogovalov et al. 2008), although the final flux density distribution is not very sensitive to this value. We note that this angle is much lower than the asymptotic opening angle of the contact discontinuity, which for this system is about $\sim 75^\circ$ assuming a pulsar with spin-down luminosity of 5×10^{36} erg s $^{-1}$, with a stellar wind with a mass loss rate of $2.5 \times 10^{-7} M_{\odot}$ yr $^{-1}$ and wind velocity at infinity of 2.4×10^3 km s $^{-1}$ (McSwain et al. 2011). We compute the electron energy distribution density $n(r, \gamma)$, where r is the linear distance from the massive star, taking into account the conservation of the number of particles along the outflow through the continuity equation $N(r, \gamma)d\gamma = N(r_0, \gamma_0)d\gamma_0$.

The outflow is bent as the particles travel away from the system because of the orbital

5.6. A model of the outflow of relativistic particles

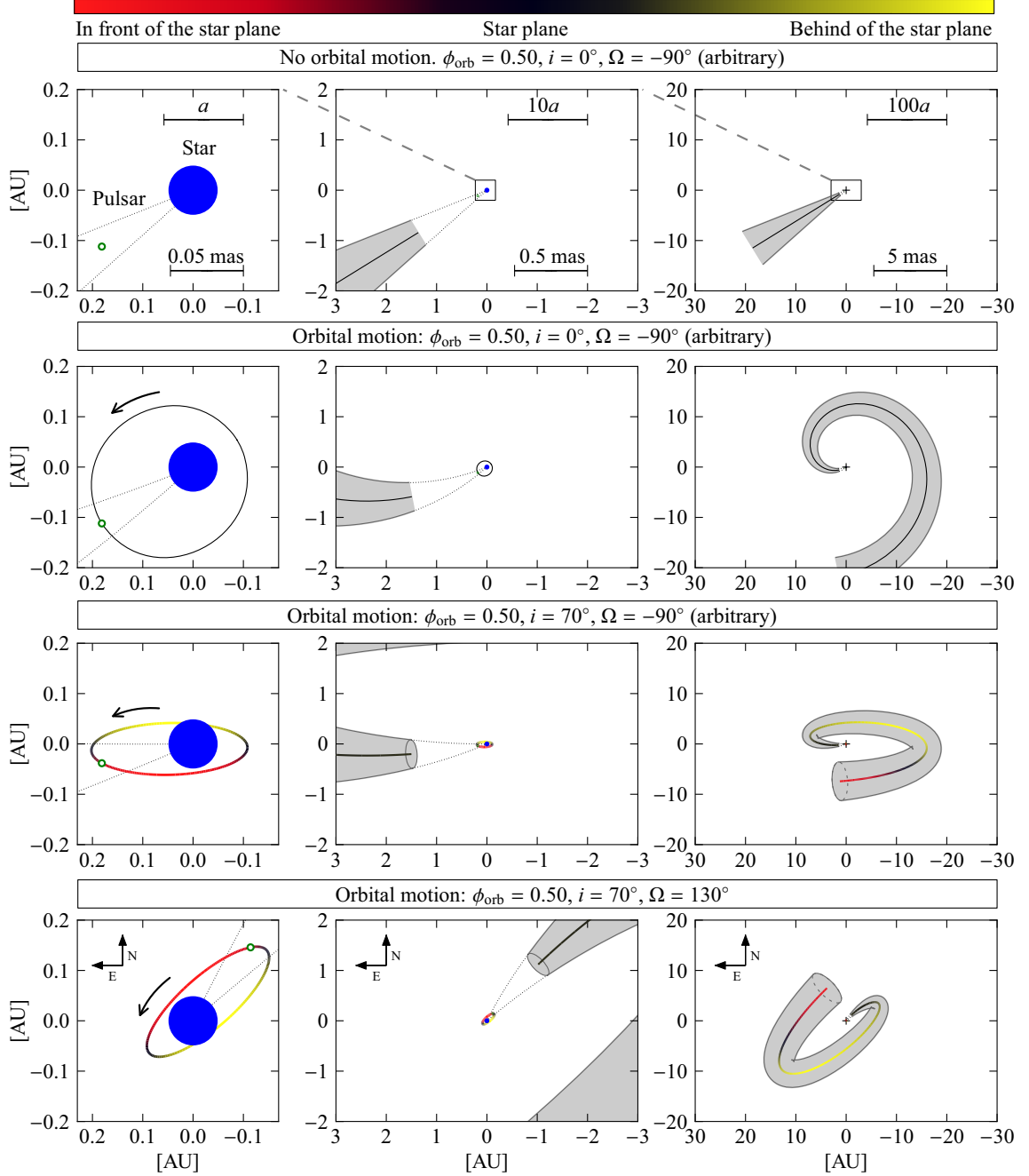


Figure 5.8: Sketch of the orbit orientation and the emission region of the model. From left to right the panels show three different scales: the orbit, the acceleration region, and the whole flow. The particle acceleration occurs at a distance of $10a$ from the massive star (blue circle) behind the pulsar (empty green circle) and the flow of emitting particles (grey area) expands forming a cone while travelling away from the binary system. The colours in the orbit and the flow indicate regions situated in front of the star plane (red) and behind the plane (yellow). The first row shows the general scenario without orbital motion, whereas the rest of the rows include the orbital motion and different projections of the orbit, indicated in the labels. The last row of panels shows the orbit projected with our best estimate of i and Ω .

5. Periodic morphological changes in the radio structure of LS 5039

motion of the pulsar (see second row of panels of Fig. 5.8). The emitting region is bent in the opposite direction of the orbital motion of the pulsar and it forms a spiral (see Dubus 2006 for a general description). The flow, similar to a cometary tail, is a projection of the orbit assuming a ballistic motion. However, the outflow, and in general the whole interaction structure, in fact should not follow a ballistic motion because of the effect of the Coriolis force and consequently the resulting spiral should be less open than for the case of simple ballistic motion (Bosch-Ramon & Barkov 2011; Bosch-Ramon et al. 2012). Nevertheless, we approximate the outflow shape assuming a constant advection velocity (flow bulk velocity) of $0.04c$, which traces an structure similar but more open than the one found in the hydrodynamical simulations by Bosch-Ramon et al. (2012), because we find a better match with the images in this case. We note that those simulations were computed for a slightly different system and using a circular orbit.

We compute the electron density along the flow for r between $10a$ and $140a$, although the farthest part ($\gtrsim 100a$) does not contribute significantly to the emission. We divide the flow in 200 steps in r . The sizes of the steps is determined by the displacement of the pulsar along the orbit and are computed at constant increments of the true anomaly of the pulsar. Therefore, steps close to periastron are shorter, corresponding to time intervals of about 500 s each, whereas steps close to apastron are longer, corresponding to time intervals of about 3000 s each. These intervals are always at least one order of magnitude shorter than the fastest cooling time at each r and γ_e . For the lower energy electrons, adiabatic cooling dominates along the flow, whereas for more energetic electrons, inverse Compton losses dominate up to distances of $\lesssim 4$ mas. We compute the emissivity of each section of the flow assuming a magnetic field of $B = 1.0 \left[\frac{2.4 \times 10^{12} \text{cm}}{r} \right]$ G, which corresponds to $B \sim 0.1$ G in the acceleration region. We note that this magnetic field is similar to the equipartition magnetic field inferred for non-thermal particles from VLBI observations, which is ~ 0.2 G (Paredes et al. 2000).

The observed outflow geometry strongly depends on the orientation of the orbit on the sky, which is basically determined by two angles (see Appendix A): the longitude of the ascending node, Ω , measured from North to the East, and the inclination of the orbit, i , which is a rotation with respect to the node axis (the orbital elements are defined in Smart 1930). In Fig. 5.8 we show different projections of these two angles at orbital phase 0.5. The images in Fig. 5.6 show a privileged North-East/South-West direction, in a P.A. of $\sim 130^\circ$. This constant direction for most part of the orbital phases suggests a high inclination of the orbit, already discussed in Ribó et al. (2008). The orbital elements determine the flow orientation and the final flux density distribution. We searched for the combination of Ω and i that better describes the source structure seen in Fig. 5.6. We used the electron density and the system geometry to compute the synchrotron emissivity of the electrons and project it on the sky. For every orbital phase in Fig. 5.6, we computed the sky flux density distribution at the corresponding frequency and convolved it with a beam equal to the corresponding synthesised beam of the image. The model accounts for

part of the core component and the extended emission. We produced synthetic images in steps of 5° in i and Ω independently and we found that the images in Fig. 5.6 are better **reproduced** by the model for an inclination of $i \sim 70^\circ$ and $\Omega \sim 130^\circ$. Based on visual inspection, a reasonable range for these parameters is $i = 60 - 75^\circ$ and $\Omega = 120 - 140^\circ$. The rotation of the pulsar around the star is counter-clockwise, and therefore $i < 90^\circ$ (see Smart 1930). Soon after the periastron passage the pulsar transits behind the star plane and after apastron it is in front of the star plane. For the inclination obtained the pulsar position is eclipsed during its superior conjunction.

Derived synthetic images

The resulting synthetic images and the projected orbit are shown in Fig. 5.9. The first contour level for all plots is set to $0.06 \text{ mJy beam}^{-1}$. The model produces total flux densities of around 10–16 mJy, which accounts for the extended flux density recovered with VLBI. However, this model does not account for the emission produced at distances below $\lesssim 0.5 \text{ mas}$, so we artificially included an additional 10 mJy point-like source at the position of the binary system to visually help to compare the results with the images in Fig. 5.6. This component approximately accounts for the peak flux density of the core component of the images. With this ad-hoc component, we recover a total flux density of the order of 15–18 mJy at 5 GHz and 13–16 mJy at 8.5 GHz, for the considered orbital phases, which are slightly below the measured values.

This model describes correctly the main features in most of the observed images, except for the observations shortly after the periastron passage. For that case (group 1), our model only accounts for the secondary component eastwards, but not for the main extended component towards West. The rest of the images are well described by this simple model. It produces a bright extended component for orbital phases 0.15–0.40 (group 2) and continuously develops extended emission towards North-West between phases 0.5 and 0.6 (group 3), while preserving the bipolar structure. The extended emission is then dominated by the North-West component until the next periastron passage. We note that this model predicts bipolar extended emission at certain orbital phases, although the outflow is not bipolar itself. In particular, the projected flow at phase 0.5, shown in the bottom-right panel of Fig. 5.8, accounts for the bipolar flux density distribution seen for instance in the image of project GR021A (see Figs. 5.6 and 5.9). At the same time, this approach justifies that the bipolar emission is not completely symmetric and that the two components show different P.A. (Ribó et al. 2008).

Limitations of the model

The differences between the model (Fig. 5.9) and the real data (Fig. 5.6), in particular the missing component in the images from group 1, can be explained by the oversimplification of the flow structure and the constant physical conditions at all orbital phases. For instance, we assumed that the acceleration region was at a constant distance from the

5. Periodic morphological changes in the radio structure of LS 5039

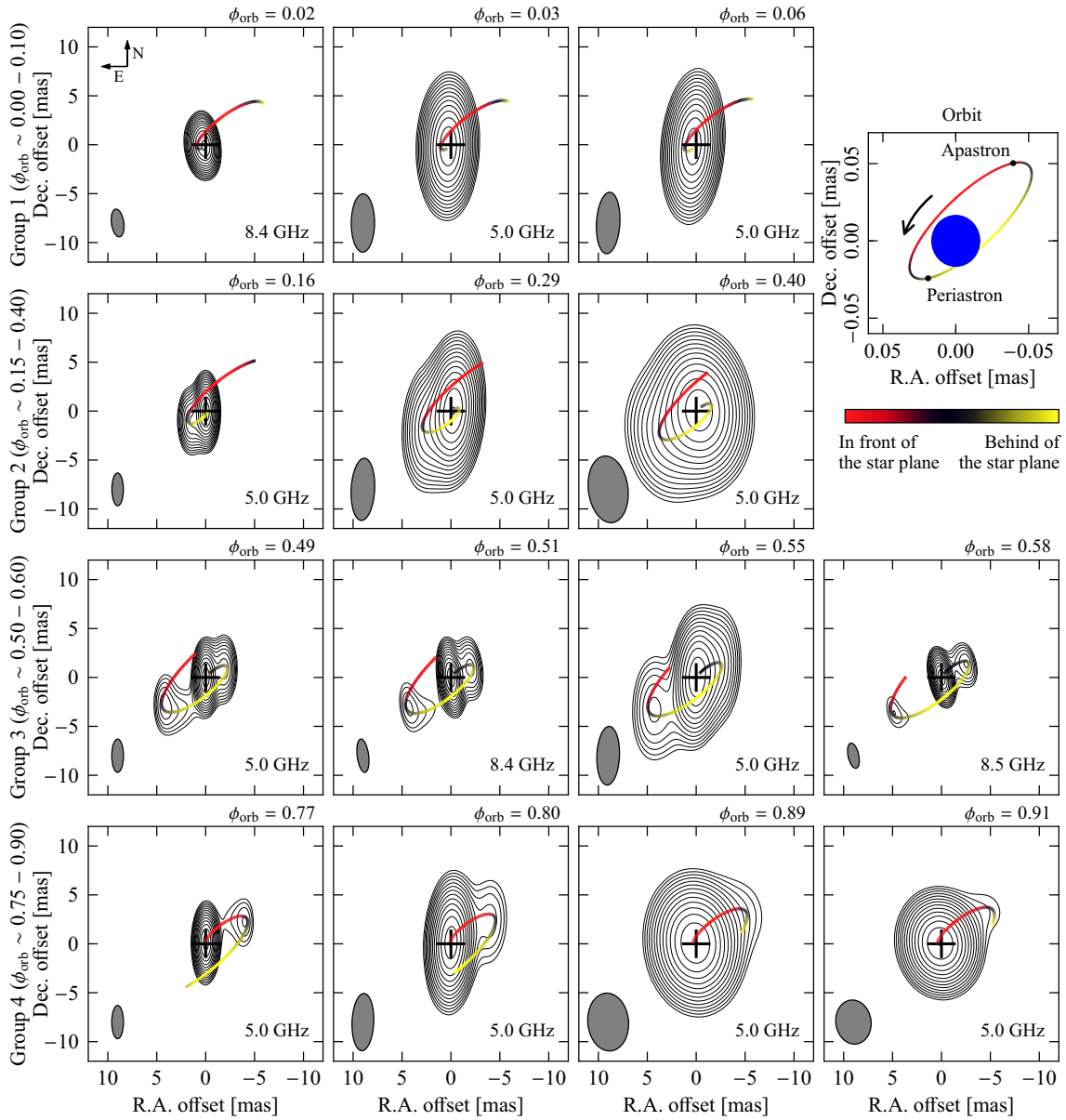


Figure 5.9: Synthetic images produced with our model, computed for the corresponding orbital phases of the different VLBI projects and convolved with the corresponding beam shown in Fig. 5.6. The coloured line traces the projected position of the flow axis of cooling particles, which is computed for linear distances from the star between 1.6 and 22 AU. The crosses mark the position of the main star, set at the origin. The panel in the top-right corner shows the system orbit, projected with an inclination of 70° and a longitude of the ascending node of 130° .

massive star and that the energy injection was constant, although it is expected that these parameters depend on the orbital phase in an eccentric binary system. Therefore, additional electron populations, as well as more realistic time-dependent physical conditions should be included to produce this additional component. The model should also include considerations on the relativistic Doppler boosting possibly affecting the synchrotron emission (Dubus et al. 2010). However, including additional particle populations and assuming time-dependent physical conditions would require the addition of several free parameters, which is outside of the scope of this paper. Therefore, we do not try to include a complete flux density analysis or to predict flux density distributions. Also, predictions of displacements of the peak of the emission, such as the hint found in Sect. 5.4.1, cannot be obtained by this model, as these are produced at smaller distances. Despite these caveats, this model traces, except for the phases close to the periastron passage, all the main features of the VLBI images and the morphological variability measured in multifrequency and multiepoch observations, even when assuming simple and constant physical conditions.

5.7 Discussion and conclusions

Summary of the results

VLBA observations at 5 GHz during five consecutive days show that LS 5039 displays orbital morphological variability, showing one sided and bipolar structures, but recovering the same morphology when observing at the same orbital phase. The P.A. of the extended emission with respect to the core changes significantly on timescales of one day. Although the total flux density remains approximately constant during the orbital cycle, the flux density of the different components varies. Remarkably, the P.A. of the extended emission changes by $\sim 160^\circ$ between phases 0.03 and 0.29 (24 h). The sensitivity of the observations is not enough to study changes on shorter timescales, within a few hours. We measured a displacement of the peak of the emission between orbital phases 0.29 and 0.55 of 2.3 ± 0.6 mas in P.A. 154° , nearly in the same direction of the extended emission. However, we consider this measurement as a hint of peak displacement because, given the limitations of the astrometry of these observations, we would require a $5\text{-}\sigma$ significance to consider it a significant displacement. Dubus (2006) predicted a continuous peak displacement forming an ellipse of a few mas along the orbit. The peak of the emission of the gamma-ray binary LS I +61 303 at 8.4 GHz traces an ellipse of semimajor axis 1.5 AU, about four times the binary semimajor axis (Dhawan et al. 2006). Unfortunately our astrometric accuracy is not enough to measure these displacements. The source morphology during two consecutive periastron passages (run A and E) is very similar, showing that the changes within the same orbital cycle are periodic. An interesting future project would be aimed to obtain accurate astrometry to explore the displacements of the peak of the emission, in particular at different frequencies, and also to measure variations of the source structure

5. Periodic morphological changes in the radio structure of LS 5039

on timescales of a few hours.

We analysed the available VLBI observations of LS 5039 in a consistent way. Images from data obtained between 1999 and 2009 at frequencies between 1.7 and 8.5 GHz show that the morphology at similar orbital phases is similar. When ordered in increasing phase, the images show an approximately continuous change. The observational conclusion of our VLBI analysis is that the morphological changes of LS 5039 are periodic and show orbital modulation stable over several years. The gamma-ray binary LS I +61 303 also shows a similar behaviour (Dhawan et al. 2006). Therefore, all gamma-ray binaries are expected to display periodic orbital modulation of their VLBI structure.

Discussion on the model

A simple model of an expanding outflow of relativistic electrons accelerated at a distance of $\sim 10a$ and travelling away from the system can account for the main changes seen in the extended emission of LS 5039. The changes are explained for an inclination of the orbit $i \sim 70^\circ$ and a longitude of the ascending node of $\Omega \sim 130^\circ$. In the last row of panels in Fig. 5.8 we show the orientation of the orbit on the sky projected with these parameters. The inclination of the orbit has deep implications in the physical properties of the binary system, because the orbital parameters restrict the mass of the compact object within the system. In particular, assuming a mass function of the binary system of $0.0045(6) M_\odot$ (Casares et al. 2012a), a mass of the star of $33 M_\odot$ implies that the mass of the compact object is $1.8\text{--}2.0 M_\odot$, for an inclination between 75 and 60° . However, the mass of the star is barely constrained between 20 and $50 M_\odot$, and consequently the inclinations inferred from the model are compatible with masses between $1.3\text{--}1.5$ and $2.4\text{--}2.7 M_\odot$, for the lower and the higher stellar mass limits, respectively. The uncertainty in the mass function adds an additional $\sim 0.1 M_\odot$ uncertainty. The values obtained are in any case below $3 M_\odot$, and therefore are compatible with the presence of a neutron star in the system. However, we note that this was one hypothesis of the model and therefore cannot be a proof. After applying a simple model, we conclude that the presence of a young non-accreting pulsar in LS 5039 agrees with the observed source structure at different orbital phases and produces a coherent scenario. However, this model does not account for all the emission produced at shorter distances and also fails to explain the main component of the extended emission seen shortly after the periastron passage. This is possibly due to unaccounted variability in the injection rate, geometry and localisation of the acceleration zone, and flow velocity.

Conclusions

For gamma-ray binaries, the nature of the compact object, either accreting or not, is a fundamental ingredient for any model aimed to understand these peculiar systems. The most straightforward indication would be the detection of pulsations. However, direct detection may be unfeasible in binary systems with close orbits and powerful massive

companions because of free-free absorption (Dubus 2006). In addition, the mass function of the known gamma-ray binaries does not allow to discriminate between black holes or neutron stars. Therefore, an ongoing debate is still open regarding the nature of the compact object of gamma-ray binaries. We have presented high resolution radio images of LS 5039 with which the scenarios can be tested. A first approach has shown that the source radio morphology can be explained with the presence of a young non-accreting pulsar. PSR B1259–63, the only gamma-ray binary with a confirmed pulsar, shows variable extended radio structures (Moldón et al. 2011a), and LS I +61 303 shows variable and periodic morphological changes (Dhawan et al. 2006). The common features among these three systems suggest that the known gamma-ray binaries contain young non-accreting pulsars.

6

On the origin of LS 5039 and PSR J1825-1446

6.1 Introduction

During a core-collapse supernova explosion of a massive star, the remaining compact object, either isolated or in a binary system, can receive a natal kick and obtain a high peculiar velocity (Hills 1983; van den Heuvel et al. 2000). A binary system can obtain a moderate velocity from a symmetric Blaauw kick (Blaauw 1961), whereas the compact object can acquire additional momentum from an asymmetric supernova kick (Stone 1982). If the system remains bound after the explosion, the parameters of the binary system before and after the supernova explosion can be related by measuring the high peculiar velocity of the system, in particular for X-ray binaries (see e.g. Brandt & Podsiadlowski 1995, and the particular cases in Tauris et al. 1999; Martin et al. 2009). On the other hand, the space velocity of a binary system can be used to determine its past Galactic trajectory (see e.g. Ribó et al. 2002b; Dhawan et al. 2007; Miller-Jones et al. 2009a). Of particular interest are the runaway systems, which have acquired very high peculiar velocities (Mirabel et al. 2001, 2002). With enough information, a complete evolutionary history of the binary system can be obtained with constraints on the progenitor and the formation of the compact object, (see e.g. Willems et al. 2005; Fragos et al. 2009). Among the binary systems receiving natal kicks we can find the special case of gamma-ray binaries, which usually form eccentric binary systems (Casares et al. 2012b).

Only a few binary systems have been associated with gamma-ray sources, and therefore it is important to understand how they formed, and how they are distributed in the Galaxy. However, the origin of most of the binaries with gamma-ray emission is still unknown. Mirabel et al. (2004) studied the origin of the gamma-ray binary LS I +61 303,

6. On the origin of LS 5039 and PSR J1825-1446

and Dhawan et al. (2006) measured a precise proper motion that allowed the authors to obtain the space velocity of the source and constrain the mass lost in the supernova event that formed the compact object of the system to $\sim 1 M_{\odot}$. The natal kick of the supernova that produced the pulsar in the system PSR B1259–63/LS 2883 was discussed in Hughes & Bailes (1999) and Wang et al. (2006), although no proper motion has been measured for this system. The Galactic motion of LS 5039 was extensively discussed in Ribó et al. (2002b) (see details in Sect. 6.2.1). Mirabel & Rodrigues (2003) and Reid et al. (2011) used high-accuracy radio astrometry to compute the Galactic velocity of Cygnus X-1, which allowed them to obtain the mass of the progenitor of the black hole, and its association with the Cyg OB2 association. They also determined that the black hole was formed without a supernova explosion. For Cygnus X-3, Miller-Jones et al. (2009b) obtained an accurate proper motion of the source that was used to better identify the position of the X-ray binary core, although the origin of the system is still unknown. Moldón et al. (2011c) determined for HESS J0632+057 that its total proper motion is below 4 mas yr^{-1} . Other recent gamma-ray binary candidates are 1FGL J1018.6–5856 (Corbet et al. 2011; Pavlov et al. 2011b; Fermi LAT Collaboration et al. 2012a) and AGL J2241+4454 (Williams et al. 2010; Casares et al. 2012b). However, the proper motion of these sources is still unknown. These examples show the potential of a good determination of the proper motion of a system, and also the need for better astrometry in this peculiar binary population.

On the other hand, accurate astrometry of isolated pulsars opens a wide field of scientific research including fundamental reference frame ties, physics in the core-collapse supernovae and imparted momentum kicks, association with supernova remnants (SNRs) and determination of the age of pulsars, model-independent estimates of distances through parallax measurements, or determination of the distribution of electron density in the interstellar medium (see for example Chatterjee et al. 2009; Brisken et al. 2002 and references therein). It is common that pulsars acquire high velocities at birth, becoming the fastest population in the Galaxy, with a mean transverse velocity of $\sim 450 \text{ km s}^{-1}$, and up to above 10^3 km s^{-1} (Lyne & Lorimer 1994; Hobbs et al. 2005; Chatterjee et al. 2005). The pulsar velocity distribution provides information about the supernova symmetry and the binary population synthesis (Brisken et al. 2003).

Here we present the results from two high-resolution astrometric projects to determine the proper motion of LS 5039, and the nearby pulsar PSR J1825–1446, the only known compact objects in the field of G016.8–01.1. In Sect. 6.2 we describe the gamma-ray binary LS 5039, its possible association with G016.8–01.1, and the motivation to obtain the proper motion of the pulsar PSR J1825–1446. In Sect. 6.3 we describe the VLBA astrometric project on PSR J1825–1446, and we obtain the proper motion of the source. In Sect. 6.4 we present three sets of radio observations of LS 5039, as well as the available radio and optical astrometry of the source, and we compute the proper motion and discuss the uncertainties of the fit. In Sect. 6.5 we compute the Galactic velocity of both sources. In Sect. 6.6 we analyse the past trajectories of the sources and discuss their possible birth

location. Finally, we summarise the obtained results in Sect. 6.7.

6.2 Compact objects in the field of G016.8–01.1

6.2.1 The proper motion of the gamma-ray binary LS 5039

The proper motion and the space velocity of the source were first determined in Ribó et al. (2002b). These authors found that LS 5039 is escaping from its own regional standard of rest with a total systemic velocity of 150 km s^{-1} . The past trajectory of LS 5039 for the last 10^5 yr computed in Ribó et al. (2002b) marginally suggests an association with SNR G016.8–01.1. These authors also discovered an H I cavity in the ISM, and argued that it may have been caused by the stellar wind of LS 5039 or by the progenitor of the compact object in the system. An in-depth discussion on the supernova process that produced the compact object in the system LS 5039 can be found in McSwain & Gies (2002), Ribó et al. (2002b), McSwain et al. (2004), and Casares et al. (2005b). The authors discussed the expected mass loss during the supernova explosion that produced the compact object, obtained from the orbital parameters and the mass of the system. This allowed them to estimate some orbital parameters of the pre-supernova system. We note that the main limitation for obtaining accurate pre-supernova properties of LS 5039 is the determination of the orbital parameters, which can be improved by means of optical observations.

The region around LS 5039, shown in Fig. 6.1, contains a complex radio structure that has initially been described in Reich et al. (1986). By means of observations with the Effelsberg 100-m telescope at 1.4, 4.8, and 10 GHz, these authors identified the complex as a composition of different objects. The brightest source corresponds to the H II region RCW 164, which coincides with the optical $8' \times 6'$ counterpart in Rodgers et al. (1960). It appears to be an optically thick thermal component that produces the inverted integrated radio emission of the global structure. Other sources within the structure are a source with 0.11 Jy at 4.8 GHz coincident with the Wolf-Rayet star WR 115 (IC14–19 in Reich et al. 1986), and an unidentified source with 0.13 Jy at 4.8 GHz, also detected with the VLA as NVSS J182535–145555 (Condon et al. 1998). Finally, diffuse emission with a size of $\sim 30'$ surrounds all the sources. The source is also visible at 2.7 GHz in the Effelsberg 11 cm radio continuum survey of the Galactic plane (Reich et al. 1990). This emission was identified as a supernova remnant because it is highly polarised (up to 40% at 4.8 GHz, Reich et al. 1986¹). The dashed and dotted contours in Fig. 6.1 delimit the diffuse and polarised emission, respectively, and should trace the shape of the supernova. Unfortunately, the high contamination of the bright RCW 164 prevents the determination of the SNR parameters, and consequently its age, distance, centre, and surface brightness

¹Sun et al. (2011), based on polarisation studies, note that the object G16.8–1.1 appears to be a misidentification and is likely an H II region. This changes the initial motivation of our study but not the results and conclusions.

6. On the origin of LS 5039 and PSR J1825-1446

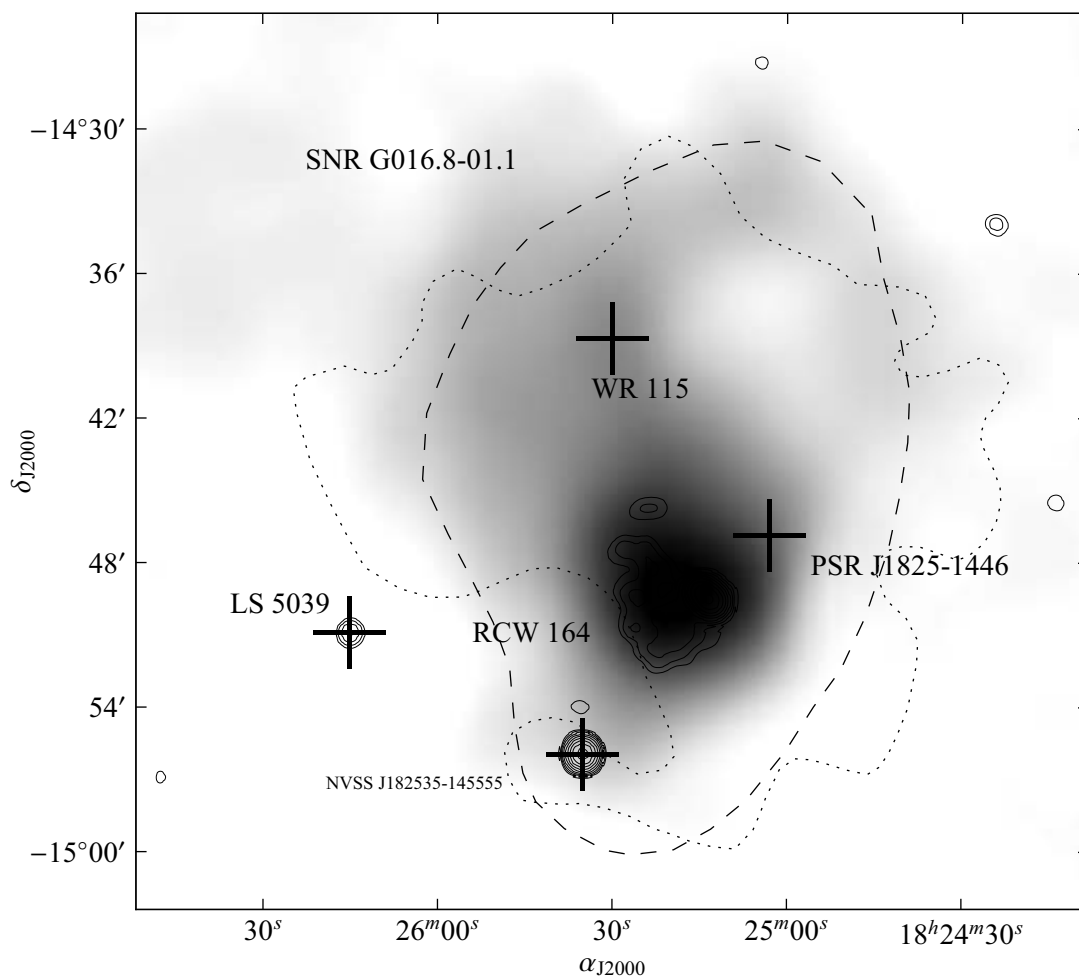


Figure 6.1: Wide field map around SNR G016.8–01.1. The grey scale corresponds to the Parkes-MIT-NRAO survey at 5 GHz (Tasker et al. 1994), and the contours, with higher resolution, to the NRAO VLA Sky Survey (NVSS) at 1.4 GHz (Condon et al. 1998). The dashed line outlines the area covered by the diffuse emission at 4.75 GHz in Reich et al. (1986), and the dotted line the polarised emission in the same image. These two components trace the morphology of SNR G016.8–01.1. The most relevant sources in the field are indicated.

are unknown. The lack of polarisation in the direction of RCW 164 indicates that the SNR is located behind RCW 164, which is located at ~ 1.8 kpc (Ribó et al. 2002b). Therefore ~ 2 kpc is the lower limit for the SNR distance. The size of the polarised structure is $\sim 30'$ and it is approximately centred at $\alpha_{J2000.0} = 18^{\text{h}}25^{\text{m}}3$ and $\delta_{J2000.0} = -14^{\circ}46'$ (Reich et al. 1986; Green 2009).

6.2.2 The nearby isolated pulsar PSR J1825–1446

As part of our project to unveil the origin of the binary LS 5039, we searched for other possible sources, such as fossil neutron stars, that may be related to SNR G016.8–01.1. The aim was to obtain the proper motion by means of VLBI of the best candidates to check any possible relation with the SNR. The most obvious candidate is PSR J1825–1446, which, in projection, lies within the SNR itself. To explore other possible candidates we used the ATNF Pulsar Catalogue, PSRCAT² (Manchester et al. 2005), which is the most complete and updated pulsar database, and accepts searches based on pulsar parameters. We restricted the search to those angular distances for which the pulsar proper motion and age make their past trajectory compatible with the location of the SNR. We note that this selection is not complete because, among the known pulsars many do not have good determinations of the proper motion and/or the age, and their trajectories are compatible only because of their large uncertainties. We discarded pulsars with distances below 1.9 kpc and above 9.0 kpc. We found no other candidate with enough constraints to justify a long-term VLBI project, and therefore we restricted our observations to PSR J1825–1446.

PSR J1825–1446 (B1822–14) is an isolated pulsar with a period of 0.28 s discovered in a high radio frequency survey conducted at Jodrell Bank by Clifton & Lyne (1986). The main properties of the pulsar are described in Table 6.1. The radio spectrum of PSR J1825–1446 can be found in Kijak et al. (2007), and it presents a turnover at 1.4 GHz. The spectral index is -1.4 ± 0.7 above this frequency, and it is inverted at lower frequencies. The proper motion in Table 6.1 was obtained by means of pulsar timing. The pulse profile obtained by Gould & Lyne (1998) shows a single component at 1.4 and 1.6 GHz. We computed the distance to PSR J1825–1446 using the pulsar dispersion measure, although it is not a direct measurement because it depends on the model of the electron distribution in the Galaxy. We used the dispersion measure quoted in Table 6.1 and the electron density model NE 2001, described in Cordes & Lazio (2002), and obtained a distance of 5.0 ± 0.6 kpc. The distance uncertainty is 10%, although the distance could be overestimated if the medium along the line of sight of the pulsar is denser than given by the model.

The possible association between SNR G016.8–01.1 and PSR J1825–1446 has been discussed in the literature. Clifton & Lyne (1986) already suggested a possible association based only on a positional coincidence. Clifton et al. (1992) mentioned the possible relation between them, and the proximity with the intense H II region RCW 164 (see Fig. 6.1). However, they already found that this H II region appears to be much closer to the Sun than

²<http://www.atnf.csiro.au/research/pulsar/psrcat/>

6. On the origin of LS 5039 and PSR J1825-1446

Table 6.1: Parameters of the isolated pulsar PSR J1825-1446. The proper motion is updated in this paper, see text.

Parameter	Symbol	Value	Ref.
Pulsar period	P	$0.279186875177(5) \text{ s}$	(1)
Frequency	f_0	$3.58183026823(6)$	(1)
Freq. derivative	f_1	$-2.909526(5) \times 10^{-13} \text{ s}^{-1}$	(1)
Freq. second derivative	f_2	$2.24(9) \times 10^{-25} \text{ s}^{-2}$	(1)
Characteristic age	τ_c	$1.95 \times 10^5 \text{ yr}$	(1)
Dispersion measure	DM	357 ± 5	(1)
Rotation measure	RM	$-899 \pm 10 \text{ rad m}^{-2}$	(1)
Distance (DM)	d	$5.0 \pm 0.6 \text{ kpc}$	(2)
Spindown luminosity	\dot{E}_{sp}	$4.1 \times 10^{34} \text{ erg s}^{-1}$	(1)
Flux density	$S_{0.6\text{GHz}}$	$1.8 \pm 0.3 \text{ mJy}$	(3)
	$S_{1.1\text{GHz}}$	$2.4 \pm 0.5 \text{ mJy}$	(3)
	$S_{1.4\text{GHz}}$	$3.0 \pm 0.2 \text{ mJy}$	(4)
	$S_{1.6\text{GHz}}$	$2.5 \pm 0.2 \text{ mJy}$	(4)
	$S_{4.8\text{GHz}}$	$1.2 \pm 0.1 \text{ mJy}$	(3)
Pulse width (1.4 GHz)	W_{10}	27 ms	(1)
Pulse width (4.8 GHz)	W_{10}	6.8 ms	(3)
Polarisation		$90 \pm 6\%$	(5)
Proper motion	$\mu_\alpha \cos \delta$	$10 \pm 18 \text{ mas yr}^{-1}$	(1)
	μ_δ	$19 \pm 115 \text{ mas yr}^{-1}$	(1)

References: (1) Hobbs et al. (2004); (2) using the model in Cordes & Lazio (2002); (3) Kijak et al. (2007); (4) Lorimer et al. (1995); (5) Von Hoensbroech (1998).

the pulsar, thus contributing to the DM of the pulsar. The authors also argued that the probability of having a pulsar in a randomly selected area of the size of SNR G016.8–01.1 at this Galactic longitude is about 1 in 18, and therefore the positional proximity may only be by chance. Some notes on associations between old ($\tau \gtrsim 10^5$ yr) pulsars and supernova remnants can be found in Gaensler & Johnston (1995).

6.3 Astrometry and proper motion of PSR J1825–1446

The previously known proper motion of the pulsar, shown in Table 6.1, has large uncertainties and did not allow us to study the origin of this pulsar. The astrometry in the literature, detailed in Sect. 6.3.2, is scarce. Therefore, we conducted a dedicated 2-yr VLBI astrometric project to measure the proper motion of the pulsar.

6.3.1 Radio VLBI observations

Before starting the VLBI project, we conducted a short VLA observation at 8.6 GHz to obtain the initial position required for the correlation of the VLBA data. The VLA observation was conducted on November 14, 2008, in the A configuration of the VLA, and lasted 30 minutes. At that epoch the VLA was performing the upgrade to the EVLA. Seventeen antennas used the new EVLA feeds, eight used the old VLA feeds, and four antennas were not available. We observed the source during three scans of 3.6 minutes, bracketed by 1.6-minute scans on the phase calibrator J1832–1035 (1832–105). The correlation position of the reference source J1832–1035 was $\alpha_{J2000.0} = 18^{\text{h}}32^{\text{m}}20^{\text{s}}.8436$ and $\delta_{J2000.0} = -10^{\circ}35'11''.299$. Standard data reduction in AIPS³ was performed, including standard normalisation of the bandpasses between EVLA and non-EVLA antennas. The data were imaged with an intermediate robust parameter of 0 within AIPS, as a compromise between angular resolution and sensitivity, providing a synthesised beam of 460×210 mas at a position angle (P.A.) of 37° . We used a cell size of 10 mas. The image shows a point-like source with a peak flux density of 0.76 ± 0.07 mJy beam⁻¹, and a total flux density of 0.8 ± 0.1 mJy. The pulsar position was measured with the AIPS task JMFIT.

The VLBI campaign consisted of three observations with the Very Long Baseline Array (VLBA) at 5 GHz separated by one year. The observations were conducted on the same day (May 4) in 2009, 2010, and 2011, during six hours between UTC 07:40 and 13:40. Observations separated by one year prevent any annual parallax displacement, which is expected to have a maximum amplitude of ~ 0.2 mas for a source at 5 kpc. Additionally, identical schedules were chosen to minimise any observational difference between epochs (e.g. source elevation, scan structure). The observations were conducted at a frequency of 5.0 GHz (6 cm wavelength), which was chosen as a compromise between angular resolution, spectral index of the pulsar ($\alpha \sim -1.4$), and the quality of the best VLBI calibrator next to the source, J1825–1718, which is partially resolved at long baselines due to interstellar

³The NRAO Astronomical Image Processing System. <http://www.aips.nrao.edu/>

6. On the origin of LS 5039 and PSR J1825-1446

scattering (see Fig. 2.5 on page 23). The first epoch was recorded with a total data rate of 256 Mbps per station distributed in four dual polarisation subbands, each of them with a bandwidth of 8 MHz, and recorded using 16 frequency channels, two-bit sampling, and 2 s of integration time. The correlation of this first epoch was performed in the hardware VLBA correlator at Socorro. The second and third epochs, observed and correlated in 2010 and 2011, respectively, were recorded at the available bit rate of 512 MHz, and eight subbands were used, which improved the sensitivity of the observation. The 2010 and 2011 correlations were performed with the DiFX (Deller et al. 2007) software correlator at Socorro. The data from the three observations of PSR J1825–1446 were also correlated using pulsar gating (see Sect. 2.3).

The observations were performed using phase-referencing on the nearby phase calibrator J1825–1718, located at 2.5° from the pulsar, switching between them with a cycling time of four minutes, which is compatible with the expected coherence time. The phase calibrator was correlated at $\alpha_{J2000.0} = 18^{\text{h}}25^{\text{m}}36^{\text{s}}.53228$ and $\delta_{J2000.0} = -17^\circ 18' 49''.8485$. However, for the final fit result we used the last available position of the source in the frame of ICRF (see Sect. 6.3.3). As an astrometric check source we observed the quasar J1844–1324, which is separated 5° from the pulsar and 6° from the phase calibrator. The source has a flux density of 65 mJy, which, in natural weighted images, is dominated by a compact core that accounts for 94% of the total emission, and displays slightly extended emission eastwards. Only the compact core is seen in the uniformly weighted images used to measure its position. Two scans of the fringe finder J1733–1304 were observed at each epoch.

The data reduction was performed in AIPS. Flagging based on predicted off-source times, owing to slewing or failures, was applied using UVFLG. A priori visibility amplitude calibration used the antenna gains and the system temperatures measured at each station. We used ionospheric total electron content (TEC) models based on GPS data obtained from the CDDIS data archive⁴ to correct the data from the sparse ionospheric variations. Several ionospheric models are produced each day by different groups (i.e. the Jet Propulsion Laboratory (JPL), the Center for Orbit Determination in Europe (CODE), the Geodetic Survey Division of Natural resources Canada (EMR), the ESOC Ionosphere Monitoring Facility (ESA), and the Universitat Politècnica de Catalunya (UPC), among others). We applied the corrections from all available models to the data to check the consistency between models. There are currently 12 models available for the data obtained in 2009, 16 for 2010, and 19 for 2011. In Table 6.2 we show the offset position between the uncorrected data and the corrected data (average value considering all models) for right ascension and declination, respectively. We also show the standard deviation of the positions measured with the different models, and the model that provides a position closer to the mean value, which was used for the final data reduction.

Standard instrumental corrections were applied (parallactic angle, instrumental offsets,

⁴The Crustal Dynamics Data Information System <http://cddis.nasa.gov/>

6.3. Astrometry and proper motion of PSR J1825–1446

Table 6.2: Ionospheric correction applied to the VLBA data on PSR J1825–1446. Units are mas.

Epoch	Mean offset		Dispersion		Best
	α	δ	α	δ	
2009	0.13	0.92	0.04	0.17	CODE
2010	−0.05	1.96	0.09	0.36	IGS
2011	0.03	2.73	0.19	0.35	IGS

Notes: CODE: Center for Orbit Determination in Europe. IGS: the International GNSS Service

and bandpass corrections). Fringe-fitting on the phase calibrator was performed with the AIPS task FRING. The amplitude and phase calibration, flags, and bandpass correction tables were applied to the target pulsar and the astrometric check source data, which were averaged in frequency, and clean images were produced with IMAGR. A cell size of 0.1 mas was used for cleaning all images, which were produced using a weighting scheme with robust parameter -2 within AIPS. A tapering of $60 M\lambda$ was applied to avoid the use of phases where the correlated flux density of the calibrator was below ~ 40 – 10 mJy. No self-calibration of the data was possible because of the low flux density of the target source.

The source has a declination of -15° , and the maximum elevation for most of the VLBA antennas is 40° . Some phase decoherence was present when using the data from the beginning and the end of the observations, presumably as a consequence of the atmospheric effects caused by the low elevation of the source and the phase calibrator. To reduce the astrometric errors, we flagged all visibilities with elevations below 20° , and only used the data closer to the transit of the source, discarding about 1.5 hours at the beginning and at the end of the observations. To reduce the effects of the extended emission of the astrometric check source, visibilities with uv -distances below $10 M\lambda$ were not used. The positions of PSR J1825–1446 and the astrometric check source were measured by fitting a Gaussian component with JMFIT within AIPS. In Table 6.3 we show some parameters of the observation, the resolution, and a comparison of the obtained signal-to-noise ratio with and without pulsar gating (see Sect. 2.3 for the details). The position errors of PSR J1825–1446 were finally computed as the standard deviation of the three positions of the astrometric check source. The final positions measured in the images from the data correlated with pulsar gating are shown in Table 6.4.

6.3.2 Archival astrometry of PSR J1825–1446

To measure the proper motion of PSR J1825–1446 we searched all currently available astrometry of this isolated pulsar. Frail & Scharringhausen (1997) imaged the field around

6. On the origin of LS 5039 and PSR J1825-1446

Table 6.3: Parameters of the observations of PSR J1825–1446, and the resulting images. The last column is the improvement factor of the signal-to-noise ratio achieved when using pulsar gating.

MJD	Array	Freq. [GHz]	HPBW _{size} [mas ²]	HPBW _{P.A.} [°]	(<i>S/N</i>) ₀	(<i>S/N</i>) _G	Gain
55607.83	VLA	8.6	460×210	37	11	—	—
54955.44	VLBA	5.0	4.9×2.2	5	3.5	9.8	2.8
55320.44	VLBA	5.0	6.2×2.7	6	6.6	11.5	1.7
55685.44	VLBA	5.0	6.9×2.9	1	6.1	8.4	1.4

several pulsars with the VLA. They observed PSR J1825–1446 (B1822–14) on March 14, 1993 at 8.4 GHz for two scans of 10 minutes each. The observations were conducted with the VLA in its B configuration. The phase calibrator was J1832–1035 (J1832–105, 1829–106). We have re-analysed the data to measure the position of the pulsar. Although the scan duration is longer than optimal for astrometry, the pulsar is detected as a point-like source with a peak flux density of 0.78 ± 0.10 mJy beam^{−1} when using uniform weighting, which yields a synthesised beam size of 1.0×0.6 arcsec². We transformed the positions of the observation from B1950 to J2000, and we updated the position of the phase calibrator to the best currently known position, quoted in Sect. 6.3.1. We fitted the position using JMFIT within AIPS, and the errors correspond to formal errors of a Gaussian fit. The fitted position can be found in Table 6.4.

The position of PSR J1825–1446 found in Hobbs et al. (2004), obtained by means of pulsar timing, is also shown in Table 6.4. The position is in the solar system centre of mass, or barycentric, frame, and it was obtained by fitting the pulsar period and period derivative, the ecliptic position and proper motion, among other variables, to the time of arrival (TOA) of the pulses during several years. However, we can see in Table 6.4 that the timing position differs from the expected position by 245 mas ($3\text{-}\sigma$) in right ascension, which appears to indicate that the uncertainty may be underestimated (see also Fig. 6.2 and the difference with the declination error). The difference between the errors in right ascension and declination can be understood considering the pulsar position. The pulsar is located near the ecliptic plane (with ecliptic latitude $\beta = 8^\circ 53'$), which has two consequences in the errors of the ecliptic coordinates (λ, β) . In particular, the uncertainty in λ and β are inversely proportional to $\cos \beta$, and $\sin \beta$, respectively⁵. For PSR J1825–1446 we have that $(\cos \beta)^{-1} \sim 1.0$, and $(\sin \beta)^{-1} \sim 6.7$, which intrinsically yields larger errors in the determination of the ecliptic latitude by means of pulsar timing. Large errors in the ecliptic latitude β produce the large error in declination, which is

⁵<http://www.cv.nrao.edu/course/ast534/PulsarTiming.html>

Table 6.4: Astrometry and fit residuals of PSR J1825–1446.

MJD	Epoch Y-M-D	Array	Freq. [GHz]	α_{J2000} [h, m, s]	$\sigma_{\alpha \cos \delta}$ [mas]	δ_{J2000} [$^{\circ}$, $'$, $''$]	σ_{δ} [mas]	Res. $_{\alpha \cos \delta}$ [mas]	Res. $_{\delta}$ [mas]
49060.53	1993-03-14	VLA-B	8.4	18 25 2.94(3)	40	−14 46 52.77(6)	60	−37	−61
49480.00	1994-05-08	Timing	0.4–1.6	18 25 2.927(5)	75	−14 46 52.6(5)	500	−245	142
54784.04	2008-11-14	VLA-A	8.6	18 25 2.9539(8)	12	−14 46 53.163(15)	15	13.4	−0.0
54955.44	2009-05-04	VLBA	5.0	18 25 2.95324(4)	0.6 ^a	−14 46 53.1767(5)	0.5 ^b	−0.6	−0.3
55320.44	2010-05-04	VLBA	5.0	18 25 2.95398(4)	0.6 ^a	−14 46 53.2047(5)	0.5 ^b	0.7	0.7
55685.44	2011-05-04	VLBA	5.0	18 25 2.95460(4)	0.6 ^a	−14 46 53.2347(5)	0.5 ^b	0.0	−0.4

Notes: ^a An additional uncertainty of 0.9 mas in right ascension due to the global astrometry errors on the phase-reference source position should be included when considering this position in the ICRF. ^bThe phase-reference source has an additional uncertainty of 1.4 mas in declination in the ICRF.

6. On the origin of LS 5039 and PSR J1825-1446

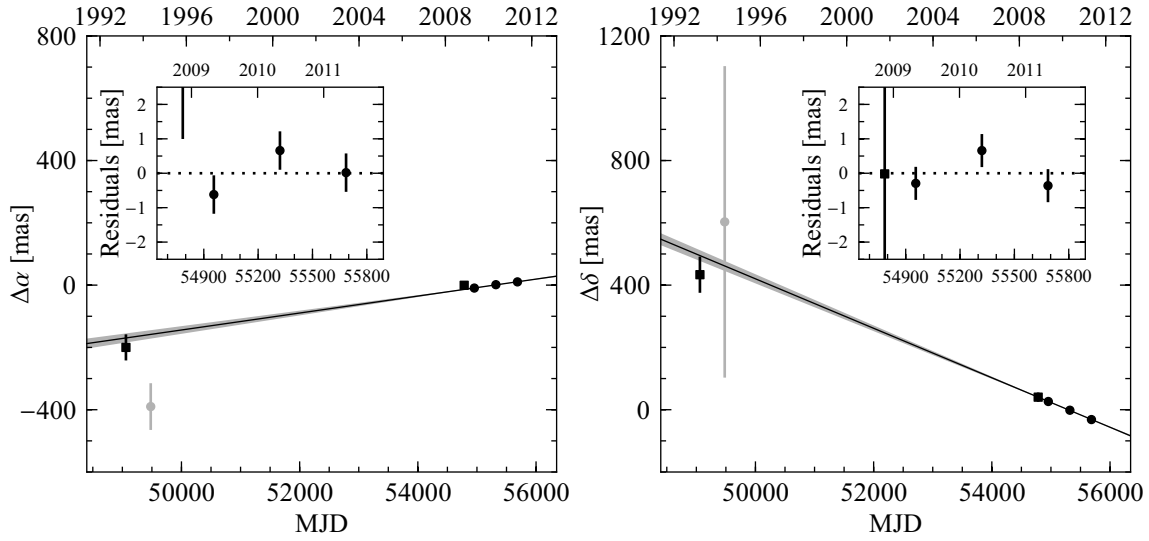


Figure 6.2: Position of PSR J1825–1446 with respect to time (MJD in lower axis and year in top axis) in right ascension (left) and declination (right). The solid black lines represent the fitted proper motion, and the grey area the uncertainty of the fit at 3- σ level. The black squares represent the VLA positions, the black circles indicate the VLBA positions, and the grey circle the position from pulsar timing (not used in the fit). The inset shows the position residuals from the fitted model for the 2008–2012 period. The source positions are plotted with uncertainties at 1- σ level.

indeed a factor 6.7 larger than the uncertainty in right ascension. Another possible source of error is the pulsar timing fit solution. Hobbs et al. (2004) fitted 197 time of arrival (TOA) data points spanning 17.4 years and obtained a proper motion of $\mu_\alpha \cos \delta = 10 \pm 18$ and $\mu_\delta = 19 \pm 115$ mas yr $^{-1}$. The fitting time residuals were 7.539 ms. If this value were underestimated, this would explain the small error in right ascension. Another possible source of error is the uncertainty in the link between the barycentric celestial reference system (BCRS) and the ICRF. However, it should be well below the 245 mas difference found between the timing position and the expected position at that epoch; for example Chatterjee et al. (2009) found differences between both reference frames below 1 mas. We have not found any clear explanation to justify the discrepancy between the right ascension position given by pulsar timing and the expected one. Given the large difference, and the intrinsic difference between an interferometric measurement and a timing fit, we have not included the timing position in our final determination of the proper motion of PSR J1825–1446, although we have included the position in Table 6.4 and Fig. 6.2 for reference.

6.3.3 Proper motion of PSR J1825–1446

To obtain the proper motion, we used the two VLA and the three VLBA observations presented above. The reference position of the phase calibrator for the VLA observations was updated to the currently known position of the phase calibrator, quoted in Sect. 6.3.1. All VLBA positions were updated according to the most recent available position⁶ of J1825–1718 $\alpha_{\text{J2000.0}} = 18^{\text{h}}25^{\text{m}}36^{\text{s}}.532278 \pm 0^{\text{s}}.00006$ (or ± 0.9 mas) and $\delta_{\text{J2000.0}} = -17^{\circ}18'49''.8482 \pm 0''.0014$ (or ± 1.4 mas). This global uncertainty of the reference source position should be included when working in the ICRF. However, in this case it is only a common offset shared by all VLBA observations. We have computed the proper motion fit using the position of J1825–1718 as a reference. This means that the 0.9 and 1.4 mas uncertainties have been included in all the non-VLBA (but not in the VLBA ones), to compute the proper motion, and it has been added afterwards to the final fitted position. All positions and uncertainties are shown in Table 6.4. We fitted the proper motion of the source as a linear model of position as a function of time for right ascension and declination separately. We fitted the data using a Levenberg-Marquardt nonlinear least-squares fit (Marquardt 1963). The solution is highly dominated by the three VLBA observations, which were performed in the same scheduled conditions (see Sect. 6.3.1). The reference epoch is computed as the weighted mean MJD, which is MJD 55291.525. The obtained astrometric parameters for PSR J1825–1446 are

$$\begin{aligned}\alpha_{\text{J2000}} &= 18^{\text{h}} 25^{\text{m}} 2^{\text{s}}.95389 (\pm 0.3 \pm 0.9 \text{ mas}), \\ \delta_{\text{J2000}} &= -14^{\circ} 46' 53''.2031 (\pm 0.3 \pm 1.4 \text{ mas}), \\ \mu_{\alpha} \cos \delta &= 10.0 \pm 0.3 \text{ mas yr}^{-1}, \\ \mu_{\delta} &= -29.0 \pm 0.3 \text{ mas yr}^{-1},\end{aligned}$$

where the first set of errors in the positions corresponds to statistical uncertainties, and the second set corresponds to the uncertainty in the phase reference position. The degrees of freedom of the fit are 4, and the reduced χ^2 is 0.95 and 0.98 in right ascension and declination, respectively.

6.4 Astrometry and proper motion of LS 5039

To fit the proper motion of LS 5039 we used new interferometric radio data together with archival radio and optical data. In this section we will only describe in detail the data reduction of three radio projects. The description of the other data used is already published, or will be published elsewhere. In particular we will describe a VLA+PT observation conducted in 2003, three VLBA observations conducted between 2004 and 2006,

⁶GSFC 2010a astro solution, from sched v10.0

6. On the origin of LS 5039 and PSR J1825-1446

Table 6.5: Parameters of the LS 5039 observations described in Sect. 6.4, parameters of the resulting images, and the total and peak flux densities measured.

MJD	Array	Freq. [GHz]	HPBW _{size} [mas ²]	HPBW _{P.A.} [°]	S_ν [mJy]	S_{peak} [mJy b ⁻¹]
52856.20	VLA+PT	15.0	148×39	23	9.6 ± 0.5	9.0 ± 0.3
53167.35	VLBA	8.5	4.5×2.2	7	10.9 ± 1.5	6.0 ± 0.6
53532.35	VLBA	8.4	2.8×1.1	6	7.1 ± 0.9	2.6 ± 0.3
53764.71	VLBA	8.4	3.2×1.0	10	4.4 ± 0.7	3.1 ± 0.3
55635.15	EVN	8.4	5.6×1.3	−15	8.0 ± 2.0	6.1 ± 1.0

and a short EVN observation conducted in 2011. The parameters of these observations are summarised in Table 6.5.

6.4.1 VLA-PT observation

We observed LS 5039 with the VLA plus the VLBA antenna in Pie Town (PT) at 15.0 GHz on August 05, 2003. We used the VLA in its A configuration plus PT, which is located at a distance of 52 km from the VLA site, and provides longer baselines with all the VLA antennas. The observation spanned from 01:00 to 08:40 UTC, and was centred at MJD 52856.2. The phase reference calibrator was J1832−1035 (1832−105), located at 4.5° from LS 5039. Two IFs of 50 MHz were used. The cycle time including the phase calibrator and the target source was 3 minutes. The ICRF source J1911−2006 (1911−201) was observed regularly during the observations. The flux calibrator was 3C 286 (1331+305). The orbital phase of the binary system at the time of the observation was 0.92, using the ephemeris from Casares et al. (2012a).

Standard reduction procedures were applied to the data, and a precise position of the source was obtained when using a uniform weighting scheme (robust −5 within AIPS), and a cellsize parameter of 5 mas. The source position, fitted with JMFIT within AIPS, has an uncertainty of 1 and 2 mas in right ascension and declination, respectively. The observational details, the obtained synthesised beam size, and the fitted components are shown in Table 6.5.

6.4.2 VLBA astrometric project

The VLBA projects BD087 and BD105 are part of a long-term astrometric project to measure the proper motion and parallax of several X-ray binaries. The segment BD087G, and the continuations BD105A and BD105G observed LS 5039 at a frequency of ∼8.5 GHz. The observations took place on June 11, 2004, June 11, 2005, and January 29, 2006, and lasted 6, 6, and 5 hours, respectively. The three observations were recorded with a total

data bit rate of 128 Mbps. In the first epoch, the data rate was distributed in 8 IF channels with a bandwidth of 4 MHz each, with one single polarisation (right circular polarisation) and two-bit sampling, while the latter two used two IF channels with 8 MHz bandwidth and dual circular polarisation, also recorded with two-bit sampling.

The phase reference source was J1825–1718, which is slightly resolved also at 8.4 GHz (although it is much more compact than at 5 GHz), and is located at 2.47° from LS 5039. The cycling time of the phase-referenced observations was three minutes. Several check sources were observed during the three epochs. In particular, the sources N1834–1433, N1819–1419, and N1818–1108 were observed in all epochs and were used to estimate the astrometric uncertainties. The fringe finder was J1733–1304. The data reduction is analogous to the one described in Sect. 6.3.1. In this case, an statistical approach to determine the best ionospheric correction was not applied, because the effect is smaller at this frequency. We note that the correction of the Earth orientation parameters was not applied to the data because it did not affect the position measurement, and therefore we preferred not to apply this additional correction to the datasets (see also Sect. 5.3).

Owing to the lower flux density of LS 5039 at 8.4 GHz, the three epochs were imaged using a weighting scheme with robust parameter 0 within AIPS, as a compromise between spatial resolution and signal-to-noise ratio. To reduce the effect of the source extended emission (see Sect. 6.4.5) we omitted the baselines with shortest uv -distances. We found a compromise between significance of the detection, and the uv -distance reduction by cutting the baselines below 20, 30, and 40 $M\lambda$ for the three epochs. For the first epoch a lower threshold was required because the data quality was worse. On the other hand, the longest baselines had to be softened because of the poor quality of the partially resolved phase reference source. We reduced the weight of baselines longer than a certain value. For the first epoch we used a tapering parameter of 60 $M\lambda$. For the latter two projects, the tapering was at 120 $M\lambda$. The resulting resolution and fitted components are shown in Table 6.5.

6.4.3 EVN observations

The most recent VLBI observation of LS 5039 was performed with the European VLBI Network (EVN). We observed several sources around LS 5039 to search for possible phase calibrators and in-beam calibrators, and test the longest EVN baselines to check the viability of an astrometric project. Among other sources, we observed the phase calibrator J1825–1718, also used in the previously described VLBI observations. The observations were conducted on March 15, 2011, between UTC 02:00 and 05:00. We only observed 11 scans on LS 5039, bracketed by scans on the phase calibrator with a cycling time of 3.4 minutes and distributed along the observation. The total time on-source was approximately 20 minutes. The antennas included in the observation were Effelsberg, Westerbork, Onsala, Medicina, Yebes, Svetloe, Badary, Zelenchukskaya, Nanshan (Urumqi), Sheshan (Shanghai), and Hartebeesthoek. The data were recorded with a total data bit rate of

1024 Mbps, providing a high-sensitivity array. The correlated parameters are eight IF channels with both circular polarisations, each of them with 16 MHz bandwidth (provided by 32 frequency channels of 500 kHz), and two-bit sampling.

The data reduction is analogous to the one described in Sect. 6.3.1 and Sect. 6.4.2. No useful FRING solutions were found between Hartebeesthoek and the rest of the antennas, which considerably reduced the North-South array extent, and therefore the resolution in declination on the final image. After the phase calibration from J1825–1718, the North-South maximum baseline was of about 20–40 M λ , while in the East-West direction it was of 160–180 M λ , although large gaps were present in the uv -plane due to the short observation time. We note that large phase instabilities appeared due to the low declination of the source. We finally imaged the source with robust parameter 0, minimum uv -distance set to 15 M λ , and uv -taper set to 120 M λ . Even with the long maximum baselines, the final synthesised beam size is 5.6×1.3 mas² in P.A. of -15° . The resolution of the images and the fitted components are shown in Table 6.5.

6.4.4 Archival data of LS 5039

Astrometry of LS 5039 can be obtained from two types of observations. On one hand we have positions from optical observations of the main star of the system. This observations, coming from large (and global) astrometric projects, cover a long time, of the order of decades, although they provide limited astrometric accuracy of about 10–300 mas. On the other hand, radio interferometric observations provide observations of the radio nebula around the binary system. These observations have been obtained in the last ~ 10 years, but their uncertainties are between 1 and 10 mas. The time span of the optical observations can be combined with the precise radio positions to fit an accurate position and proper motion of the source. However, combining datasets with considerable different properties brings important caveats that have to be taken into account. These will be described in Sect. 6.4.6. The astrometry described here is summarised in Table. 6.6. The corresponding orbital phases were computed using the ephemerides in Casares et al. (2012a).

Archival optical astrometry of LS 5039

Optical observations of LS 5039 are available from historical photographic catalogues since 1905. Updated global solutions have been obtained for the historical photographic plates by using more recent reference catalogues. The updated versions of the classical catalogues provide improved systematic uncertainties on the star position. However, some newer versions combine catalogues from different epochs to fit a global solution that considers the proper motion of the stars. Therefore, they are not suitable for our proper motion determination because they are not independent, and they include a proper motion estimation in their own position fitting. This is the case, for example, of the Palomar Observatory Sky Survey plates used to produce the USNO-A2.0 catalogue (Monet 1998), which uses only the blue and red original plates, while the new version of the catalogue, USNO-B1.0

Table 6.6: Astrometry and fit residuals of LS 5039 for optical and radio projects.

Project	MJD	Epoch Y-M-D	ϕ_{orb}	α_{J2000} [h, m, s]	$\sigma_{\alpha \cos \delta}$ [mas]	δ_{J2000} [$^{\circ}$, $'$, $''$]	σ_{δ} [mas]	Res. $_{\alpha \cos \delta}$ [mas]	Res. $_{\delta}$ [mas]
AC2000.2 (O)	17408.47	1906-07-17	0.8(2)	18 26 15.015(8)	120	-14 50 53.27(11)	110	40	160
USNO-A2.0 (O)	33857.61	1951-07-30	0.0(1)	18 26 15.034(17)	260	-14 50 53.59(25)	250	10	230
TAC2.0 (O)	44050.66	1979-06-26	0.57(5)	18 26 15.056(5)	80	-14 50 54.08(5)	50	140	-8
GSC1.2 (O)	46669.35	1986-08-27	0.99(4)	18 26 15.06(2)	300	-14 50 54.3(3)	300	80	-145
Tycho-2 (O)	48559.95	1991-10-30	0.01(3)	18 26 15.043(10)	150	-14 50 54.23(12)	120	-150	-55
AP357 (R)	50913.00	1998-04-10	0.43(2)	18 26 15.0559(7)	10	-14 50 54.240(10)	10	5.5	-8.1
2MASS (O)	51401.02	1999-08-11	0.37(2)	18 26 15.056(4)	60	-14 50 54.23(6)	60	-7.3	18
UCAC1 (O)	51649.00	2000-04-15	0.85(2)	18 26 15.0563(9)	13	-14 50 54.277(13)	13	-2.9	-28
GR021A (R)	51698.40	2000-06-03	0.49(2)	18 26 15.05645(10)	1.5 ^a	-14 50 54.2512(15)	2 ^b	-1.6	-0.5
AP453 (R)	52856.20	2003-08-05	0.92(2)	18 26 15.05812(11)	1.6	-14 50 54.280(2)	2	1.0	-1.6
BD087G (R)	53167.35	2004-06-11	0.58(2)	18 26 15.05831(14)	2 ^a	-14 50 54.2865(20)	2 ^b	-2.3	-0.7
BD105A (R)	53532.35	2005-06-11	0.02(2)	18 26 15.05890(8)	1.3 ^a	-14 50 54.2964(14)	1.4 ^b	-0.4	-1.7
BD105G (R)	53764.71	2006-01-29	0.51(2)	18 26 15.05916(7)	1.1 ^a	-14 50 54.2996(12)	1.2 ^b	-1.1	0.6
EF018A-C (R)	54160.71	2007-03-01	0.89(2)	18 26 15.0597(2)	4 ^a	-14 50 54.3092(12)	1.2 ^b	-0.2	0.5
BR127A-E (R)	54290.27	2007-07-09	0.06(2)	18 26 15.06003(8)	1.3 ^a	-14 50 54.3096(12)	1.2 ^b	1.8	3.3
EM085 (R)	55635.15	2011-03-15	0.37(2)	18 26 15.06184(8)	1.3 ^a	-14 50 54.3452(20)	2.0 ^b	2.7	-0.2
BC196 (R)	55803.13	2011-08-30	0.37(2)	18 26 15.06188(7)	1.1 ^a	-14 50 54.3511(14)	1.4 ^b	1.4	-2.0

Notes: ^a An additional uncertainty of 0.9 mas in right ascension due to the global astrometry errors on the phase-reference source position should be included when considering this position in the ICRF. ^bThe phase-reference source has an additional uncertainty of 1.4 mas in declination in the ICRF.

6. On the origin of LS 5039 and PSR J1825-1446

(Monet et al. 2003), with better uncertainties, uses data from 1949 to 2002, combined using a proper motion of 4, and -14 mas yr^{-1} in right ascension and declination, respectively. It is also the case of GSC 1.2 compared to the newer versions (GSC 2.2 and GSC 2.3.2), or UCAC1 when compared to UCAC2 and UCAC3, which have improved references and systematic error treatment. Therefore, although new catalogues are currently available, we have used only the versions that are not compilation catalogues. This means that most of the optical values used here were already available at the time of writing of Ribó et al. (2002b).

In particular, for the proper motion determination we used the following catalogues. AC2000.2 is the second version of the Astrographic Catalog 2000 and provides accurate optical positions of LS 5039 on 1906 in Hipparcos Celestial Reference System (HCRS, coincident with J2000.0). USNO-A2.0 contains a global reduction of the data in the Palomar Observatory Sky Survey plates obtained around 1950. The Twin Astrographic Catalog version 2 (TAC 2.0) provides a position based on four observations (the plates were compiled between 1977 and 1986). Following Ribó et al. (2002b), we included an additional uncertainty of 15 mas in each coordinate, as suggested in Zacharias et al. (1999). We also used the Guide Star Catalog (GSC) version 1.2, which consists of a single-epoch collection of $6.4^\circ \times 6.4^\circ$ Schmidt plates (the newer versions of the catalog are compiled, and proper motions are fitted using Tycho positions). The GSC position is less relevant for the fit because of the relatively large errors (300 mas) for a position obtained in 1986. The Tycho-2 Catalog was obtained from the Tycho star mapper observations of the ESA *Hipparcos* satellite (Høg et al. 2000). It provides the mean position at epoch J2000, corrected from proper motion, as well as the observed position, which is the one used in our analysis. Following Ribó et al. (2002b), we have used the conservative error estimate of $\sigma_\alpha \cos \delta = 149 \text{ mas}$ and $\sigma_\delta = 120 \text{ mas}$. Skrutskie et al. (2006) detected LS 5039 at near-infrared bands with the all-sky Two Micron All-Sky Survey (2MASS), and a very precise position was obtained. The three observed bands (J , H , and K_s) were tied with the Tycho-2 Reference Catalog, so it is in the ICRS frame. Finally, accurate astrometry of LS 5039 can be found in the latest versions of the US Naval Observatory CCD Astrograph Catalog (Zacharias et al. 2010). However, we can only use the position from the UCAC1 version (Zacharias et al. 2000). All these optical positions and their uncertainties are quoted in Table 6.6.

Archival radio astrometry of LS 5039

The binary system LS 5039 is a known radio emitter discovered by Martí et al. (1998). Since then, several radio interferometric observations have been conducted to study its morphological and spectral properties at different orbital phases. Here we list the radio projects in which the system has been observed with sufficient resolution to provide an accurate position of the source. In particular, it has been observed with the VLA, the VLBA and the EVN at frequencies between 5 and 15 GHz. Observations at lower frequencies

with the VLA are excluded because they provide positions with uncertainties above $0''.1$ for relatively recent epochs, and do not contribute to the proper motion fit when compared to the 1–10 mas accuracy of the other radio observations.

We briefly summarise the observations included in the fit. Martí et al. (1998) conducted a multi-epoch and multi-frequency project of the system with the VLA at four frequencies between 1 and 15 GHz. They provided a single position derived from the 15 GHz data obtained with the highest resolution configuration (A) of the VLA. The reference source was the ICRF source J1911-2006 (1911-201), and their error estimate is 10 mas. The source was next observed with the VLBA and the VLA for two epochs in June 2000 at 5 GHz (Ribó et al. 2008). Only one of the two epochs provides good astrometry. The source was also observed with the EVN within project EF018 in March 2007. The project consists of three observations at 5 GHz, observed every two days. The low elevation of LS 5039 during the observations affects the phase calibration of the data and therefore the astrometry. To obtain a reliable position, we removed the data with the lowest elevations and then averaged the three measurements. The uncertainty of this position was computed as the standard deviation of the three runs. We conducted a similar project, observing the source with the VLBA during five consecutive days in July 2007 at 5 GHz (see details in Moldón et al. 2012a). A similar procedure was used in this case, computing the average position of the source from the five images produced with uniform weighting. Finally, we used a recent position obtained within the VLBA large project BC196⁷ (PI: J. Condon), whose solutions are available online. The positions, uncertainties (see the overview in Condon et al. 2011), and residuals with respect to the final proper motion fit are shown in Table 6.6.

6.4.5 Uncertainties in the position of LS 5039

LS 5039 is known to be extended at mas scales, and a bipolar jet-like structure is present in all VLBI (VLBA and EVN) radio observations of the source (Paredes et al. 2000, 2002; Ribó et al. 2008; Moldón et al. 2011d, 2012a). Although the source displays a bright core, we do not know the offset between the peak of the radio core and the position of the binary system. There are two main reasons. First, the particles accelerated in the system travel distances much longer than the system orbit, and the location of the peak of the emission at any moment depends on the physical conditions (basically the electron distribution, and the synchrotron cooling time). Second, for each observed frequency, each interferometer array is sensitive to different ranges of spatial scales, therefore inter-comparison is not straightforward because we are seeing different regions of the particle flow. In summary, the unknown position of the system within the radio outflow is variable (at time scales of 1 or more days), and depends on the observed frequency and array. We tried to minimise this effect by measuring positions derived from the uniformly weighted images, which trace the most compact emission from the core component of the source.

⁷<https://science.nrao.edu/observing/largeproposals/blackholesearch/>

Preliminary fits of the position and proper motion of LS 5039 using the formal astrometric errors of the radio positions yielded reduced χ^2 of 4.1 and 2.3 in right ascension and declination, respectively, which indicated that a linear model did not completely describe the source positions. This means that the formal astrometric errors for the radio observations underestimate our real knowledge of the position of the binary system within the radio emission. A shift on the peak of the emission was observed in LS I +61 303, PSR B1259–63, and HESS J0632+057 (Dhawan et al. 2006; Moldón et al. 2011a,c). Based on these observations, and the estimations in Dubus (2006) and Bosch-Ramon & Khangulyan (2011), we expect the peak of the emission to follow an ellipse with semimajor axis of about ~ 1 mas, although the size should depend on the frequency, and should be larger at low frequencies. It is not possible to measure this unknown deviation with the current resolution and data sampling, especially when observing at different frequencies and resolutions. Therefore, we increased the position uncertainty of the radio positions to compensate our ignorance of this time-dependent offset. In particular, we added in quadrature an *ad-hoc* uncertainty of 1.0 mas to all radio positions before performing the fit. This uncertainty is already included in Table 6.6.

Another source of uncertainty is the systematic errors on the position of the phase calibrators, which are the reference of the measured positions. Fortunately, the phase reference calibrator for all VLBI observations was J1825–1718. Although the calibrator was correlated at different positions, we have shifted all measurements to the common reference position quoted in Sect. 6.3.3. We followed the same procedure as with PSR J1825–1446, and these uncertainties were not included in the proper motion determination, but were added afterwards to the final fitted position.

We also included the effect of the annual parallax of LS 5039, assuming a distance of 2.9 kpc, which corresponds to a deviation of 0.3 mas. The equations governing the parallax displacements can be found, for example, in Brisken et al. (2002) and Loinard et al. (2007). The additional displacements were added to the data before performing the fit, and are not included in Table 6.6.

6.4.6 Proper motion of LS 5039

We fitted the reference position and the proper motion to the data in right ascension and declination independently for the 16 positions available, using the Levenberg-Marquardt nonlinear least-squares fit. The reference epoch for the fit, computed as the weighted mean of the dates of observations, is MJD 53797.064. The resulting astrometric parameters for LS 5039 are

$$\begin{aligned}
\alpha_{\text{J2000}} &= 18^{\text{h}} 26^{\text{m}} 15^{\text{s}}.05927 (\pm 0.5 \pm 0.9 \text{ mas}), \\
\delta_{\text{J2000}} &= -14^{\circ} 50' 54''.3010 (\pm 0.5 \pm 1.4 \text{ mas}), \\
\mu_{\alpha} \cos \delta &= 7.10 \pm 0.13 \text{ mas yr}^{-1}, \\
\mu_{\delta} &= -8.75 \pm 0.16 \text{ mas yr}^{-1},
\end{aligned}$$

where the first set of errors in the positions corresponds to statistical uncertainties, and the second set corresponds to the uncertainty in the phase reference position. The reduced χ^2 of the right ascension and declination fits were 0.75 and 1.35, respectively. The positions, fit, and uncertainties are shown in Fig. 6.3. The solution is dominated by the radio observations, but the optical observations provide better stability to the fit. We note that the effect of the parallax correction on the data is small. If the correction is not included, the reduced χ^2 in right ascension increases by 0.02, and does not change in declination. We also tried to fit the parallax to the data, with and without the *ad hoc* 1 mas uncertainty, but the parallax is too small to be measured with the current data.

Determination of systematic uncertainties

To better understand the systematic fit uncertainties, we analysed the distribution of fit solutions following a procedure similar to the one discussed in Chatterjee et al. (2009). The bootstrap method used consists of fitting the proper motion and reference position from different samples of the available positions. For each iteration we randomly selected 16 positions, with replacement, and produced a proper motion fit. By repeating the fit for different combinations of positions, we obtained a probability distribution of proper motions obtained with all possible combinations of the data. The probability distribution functions (PDF) and the cumulative distribution functions (CDF) of these PDFs are plotted in Fig. 6.4. The distributions were computed with a bin width of 0.01 mas yr^{-1} . The number of iterations (different combinations with replacement) is 2×10^7 , which is more than necessary to smoothly cover the one-dimensional range of values, but it is required for the 2D distribution (see below). The shaded grey areas in Fig. 6.4 indicate the minimum regions containing the 68.2, 95.4 and 99.7% of the samples, from darker to lighter, respectively. The best-fit value of the proper motion can be computed in two ways: as the mode of the distribution (value that occurs most frequently), which is marked as the vertical line in the top panels, or as the value that accumulates the 50% of the events (the median), which is marked as the vertical line in the bottom panels of Fig. 6.4. These two values are not identical, but the difference is well below the $1\text{-}\sigma$ uncertainty of the proper motion estimation. We can clearly see that the distribution is approximately Gaussian at the central region, but it shows considerable asymmetric wings. The mode and the confidence intervals are $\mu_{\alpha} \cos \delta = 7.09_{-0.11}^{+0.19} \text{ mas yr}^{-1}$ and $\mu_{\delta} = -8.82_{-0.12}^{+0.27} \text{ mas yr}^{-1}$.

6. On the origin of LS 5039 and PSR J1825-1446

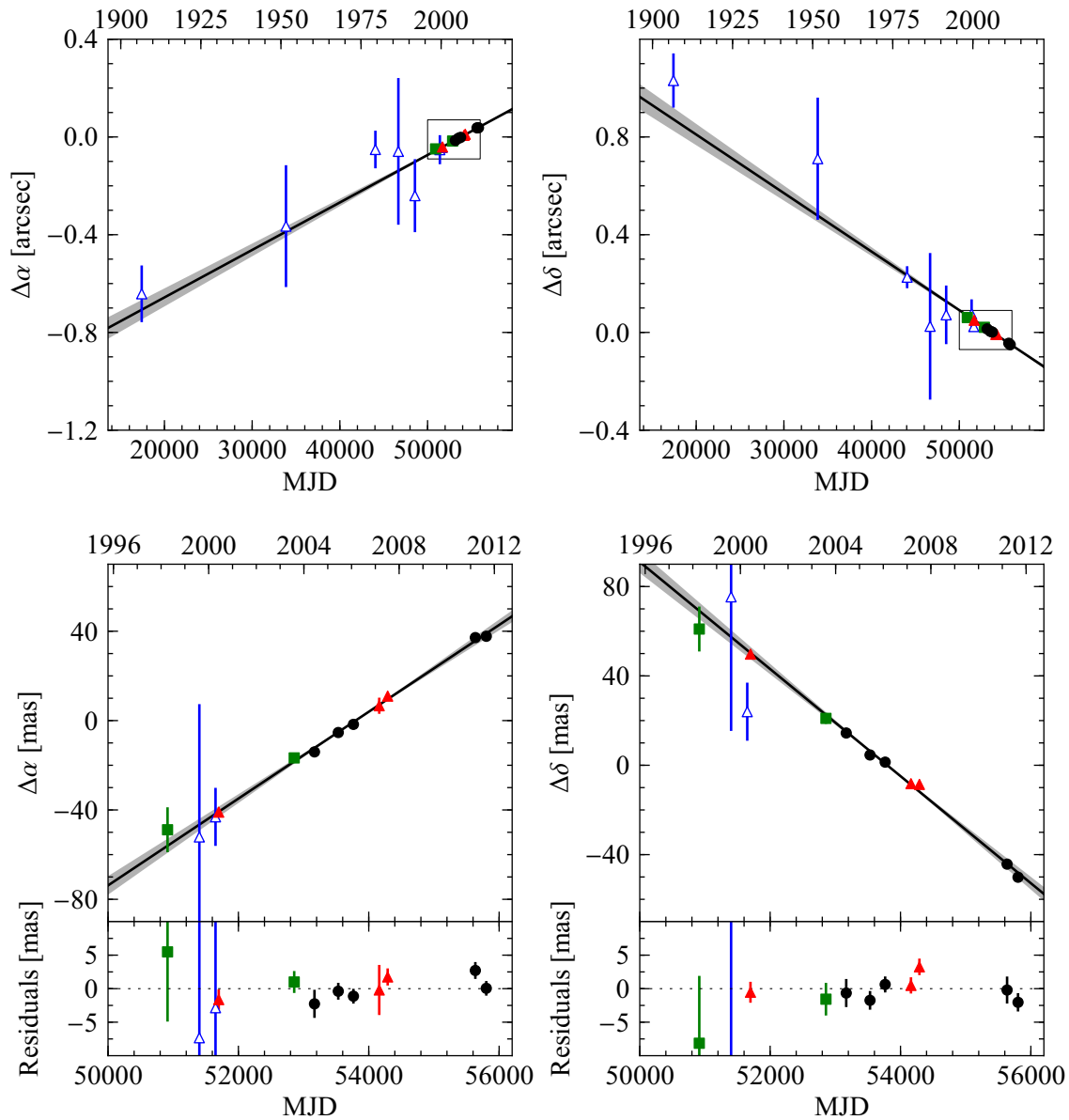


Figure 6.3: Offsets in right ascension (left) and declination (right) of LS 5039 with respect to time in MJD and year. The solid black lines in each panel represent the fitted proper motion, and the grey area the uncertainty of the fit at 3σ level. The upper panels include all data points used for the fit, and the lower panels are the zoom of the last 16 years (marked by the small rectangles), and include the residuals with respect to the fitted model. The empty blue triangles represent the optical data, the green squares show the VLA data, the red triangles correspond to the VLBI observations at 5 GHz, and the black circles are the VLBI data at 8.6 GHz. The source positions are plotted with uncertainties at 1σ level.

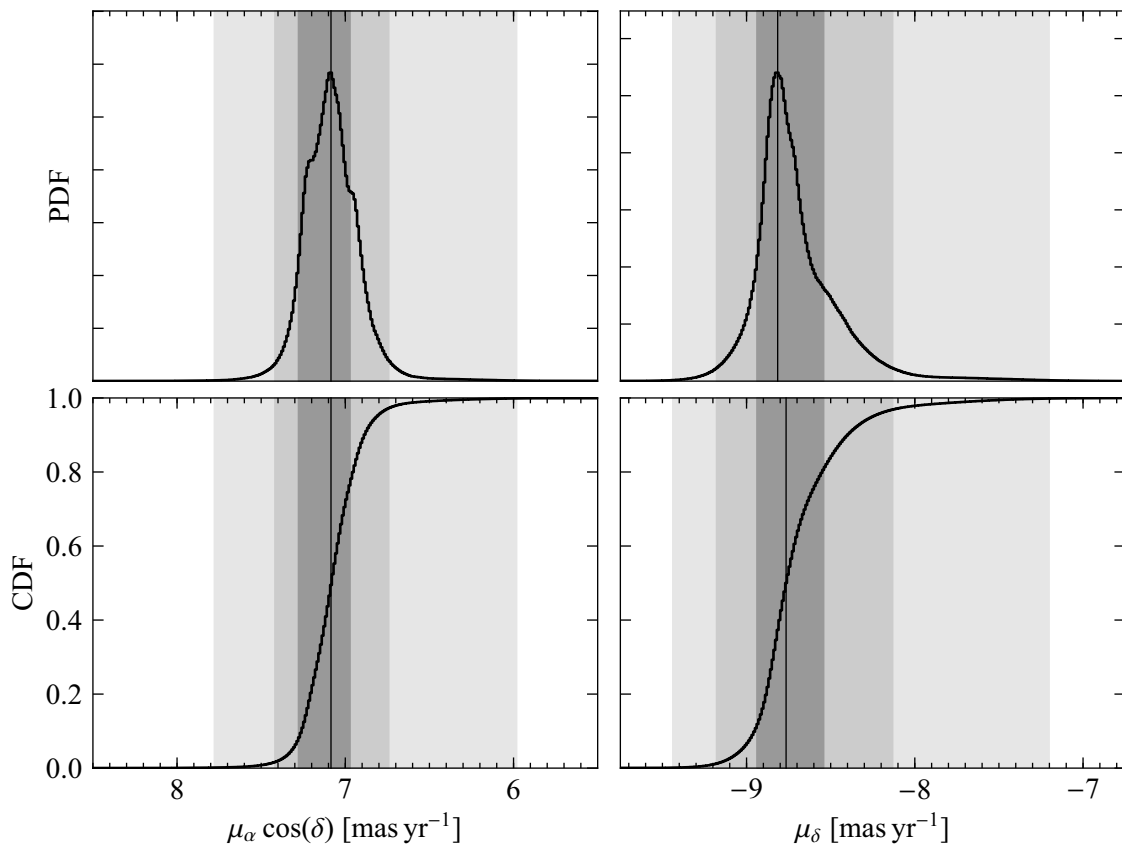


Figure 6.4: *Top*: distribution of proper motion fit results for LS 5039 estimated with the bootstrap method, which is equivalent to an un-normalised probability distribution function (PDF) for right ascension and declination independently. *Bottom*: corresponding cumulative distribution functions (CDF). For all panels, the grey shaded areas correspond to the minimum region that includes the 68.2, 95.4 and 99.7% of the events, from dark grey to light grey. The vertical line marks the most common value (the mode) for the PDF distributions, and the value covering the 50% of the events for the CDF.

Owing to the asymmetry in the distributions of Fig. 6.4 we computed the 2D distribution of proper motions obtained with the bootstrap method in right ascension and declination simultaneously to better identify any other correlation or asymmetry between the confidence regions. The simulated fit results were gridded with a bin size of 0.01 mas yr^{-1} in both directions. The minimum regions covering the 68.2, 95.4 and 99.7% of the events were obtained, and they were smoothed with a Gaussian filter with a size of 18 bins. The corresponding confidence regions are shown in Fig. 6.5. We can see that the distribution is clearly skewed towards lower values of μ_δ and more moderately to lower values of $\mu_\alpha \cos \delta$.

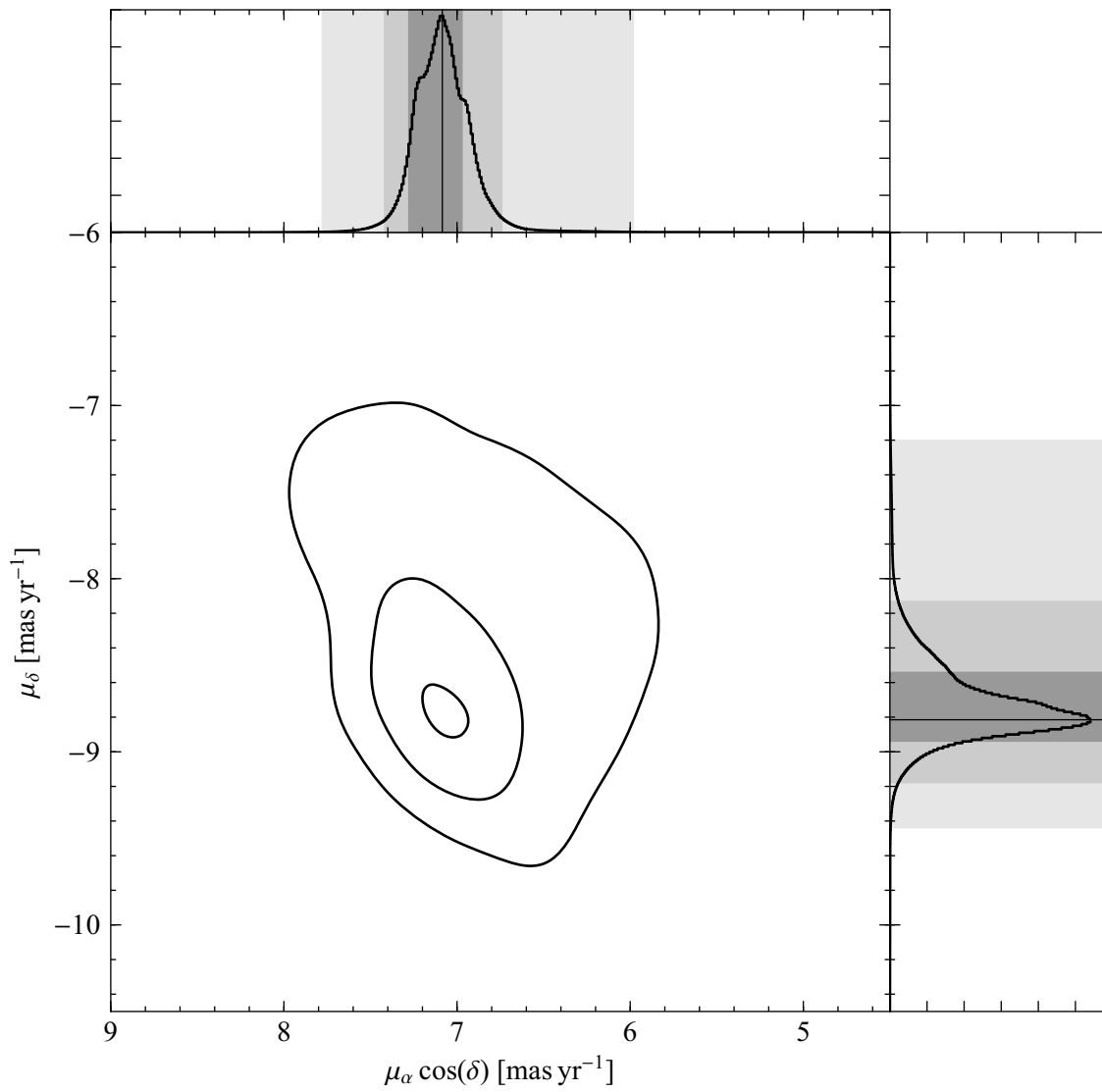


Figure 6.5: Distribution of proper motion fits for LS 5039 computed with the bootstrap method. The central contours represent, from inside to outside, the minimum smoothed regions containing 68.2, 95.4, and 99.7% of the events. The two histograms are the projected 1D distributions shown in Fig. 6.4.

6.5 Galactic space velocity

We can now study the Galactic space velocity of LS 5039 and PSR J1825–1446, following the work in Ribó et al. (2002b), Dhawan et al. (2007), and Miller-Jones et al. (2009a). The space velocity of each source can be obtained by combining the proper motion and the radial velocity of the source (optical systemic velocity, γ , in velocity light curves) to form a space velocity vector $(\mu_\alpha \cos \delta, \mu_\delta, \gamma)$. This velocity can be rotated to the cartesian coordinates U , V , W , defined as U positive towards the Galactic Centre, V positive towards $l = 90^\circ$ (sense of the Galactic rotation), and W positive towards the North Galactic Pole (NGC). The rotation is described in Johnson & Soderblom (1987), although we used the updated definition of the North Galactic Pole direction from Reid & Brunthaler (2004) (the direction of the NGP is $\alpha_p^{J2000.0} = 12^{\text{h}}51^{\text{m}}26^{\text{s}}.282$ and $\delta_p^{J2000.0} = +27^\circ07'42''.01$, with the zero longitude at $\theta_0^{J2000} = 122^\circ.932$). We computed the heliocentric Galactic space velocity by subtracting the peculiar velocity of the Sun with respect to the local standard of rest (LSR). We used the recent determination from Schönrich et al. (2010) of $U_\odot = 11.1_{-0.75}^{+0.69}$, $V_\odot = 12.24_{-0.47}^{+0.47}$, $W_\odot = 7.25_{-0.36}^{+0.37}$ km s⁻¹. We note that V_\odot is significantly larger than in previous estimations. The obtained heliocentric Galactic velocities $(U, V, W)_{\text{LSR}}$ for LS 5039 and PSR J1825–1446 are shown in Table. 6.7.

We note that the distance to the source is the highest source of error when converting from angular to linear velocities. We used the most recent determination of the distance to LS 5039, 2.9 ± 0.8 kpc (Casares et al. 2012a). The distance to PSR J1825–1446 is 5.0 ± 0.6 kpc. The first set of errors in the Galactic velocities in Table 6.7 corresponds to the proper motion uncertainty, and the second set of errors corresponds to the contribution of the distance uncertainty.

We can now compute the Galactic space velocity as measured from the Galactic Centre (GC). We need to transform the velocity vector to the reference frame of an observer situated at the position of the source that participates in the Galactic rotation. This reference frame is the regional standard of rest (RSR). The transformation from the LSR to the RSR takes into account the distance from the Sun to the GC, 8.0 ± 0.5 kpc (Reid 1993), and the circular rotation about the GC, 236 km s⁻¹ (Reid & Brunthaler 2004), which we consider constant. From the Galactic velocity $(U, V, W)_{\text{RSR}}$, we directly obtain the Galactocentric velocity of a source, with the radial velocity v_{rad} away from the GC, v_{cir} , in the direction of the Galactic rotation at each point, and v_z , perpendicular to the Galactic Plane, and positive towards the NGP. The expected velocity of a system following the Galactic rotation is zero for v_{rad} and v_z , whereas v_{cir} is expected to be 236 km s⁻¹. The deviation from the expected circular rotation is the peculiar velocity $v_{\text{pec}} = [v_{\text{rad}}^2 + (v_{\text{cir}} - 236 \text{ km s}^{-1})^2 + v_z^2]^{1/2}$. The Galactic velocities from the GC for LS 5039 and PSR J1825–1446 are shown in Table. 6.7.

The large error in the distance of the sources limits the determination of their space velocities. In this case it is convenient to plot the Galactic velocities as a function of the distance from the Sun. In Figs. 6.6 and 6.7 we show the computed velocities (black lines)

6. On the origin of LS 5039 and PSR J1825-1446

Table 6.7: Galactic coordinates and Galactic space velocities of LS 5039, and PSR J1825–1446. In the Galactic velocities, the first set of errors corresponds to the proper motion uncertainty, while the second set (in parentheses) corresponds to the distance uncertainty.

Parameter	LS 5039	PSR J1825–1446
Galactic Longitude l	16°882	16°805
Galactic Latitude b	-1°289	-1°001
Distance d (kpc)	2.9 ± 0.8	5.0 ± 0.6
$\mu_\alpha \cos \delta$ (mas yr ⁻¹)	$7.09^{+0.19}_{-0.11}$	10.0 ± 0.3
μ_δ (mas yr ⁻¹)	$-8.82^{+0.27}_{-0.12}$	-29.0 ± 0.3
Sys. velocity (γ) (km s ⁻¹)	17.2 ± 0.5	–
μ_l (mas yr ⁻¹)	$-4.50^{+0.25}_{-0.12}$	-21.0 ± 0.3
μ_b (mas yr ⁻¹)	$-10.38^{+0.21}_{-0.11}$	-22.4 ± 0.3
U_{LSR} (km s ⁻¹)	$42.5^{+1.0}_{-1.3} (\pm 4)$	$146 \pm 2 (\pm 16)$
V_{LSR} (km s ⁻¹)	$-43^{+3}_{-1.6} (\pm 17)$	$-466 \pm 7 (\pm 60)$
W_{LSR} (km s ⁻¹)	$-136^{+2}_{-2} (\pm 40)$	$-523 \pm 7 (\pm 60)$
v_{rad} (km s ⁻¹)	$-11.2^{+1.1}_{-1.4} (\pm 5)$	$227 \pm 3 (\pm 40)$
v_{cir} (km s ⁻¹)	$197^{+3}_{-1.6} (\pm 17)$	$-150 \pm 6 (\pm 60)$
v_z (km s ⁻¹)	$-136^{+2}_{-2} (\pm 40)$	$-523 \pm 7 (\pm 60)$
v_{pec} (km s ⁻¹)	$142^{+2}_{-2} (\pm 40)$	$690 \pm 7 (\pm 60)$

and their uncertainties (dark grey areas) for a range of distances. The horizontal dashed lines mark the expected velocity when following the Galactic rotation. The grey areas indicate the cosmic velocity dispersion of the Galactic young disc stars, which depends on the age of the stellar system. LS 5039 is an O-type star and its companion could have been more massive.

The progenitor of PSR J1825–1446 is unknown, but collapse to form a neutron star usually occurs for stars with total mass between 8 and 15 M_{\odot} (Lyne & Graham-Smith 2005). Therefore, we assumed that the progenitor was a young star formed in the Galactic thin disc. The measured velocity dispersion of young OB stars is biased towards local values because the stars with known 3D velocities and radial distances are predominantly located in the solar neighbourhood. However, the velocity dispersion of young stars should follow the velocity dispersion of the gas in the Galactic disc. This dispersion is of about 4–5 km s^{-1} in the plane (σ_U, σ_V) , and can be as low as 1–2 km s^{-1} in the direction perpendicular to the plane (σ_W) , although spiral shocks can induce higher in-plane velocities of about $\sim 7 - 10 \text{ km s}^{-1}$ (Kim et al. 2006). This agrees with values measured in Torra et al. (2000) for stars of 0–30 Myr of $(\sigma_U, \sigma_V, \sigma_W) = (7.9, 7.2, 4.3) \text{ km s}^{-1}$. We assume that the expected velocity dispersion of young stars is $(\sigma_U, \sigma_V, \sigma_W) = (10, 10, 5) \text{ km s}^{-1}$.

We can see in Fig. 6.6 that LS 5039 has a high peculiar velocity, mainly perpendicular to the Galactic plane, and it is not compatible with the expected velocity dispersion for any of the considered distances. This reaffirms the runaway nature of the system, which was originally discussed in Ribó et al. (2002b). On the other hand, PSR J1825–1446 shows a much higher space velocity. This is an isolated pulsar, and therefore it is not possible to measure any radial velocity from the Sun. In Fig. 6.7 we show the Galactic velocities assuming a radial velocity of 0, +500, and -500 km s^{-1} (black, red, and blue lines, respectively). This covers a generous range of possible radial velocities. We note that this contribution is less notorious in the direction perpendicular to the Galactic Plane because both the pulsar and the Sun are at a similar distance from the Galactic plane. For PSR J1825–1446 we plot a wide range of distances, considering that the distance estimate could be overestimated by the DM determination. The pulsar space velocity is not compatible with the expected rotation of the Galaxy. Remarkably, the pulsar has a velocity perpendicular to the Galactic Plane of $\sim 550 \text{ km s}^{-1}$ and away from it. Therefore, PSR J1825–1446 is clearly a runaway pulsar that has been ejected from the Galactic disc at a very high speed. The transverse peculiar velocity for the nominal distance of 5.0 kpc is $690 \pm 7 \text{ km s}^{-1}$. This transverse velocity is high even for a runaway isolated pulsar, because it lays in the tail of the transverse velocity distribution of young pulsars shown in Hobbs et al. (2005). The transverse peculiar velocity would be lower if the distance is overestimated, and would be $500 \pm 5 \text{ km s}^{-1}$ for a distance of 3.6 kpc.

6. On the origin of LS 5039 and PSR J1825-1446

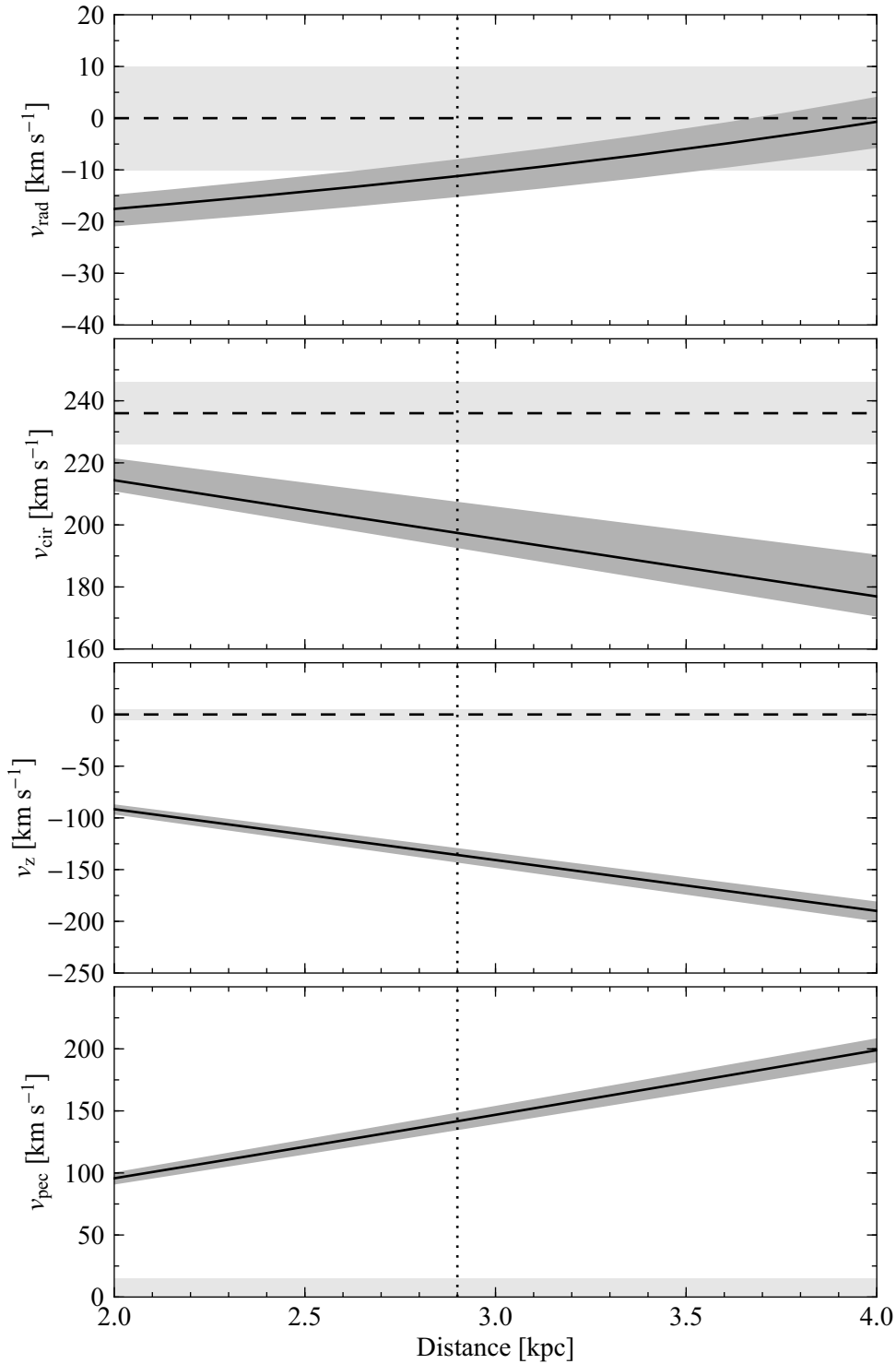


Figure 6.6: Components of the Galactic and peculiar velocity of LS 5039 (solid black lines) and their uncertainties at 3- σ level (dark grey areas). The horizontal dashed lines and light grey areas mark the expected Galactic velocity, and the velocity dispersion expected for young stars, respectively. The vertical dotted lines indicate the measured distance to the source.

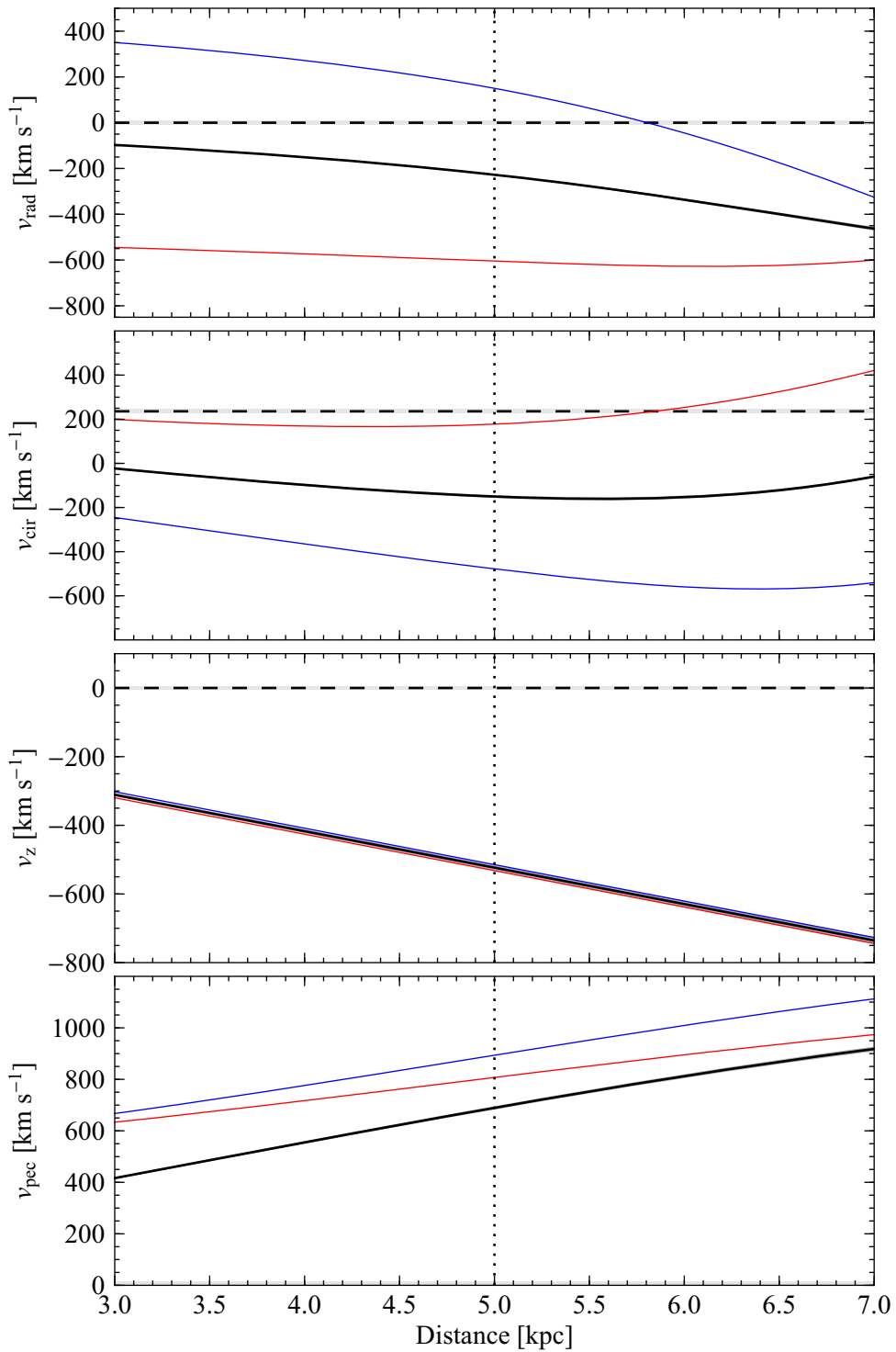


Figure 6.7: Same as Fig. 6.6 for PSR J1825–1446. The solid black line in each panel indicates the Galactic velocity assuming a radial velocity of 0 km s^{-1} . The velocity uncertainties at $3\text{-}\sigma$ level are smaller than the black lines. The red thin line corresponds to an hypothetical radial velocity from the Sun of $+500 \text{ km s}^{-1}$ (away from the Sun) and the blue thin line to -500 km s^{-1} (towards the Sun).

6.6 The origin of LS 5039 and PSR J1825–1446

LS 5039 is a young O6.5 main sequence star, which has a total lifetime of a few million years. This sets an upper limit to the age of the binary system LS 5039/compact object, which allows us to constrain the possible locations where the supernova took place, and therefore where the system originated. We have explored possible origins of LS 5039 in the last 1–10 Myr, even though for ages older than 1–2 Myr the source birthplace lies well outside the Galactic plane, which is unlikely. Therefore, we only consider the projected past trajectory of LS 5039 during the last $\sim 10^6$ yr, and discuss possible associations that cross this trajectory. On the other hand, we know that the characteristic age of PSR J1825–1446 is 1.95×10^5 yr. This value is computed as the ratio between the period and the period derivative of the pulsar, and it is valid under certain assumptions: the initial spin period of the pulsar was much shorter than that observed today ($P_0 \ll P$), there is no magnetic field decay ($P\dot{P}$ is constant), and the energy loss corresponds to a spinning dipolar magnet in perfect vacuum. The slowdown model of a pulsar is generally parametrised by the braking index, which is usually considered close to 3, although it can take a range of values (see Faucher-Giguère & Kaspi 2006). The uncertainty on this parameter prevents the characteristic age from being a faithful estimate. It has been shown that the characteristic age of a pulsar can be significantly lower than the true age of the pulsar (e.g. Gaensler & Frail 2000) or even higher than the real age of the pulsar (e.g. Kramer et al. 2003). Therefore, a wide range of ages, and consequently possible angular distances from the current location of the pulsar, should be explored.

In Fig. 6.8 we show the region around the current position of the gamma-ray binary LS 5039 and the isolated pulsar PSR J1825–1446 (green and red crosses, respectively) in Galactic coordinates. We also plot different objects related with young stars. The ellipses in green, red, and blue mark the positions of the supernova remnants, the open clusters and the OB associations, respectively. To have a better context of the distribution of young systems, we include the O and B stars, the star-forming regions, and the H II regions in this part of the Galactic plane. The past trajectories in the last 10^6 yr for LS 5039, and 1.95×10^5 yr for PSR J1825–1446 are indicated by the green and red continuous lines, respectively. The plotted trajectories are linear, and therefore not affected by the Galactic potential. We checked the validity of this assumption using the software package *galpy*⁸ to compute the trajectories under a standard Milky Way potential (combination of a Miyamoto-Nagai disc, a Navarro-Frenk-White halo, and a Hernquist bulge potentials, see the documentation for details). For all aspects discussed in this Section the slight difference between the integrated orbit in the Galactic potential and the free (linear) trajectory are irrelevant. Therefore, we do not use the orbit integration to avoid using additional parameters to describe the Galaxy. We used the software to check that the space velocity of PSR J1825–1446 is above the escape velocity, and therefore it will be

⁸<https://github.com/jobovy/galpy>

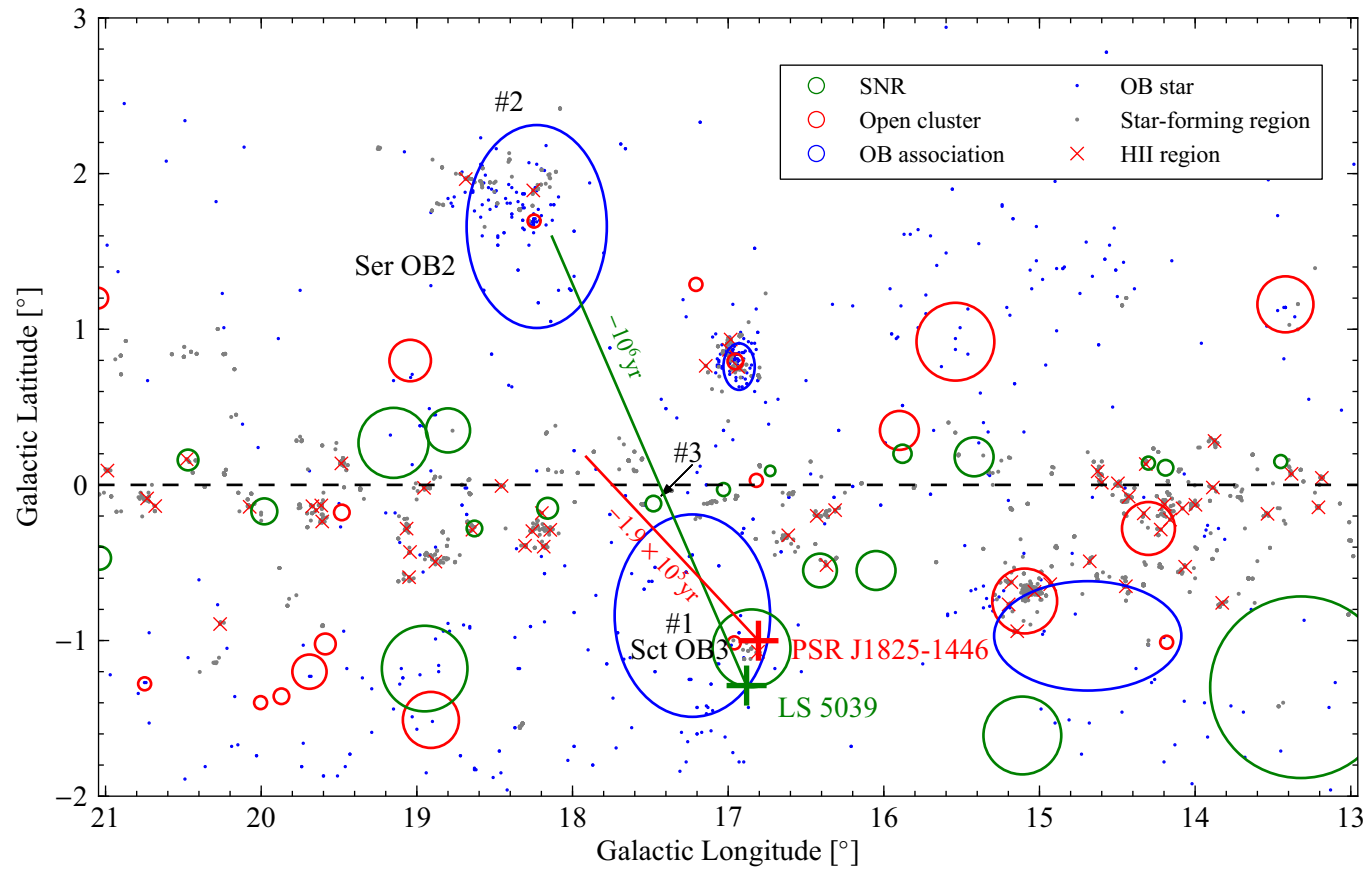


Figure 6.8: Area around LS 5039 and PSR J1825–1446 in Galactic coordinates. The lines mark the past trajectory in the last 10^6 yr for LS 5039, and 1.95×10^5 yr for PSR J1825–1446. The green circles are supernova remnants from the catalogue compiled in Green (2009). The red circles are open clusters from the WEBDA database, and the blue ellipses mark the position of the known OB associations (Mel’Nik & Efremov 1995). The OB stars (Reed 2003) and the star-forming regions (Avedisova 2002) are marked with blue and grey dots, respectively, and provide a general view of the young system distribution in this region of the Galaxy. The red crosses mark the H II regions (Lockman 1989). The objects in regions #1, #2, and #3 are described in the text.

ejected from the Galaxy.

Region #1

As can be seen in Fig. 6.8, the past trajectories of LS 5039 and PSR J1825–1446 cross three interesting regions, marked with numbers from #1 to #3. The first region (#1) is composed of the objects at short angular distances from the systems. In the WEBDA database⁹ we can see that LS 5039 and PSR J1825–1446 are within the open cluster Dolidze 28 (C 1822–146), whose central star is WR 115. Manchanda et al. (1996) determined the distance to the cluster to be 2.2 kpc (note that the cluster is wrongly named Do 78 instead of Do 28 in Table 1 of Manchanda et al. 1996). We used the 2MASS photometric magnitude of WR 115 (Wolf-Rayet of type WN6) from Table A1 in Crowther et al. (2006), $M_{Ks} = -5.10$, and colours for a nominal subtype WN6 star $(J - K)_0 = 0.17$ and $(H - K)_0 = 0.15$. The absorption estimate of the source is $A_K = 0.59$, which yields a distance of 2.0 kpc, compatible with the distance quoted above. In the same field we find the OB association Sct OB3 (see Mel’Nik & Efremov 1995), with ten members in a region of 25.8×33.6 pc², and an estimated distance of 1.5 kpc. This distance is compatible with the estimate in Dambis et al. (2001), obtained from a parallax measurement, of 1.4 kpc. They also provide an age of Sct OB3 of 4–5 Myr. The closest H II ionised region is RCW 164, already discussed in Sect. 6.2.1.

In Fig. 6.9 we show the most relevant objects of region #1 together with the past trajectories of LS 5039 and PSR J1825–1446. We can see that although PSR J1825–1446 is currently very close to RCW 164, it comes from the opposite direction at high speed. The trajectory is not compatible with the central region of SNR G016.8–01.1 either. Although it is not possible to determine the kinematic centre of the SNR precisely, the projected past trajectory of LS 5039 seems to be far away from the central region of the remnant (see Fig. 6.1), although an association cannot be discarded. We note that the $1\text{-}\sigma$ accuracy in the position of LS 5039 10^5 yr ago is approximately 18 arcsec, although the uncertainties do not follow a Gaussian distribution, as shown by the contours in Fig. 6.9.

The past trajectory of LS 5039 shown in Fig. 6.9 suggests an interesting possibility, namely that the binary system LS 5039 and WR 115 come from the same point on the sky, and that they might have been a triple system, from which WR 115 was ejected in the opposite direction after the supernova explosion. This would tightly restrict the age of the triple system. However, we have computed a proper motion of WR 115 using positions from optical catalogues, in particular from AC2000.2, GSC 1.2, *Hipparcos*, UCAC3, and 2MASS, see Sect. 6.4.4. The proper motion obtained is 4.5 ± 0.6 and -5 ± 4 mas yr⁻¹ in right ascension and declination, respectively. The proper motion in right ascension discards the possibility of a triple system with WR 115 because the linear momentum conservation would require that the system pre-supernova already had a runaway velocity much higher than expected from Galactic diffusion.

⁹<http://www.univie.ac.at/webda/>

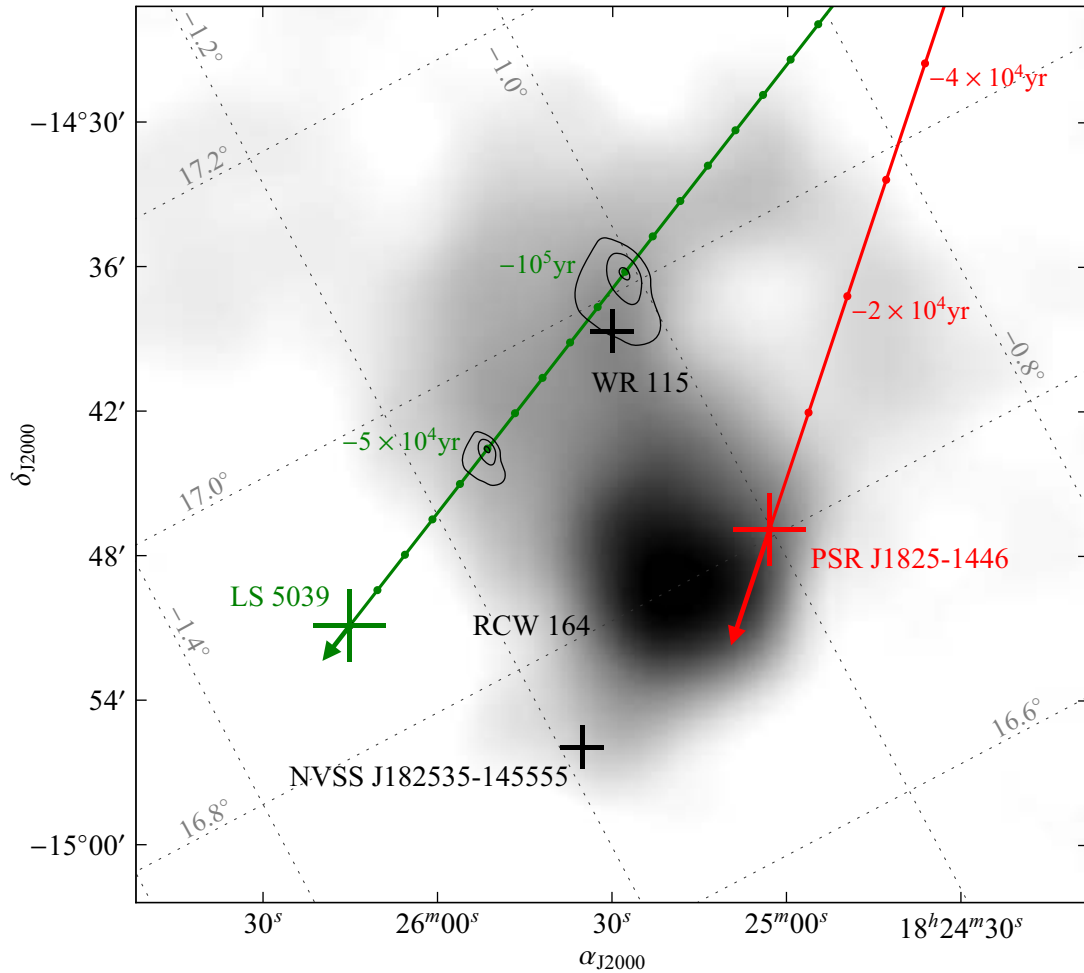


Figure 6.9: Wide-field map around SNR G016.8–01.1. The grey scale corresponds to the Parkes-MIT-NRAO survey at 5 GHz (Tasker et al. 1994). The green and red lines mark the past trajectory of LS 5039 and PSR J1825–1446, respectively. The arrows mark the proper motion sense. Circles are plotted in the trajectories every 10^4 yr. The contours represent the 68.2, 95.4 and 99.7% confidence levels on the position that LS 5039 had 10^5 and 5×10^4 years ago (see uncertainties in the proper motion shown in Fig. 6.5). The grey dotted lines show the Galactic coordinates.

Region #2

Region #2 is found at an angular distance of $\sim 3^\circ$ from both sources, and harbours an active site of star formation and young stars. The OB association shown in region #2 is Ser OB2 (Mel’Nik & Efremov 1995), with a size of 22.8 and 33.0 pc in Galactic longitude and latitude, respectively, an average radial velocity relative to the Sun of $-2.4 \pm 3.9 \text{ km s}^{-1}$, and an average distance of 1.45 kpc. Forbes (2000) provides a distance to the association of $1.9 \pm 0.3 \text{ kpc}$, and an average age of $5 \pm 1 \text{ Myr}$. Dambis et al. (2001) provide a parallax measurement based on *Hipparcos* stars of 0.63 mas, which correspond to a distance from the Sun of 1.6 kpc and Tetzlaff et al. (2010) sets an age of the association of 4–5 Myr. On the other hand, the open cluster in the centre of region #2 is NGC 6604, which can be found in the WEBDA catalogue, with a distance of 1.7 kpc, and an age of $\sim 6 \text{ Myr}$. Loktin & Beshenov (2003) measured an average proper motion of this cluster, formed by ~ 97 stars, and obtained -0.66 ± 0.19 and $-0.88 \pm 0.17 \text{ mas yr}^{-1}$ in right ascension and declination, respectively, as well as the distance quoted in the WEBDA database. Dambis et al. (2001) set a parallax of 0.59 mas, corresponding to a distance from the Sun of 1.7 kpc, and an age of 4–5 Myr. There is also an interesting H II region that might be associated with this complex, SH 2-54, from the catalogue of H II regions in Sharpless (1959). Its radial velocity was measured by Blitz et al. (1982) to be $27.6 \pm 0.5 \text{ km s}^{-1}$, much higher than the average velocity of Ser OB2 quoted above, and the distance from the Sun is $2.0 \pm 0.2 \text{ kpc}$, which is compatible within errors with the structures discussed above. In summary, region #2, which harbours many young stars and star-forming regions, is undergoing intense formation of new stars, it is at a distance of 1.5–2.0 kpc from the Sun, and has an age of 4–5 Myr. The age of the complex is enough to allow LS 5039 to have travelled from that region of the sky to its current position. Considering the large uncertainties in the distance to the system, this is a plausible birth region for LS 5039 provided that it is located between 1.5 and 2.0 kpc from the Sun. For this distance range, Fig. 6.6 shows that LS 5039 would have a lower peculiar Galactic velocity of about $70\text{--}95 \text{ km s}^{-1}$. In this case, LS 5039 would have an age between 1.0 and 1.2 Myr.

Region #3

Finally, region #3 in Fig. 6.8 marks the position of SNR G017.4–00.1, which has a diameter of $6'$, a flux density of 0.4 Jy, and a spectral index of +0.7 (Brogan et al. 2006; Green 2009). This partial shell remnant is of class II, which corresponds to a gravitational collapse supernova explosion. The minimum projected distance between the past trajectory of LS 5039 and this SNR took place $4 \times 10^5 \text{ yr}$ ago, and for PSR J1825–1446 it took place $0.13 \times 10^5 \text{ yr}$ ago. For these high ages we do not expect to still detect the SNR, consequently it is unlikely that PSR J1825–1446 and SNR G017.4–00.1 are related, whereas it is not possible that LS 5039 and SNR G017.4–00.1 are related. On the other hand, Bochow (2011) used the $\Sigma - D$ relationship to estimate the distance to SNR G017.4–00.1, and obtained 12 kpc. The distance to the SNR seems considerably larger than the distance

Table 6.8: Crossing times of LS 5039 and PSR J1825–1446 through the Galactic thin disc, with a scale height for OB stars of ± 45 pc, for different distances from the Sun.

LS 5039		PSR J1825–1446	
Distance [kpc]	Age [kyr]	Distance [kpc]	Age [kyr]
2.0	0–890	3.0	20–300
2.9	140–750	5.0	80–245
4.0	220–670	7.0	100–220

to the sources, although we note that this estimate can be very uncertain.

Crossing times through the Galactic disc

Besides the specific regions on the sky in the past trajectory of both systems, we can constrain the lifetime of the systems considering that the systems had contained young massive stars, which are generally formed in a specific region of the Galactic plane, the thin disc. The stellar space density decays exponentially as a function of the distance above or below the Galactic plane, and each stellar population has a particular scale height h . For young OB stars $h_{\text{OB}} = 45$ pc (Reed 2000), while Maíz-Apellániz (2001) found that the O–B5 stellar population is distributed with a scale height of $34.2 \pm 0.8 \pm 2.5$ pc. No good determination for the O-type population alone has been found, basically due to the lack of good statistics with this population, and therefore we used the more conservative value of 45 pc both for LS 5039 and PSR J1825–1446. From the Galactic latitudes quoted in Table 6.7, the current height with respect to the Galactic plane is -65 and -96 pc for LS 5039 and PSR J1825–1446, respectively. With the proper motion of the systems, we compute for different distances from the Sun the time when they were crossing the Galactic plane at a height within ± 45 pc. The expected ages are quoted in Table 6.8.

6.7 Discussion and conclusions

PSR J1825–1446

We have obtained a set of accurate positions of the isolated pulsar PSR J1825–1446 by means of VLBI observations. We used the pulsar gating technique to enhance the detected pulsar flux density to improve the astrometry. We fitted a linear proper motion to new and archival astrometry and obtained a proper motion of $\mu_{\alpha} \cos \delta = 10.0 \pm 0.3$ mas yr $^{-1}$, and $\mu_{\delta} = -29.0 \pm 0.3$ mas yr $^{-1}$. For a distance from the Sun of 5.0 kpc, the proper motion of PSR J1825–1446 corresponds to a projected transverse velocity of 690 ± 7 km s $^{-1}$, which makes it a high-velocity pulsar ejected from the Galactic plane.

6. On the origin of LS 5039 and PSR J1825-1446

We note that the high space velocity of PSR J1825–1446 suggests that it is possible that a bow-shock has formed in front of the pulsar. For example, the pulsar wind nebula G359.23–0.82 is the bow shock produced by the young pulsar J1747–2958, which has a spin-down luminosity of 2.5×10^{36} erg s⁻¹, and a transverse velocity of 300 km s⁻¹ in a medium with hydrogen number density of 1.0 cm⁻³ (Hales et al. 2009). However, the spin-down luminosity of PSR J1825–1446 is only 4.1×10^{34} erg s⁻¹, and therefore a such structure would only be visible if the medium surrounding PSR J1825–1446 were much denser than in the case of J1747–2958.

The space velocity of the source has allowed us to investigate possible origins of PSR J1825–1446. The characteristic age of PSR J1825–1446 is approximately 0.2 Myr. The velocity and age of PSR J1825–1446 make it incompatible with SNR G016.8–01.1. There are no clear OB associations or SNRs crossing the past trajectory of the pulsar. Our estimate of the age of the pulsar, assuming that its progenitor died in the Galactic disc, is 80–245 kyr, compatible with its characteristic age. We have seen that the space velocity of this pulsar is high enough to escape from the Galactic potential.

LS 5039

We compiled all radio interferometric observations of LS 5039 with accurate astrometry, and reduced all data in a consistent way. Combining the radio positions with archival optical astrometry from global catalogues we obtained a proper motion of the source of $\mu_\alpha \cos \delta = 7.09_{-0.11}^{+0.19}$ mas yr⁻¹, and $\mu_\delta = -8.82_{-0.12}^{+0.27}$ mas yr⁻¹. We have reduced the uncertainty on the proper motion by approximately one order of magnitude with respect to the one obtained in Ribó et al. (2002b), which is compatible at 2- σ level. The data were collected from very heterogeneous observations (completely different instruments, conditions, frequencies, and reference calibrators), and the fit is affected by systematic errors. We investigated the effects of these unknown uncertainties using a bootstrap method, which provides realistic uncertainties of our measurement. We confirmed the runaway nature of the system, which has a peculiar space velocity of 141_{-3}^{+4} km s⁻¹, with a main component of -136_{-2}^{+3} km s⁻¹ perpendicular to the Galactic plane, for a distance to the source of 2.9 kpc.

We were unable to identify a secure origin for LS 5039. We restricted the proper motion of the system, and the past trajectory is not far from the putative centre of SNR G016.8–01.1, which is very uncertain. However, this association would imply an age of 10⁵ yr for the SNR, which is above the expected lifetime for such a bright SNR (Frail et al. 1994). The age of the SNR depends on the ambient density and its distance, which are unknown parameters (Ribó et al. 2002b; Sun et al. 2011). However, even if SNR G016.8–01.1 is not related to LS 5039, the entire region shown in Fig. 6.9 is an active region of stellar formation, with the open cluster Dolidze 28, WR 115, and the H II region RCW 164. It is possible that the compact object was formed within this complex. In this case, LS 5039 should be at a distance of around 2 kpc, and the age of the binary

would be below 0.1–0.2 Myr. On the other hand, the region of Ser OB2 lies within the past trajectory of LS 5039, at a distance from the Sun of 1.5–2.0 kpc, which is still compatible at $2\text{-}\sigma$ level with the distance to LS 5039, 2.9 ± 0.8 kpc. In this case the age of the system would be 1.0–1.2 Myr, and the peculiar Galactic velocity would be 70–95 km s⁻¹. A third possibility is that the system LS 5039 was formed in the Galactic plane, but it was not associated to any known young stellar association. In this case the age of the system would be between 0.1 and 0.8 Myr, assuming a distance of 2.9 kpc.

Age of LS 5039 and pseudo-synchronisation of the orbit

The age of LS 5039 has consequences on the nature of the compact object. When the compact object was formed, the system received a powerful kick, and therefore the orbit could not be pseudo-synchronised after the explosion. Pseudo-synchronous rotation is reached through tidal forces in an eccentric binary, when the rotation of the massive star and the motion of the compact object at periastron are synchronised (Hall 1986). Casares et al. (2005b) determined that the compact object should be a black hole (low system inclination and high compact object mass) if the orbit of the system is pseudo-synchronised. They estimated the time for this system to reach orbital pseudo-synchronism to be ~ 1 Myr, although it is highly uncertain. If the system was formed in Sct OB3 region, its age would be below 0.2 Myr, and the hypothesis in Casares et al. (2005b) would be unlikely. Only if the source was formed close to Ser OB2 region, 1–2 Myr ago, would it be possible to reach orbital pseudo-synchronism. Based on the proper motion of the source, it is not expected that the system age is greater than 1–2 Myr if the system was born in the Galactic disc.

Concluding remarks

We have seen that any determination of the age and origin of LS 5039 is limited by the uncertainty in its distance to the Sun. This distance cannot be obtained by means of parallax VLBI measurements with the current resolution, and the effects of the source structure and variability. An accurate distance will be obtained by the Gaia satellite (see de Bruijne 2012, and references therein) through measurements of the parallax of the massive companion. The satellite will also determine the distance to the OB associations with high accuracy, and therefore any identification or association should be much more straightforward, and will help to clarify the origin of the system. On the other hand, the distance to PSR J1825–1446 could be obtained by means of a challenging long-term VLBI project. This would provide a model-independent distance that can be compared to the estimated one from the dispersion measure. Finally, there is no obvious approach to accurately determine the distance to SNR G016.8–01.1, whose radio structure is severely contaminated by the H II region RCW 164.

7

VLBI observations of LS I +61 303 within a MAGIC multiwavelength campaign

7.1 Introduction

LS I +61 303 is a high-mass binary system located at a distance of 2.0 ± 0.2 kpc (Frail & Hjellming 1991). It contains a rapidly rotating B0e main sequence star with a stable equatorial shell, and a compact object orbiting it every 26.5 d (Hutchings & Crampton 1981). Quasi-periodic radio outbursts monitored during 23 years have provided an accurate orbital period value of $P_{\text{orb}} = 26.4960 \pm 0.0028$ d (Gregory 2002). The orbit is eccentric ($e = 0.72 \pm 0.15$) and periastron takes place at phase 0.23 ± 0.02 (Casares et al. 2005a). Phase zero is defined at the time of the discovery of the radio emission, JD 2443366.775 (Gregory & Taylor 1978). The mass of the Be star, between 10 and 15 M_{\odot} , and the binary mass function of $f(M) = 0.0107^{+0.0163}_{-0.0077} M_{\odot}$ yield an uncertain mass of the compact object in the range of 1–5 M_{\odot} (Casares et al. 2005a). The compact object would be a neutron star for inclinations $25^{\circ} \lesssim i \lesssim 60^{\circ}$ and a black hole if $i \lesssim 25^{\circ}$. We note that an update of the orbital parameters, but using the Balmer lines that are known to be contaminated by the stellar wind, yields a different eccentricity of 0.55 (Grundstrom et al. 2007; Aragona et al. 2009). Hereafter, we will use the orbital elements obtained in Casares et al. (2005a).

The source displays radio emission with negative spectral index and flux densities at GHz frequencies below ~ 50 mJy during most part of the orbital cycle, although the source displays periodic radio outbursts with slightly positive spectral index and flux densities between 100 and 150 mJy (Strickman et al. 1998). The maximum flux density of the radio outbursts and the orbital phase at which they occur are modulated by a long-term

7. VLBI observations of LS I +61 303 within a MAGIC multiwavelength campaign

periodicity of ~ 4.6 yr (Paredes 1987; Gregory 1999, 2002). The peak occurs periodically between orbital phases 0.45 and 0.95. These changes are possibly related to variations of the wind structure of the star, in particular in the equatorial disc, which is expected to suffer important interactions with the compact object during the periastron passage. X-ray outbursts, starting around orbital phase 0.4 and lasting up to phase 0.6, have been detected (Harrison et al. 2000, and references therein). Orbital X-ray periodicity has also been found using *RXTE*/ASM data (Paredes et al. 1997), which revealed a broad maximum covering orbital phases 0.4–0.6. The source also shows short-term flux and spectral variability on time scales of kiloseconds (Sidoli et al. 2006; Rea et al. 2011). Hints of extended X-ray emission at scales of $1''$ were reported in Paredes et al. (2007). At higher energies, LS I +61 303 was first identified as a gamma-ray source (CG 135+1) by *COS-B* (Hermsen et al. 1977). The system is spatially coincident with a source detected by EGRET above 100 MeV (Kniffen et al. 1997). Interestingly, LS I +61 303 was detected at TeV energies with the MAGIC Cherenkov telescope (Albert et al. 2006) and with VERITAS (Acciari et al. 2008). Further observations by the MAGIC collaboration led to the discovery of the orbital variability of TeV emission with a period of 26.8 ± 0.2 days (Albert et al. 2009). Simultaneous observations of MAGIC and the *XMM-Newton* and *Swift* X-ray satellites revealed a correlation between the X-rays and VHE bands (Anderhub et al. 2009). No correlation was detected by Acciari et al. (2009a) between the X-ray emission and the TeV emission of the source, possibly because of the limited sampling of the TeV observations. The *Fermi* Large Area Telescope (*Fermi*/LAT) reported the first detection of the orbital modulation at HE with a period of 26.6 ± 0.5 days roughly anti-correlated with the X-ray emission (Abdo et al. 2009a). The X-ray, HE, and VHE detections reported in the last few years have shown changes in the source emission. Variation in the long-term X-ray light curve (Li et al. 2012), in the GeV behaviour (Hadasch et al. 2012), as well as a change in the VHE light-curve (Acciari et al. 2011; Aleksić et al. 2012b) have been reported. These changes are probably related to the periodic long-term (~ 4.6 yr) structural changes of the circumstellar disc detected through variations of the equivalent width and the peak separation of the H_α emission line (Zamanov et al. 1999).

7.1.1 Previous VLBI observations of LS I +61 303

LS I +61 303 has been observed several times with VLBI, showing different and puzzling morphologies (Massi et al. 1993; Peracaula et al. 1998; Paredes et al. 1998; Massi et al. 2001, 2004). Dhawan and collaborators conducted a multiwavelength and multiepoch VLBA campaign (project BD117) to monitor the behaviour of the source during a whole orbital cycle in a consistent way. The campaign consisted of ten VLBA observations separated by 3/4 days during July 2006, covering slightly more than one orbital cycle. For each epoch, the source was observed during 5 hours at 8.4/2.3 GHz (3.6/13 cm) simultaneously. The observations were phase-referenced, and provided accurate relative astrometry during the whole orbital cycle. Preliminary results were reported in Dhawan et al. (2006). The

images show a changing morphology and displacements of the peak of the emission that these authors interpreted as the signature of a cometary tail produced in the colliding winds scenario. The astrometry at 8.4 GHz shows that the peak of the emission describes an erratic ellipse, almost 4 times larger than the orbit. At orbital phase 0.75 the peak of the emission showed a significant displacement from the ellipse traced by the rest of the points. Remarkably, the astrometric jump occurred shortly after the orbital phases in which the TeV maximum occurs, ~ 0.65 (Albert et al. 2009; Anderhub et al. 2009). The elliptical path described by the peak of the emission can be understood in the context of the non-accreting pulsar scenario considering that the position of the peak of the emission is at the place downstream the outflow where synchrotron opacity is ~ 1 , as described in Dubus (2006). The 2.3 GHz positions trace an even larger ellipse and seem to lag behind the 8.4 GHz positions by a few days. This may show that the opacity has a gradient along the tail. The images at 8.4 GHz show extended structures at scales of 1–10 mas with changing P.A. along the orbital cycle. The P.A. of the extended emission displays a nearly continuous and relatively slow change of 180° during most part of the orbit, around apastron, and a fast rotation at orbital phases around periastron.

Massi et al. (2012) presented another interpretation of the VLBA observations presented in Dhawan et al. (2006), project code BD117, based on a re-reduction of the data that improved the dynamic range of the images. The authors showed that in addition to the images with a one-sided structure, there are several images with a double-sided structure. The astrometry at 8.4 GHz shows a clear ellipse, as previously seen, although at 2.3 GHz the peak of the emission does not form a “delayed” ellipse behind the 8.4 GHz peak. Despite the large uncertainties at 2.3 GHz, the peaks of the emission at this frequency appear systematically displaced westwards from the 8.4 GHz peaks. These authors interpret these results as a core shift displacement of a microblazar jet, which is frequency-dependent.

Further observations in the context of a multiwavelength campaign were reported in Albert et al. (2008). Observations were conducted with MERLIN, the EVN (also e-EVN), and the VLBA at 5 and 6 GHz. The results show that images at similar orbital phases from different cycles show similar morphologies. The authors constrained the radio emitting region below 6 mas (12 projected AU), excluding the presence of persistent radio jets above this scale.

7.1.2 The September 2007 multiwavelength campaign

To gain knowledge on the physics of LS I +61 303, especially around the orbital phases of the TeV maximum, we organised a multiwavelength campaign in September 2007 on behalf of the MAGIC Collaboration (Anderhub et al. 2009). The campaign included MAGIC observations from September 4 to 21, 2007, which correspond to orbital phases from 0.47 to 1.08 (the Moon prevented observations outside this phase interval). The final effective total observation time with MAGIC was 54.2 h. Simultaneously, we conducted

7. VLBI observations of LS I +61 303 within a MAGIC multiwavelength campaign

XMM-Newton observations from September 4 to 11 (orbital phases 0.43 to 0.70) on a daily basis. The total observing time was 104.3 ks. Additional observations were obtained with the *Swift* X-ray Telescope (XRT) from September 11 to 22 for a total observing time of 28.5 ks. Radio observations with the RATAN radio telescope were conducted at four frequencies between phases 0.3 and 0.8. Optical spectroscopic observations of the H_α line at 6563 Å were obtained nearly on a nightly basis from September 4 to 15 (phases 0.45 to 0.90) using the 1.3-m telescope in the Skinakas observatory. We also conducted simultaneous VLBA observations, as will be explained in Sect. 7.2.

The most remarkable discovery from this campaign was the correlation between the X-ray and the TeV emission of LS I +61 303 during outburst. The simultaneous outbursts peaked at orbital phase 0.62 and displayed a similar shape at both wavelengths. The correlation found indicates that a single particle population of leptonic nature can explain the emission at these bands. This result was reported in Anderhub et al. (2009), whereas the results from the rest of the observatories were used only as a check of the general behaviour of the source, but were not explicitly detailed in the publication. The properties of the H_α line (EW, B/R, ratio, etc.) appeared to be similar to those previously found by Zamanov et al. (1999). The radio flux density monitored with RATAN showed a peak at orbital phase 0.55. We reduced and analysed the VLBA data, and the results from the monitoring are detailed below.

7.2 Observations and data reduction

One of the aims of the VLBI observations during the multiwavelength campaign (project code BP141) was to check the stability of the radio structure of the source, and thus we conducted five observations covering the nearly simultaneous VHE observations. The five runs (BP141A–E) were separated by 2 days, between September 4 and 12, 2007. Each run lasted 5 h, between UTC 08:00 and 13:00 for runs A, B, and C, and between UTC 07:30 and 12:30 for runs D and E. A log of the observations is shown in Table 7.1. A sketch of the orbit in an arbitrary orientation and seen from above is shown in Fig. 7.1, where we indicate the position of the compact object at the orbital phase of each observation. The observations cover all the X-ray/gamma-ray outburst of the source. The main outburst was clearly detected at three epochs, between orbital phases 0.621 and 0.702 (Anderhub et al. 2009). A log of the observations can be found in Table 7.1. We obtained two VLBA images a few days before the beginning of the high-energy outburst (runs A and B), run C was observed between 18 and 13 hours before the detected peak of the outburst, run D was observed during the outburst decay, and run E after the main outburst finished.

The VLBA observations were conducted simultaneously at 8.4 and at 2.3 GHz (3.6 and 13 cm, respectively). Three IFs were dedicated to the higher frequency and one to the lower one to have similar S/N taking into account the negative spectral index of the source. Only nine antennas of the VLBA participated in the observations (Hn was missing

Table 7.1: Log of VLBA observations of project BP141, conducted at 8.4 and 2.3 GHz. The orbital phases have an uncertainty of 0.04. The peak of the X-ray/VHE outburst in this orbital cycle took place at orbital phase 0.62.

Run	Date (Y-M-D)	MJD	Phase range	Freq. [GHz]
A	2007-09-04	54347.33–54347.54	0.442–0.450	8.4/2.3
B	2007-09-06	54349.33–54349.54	0.518–0.525	8.4/2.3
C	2007-09-08	54351.33–54351.54	0.593–0.601	8.4/2.3
D	2007-09-10	54353.31–54353.52	0.668–0.676	8.4/2.3
E	2007-09-12	54355.31–54355.56	0.743–0.753	8.4/2.3

because the azimuth axis was broken), each of them providing a total data rate of 256 Mbits/s, distributed in eight subbands of 8 MHz each, dual circular polarisation and 2-bit sampling. The weather conditions during the observations were normal, without any major weather problems apart from sporadic rain at Sc during run C.

The observations were conducted using phase referencing on the phase calibrator J0244+6228 separated 1.34° from the target source. We used a cycling time of 3.4 minutes, 2.4 min on the target and 1 min on the phase calibrator. The astrometric check source J0239+6005 was observed for 3 min every ~ 20 min. A sketch of the positions of these three sources in the sky is shown in Fig. 7.2. The fringe finders J0555+3948 and J0319+4130 were observed for one scan of 6 minutes each. The phase calibrator, used as reference source, was correlated at $\alpha_{J2000.0} = 02^{\text{h}}44^{\text{m}}57^{\text{s}}.6967$ and $\delta_{J2000.0} = +62^\circ 28' 06''.51503$, obtained from the SCHED database (NASA catalogue 2005f.astro). This position has an absolute uncertainty in the ICRF of 2.5 and 1.0 mas in right ascension and declination, respectively. The astrometric check source J0239+6005 was correlated at $\alpha_{J2000.0} = 02^{\text{h}}39^{\text{m}}37^{\text{s}}.95235$ and $\delta_{J2000.0} = +60^\circ 05' 41''.9112$. The target source LS I +61 303 was correlated at $\alpha_{J2000.0} = 02^{\text{h}}40^{\text{m}}31^{\text{s}}.66380$ and $\delta_{J2000.0} = +61^\circ 13' 45''.5920$.

Data reduction

The data reduction was performed using AIPS¹. All the process was repeated for the two bands observed, which were treated independently but using the same procedures. Flagging based on predicted off-source times, owing to slewing or failures, was applied using UVFLG. A priori visibility amplitude calibration used the antenna gains and the system temperatures measured at each station. Standard ionospheric corrections were applied (see for example Sect. 5.3.1). The phase calibration using FRING was obtained from the phase calibrator J0244+6228. We note that the fringe-fitting of the data at 2.3 GHz yielded bad solutions for the longer baselines, in particular the number of bad

¹The NRAO Astronomical Image Processing System. <http://www.aips.nrao.edu/>

7. VLBI observations of LS I +61 303 within a MAGIC multiwavelength campaign

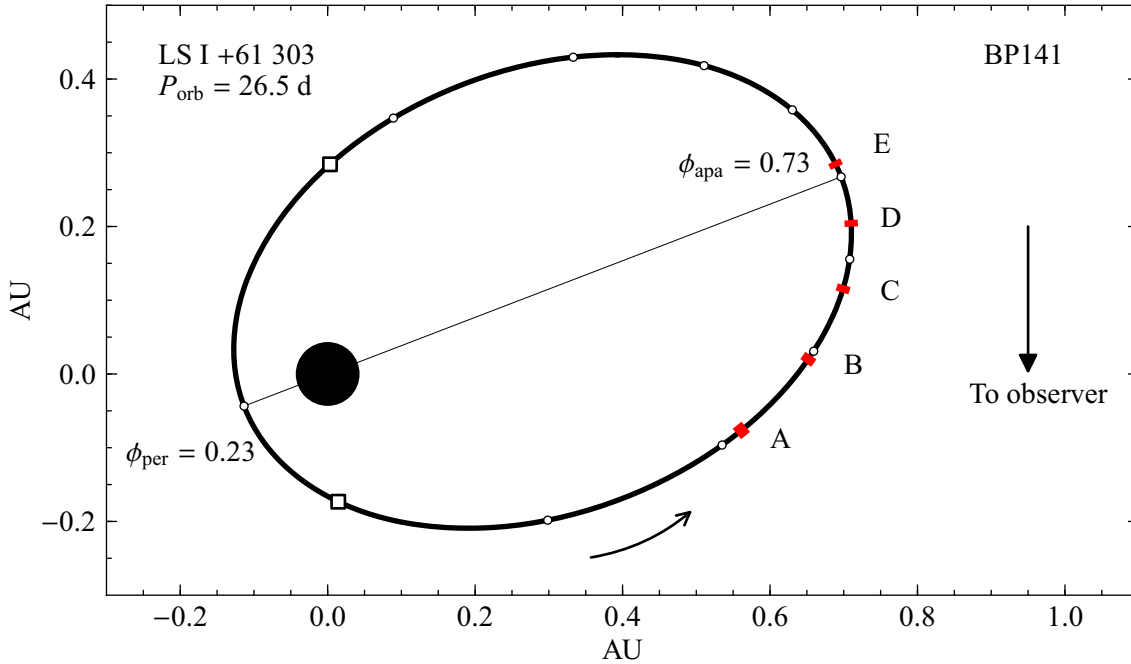


Figure 7.1: Sketch of the orbit of LS I +61 303 with the position of the compact object during the five runs of project BP141 marked in red. The white dots are plotted every 0.1 orbital phases. The empty squares mark the inferior and superior conjunction of the compact object, which occur at orbital phases 0.26 and 0.16, respectively. The orbit was computed using the orbital solution reported in Casares et al. (2005a). The orbit, size of the star, and the duration of the runs are scaled to the real values. The orientation of the orbit is arbitrary, and it is seen face-on (see Fig. A.2 on page 180 for examples of other possible projections of the orbit).

solutions for the five runs (A–E) was 16, 10, 9, 6, and 7%, respectively. This is because this calibrator is partially resolved at 2.3 GHz due to scatter broadening. We transferred the phase solutions from the phase reference J0244+6228 to the target source LS I +61 303, and the astrometric check source phase calibrator J0239+6005. We note that we also explored different phase-referencing calibrations using LS I +61 303 and J0239+6005 as reference (see below). After inspecting the phase solutions we splitted each source in single-source files and proceeded with the imaging. The astrometry was obtained fitting the peak of the emission of the phase-referenced images using JMFIT, whereas the final images were obtained after self-calibration.

Scatter broadening

The phase calibrator J0244+6228 is resolved due to Galactic scatter broadening (a general discussion on this effect can be found in Fey et al. 1991), which is important at 8.4 GHz,

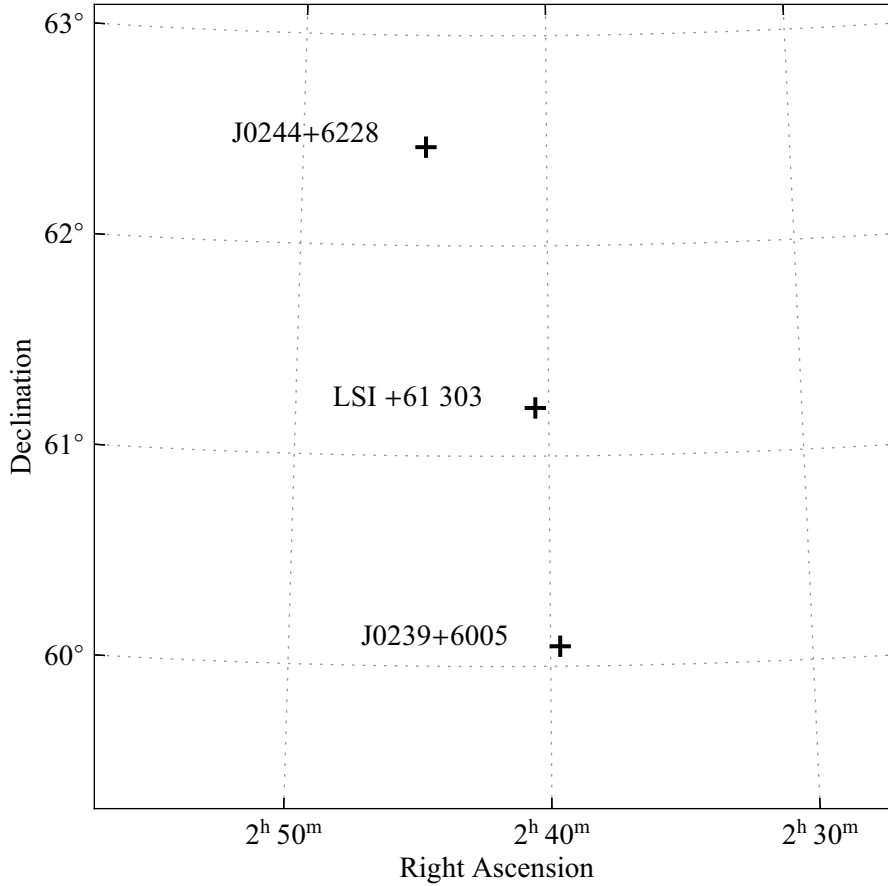


Figure 7.2: Distribution on the sky of LS I +61 303, the phase calibrator J0244+6228, and the astrometric check source J0239+6005. The angular separations from J0244+6228 to LS I +61 303 and J0239+6005 are 1.34 and 2.46°, respectively. The separation between LS I +61 303 and J0239+6005 is 1.14°. The Galactic position of LS I +61 303 is $l = 135.6753^\circ$ and $b = +01.0861^\circ$.

and severe at 2.3 GHz. The flux density of J0244+6228 at 8.4 GHz is about 1.1 Jy, but the phase calibration is only good up to uv distances of 130–150 $M\lambda$. We measured the size of the core of J0244+6228 by fitting Gaussian components to the self-calibrated combined uv data at 8.4 GHz to describe the source structure. The same procedure was used for the combined data set at 2.3 GHz. We used three components for the image at 8.4 GHz and one single component for the image at 2.3 GHz. The effect of the scatter broadening is determined by the size (FWHM) of the minor axis of the component describing the core at each frequency. The results are quoted in Table. 7.2. We also measured the size of the core of the astrometric check source J0239+6005, which is much more compact than J0244+6228 at both frequencies. The FWHM of the minor axis of the core component at 8.4 and 2.3 GHz are also quoted in Table. 7.2. We see that the relation of the core size at

7. VLBI observations of LS I +61 303 within a MAGIC multiwavelength campaign

Table 7.2: Scatter broadening of the two extragalactic calibrators observed. θ is the total size (FWHM) of the component describing the core, which was fitted to the uv data. The last column shows the index for the scatter broadening following $\theta_{8.4\text{GHz}} = \theta_{2.3\text{GHz}} \left(\frac{2.3\text{GHz}}{8.4\text{GHz}}\right)^n$.

Source	Scheduled as	$\theta_{8.4\text{ GHz}}$ [mas]	$\theta_{2.3\text{ GHz}}$ [mas]	n
J0244+6228	Phase calibrator	1.0	11.5	1.9
J0239+6005	Astrometric check	0.15	1.4	1.7

the two observed frequencies is well explained by Galactic scatter of these two extragalactic sources, which is expected to produce a broadening following $\theta_{8.4\text{GHz}} = \theta_{2.3\text{GHz}} \left(\frac{2.3\text{GHz}}{8.4\text{GHz}}\right)^2$, where θ is the angular size of the core. In Table. 7.2 we show the measured exponent, similar to 2, obtained from our data. We note that the Galactic scatter broadening is not expected to be important for LS I +61 303, which is only located at 2 kpc.

7.3 Analysis and results I: astrometry

7.3.1 Standard phase referencing

We measured the peak positions of LS I +61 303 and J0239+6005 using the phase solutions fitted to the phase reference source J0244+6228 at 8.4 GHz. The results are shown in the left panel of Fig. 7.3. The positions of LS I +61 303 are indicated with black circles, and are relative to the position of run A. As expected, the check source describes a random movement (grey squares). We used the standard deviation of this random displacement to find the uncertainty of the astrometry of LS I +61 303, which is 0.03 and 0.04 mas in right ascension and declination, respectively. In principle, it is expected that the systematic errors scale with the angular separation between the target source and the phase reference calibrator (Pradel et al. 2006), and therefore the astrometry for LS I +61 303 should be slightly more accurate than for the astrometric check source. However, we have not scaled the errors because the number of measurements, five, may be too low to provide good statistics in the determination of the dispersion. Also, the observations lasted 5 h instead of the 12-h of a full track and consequently the uncertainties could scale in different proportions in right ascension and declination, and not simply linearly with the source separation. Therefore we prefer to be conservative and estimate the uncertainty of the astrometry of LS I +61 303 as the dispersion of the check source, being this an upper limit of the uncertainty. We note that the angular separation ratio is 0.54.

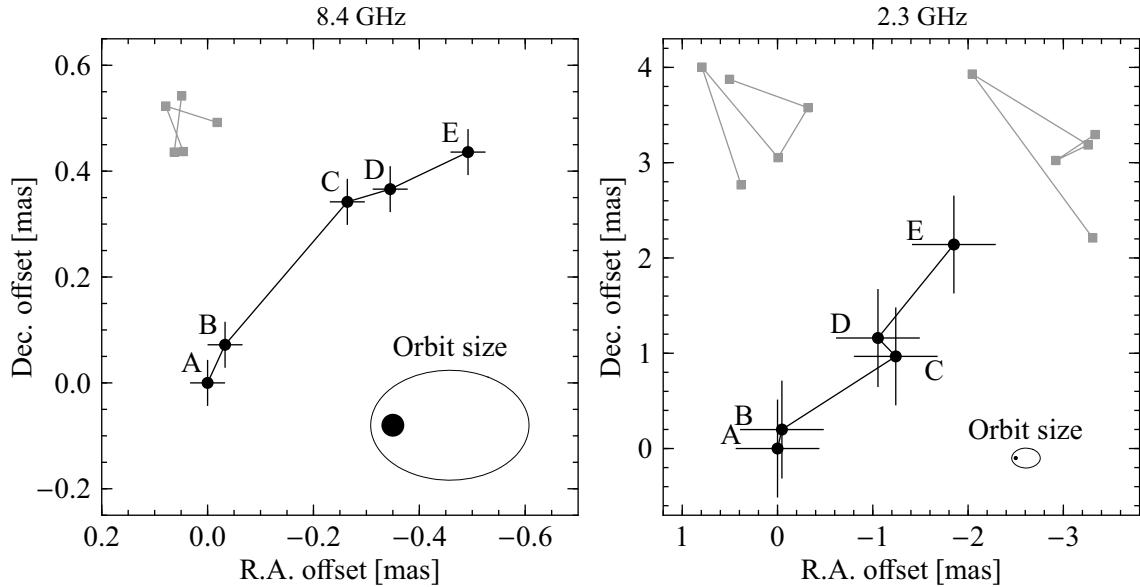


Figure 7.3: Astrometry of LS I +61 303 at 8.4 (left panel) and 2.3 GHz (right panel) for the five runs of project BP141. The black circles indicate the measured positions with respect to the position of run A. The error bars show the uncertainties at $1\text{-}\sigma$ level. The grey squares on the left panel are the positions of the check source J0239+6005 measured from J0244+6228. In the right panel, the grey squares on the left correspond to the positions of J0244+6228 measured using phase referencing from J0239+6005, and the ones on the right are the positions of J0239+6005 measured using phase referencing from J0244+6228 (see text for details). The three sets of grey values are plotted with different arbitrary offsets for better visualisation. A sketch of the orbit is plotted at an arbitrary orientation to show the scale of the system.

Inverse phase referencing at 2.3 GHz

In the case of the observations at 2.3 GHz there is a problem: the phase reference calibrator J0244+6228 has a notorious scatter broadening and it is not really useful as an astrometric reference. Therefore, we have obtained the astrometry at 2.3 GHz by using LS I +61 303 as phase calibrator, and measuring the peak displacement of the check source J0239+6005. This is far from optimal, because the observations were not scheduled with this purpose. However, the short scans aimed to provide good phase stability for the 8.4 GHz data help the phase solution transfer considered here. We use the opposite of the relative peak position of J0239+6005 to infer the relative astrometry of LS I +61 303, which is shown in the right panel of Fig. 7.3. A caveat of this procedure is that we cannot estimate the uncertainties of the astrometry by measuring the dispersion of the check source, because all sources measured from LS I +61 303 are “contaminated” by its displacements. We describe now a method to estimate the uncertainties of the astrometry of the observations at 2.3 GHz. We obtained two astrometries by crossing the phase-reference sources: first

7. VLBI observations of LS I +61 303 within a MAGIC multiwavelength campaign

we transferred the phase solutions from J0244+6228 to J0239+6005 and measured the dispersion of the peak of J0239+6005, and second we inverted this phase referencing and transferred the phase solutions from J0239+6005 to J0244+6228, and measured the dispersion of the peak of J0244+6228. None of these measurements are optimal, but they are useful to estimate our uncertainties because LS I +61 303 lies between the two calibrators (see Fig. 7.2). We note that using J0239+6005 as a phase reference source is the less suitable configuration, at least a priori, because the source was only observed every 20 minutes, which is longer than the expected coherence time of a few minutes in normal weather conditions. Despite this limitation, the results were much better than expected (see below). The two sets of random points obtained by this method are plotted as grey squares in the right panel of Fig. 7.3. We note that the set on the left, which has a slightly lower dispersion, corresponds to the phases transferred from J0239+6005 to J0244+6228, and the one on the right is the inverse case. This shows that using J0239+6005 as phase reference is still possible and provides good astrometry, even better than the astrometry from J0244+6228, at least for these observations. We computed the average dispersion from each of the crossed phase-referenced measurements. The final uncertainties on the astrometry at 2.3 GHz are 0.4 and 0.5 mas in right ascension and declination, respectively. We note that also in this case the uncertainties, not scaled with the source distance, are conservative.

There is an alternative procedure to estimate the uncertainties. Using LS I +61 303 as the phase-reference source, we could measure the displacements of J0239+6005 and J0244+6228, and subtract them. Ideally, the remaining quantity should be free of the intrinsic displacement of LS I +61 303. However, the errors are high enough to possibly lose this information, and we do not have any reliable a-priori knowledge of the behaviour of LS I +61 303. Therefore, we do not use this second method.

7.3.2 Connecting the astrometry at 8.4 and 2.3 GHz

When trying to compare the positions of LS I +61 303 at 8.4 and 2.3 GHz we found a problem. To illustrate it we plot the resulting astrometry from different reference sources in Fig. 7.4. To visually reduce the intrinsic jitter of the positions, and the displacement of LS I +61 303 from South-East to North-West, we plot a cross at the average value of the five positions for each source and frequency. We plot an arrow between these average positions to indicate the offset between the position of the peak at 2.3 GHz with respect to the position of the peak of the emission at 8.4 GHz. We will use the name core shift to describe the peak offset from 8.4 GHz to 2.3 GHz as an analogy of the core shift detected in AGN. The core shift is an effect of a frequency dependent shift of the VLBI core position (Sokolovsky et al. 2011). The shift is produced because the jet reaches optical depth $\tau_\nu = 1$ at different positions of the jet depending of the observed frequency. The magnitude of this effect in AGN is of about 1.2 mas for observations between 1.4 and 15.4 GHz. In our case, when using J0244+6228 as the phase reference source, the peak of

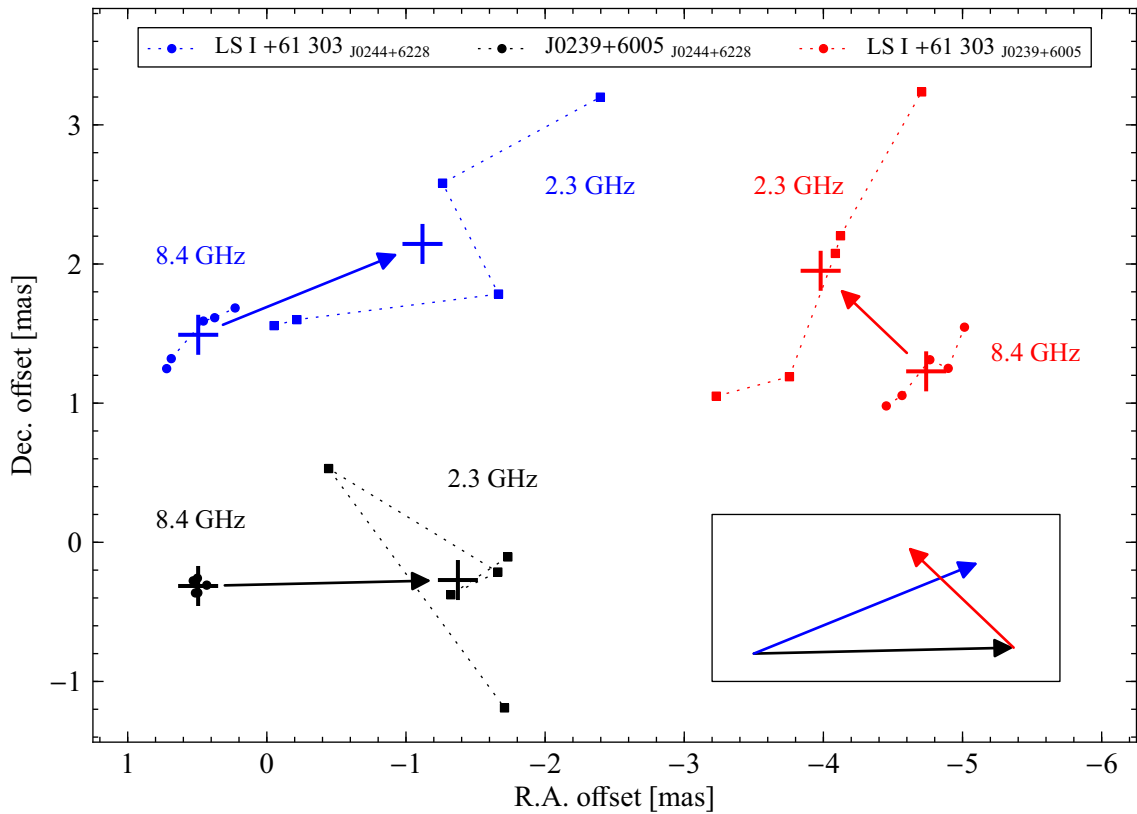


Figure 7.4: Relative astrometry from three different phase-referenced measurements. The phase calibrator used in each case is indicated with a subscript in the legend. Circles correspond to observations at 8.4 GHz and squares to observations at 2.3 GHz. Each set of values (colours) are plotted with an arbitrary offset for clearer visualisation. The arrows indicate the core shift, or average relative offset between the peak of the emission at 8.4 GHz and 2.3 GHz. The relative offset measured for LS I +61 303 using J0244+6228 as phase reference source (blue arrow) appears unreal because the check source J0239+6005 shows a very similar displacement (black arrow). The astrometry of LS I +61 303 using J0239+6005 as reference source shows a completely different offset (red arrow). Interestingly, a sum of the offsets over a closed loop shows that $(J0239+6005_{J0244+6228}) + (LS\ I\ +61\ 303_{J0239+6005}) \simeq (LS\ I\ +61\ 303_{J0244+6228})$. This indicates that the displacement between the 8.4 and 2.3 GHz peaks of LS I +61 303 is in fact a reflection of the intrinsic offsets of the calibrators.

7. VLBI observations of LS I +61 303 within a MAGIC multiwavelength campaign

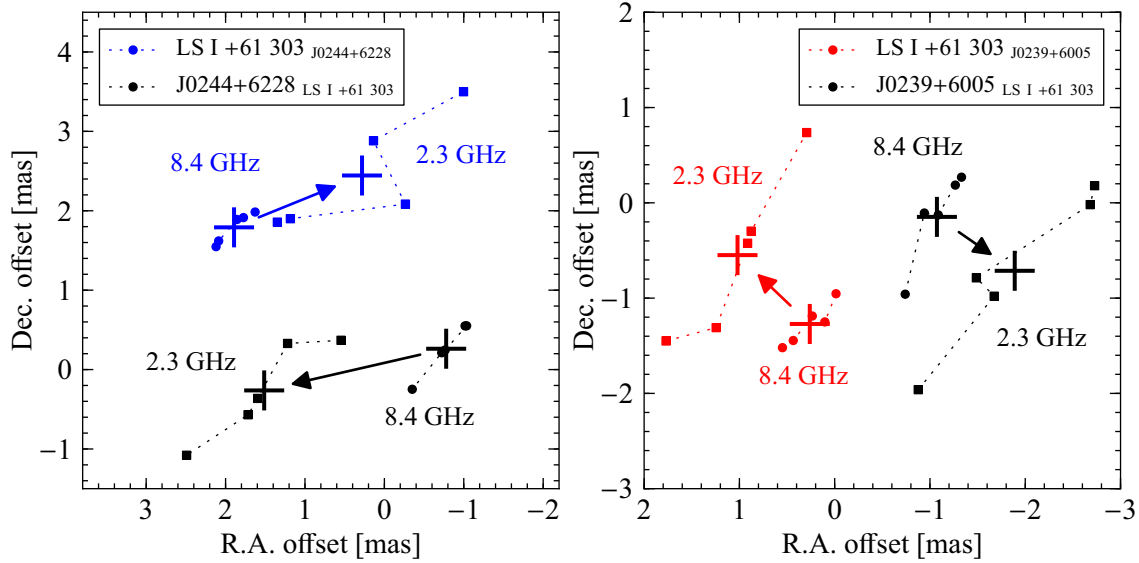


Figure 7.5: Same as Fig. 7.4 but showing together crossed phase-referenced astrometry of LS I +61 303 from/to the two phase calibrators. The different sets are plotted with arbitrary offsets.

LS I +61 303 at 2.3 GHz is shifted towards West (blue points in Fig. 7.4). However, the peak of the emission of the astrometric check source J0239+6005 displays a very similar offset (black points in Fig. 7.4). This similar behaviour for the two sources suggests that this displacement is in reality a core shift produced in the reference source with opposite sense. We checked that possibility by obtaining the astrometry of LS I +61 303 using as a phase reference J0239+6005. The relative positions are shown as red points in Fig. 7.4, where we can see that the core shift of LS I +61 303 shows a completely different P.A., nearly perpendicular to the estimated from J0244+6228. Interestingly, a sum of the offsets over a closed loop of the three sources shows a nearly zero offset. This suggests that the three sources are probably contributing to the measured core shift.

In order to explore the possibility of three different core shifts contributing to the measurements, we obtained the relative astrometry for the three sources, using all of them as phase reference and as target source. In Fig. 7.5 we show the astrometry at 8.4 and 2.3 GHz from the four cases involving LS I +61 303. All of them show the clear displacement from South-East to North-West discussed above. The relative displacement from the direct and the inverse phase referencing with J0244+6228 are consistent (see left panel in Fig. 7.5). The displacements estimated from the direct and inverse phase referencing with J0239+6005 are also consistent (see right panel in Fig. 7.5). We note that in Fig. 7.5 the positions for each phase-reference configuration are plotted with arbitrary offsets.

The next step is to match all the measured points. We do so in Fig. 7.6 by plotting

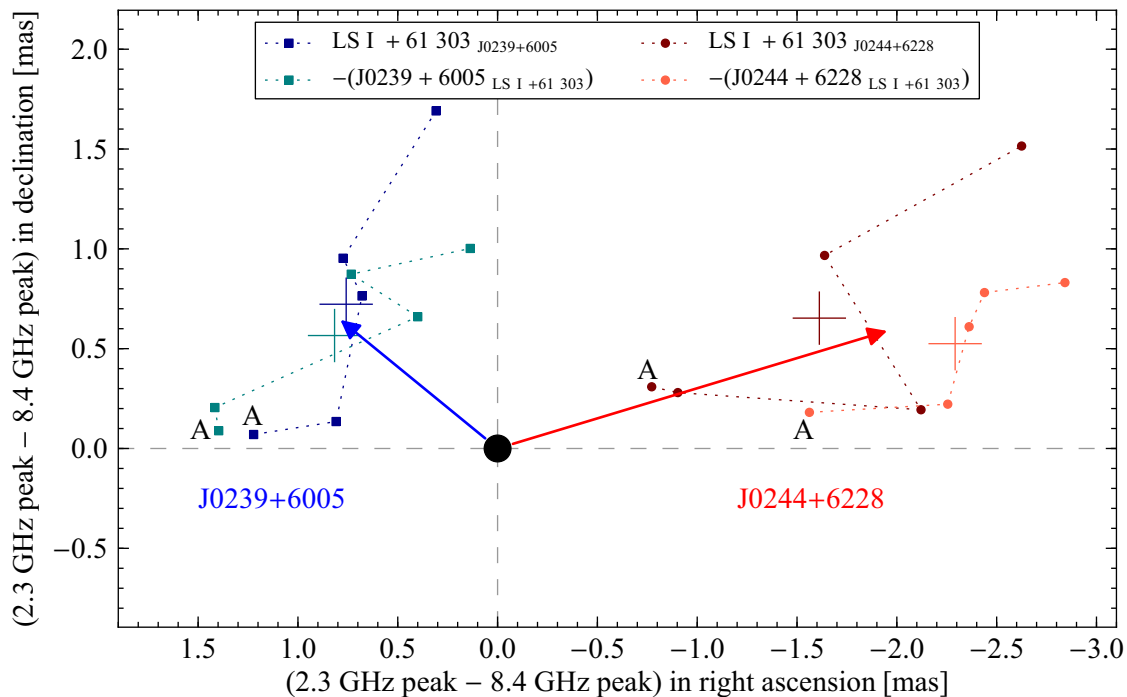


Figure 7.6: In this plot we show the relative separations between the peaks at 8.4 and 2.3 GHz for the different astrometries considered in Figs. 7.4 and 7.5 (note the different magnitudes plotted here). The measured core shift of LS I +61 303 from J0239+6005 (blue tones) and from J0244+6228 (red tones) are different from 0 and different between them. If we assume that the intrinsic core shift of LS I +61 303 is zero (black circle), the measured separations, indicated by the blue and red arrows, would correspond to the opposite of the intrinsic core shift of J0239+6005 and J0244+6228, respectively. We have labelled the points corresponding to run A as a reference of the run order.

directly the core shifts instead of positions at each frequency. For direct comparison, we plot the opposite value of the two inverted phase-referencing measurements, so all the points correspond to relative displacements of LS I +61 303. First, we can see a privileged direction when working with J0239+6005, marked with points with two tones of blue. The arrow points towards the average value. A different privileged direction can be seen for the data involving J0244+6228 (red tones). These directions are similar to the direction of the jets of the extragalactic calibrators. In Fig. 7.7 we show the self-calibrated images of J0244+6228 and J0239+6005 at 8.4 GHz obtained by combining the five data sets of each source. We fitted two circular Gaussian components to the uv data of each source. The P.A. of the extended component of J0244+6228 is 120.4° , which is nearly opposite to the core shift of LS I +61 303 when obtained with this calibrator (red arrow in Fig. 7.6). The P.A. of the extended component of J0239+6005 is 207.1° , which is also nearly opposite to the core shift of LS I +61 303 when obtained with this calibrator (blue arrow in Fig. 7.6).

7. VLBI observations of LS I +61 303 within a MAGIC multiwavelength campaign

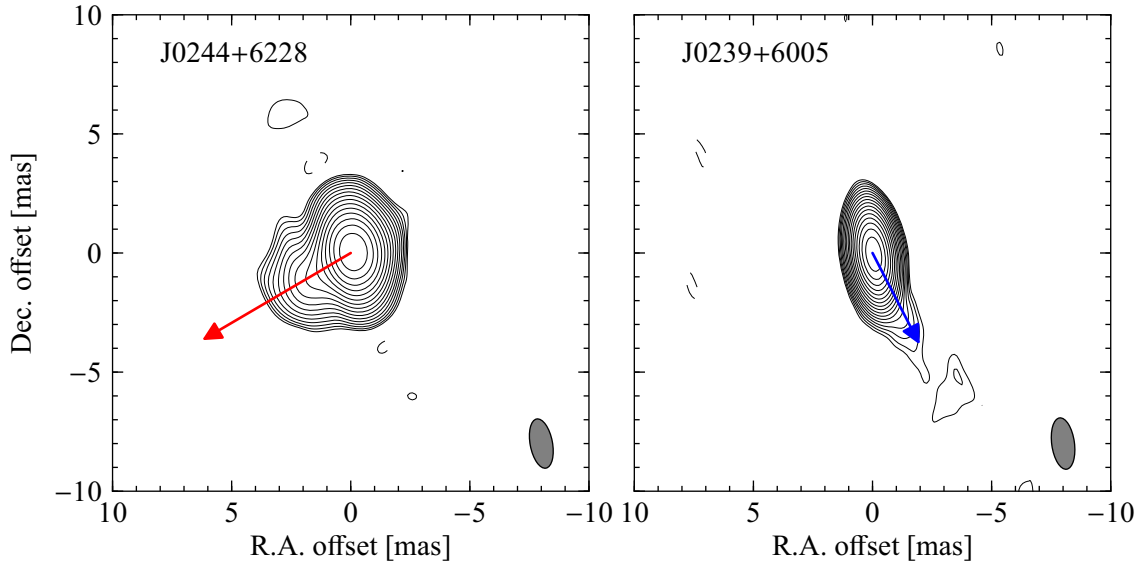


Figure 7.7: Self-calibrated images of the combined data set of the two calibrators at 8.4 GHz. The arrows indicate the P.A. of the extended emission of the sources. The P.A. of J0244+6228 is 120.4° . The P.A. of J0239+6005 is 207.1° . In Fig. 7.8 we assume that the core shift of these sources is restricted to these two directions.

Core shift of the three sources

It is not possible to disentangle between the contribution of each source to the measured core shift because phase-referenced observations are always relative, and because we do not have information about the intrinsic core shifts of any of the sources. Therefore, we need to make some assumption to fix this degeneracy. The most simple assumption would be to consider that one of the sources, for example LS I +61 303, does not display any core shift, and that all the offsets are produced by the other two sources. That possibility is implicitly plotted in Fig. 7.6 because the black circle, which marks the core shift of LS I +61 303, is at position (0, 0). However, this assumption is artificial and unrealistic. A more natural consideration is to assume that the core shift of each of the calibrators is only produced on the direction of their extended emission. This restriction breaks the degeneracy because only one position in the core shift diagram is acceptable. By fixing the directions of the core shifts of the two sources, we can find the absolute core shift of the three sources. This result is plotted in Fig. 7.8. The obtained core shift values are quoted in Table 7.3. We note that this approach has provided values for a very specific case based on two conditions. First, all values depend on the assumption that the core shifts of the calibrators are in the direction of their jets imaged at 8.4 GHz with the particular resolution of these observations. We also note that we have assumed that the core shift of the calibrators is constant. This assumption is justified given the stability of the flux density of the calibrators during the 10 days of the campaign. Second, the core shift of

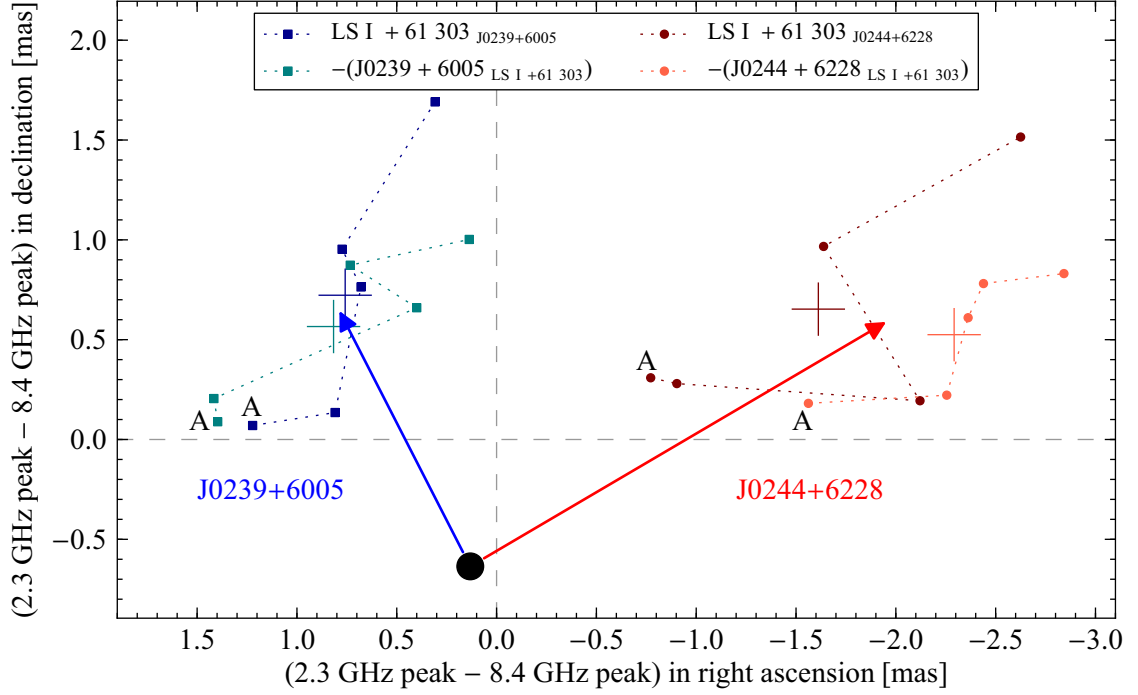


Figure 7.8: Same as in Fig. 7.6 but assuming that the core shift induced by the calibrators, indicated by the arrows, is produced only in the direction of their jets (see Fig. 7.7). Under this assumption, the intrinsic core shift of LS I +61 303 is indicated by the point of the diagram where the two arrows cross (black circle). Therefore we estimate that the core shift of LS I +61 303 is $+0.13$ mas in right ascension and -0.64 mas in declination. We have labelled the points corresponding to run A as a reference of the run order.

LS I +61 303 only accounts for the displacement at a particular range of orbital phases, between 0.446 and 0.747, although it is expected to be variable along the orbit.

Table 7.3: Core shifts, $\Delta \equiv (\vec{r}_{2.3 \text{ GHz}} - \vec{r}_{8.4 \text{ GHz}})$, estimated for the three sources. All the quoted core shifts correspond to average values over the five epochs.

Source	$\Delta_{\text{R.A.}}$ [mas]	$\Delta_{\text{Dec.}}$ [mas]	Δ_{tot} [mas]	$\Delta_{\text{P.A.}}$ [$^{\circ}$]
LS I +61 303	0.13	-0.64	0.65	168.5
J0244+6228	-2.08	1.22	2.18	120.4
J0239+6005	0.66	1.28	1.44	-152.7

We have determined the average core shift of LS I +61 303. However, Fig. 7.8 clearly shows that the core shift is not constant but has a displacement in the South-East/North-

7. VLBI observations of LS I +61 303 within a MAGIC multiwavelength campaign

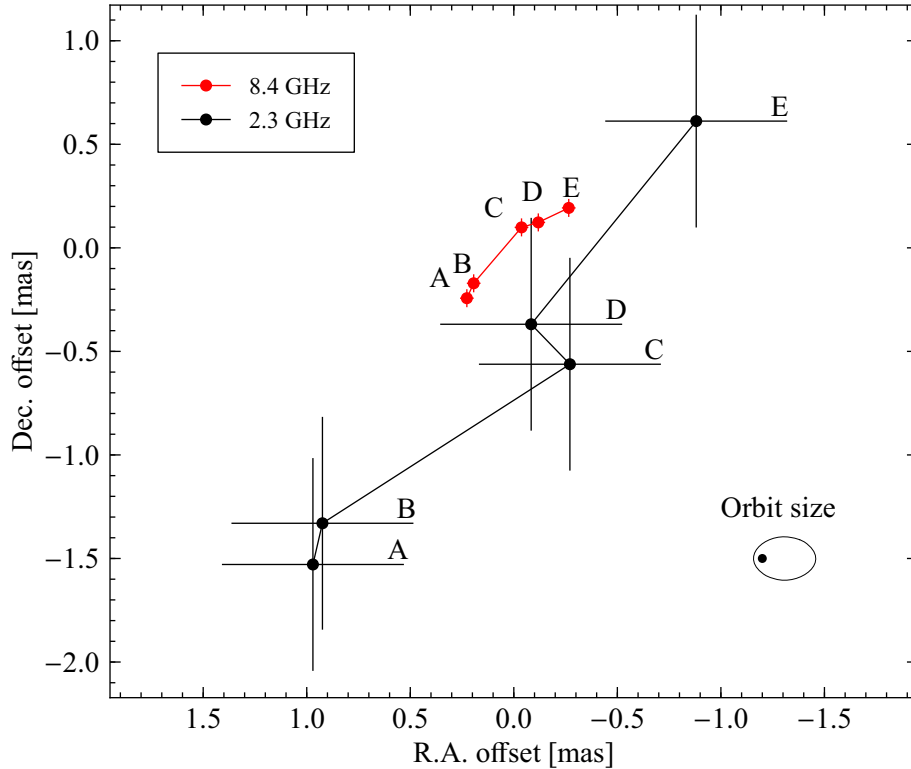


Figure 7.9: Astrometry of LS I +61 303 at 8.4 (red circles) and 2.3 GHz (black circles) for the five runs of project BP141. The origin of coordinates is set to the average position at 8.4 GHz. The error bars show the uncertainties at $1\text{-}\sigma$ level. The estimated uncertainties at 8.4 GHz are 0.03 and 0.04 mas in right ascension and declination, respectively. At 2.3 GHz the uncertainties are 0.4 and 0.5 mas, for right ascension and declination, respectively (see Fig. 7.3).

West direction. We note that the core shift is a relative offset between the position of the peak at 2.3 GHz from the position at 8.4 GHz. This means that, apart from the core displacement at each frequency shown in Fig. 7.3, the 2.3 and 8.4 GHz peaks display changing relative offsets. To show this, the next natural step in the analysis is to match the astrometry at each frequency, which can be done using the average core shift found above for LS I +61 303 (+0.13 mas in right ascension and -0.64 mas in declination). In Fig. 7.9 we show the final astrometry of LS I +61 303 at 8.4 and 2.3 GHz with the correct relative positions.

Finally, Dhawan et al. (2006) obtained an accurate measure of the proper motion of LS I +61 303 from VLBI data spanning from 1991 to 2006. Our astrometry, obtained in 2007, provide a new accurate position relative to the calibrator J0244+6228. The mean value of our five observations, centred at MJD 54351.4479 (orbital phase 0.597), is $\alpha_{J2000.0} = 02^{\text{h}}40^{\text{m}}31^{\text{s}}.663686 \pm 0^{\text{s}}.000004$ (or ± 0.03 mas) and $\delta_{J2000.0} = +61^{\circ}13'45''.59234 \pm$

0''00004 (or ± 0.04 mas), measured with respect to the correlation position of J0244+6228, quoted in Sect. 7.2, which has its own uncertainties in the ICRF. This position is compatible with the proper motion reported in Dhawan et al. (2006).

7.4 Analysis and results II: morphology

7.4.1 Morphology at 8.4 GHz

After obtaining the astrometric results, we self-calibrated the data of LS I +61 303. At 8.4 GHz we used the data from the phase-referenced observations from the calibrator J0244+6228, whereas the data at 2.3 GHz were fringe fitted directly, and then self-calibrated (see below). We performed the self-calibration for each individual data set in AIPS. For each epoch at 8.4 GHz we took the corresponding phase-referenced image and ran CALIB using the image as a model to self-calibrate the phases. The obtained calibrated file was then used to repeat the process. We began with two soft phase (P) self-calibrations with a time interval of 10 minutes. Then we performed an amplitude and phase (A&P) self-calibration with solution interval of 300 minutes (the whole observation). Then, we repeated the P, P, A&P self-calibration steps, reducing the A&P time interval to 60, 25, and 10 minutes. All the process was done using robust 0, and without applying any tapering. The final self-calibrated images were obtained after two more phase self-calibration steps. For a direct comparison with previous results, we produced the final images at 8.4 GHz with an artificial restoring beam of 1.5×1.0 mas², the same used in Dhawan et al. (2006), for direct comparison. The five resulting images at 8.4 GHz are shown in Fig. 7.10, ordered in increasing orbital phase from left to right and from top to bottom. The cross in the middle of each panel indicates the position of run A as a reference, and its size is the astrometric uncertainty at $3\text{-}\sigma$ level as computed from the standard phase reference from the phase calibrator J0244+6228 (see Sect. 7.3 and Fig. 7.3). In the bottom-right panel we include these astrometric results for a quick reference.

The images, obtained every two days, allow us to have a continuous view of the source morphology (see Fig. 7.10). The image from run A shows extended emission towards South-East at orbital phase 0.446. The extended emission contains at least two blobs approximately perpendicular to the main direction of the extended emission. During run B this structure appears divided in three blobs. At orbital phase 0.60, run C, the extended emission appears fainter but at approximately the same P.A. Run D shows that, as this component gets fainter, another component towards North appears. Finally, run E, obtained at orbital phase 0.75 shows how the northern component appears to suffer a rotation of its P.A. of about 45° with respect to the image of run D, whereas the South-East component is not detected.

7. VLBI observations of LS I +61 303 within a MAGIC multiwavelength campaign

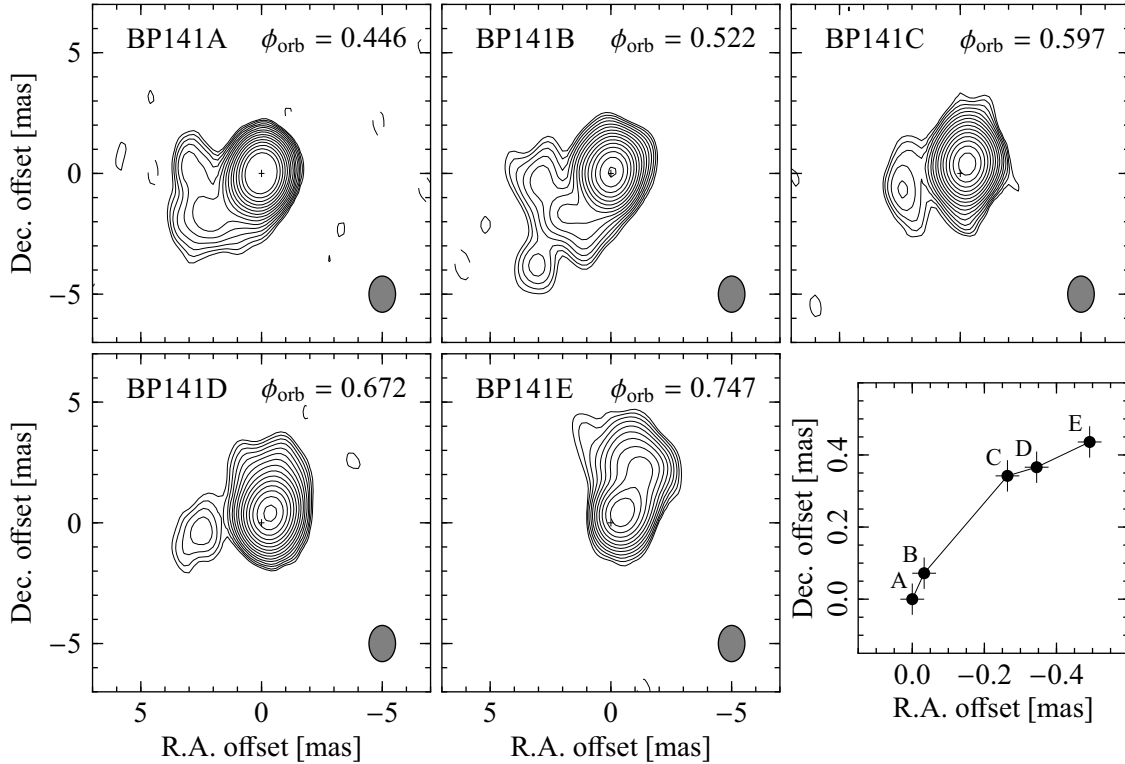


Figure 7.10: Self-calibrated images LS I +61 303 at 8.4 GHz obtained with the VLBA. North is up and East is to the left. The restoring beam, plotted in the lower right corner of each panel, was set to $1.5 \times 1.0 \text{ mas}^2$ at P.A. of 0° for direct comparison with the images in Dhawan et al. (2006). The first contour corresponds to 3 times the rms noise of the image (0.12, 0.10, 0.10, 0.10, and 0.14 mJy beam^{-1} , respectively), while consecutive ones scale with $3^{1/2}$. The cross in the middle of each panel indicates the position of run A as a reference, and its size is the astrometric uncertainty at $3\text{-}\sigma$ level. The central orbital phase during the observations is quoted in the top right corner of each panel. The bottom right panel shows the astrometric results at 8.4 GHz, with uncertainties at $1\text{-}\sigma$ level.

7.4.2 Morphology at 2.3 GHz

A similar procedure was used to self-calibrate the data at 2.3 GHz. As mentioned above, the phase calibrator J0244+6228 is very resolved, and the fringe solutions at this frequency are not good. Therefore, we did not use phase referencing in this case but directly calibrated the phases of LS I +61 303. The self-calibration iterations were similar to the ones described above. To have a better view of the extended emission with a resolution similar to the one used to obtain the images at 8.4 GHz, we produced the final images at 2.3 GHz using a uniform weighting scheme. The obtained synthesised beams at 2.3 GHz were $8.0\text{--}9.2 \times 3.9\text{--}7.3 \text{ mas}^2$ at P.A. between -3 and 10° . The resulting images are shown in Fig. 7.11, together with the astrometry obtained in Sect. 7.3. The crosses plotted in

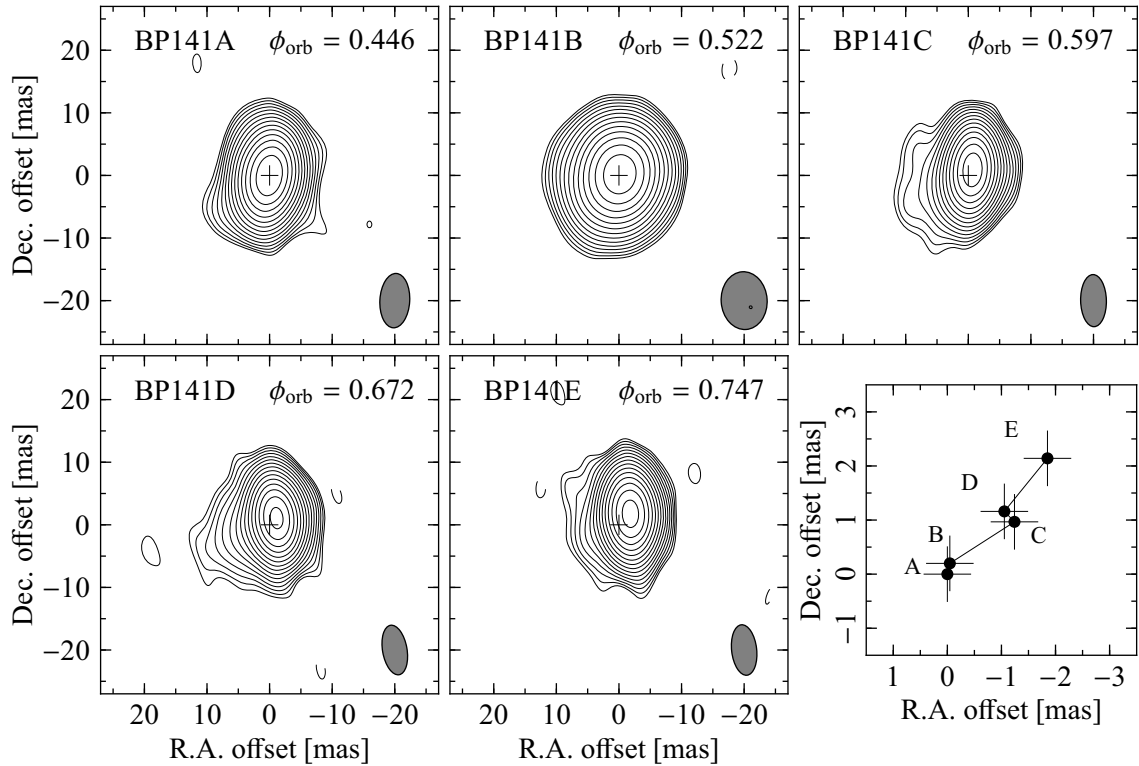


Figure 7.11: Self-calibrated images LS I +61 303 at 2.3 GHz obtained with the VLBA using a uniform weighting scheme. North is up and East is to the left. The restoring beams, plotted in the lower right corner of each panel, are in the range $8.0\text{--}9.2 \times 3.9\text{--}7.3 \text{ mas}^2$ at P.A. between -3 and 10° . The first contour corresponds to 3 times the rms noise of the image (0.16, 0.2, 0.19, 0.17, and 0.16 mJy beam^{-1} , respectively), while consecutive ones scale with $3^{1/2}$. The cross in the middle of each panel indicates the position of run A as a reference, and its size is the astrometric uncertainty at $3\text{-}\sigma$ level. The central orbital phase during the observations is quoted in the top right corner of each panel. The bottom right panel shows the astrometric results at 2.3 GHz, with uncertainties at $1\text{-}\sigma$ level.

each panel indicate the position of the peak of run A, for reference, and its size is the astrometric uncertainty at $3\text{-}\sigma$ level.

The self-calibrated images at 2.3 GHz (Fig. 7.11) show an extended component towards South-East. The component is faint during the first two runs, and appears to grow in flux density and size after the apastron passage (orbital phase 0.73). Remarkably, the peak of the emission is displaced in the opposite direction of the extended emission. The position angle of the extended emission does not change significantly for the last three runs.

In Fig. 7.12 we show a composition of the self-calibrated images LS I +61 303 at 8.4 GHz (red contours) and 2.3 GHz (black contours). The positions of the peaks of the source in each image account for the astrometric results reported in Sect. 7.3.

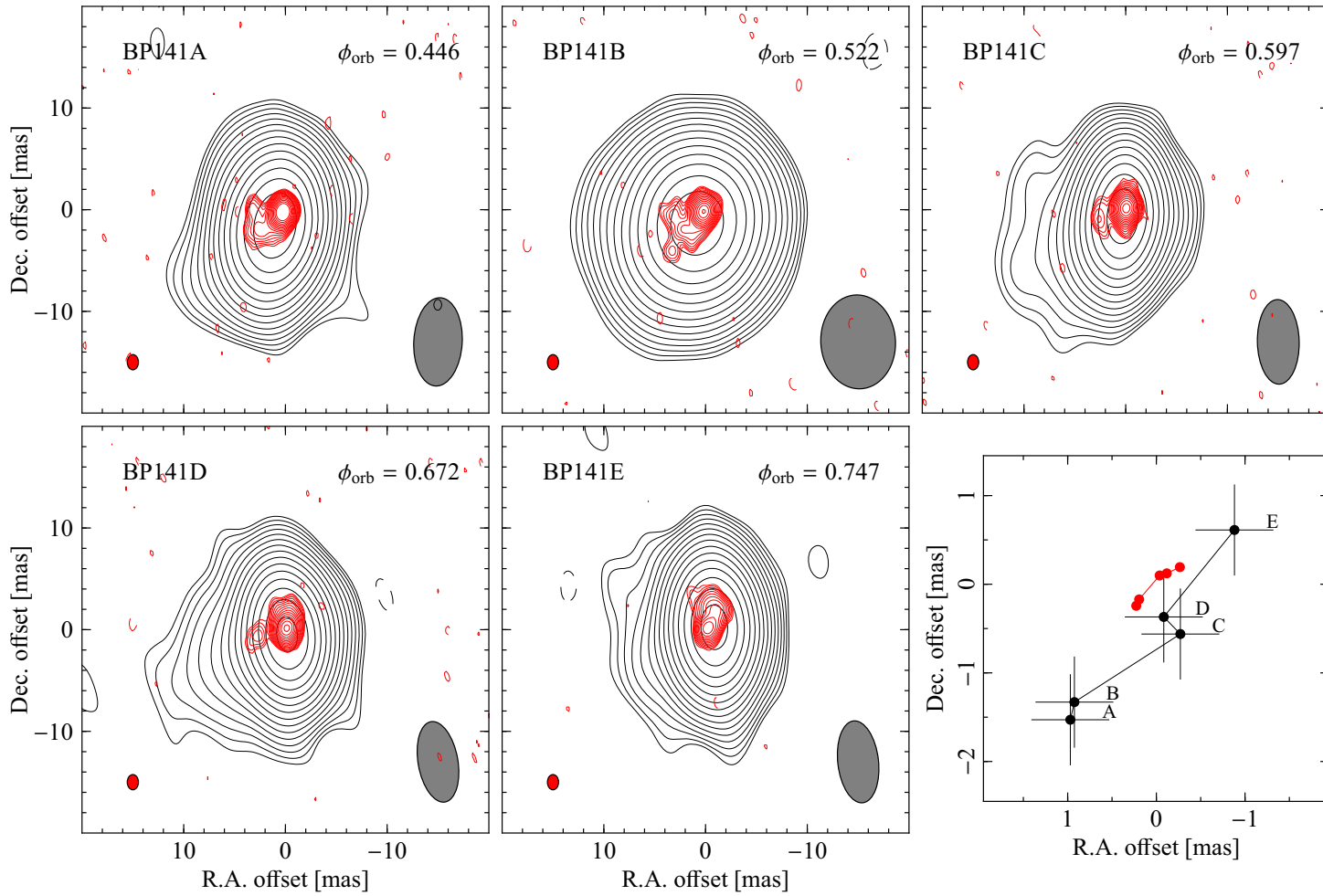


Figure 7.12: Self-calibrated images LS I +61 303 at 8.4 GHz (red contours) and 2.3 GHz (black contours). The images parameters are the same as in Figs. 7.10 and 7.11. The synthesised beam size at 8.4 and 2.3 GHz are plotted in the lower left and lower right corner of each panel, respectively. The astrometry, shown in the lower right panel, contains the relative offsets between frequencies.

7.5 Discussion and conclusions

Our results show that the peak of the emission of LS I +61 303 at 8.4 GHz moves from South-East to North-West between orbital phases 0.446 and 0.747. The total displacement is about -0.50 mas in right ascension and $+0.45$ mas in declination, with uncertainties of 0.03 and 0.04 mas in right ascension and declination, respectively. This relative astrometry agrees with the previous astrometry at 8.4 GHz presented in Dhawan et al. (2006) and Massi et al. (2012) for observations obtained 1 year before, and at similar orbital phases. In the case of the observations at 2.3 GHz we measured a continuous displacement of the peak of the emission, not seen before, thanks to the inverse phase referencing astrometry. The peak of the emission at 2.3 GHz shows a displacement in the same direction found at 8.4 GHz, with a total offset of approximately -2 mas in right ascension and $+2$ mas in declination, with estimated uncertainties of 0.4 and 0.5 mas in right ascension and declination, respectively.

We have also been able to estimate the real offset between the peaks at 2.3 GHz and the peaks at 8.4 GHz (core shift). This is just a tentative estimate that is limited by the assumptions described in Sect. 7.3 and the observation’s structure, not optimised for this kind of measurements. We have estimated the core shifts for LS I +61 303 and the two phase calibrators. For LS I +61 303 we see that the 2.3 GHz peaks are displaced with respect to the 8.4 GHz peaks $+0.1$ mas in right ascension and -0.6 mas in declination on average (black circle in Fig. 7.8). However, the core shifts of the individual runs also show a drift from South-East to North-West. It is important to note that we have two superposed relative displacements. On one hand, the peak of the emission at both frequencies are displaced from South-East to North-West for runs A–E (see Fig. 7.3). On the other hand, the core shift also changes in the same direction and sense: the 2.3 GHz peak is located towards South-East from the 8.4 GHz peak at orbital phase 0.446, and changes towards North-West at orbital phase 0.747 (see Fig. 7.9). Consequently, the 2.3 GHz peak “overtakes” the 8.4 GHz peak in ten days. Below we discuss these changes considering also the morphological changes.

We note that the core shifts found for the two extragalactic calibrators, of the order of 2.2 and 1.4 mas (see Table 7.3), are larger than the mean core shift measured for other AGN jets, which are in general below ~ 1.5 mas (see Fig. 6 in Sokolovsky et al. 2011). The most natural explanation for our large core shifts is that the measured shifts are not only due to intrinsic core shifts of the sources, but also due to a bias caused by the poor resolution at 2.3 GHz for the calibrators, affected by Galactic scatter broadening (see Sect. 7.2). This agrees with the different shifts quoted in Table 7.3 because the values obtained for J0244+6228, which suffers an important scatter broadening, are larger than the shifts obtained for J0239+6005, which is significantly more compact.

In summary, the obtained astrometry shows a clear correlation between the peak displacements at 8.4 and 2.3 GHz. The relative astrometry at 8.4 GHz between orbital phases 0.446 and 0.747 shows the same behaviour already seen at the same orbital phases from

7. VLBI observations of LS I +61 303 within a MAGIC multiwavelength campaign

observations conducted one year before. We note that, however, we do not measure a significant displacement of the peak at orbital phase 0.75, as seen in the data from project BD117 (Dhawan et al. 2006; Massi et al. 2012).

Morphology of LS I +61 303

We can now discuss the morphology of the self-calibrated images of LS I +61 303. The first three images are very similar to the images from project BD117 obtained at orbital phases 0.450 and 0.600, respectively (see Dhawan et al. 2006 and Massi et al. 2012). However, the extended component at orbital phase ~ 0.75 is very different: towards North in our case, and towards South for BD117. On the other hand, the EVN image in Massi et al. (1993), obtained at orbital phase 0.74 but in June 1990, also shows a component towards North, although with a P.A. of $\sim 30^\circ$, significantly different to the one found here. We note that the astrometry for this orbital phase for BD117 shows a very significant displacement, which is not found in our data. This displacement, only seen in the data from BD117, and the consistent evolution of the northern component in our data for runs D and E suggest that the morphology in BD117 at orbital phases around 0.75 is affected by some transient phenomena, possibly related to the high-energy outburst and/or variations in the circumstellar equatorial disc (see below). Only new images obtained during different orbital cycles around orbital phases 0.7–0.8 can verify this. On the other hand, the morphology seen at 8.4 GHz between orbital phases ~ 0.45 – 0.60 is very similar to the one in the images at 2.3 GHz at orbital phases ~ 0.60 – 0.75 . This suggests that the low frequency structure is following the behaviour of the structure at 8.4 GHz but at larger scales and with a time delay of more than one day.

In Fig. 7.12 we show the morphology of LS I +61 303 at 8.4 and 2.3 GHz superimposed taking into account the astrometric displacements between epochs and between frequencies. We can see that the peak of the emission at 2.3 GHz approximately follows the behaviour of the extended emission at 8.4 GHz (from South-East to North-West). On the other hand the extended emission at 2.3 GHz shows a morphology similar, although at larger scales, to the morphology seen at 8.4 GHz a few days before. This is clearly showing the inertia of the outflow. These changes are expected in the context of the young non-accreting pulsar scenario when there is a significant change in the projected direction of the velocity of the pulsar (see the model sketch in Fig. 5.8 on page 81). In this context, it is also expected to see the displacement of the peak of the emission opposite to the extended emission, as shown for instance in the 2.3 GHz image of run D (Fig. 7.11).

In previous works the P.A. of the extended emission from one run to the next one appears to change counter-clockwise during the whole orbital cycle. However, the extended emission at 8.4 GHz observed at orbital phase 0.747 (run E) in our data appears to rotate clockwise with respect to the P.A. of the northern component detected at orbital phase 0.672 (run D). Also, the images at 8.4 GHz show that the extended emission of the source appears to be composed of several components. Remarkably, at orbital phase 0.672

(run D), there is one component towards South-East and one towards North, i.e., with a P.A. difference of $\sim 90^\circ$. These two striking results are not easy to explain in any of the proposed scenarios, and more data would be needed to understand the real behaviour of LS I +61 303. The most natural explanation appears to be related to the properties of the circumstellar disc surrounding the star. The truncated equatorial circumstellar disc of LS I +61 303 displays long-term variations with a periodicity of 4.6 yr, as seen in the properties of the H_α line (Zamanov et al. 1999). These variations could explain the differences with the previous observations of 2006. McSwain et al. (2010) recently reported strong variability during the orbital cycle in the H_α line, with dramatic emission bursts shortly before apastron ($\phi_{\text{apastron}} = 0.73$). The highly perturbed material of the equatorial disc, and the tidal streams of this material, are probably the origin of the differences between the radio morphologies shown by LS I +61 303 at similar orbital phases corresponding to different cycles.

Conclusions

As a conclusion of this work, we see that LS I +61 303 shows stable properties from VLBI images obtained at different epochs, separated by years, which suggest that the changing morphology is in general stable. However, significant changes are seen at particular orbital phases, for instance at phase ~ 0.75 . These changes might be related to stochastic interactions between the stellar equatorial disc and the compact object/outflow, or could also be caused by some recurrent phenomena related to the outburst at different wavelengths. The obtained astrometry and changing morphology is similar to the one expected from an outflow whose axis passes close to the line of sight of the observer. This can be explained by the young non-accreting pulsar scenario (see Dubus 2006), and it is expected from a model similar to the one described in Chapter 5. Therefore, these results suggest that LS I +61 303 contains a young non-accreting pulsar and that its high-energy emission is powered by rotational energy instead of by accretion.

8

Study of new gamma-ray binary candidates

8.1 Introduction

In previous chapters we have described in detail the radio emission of the “classical” gamma-ray binaries PSR B1259–63, LS 5039, and LS I +61 303, which are known to display HE and VHE emission, and extended radio structures. However, as explained in Chapter 1, the scarce number of robust gamma-ray binaries, together with the wide variety of properties, show the necessity to expand the number of gamma-ray binaries in order to better understand these systems. Three sources have been proposed to be new gamma-ray binaries, namely HESS J0632+057 (Hinton et al. 2009), AGL J2241+4454 (Williams et al. 2010), and 1FGL J1018.6–5856 (Fermi LAT Collaboration et al. 2012a), and it is expected that they contain relativistic outflows producing radio emission at AU scales. Consequently, the detection of radio structures at mas scales in these candidates by means of VLBI observations would allow us to compare them with the already known sources and broaden our knowledge on this population as a whole.

With this motivation we have conducted two projects aimed to obtain the VLBI radio counterpart of high-energy sources suspected to be gamma-ray binaries. On one hand, the VHE source HESS J0632+057 was proposed to be related to the Be star MWC 148 (HD 259440). Following an X-ray outburst in February 2011, we conducted a ToO e-EVN observation that revealed for the first time the compact radio emission of the source, and unambiguously identified the Be star MWC 148 with a transient and non-thermal radio emitter, strongly supporting this association¹.

¹Published in Moldón, J., Ribó, M., & Paredes, J. M. 2011, A&A, 533, L7.

8. Study of new gamma-ray binary candidates

On the other hand, we conducted a VLBI campaign to search for the radio counterpart of the gamma-ray binary candidate AGL J2241+4454, whose proposed optical counterpart is MWC 656/HD 215227. However, the search was not fruitful for this source, for which most of the parameters were unknown at the time of the observations (between January and February 2011). In particular, the orbital period was suggested to be ~ 60 days, but no information on the phase of the periastron passage was available. Also, no previous radio observations had revealed its flux density or light curve. At the time of writing this thesis the binary parameters have been determined (Casares et al. 2012b), although the source has not yet been detected in the radio band.

8.2 The gamma-ray binary candidate HESS J0632+057

8.2.1 Introduction

HESS J0632+057 was suggested to be a candidate to the selected group of gamma-ray binaries. The H.E.S.S. Collaboration discovered the point-like TeV source HESS J0632+057 (Aharonian et al. 2007), which was variable at TeV energies (Acciari et al. 2009b). The source has a variable X-ray counterpart (Hinton et al. 2009; Acciari et al. 2009b), as well as a variable radio counterpart (Skilton et al. 2009). The massive B0pe star MWC 148 (HD 259440), located at ~ 1.5 kpc, was proposed as the optical counterpart (Hinton et al. 2009). The SED from radio to TeV energies is very similar to the one of LS I +61 303, which also contains a Be star (Hinton et al. 2009). All these results suggest that HESS J0632+057 is a new gamma-ray binary, displaying an SED one order of magnitude fainter than LS I +61 303. This is an important fact that could shed light on the luminosity distribution of this new population of binary systems in the Galaxy.

The properties of the main star were described in Aragona et al. (2010), who did not detect radial velocity shifts, ruling out periods shorter than ~ 100 days. The mass of the star is $13.2\text{--}19.0 M_{\odot}$, and has a radius of $6.0\text{--}9.6 R_{\odot}$. Recently, a periodicity of 321 ± 5 d was revealed thanks to long-term X-ray observations conducted with *Swift*/XRT, strongly supporting the binary nature of the source (Bongiorno et al. 2011). This orbital period is between the period of PSR B1259–63 (1237 days) and the one of LS I +61 303 (26.5 days). The reported X-ray light curve, covering three orbital cycles, shows a bright peak and a fainter secondary peak separated ~ 0.5 in phase. Finally, the source was identified as a binary system in Casares et al. (2012b). These authors found an eccentricity of 0.83 ± 0.08 , a mass function of $0.06^{+0.15}_{-0.05} M_{\odot}$, an argument of the periastron of the optical star of $129 \pm 17^{\circ}$, which occurs at orbital phase 0.967 ± 0.008 . The nature of the compact object is unknown, with a possible mass in the range $1.3\text{--}7.1 M_{\odot}$.

How to detect VLBI emission from HESS J0632+057?

Based on the extended and variable radio structures detected in other gamma-ray binaries HESS J0632+057 is expected to display faint emission at mas scales as well. However, it is difficult to make predictions on the best epoch to conduct the observations based on the behaviour of the other gamma-ray binaries. The radio structures in LS 5039 are variable but are detected along all its short orbital period (Moldón et al. 2012a and Chapter 5). LS I +61 303 shows radio outbursts close to apastron (Gregory 2002), and extended emission during all the orbital cycle (Dhawan et al. 2006). PSR B1259–63 shows transient and extended radio emission close to periastron (Moldón et al. 2011a). Because of the variety of orbital phases in which enhanced flux density and/or extended emission is detected, it is not possible to find the optimal time to observe HESS J0632+057. Also, we note that before 2011 the only orbital information about the system was that the orbital period should be > 100 days (Aragona et al. 2010). Moreover, no radio light curve was available, although the source was known to display non-persistent radio emission with a flux density of ~ 0.7 mJy at 1.3 GHz (Skilton et al. 2009). With no good reference from the other binaries, and without a radio light curve for HESS J0632+057, it was not possible to plan the best epoch to conduct VLBI observations for this faint source. Fortunately, an X-ray/gamma-ray outburst occurring in early 2011 was the best opportunity to organise VLBI observations of HESS J0632+057 aimed to reveal the radio structure of the source.

The multiwavelength outburst of early 2011

There was a bright X-ray outburst of HESS J0632+057 in February 2011. Falcone et al. (2011) reported increased X-ray activity detected by *Swift*/XRT between January 23 and February 6, 2011 (MJD 55584–55598). The VERITAS Collaboration reported increased activity at energies above 300 GeV between February 7 and 8, 2011 (MJD 55599–55600) (Ong 2011). The MAGIC Collaboration reported increased gamma-ray flux above 200 GeV during February 7–9, 2011 (MJD 55599–55601) (Mariotti 2011), confirming the VHE active state and lowering the measured energy threshold (Aleksić et al. 2012a). During the outburst, we conducted two e-VLBI observations with the European VLBI Network (EVN) in Target of Opportunity (ToO) mode to explore the radio emission of HESS J0632+057 at mas scales².

In the first part of this Chapter we present the first VLBI images of HESS J0632+057, obtained during and after the high-energy activity period in 2011. Thanks to the rapid response of the EVN, the preliminary results were presented as an Astronomer’s Telegram (Moldón et al. 2011b) shortly after the X-ray/gamma-ray outburst. The observations and data reduction are described in Sect. 8.2.2. The results can be found in Sect. 8.2.3. A discussion of these results in the context of gamma-ray binaries can be found in Sect. 8.2.4.

²We thank the EVN PC Chair, Tiziana Venturi and the EVN scheduler Richard Porcas for supporting our ToO observations and to the EVN stations who made this possible

8. Study of new gamma-ray binary candidates

Table 8.1: Log of the observations and parameters of the corresponding images.

Run	Date Y-M-D	MJD	ϕ_{orb}	Num. anten.	HPBW _{size} [mas ²]	HPBW _{P.A.} [°]	rms [$\mu\text{Jy beam}^{-1}$]
A	2011-02-15	55607.83	0.34 ± 0.04	7	36×23	2	50
B	2011-03-17	55637.75	0.43 ± 0.04	12	35×19	-7	13

8.2.2 Observations and data reduction

Following the report of X-ray activity from HESS J0632+057 between January 23 and February 6, 2011 (Falcone et al. 2011), we observed the source with the EVN in target of opportunity (ToO) mode in two epochs separated by 30 days (~ 0.1 orbital phases). The EVN project codes for the observations are RR005 and RM006, respectively. From now on, we will refer to the observations of RR005 as run A, and to the observations of RM006 as run B. A log of the observations is shown in Table 8.1. The first radio continuum observation (run A) was conducted at 1.6 GHz (18 cm) during eight hours on February 15, 2011 (MJD 55607), UTC 15:50 to 00:00. The antenna network consisted of seven antennas: Effelsberg, Jodrell Bank Lovell, Medicina, Onsala, Torun, Westerbork, and Hartebeesthoek, providing baselines ranging from 200 to 8000 km (200 to 1000 km without Hartebeesthoek). A data rate of 1024 Mbps per station was directly streamed to the central processor at JIVE and correlated in real time (e-VLBI). The rapid response of the e-EVN observations and correlation allowed us to perform a second ToO (run B) based on the results from the first run in a disc-recorded session. The observations were conducted with 12 EVN antennas: Effelsberg, Jodrell Bank Lovell, Medicina, Onsala, Torun, Westerbork, Hartebeesthoek, Svetloe, Badary, Zelenchukskaya, Nanshan (Urumqi), and Sheshan (Shanghai), providing baselines ranging from 200 to 10000 km. The observation lasted ten hours and was conducted on March 17, 2011 (MJD 55637), UTC 13:00 to 23:00, with a data rate of 1024 Mbps. This second epoch provides considerably better sensitivity. A sketch of the orbit in an arbitrary orientation and seen from above is shown in Fig. 8.1, where we indicate the phases of the observations.

Both observations have a similar structure, switching between HESS J0632+057 and the phase reference calibrator J0619+0736, separated $3^\circ 9'$, with cycling times of five minutes to avoid losing phase coherence. The phase reference calibrator was correlated at the position $\alpha_{\text{J2000.0}} = 06^{\text{h}}19^{\text{m}}09^{\text{s}}.9710$ and $\delta_{\text{J2000.0}} = 07^\circ 36' 41''.220$ in the frame of the ICRF (Goddard VLBI global solution 2010a³). This position has absolute uncertainties of 2.0 and 1.1 mas in right ascension and declination, respectively. The fringe finders DA193, 3C147, and OQ208 were observed during run A and 0528+134, and DA193 during run B.

³<http://gemini.gsfc.nasa.gov/solutions/2010a/2010a.html>

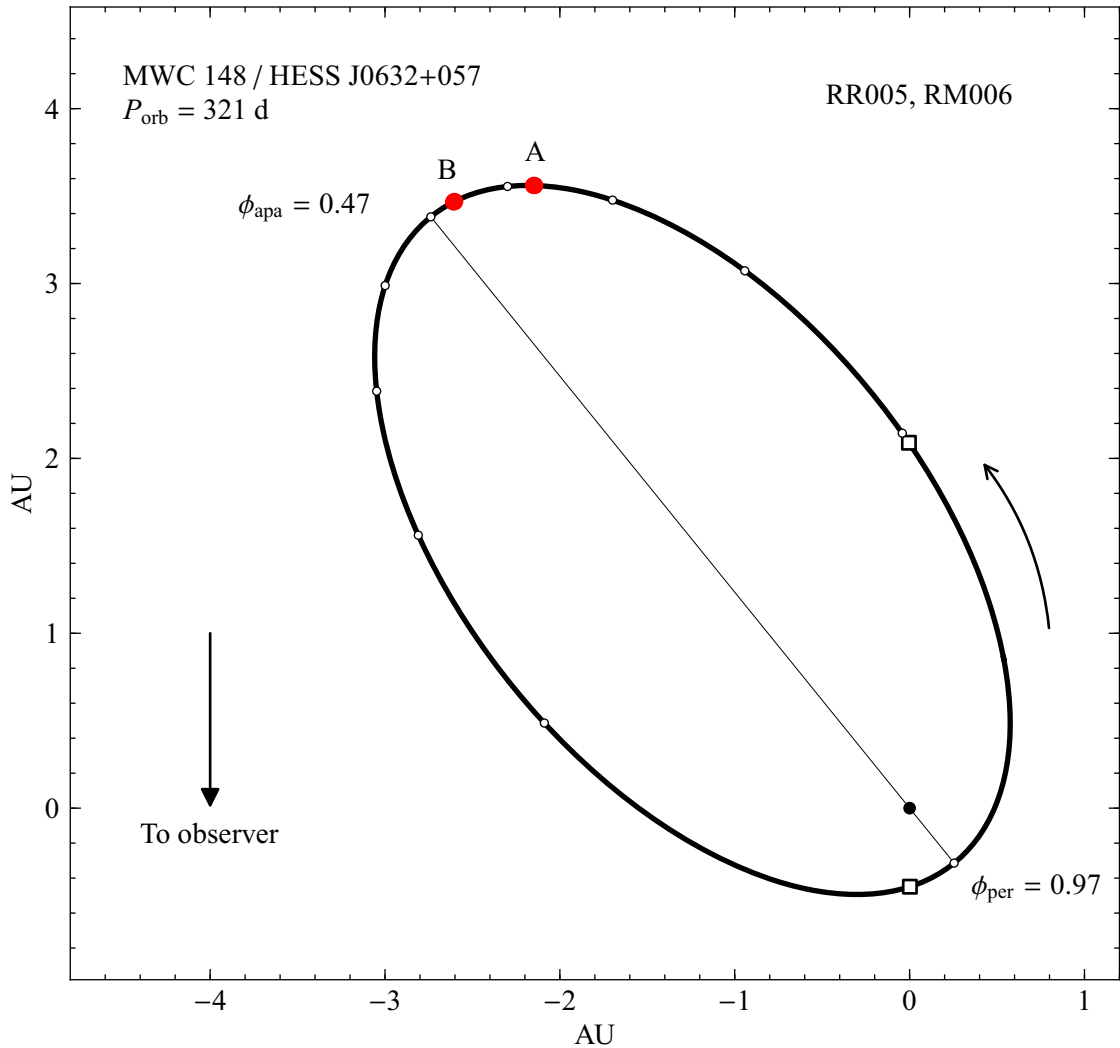


Figure 8.1: Sketch of the orbit of MWC 148/HESS J0632+057 with the position of the compact object during the observations of projects RR005 and RM006 marked as red circles. The white dots are plotted every 0.1 orbital phases. The empty squares mark the inferior and superior conjunction of the compact object, which occur at orbital phases 0.961 and 0.063, respectively. The orbit was computed using the orbital solution reported in Casares et al. (2012b). The orbit and the size of the star are scaled to the real values. The orientation of the orbit is arbitrary, and it is seen face-on (see Fig. A.2 on page 180 for examples of other possible projections of the orbit).

The data reduction was performed using AIPS⁴. Flagging based on predicted off-source times, owing to slewing or failures, was applied using UVFLG. A priori visibility amplitude calibration used the antenna gains and the system temperatures measured at each station.

⁴The NRAO Astronomical Image Processing System. <http://www.aips.nrao.edu/>

8. Study of new gamma-ray binary candidates

The amplitude calibration was improved by scaling the individual antenna gains by a factor obtained from the phase calibrator and fringe-finder models. We used ionospheric total electron content (TEC) models based on GPS data obtained from the CDDIS data archive⁵ to correct the global phase variations due to the ionosphere. The parallactic angle correction was applied with VLBPANG. Fringe fitting on the phase reference calibrator (without an input model) was performed with the AIPS task FRING, and the solutions were applied to the target source. The instrumental bandpasses were corrected using BPASS. The data were averaged in frequency and time, and clean images were produced with IMAGR. A cell size of 1 mas was used for cleaning both epochs. The images were produced using a weighting scheme with robust parameter 0 for run A, and 2 (which is slightly more sensitive to extended emission) for run B. A tapering of 30 $M\lambda$ was applied to avoid the presence of possible unreliable high-resolution features due to sidelobes of the synthesized beam. No self-calibration of the data was possible because of the low flux density of the target source.

8.2.3 Revealing the extended emission of HESS J0632+057

The resulting VLBI images at 1.6 GHz are shown in Fig. 8.2. The synthesized beam (HPBW) size and P.A., and the rms of the images are listed in Table 8.1. Run A shows a $410 \pm 90 \mu\text{Jy}$ point-like source. Run B, observed 30 days later, shows a $180 \pm 30 \mu\text{Jy}$ (measured using TVSTAT within AIPS) faint source with extended emission towards North. The rms noise close to the source is $50 \mu\text{Jy beam}^{-1}$ and $13 \mu\text{Jy beam}^{-1}$ for run A and B, respectively. In Table 8.2 we show the parameters of the fitted components to the source (Gaussian components obtained with JMFIT within AIPS). Although in run A no extended emission is detected, we note that extended emission with a flux density similar to the one seen in the image from run B could not be detected in the image from run A because of the much higher rms noise of the image from run A. The first contour in Fig. 8.2 corresponds to 3 times the rms noise.

The emission in run A is well described by a single component located at $\alpha_{\text{J2000.0}} = 06^{\text{h}}32^{\text{m}}59^{\text{s}}.2567(1)$ and $\delta_{\text{J2000.0}} = 05^{\circ}48'01''.162(2)$. The values in parentheses refer to the uncertainty in the last digit (1.3 and 2 mas, respectively), and correspond to the formal errors of the fit. Run B is described well by a point-like core (see Table 8.2) and an extended component (B2, which has an intrinsic P.A. of $4 \pm 20^{\circ}$) located at 21 ± 6 mas in P.A. $30 \pm 10^{\circ}$ with respect component B1. The total extension of the source is ~ 50 mas.

The relative astrometry shows that the peak of the emission suffers a total displacement of 14 ± 3 mas in P.A. $190 \pm 9^{\circ}$ between runs A and B. This displacement is aligned with the direction of the extended emission. The separation between the peak positions corresponds to a projected linear distance of 21 ± 5 AU. Covering this distance in the 30 days between runs requires a constant projected velocity of $1200 \pm 300 \text{ km s}^{-1}$.

⁵The Crustal Dynamics Data Information System <http://cddis.nasa.gov/>

8.2. The gamma-ray binary candidate HESS J0632+057

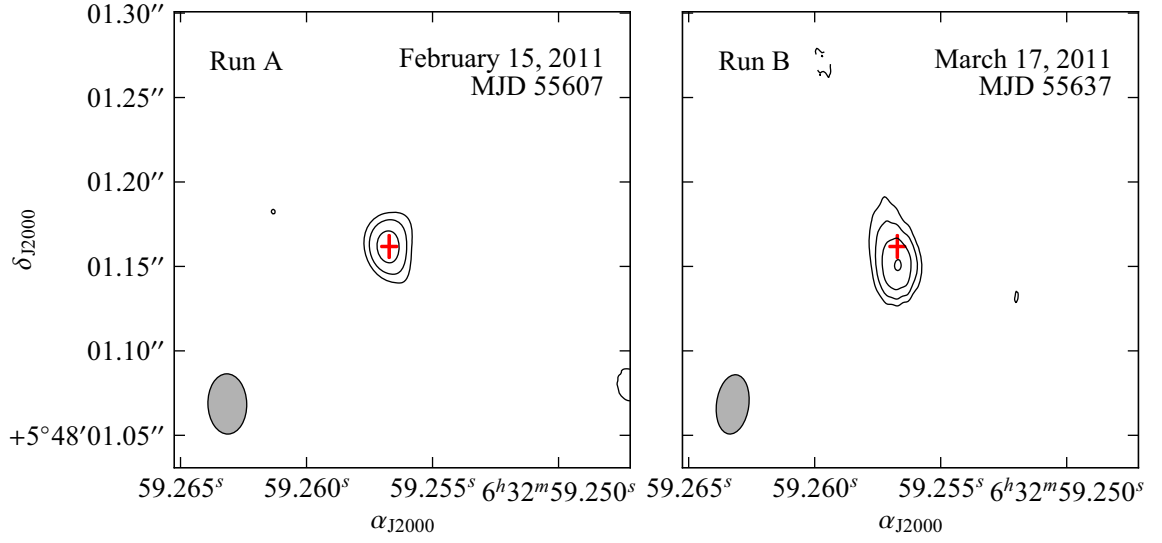


Figure 8.2: EVN radio images of HESS J0632+057 at 1.6 GHz during the X-ray outburst and 30 days later. North is up and East to the left. The observation dates are quoted at the top of each panel. The synthesized beam (see Table 8.1) is displayed in the bottom-left corner of each image. The red crosses mark the position and 3σ uncertainty of the fitted component of run A. For each image, the displayed contours start at 3σ and increase by factors of $2^{1/2}$; the $1\text{-}\sigma$ rms close to the source is $50 \mu\text{Jy beam}^{-1}$ in run A and $13 \mu\text{Jy beam}^{-1}$ in run B.

Table 8.2: Parameters of the Gaussian components fitted to the images. For each component the peak and flux density are shown in columns 3 and 4, the relative astrometry with respect to the core of run A is shown in columns 5 and 6, for right ascension and declination, respectively. The size of the components is shown in columns 7 and 8. The position angle of component B2 is $4 \pm 20^\circ$.

Run	Comp.	S_{peak} [$\mu\text{Jy b}^{-1}$]	$S_{1.6 \text{ GHz}}$ [μJy]	$\Delta\alpha$ [mas]	$\Delta\delta$ [mas]	Maj. Axis [mas]	Min. Axis [mas]	Type
A	A1	340 ± 50	410 ± 90	—	—	12 ± 13	12 ± 10	Point-like
B	B1	81 ± 14	90 ± 25	-3 ± 2	-14 ± 3	9 ± 11	12 ± 12	Point-like
	B2	56 ± 13	110 ± 40	6 ± 3	5 ± 6	48 ± 18	11 ± 10	Extended

8.2.4 Discussion

The first VLBI image of HESS J0632+057 at 1.6 GHz, taken a few days after the peak of the X-ray/gamma-ray outburst in January–February 2011, shows a compact $410 \mu\text{Jy}$

8. Study of new gamma-ray binary candidates

point-like source (see Fig. 8.2). After 30 days, the source displays one-sided extended emission with a total flux density of $180 \mu\text{Jy}$ and with an extension of 50 mas (75 AU assuming a distance to the system of 1.5 kpc) in P.A. 30° . The peak of the emission is displaced 14 mas (21 AU) in P.A. 190° . We note that, given the rms noise of the first image, the $3\text{-}\sigma$ flux density threshold is above the flux density of the extended emission in the second image.

The semimajor axis of the orbit is 2.4 ± 0.1 AU, which corresponds to a projected angular distance of 1.6 ± 0.1 mas. However, we can see in Fig. 8.1 that the positions of the compact object during the two observations are within ~ 0.5 AU, or 0.2 mas. The peak displacement reported here, 14 ± 3 mas, cannot be explained by this or any other motion within the orbit.

The measured position in run A is clearly compatible with the UCAC3 catalogue position of the Be star MWC 148, which has an uncertainty of 14 mas in each coordinate (Zacharias et al. 2010). In Fig. 8.3 we show a wide area around MWC 148, where we mark the positions and uncertainties of previous radio and X-ray identifications (left panel), and our identification with the optical star (right panel). Given the positional coincidence at mas scales, the detected compact radio emission is unambiguously related to the Be star MWC 148. We computed the proper motion of the source using the position from run A with an uncertainty of 25 mas to include possible peak displacements, the position of MWC 148 from UCAC3, obtained at mean epoch 1984.2 (Zacharias et al. 2010), and the VLA-D and GMRT positions from Skilton et al. (2009) (with uncertainties of 300 and 500 mas, respectively). Despite the time span of 27 years of observations, the proper motion is compatible with no motion. The result is $\mu_\alpha \cos(\delta) = 0.2 \pm 1.0 \text{ mas yr}^{-1}$ and $\mu_\delta = -0.2 \pm 0.9 \text{ mas yr}^{-1}$. However, we note that this proper motion is computed from data obtained from very different instruments, observing at different frequencies and resolutions.

The brightness temperature corresponding to the radio source in run A (see Table 8.2) at 1.6 GHz is 2×10^6 K. Such a high value, together with non-simultaneous radio observations suggesting a negative spectral index around ~ -0.6 (Skilton et al. 2009), rules out a thermal emission mechanism. Non-thermal synchrotron radiation remains, therefore, as the most plausible interpretation for the HESS J0632+057 radio emission. In this case, and assuming equipartition between the relativistic electrons and the magnetic field, the observed properties correspond to a total energy between 0.1 and 100 GHz of 4×10^{38} erg, with an equipartition magnetic field of ~ 0.02 G. These values are approximately ten times fainter than those obtained for LS 5039 from VLBI observations (Paredes et al. 2000).

Comparison with other gamma-ray binaries

The gamma-ray binaries PSR B1259–63, LS 5039, and LS I +61 303 show a radio morphology with a central core and one-sided extended radio emission on scales of a few AU, although bipolar extended emission has also been detected at some orbital phases

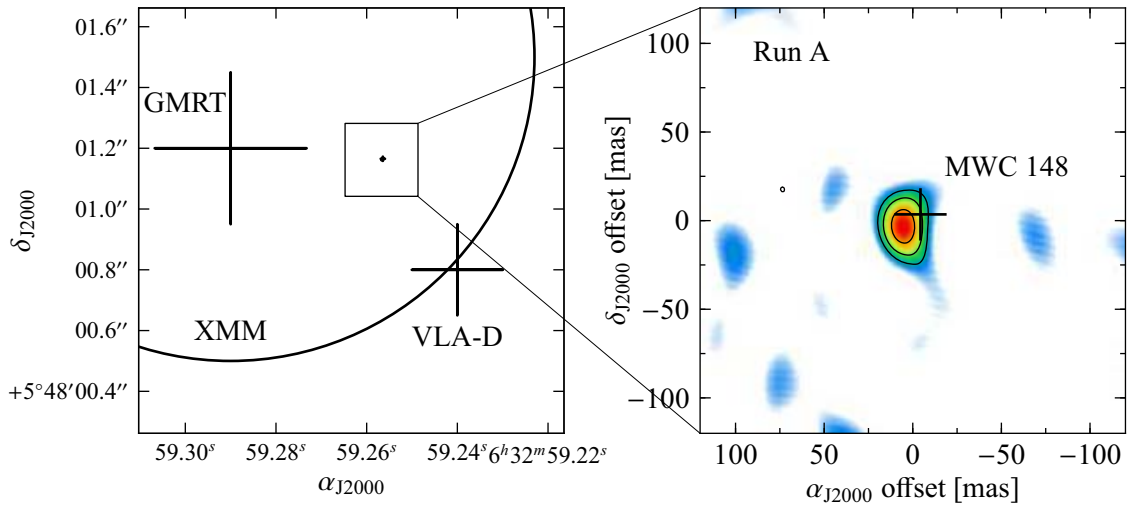


Figure 8.3: *Left*: sketch of the area around HESS J0632+057. We indicate the positions and uncertainties of the X-ray and radio counterparts of the source. *Right*: zoom of the area close to the optical star MWC 148. The star position is displayed as a black cross, whose size indicates the optical position uncertainty at $3\text{-}\sigma$ level. The colour scale shows the image from run A.

(Dhawan et al. 2006; Ribó et al. 2008; Moldón et al. 2011a,c, 2012a). In all these cases, the authors found morphological changes on time scales shorter than the orbital period, and displacements of the peak of the emission bigger than the orbit size. The morphology and peak displacement reported here show that the radio emission of HESS J0632+057 is similar to the ones observed in the other known gamma-ray binaries, suggesting a similar nature for HESS J0632+057, as later confirmed by Casares et al. (2012b).

In Fig. 8.4 we show the phase-folded light curve of the X-ray data from Bongiorno et al. (2011), together with radio (top panel) and TeV (bottom panel) data. Our two EVN measurements suggest a radio flux decrease of the most compact region of the source similar to the X-ray one after the outburst, although at a slower rate. However, a VLBI monitoring of the outburst is required to understand the flux changes better. On the other hand, a persistent and higher flux was measured in previous lower resolution GMRT observations at a similar frequency up to ~ 100 days after the outburst. This can be explained by the presence of diffuse emission, which is lost on VLBI scales (the shortest significant baseline in our data samples spatial frequencies around $1\text{ M}\lambda$, which corresponds to angular scales of 200 mas).

LS I +61 303 shows an X-ray outburst before apastron that is correlated with the TeV outburst (Anderhub et al. 2009; Zabalza et al. 2011). The duration of the X-ray outburst of HESS J0632+057 is ~ 5 times longer (although ~ 0.1 in phase in both cases). Although

8. Study of new gamma-ray binary candidates

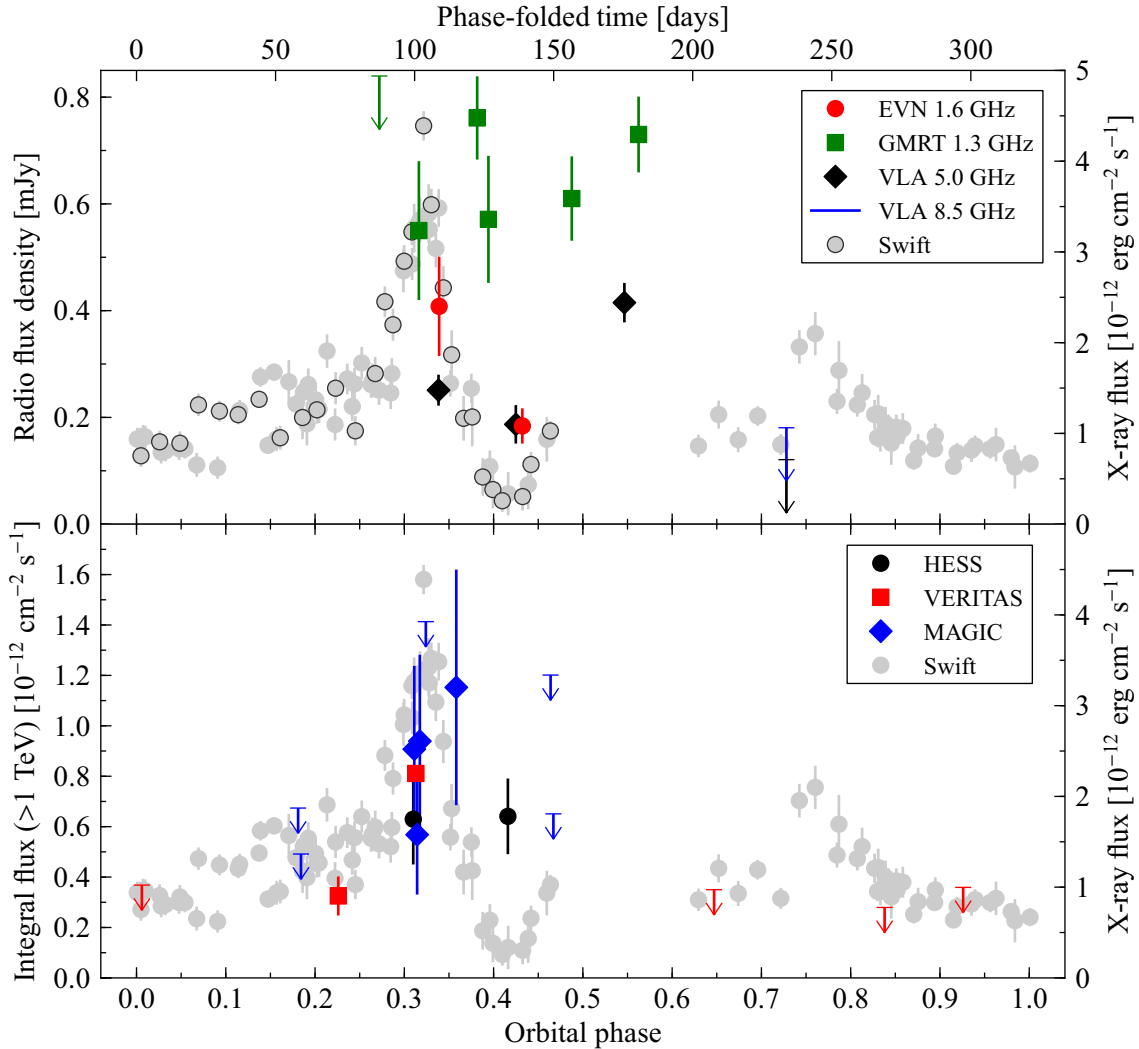


Figure 8.4: Multiwavelength light curve of HESS J0632+057. The data were folded with a period of 321 days. Zero phase has been arbitrarily defined at MJD 54857 (Bongiorno et al. 2011), while periastron passage takes place at orbital phase 0.97. The grey circles are X-ray observations by *Swift*/XRT (0.3–10 keV) from Bongiorno et al. (2011). *Top*: the red circles are the EVN observations from this work. The other radio data are from Skilton et al. (2009). The black circles (filled in grey) are *Swift*/XRT data obtained during the same cycle as the EVN data. *Bottom*: TeV emission from Acciari et al. (2009b); Ong (2011); Mukherjee (2011); Aleksić et al. (2012a).

for HESS J0632+057 the X-ray outburst and the TeV emission have been detected at similar orbital phases, the VHE light curve does not appear to follow the decay of the X-ray emission before and after the outburst, as seen in LS I +61 303 during outburst. However, we note that a better sampling would be needed in order to analyse any possible correlation during outburst. On the other hand, we computed non-simultaneous TeV/X-ray flux ratios during the 2011 outburst (around phase 0.31) and compared them with the ones of LS I +61 303. The TeV/X-ray flux ratio of HESS J0632+057 is ~ 5 times higher than the one of LS I +61 303, which means that the X-ray emission from HESS J0632+057 is lower than the expected from a correlation like the one found by Anderhub et al. (2009) for LS I +61 303 during outburst. This is consistent with a lower magnetic field in HESS J0632+057, which would naturally explain the lower observed radio flux densities as well. When comparing the average radio to X-ray flux ratios, we see that the radio emission is lower in HESS J0632+057 by a factor ~ 30 . The outbursts from these two sources seem observationally very different, although they happen at similar orbital phases, close before apastron, regardless of the different orbital periods (26.5 d for LS I +61 303 and 321 d for HESS J0632+057).

As a final comment, we could interpret the displacement between the peaks of runs A and B (14 mas in 30 days) as produced by the proper motion of a blob ejected within a microquasar (see Mirabel & Rodríguez 1994 for GRS 1915+105). Given the relatively small proper motion, a blob velocity above $0.1c$ requires that the jet is pointing towards the observer with an angle below 2° , which would be either very restrictive or fine tuned.

In conclusion, HESS J0632+057 displays extended and variable radio emission at 50–100 AU scales, with a projected displacement of the peak of the emission of 21 AU in 30 days. Similar morphologies and behaviours have been found in the other gamma-ray binaries. However, a more detailed monitoring of the variability of the source with high-sensitivity VLBI observations along the orbital cycle is required to measure the total extension and morphology of the extended emission, to measure the morphologic and astrometric changes at different orbital phases, and to search for periodicity in these changes.

8.3 The gamma-ray binary candidate AGL J2241+4454

8.3.1 Introduction

The unidentified high-energy source AGL J2241+4454 was proposed to be a gamma-ray binary, whose optical counterpart would be the Be star MWC 656 (HD 215226). Based on previous results, a direct association of the Be star with radio emission with VLBI, specially if showing variability and/or structure, would strongly support this hypothesis. We conducted a VLBI campaign aimed to search for compact radio emission in the region close to the Be star MWC 656, the putative optical counterpart of AGL J2241+4454.

8.3.2 The candidate counterpart to the HE source AGL J2241+4454

Lucarelli et al. (2010) reported the detection by the *AGILE* satellite of a new unidentified point-like source at energies above 100 MeV, AGL J2241+4454, which has a position uncertainty of 0.6° . Williams et al. (2010) pointed out two possible low-energy counterparts of this source. The X-ray source RX J2243.1+4441, a possible quasar (Brinkmann et al. 1997), could be a source of gamma-ray flaring activity (Vercellone et al. 2008). Its radio emission at 1.6 GHz is shown in the wide-field map in Fig. 8.5. However, these authors noted the lack of an optical counterpart, expected to have a magnitude $V \sim 16$ based on the observed X-ray flux. Therefore, the association of this quasar with the HE source is unlikely. The second possible counterpart is the Galactic Be star MWC 656, which contains a circumstellar equatorial disc as PSR B1259–63, LS I+61 303 and HESS J0632+057. Williams et al. (2010) reported an optical photometric periodicity of 60.37 ± 0.04 days, which suggested that MWC 656 was a binary system. On the other hand, the Galactic position of the star ($l = 100.1755^\circ$, $b = -12.3985^\circ$) indicates that it is far from the Galactic plane, and hence it may be a runaway star formed by a supernova explosion in a binary system. Williams et al. (2010) also estimated the distance to the system to be 2.6 ± 1.0 kpc, which yields a distance from the Galactic plane of $z = -0.56 \pm 0.20$ kpc (the average distance for Be stars is just 69 pc). However, the proper motion is not well constrained. *Hipparcos* provided $\mu_\alpha \cos \delta = -2.8 \pm 1.3$ mas yr $^{-1}$, $\mu_\delta = -3.2 \pm 0.9$ mas yr $^{-1}$, but no proper motion is quoted in UCAC3.

Very recently, MWC 656 was finally identified as a binary system in Casares et al. (2012b) through optical spectroscopic observations that revealed a 60 day variability in the equivalent width, FWHM and radial velocity of H α emission line, as well as in the radial velocity of several He I lines. The authors also obtained, for the first time, the orbital parameters of this binary system. They fixed the orbital period to the value obtained by Williams et al. (2010), and fixed an eccentricity of 0.4 to guarantee the convergence of the radial velocities fit. The phase of the periastron occurs at 0.74 ± 0.05 , the mass function is $0.35_{-0.15}^{+0.20} M_\odot$, and they obtain $a_1 \sin(i) = 45.6 \pm 7.3 R_\odot$. The argument of the periastron is $71 \pm 23^\circ$. This orbital solution revealed that the *AGILE* flare took place around periastron, and that the maximum of the optical photometric modulation takes place 0.3 orbital phases after periastron (as it happens in the gamma-ray binary LS I +61 303). All these results strongly suggest that MWC 656 is the optical counterpart of AGL J2241+4454.

We have analysed archival VLA data from the region around MWC 656 (see Table 8.3). A snapshot of 10 seconds at 4.8 GHz was performed with the VLA in A configuration in 1992 on the source J2243+444, which is located at $2.3'$ from MWC 656. The image yields an upper limit of 1.2 mJy beam $^{-1}$ at the $3\text{-}\sigma$ level at the position of the star. Observations at 1.5 GHz with the VLA in BC configuration during 120 seconds were conducted in 1989 on a source located $8.8'$ away from our target. The resulting image (see Fig. 8.5) has a noise of 0.4 mJy beam $^{-1}$, and yields an upper limit at $3\text{-}\sigma$ level of 1.2 mJy beam $^{-1}$ at 1.5 GHz. The nearby quasar commented above is perfectly detected with a total flux density of

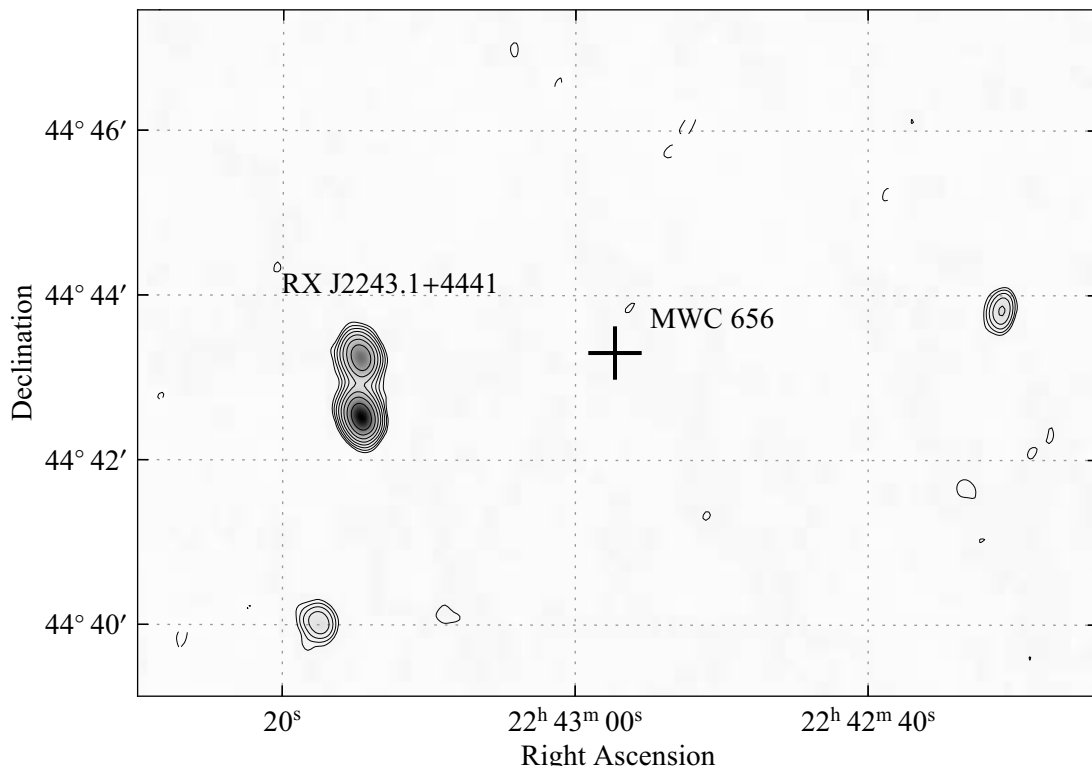


Figure 8.5: VLA snapshot image at 1.5 GHz of the field around the position of MWC 656, indicated by the cross. The nearby quasar RX J2243.1+4441 is the bright double source to the East of MWC 656. The rms of the image is $0.4 \text{ mJy beam}^{-1}$. The contours start at 3 times the rms and scale with $3^{1/2}$. We note that the uncertainty in the position of the gamma-ray source AGL J2241+4454, 0.6° is larger than the field shown here. The other two bright sources on the field are unidentified. The source towards West of MWC 656 is NVSS 224230+444351. The source towards South of RX J2243.1+4441 is NVSS 224317+444002.

8. Study of new gamma-ray binary candidates

Table 8.3: Log of the archival VLA observations and the three EVN observations of project EM090.

Run	Array	Date (Y-M-D)	MJD	ϕ_{orb}	Freq. [GHz]
AH355	VLA	1989-06-02	47679.54	0.85 ± 0.07	1.5
AF233	VLA	1992-10-20	48915.34	0.32 ± 0.06	4.8
EM090A	e-EVN	2011-01-25	55586.35–55586.52	0.82 ± 0.04	1.6
EM090B	e-EVN	2011-02-15	55607.30–55607.47	0.17 ± 0.04	1.6
EM090C	EVN	2011-02-28	55620.17–55620.64	0.38 ± 0.04	1.6

264 mJy. The brightest component has a peak flux density of 112.1 ± 0.4 mJy beam $^{-1}$, and is located at $190''$ from MWC 656.

8.3.3 VLBI observations of MWC 656

We conducted three observations with the EVN. In order to cover a wide range of orbital phases of the system, we prepared two e-EVN observations lasting 4 h and one epoch in a regular EVN session lasting 12 hours (project code EM090). The aim of conducting the full EVN session, apart from the search of compact radio emission, was to provide a very sensitive image at very high resolution to explore in detail the putative extended emission of the source. The log of the observations is listed in Table 8.3. The sketch of the orbit in an arbitrary orientation and seen from above is shown in Fig. 8.6, where we indicate the position of the compact object during the observations. The e-EVN observations (runs A and B) lasted 4 hours and included nine antennas, Ef, Jb, Mc, On, Tr, Wb, Hh, Sh, Cm. The full EVN observation (run C) lasted 12 hours and included eleven antennas, Ef, Wb, On, Mc, Tr, Sv, Zc, Bd, Ur, Sh, Jb. The name, size, and location of these antennas can be found in Table 2.1 on page 28. The observations were conducted with a total data rate of 1024 Mbps provided by 16 subbands of 16 MHz each, dual polarisation and 2-bit sampling.

Two good phase calibrators are listed in the NRAO’s VLBA calibrator list⁶ J2237+4216 and J2233+4245, both at a very similar distance from the source, 2.7° and 2.6° , respectively. J2237+4216 was used as the reference phase calibrator for the first epoch, EM090A, because it appeared slightly more compact at higher frequencies. The data from this run was available before the second one was scheduled, and we found that the peak flux density of the phase calibrator was lower than expected, ~ 60 mJy beam $^{-1}$ at 1.6 GHz. Although the phase calibration was possible with this calibrator, we decided to use for runs B and C J2233+4245 instead, which showed peak flux density at 1.6 GHz of 220 mJy beam $^{-1}$. The cycling time for the three runs was of 5 minutes, spending 1.5 minutes on the cal-

⁶<http://www.vlba.nrao.edu/astro/calib/>

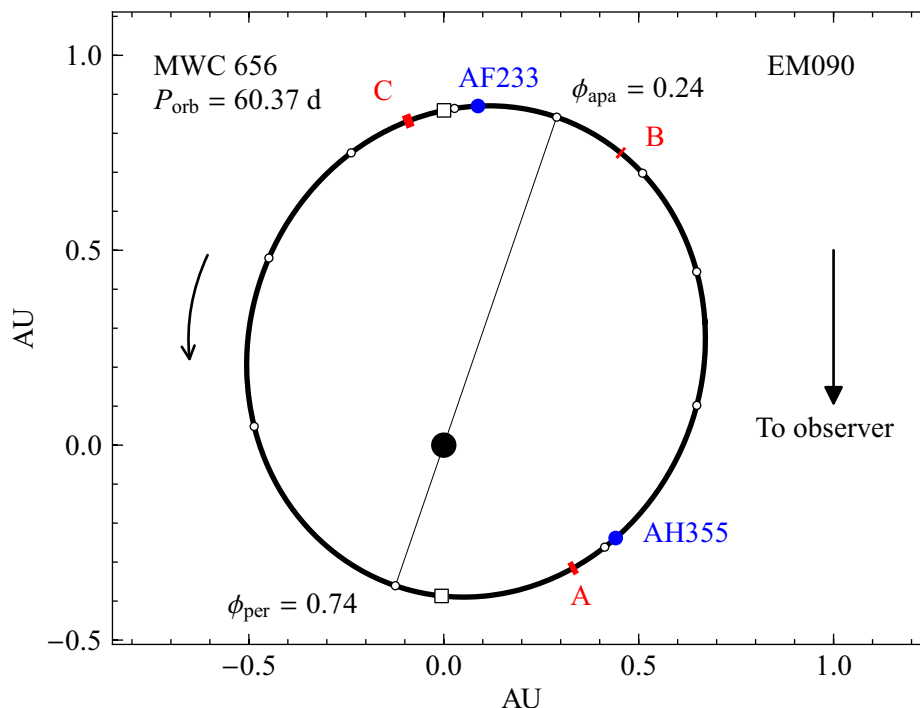


Figure 8.6: Sketch of the orbit of MWC 656 with the position of the compact object during the three runs of project EM090 marked in red, and the VLA archival snapshots in blue, for which the duration was shorter than the size of the point. The white dots are plotted every 0.1 orbital phases. The empty squares mark the inferior and superior conjunction of the compact object, which occur at orbital phases 0.76 and 0.35, respectively. The orbit was computed using the orbital solution reported in Casares et al. (2012b). The orbit, size of the star, and the duration of the runs of EM090 are scaled to the real values. The orientation of the orbit is arbitrary, and it is seen face-on (see Fig. A.2 on page 180 for examples of other possible projections of the orbit).

ibrator and 3.5 on the target source. No astrometric check source was observed during runs A and B (e-EVN) because the total observation time was limited to 4 h. For the EVN run (C) we included scans on J2237+4216 and J2243+4442 every 30 minutes each to be used as amplitude calibrators and/or astrometric check sources. The correlation position of J2237+4216 was $\alpha_{J2000.0} = 22^{\text{h}}37^{\text{m}}04^{\text{s}}.209761$ and $\delta_{J2000.0} = +42^{\circ}16'48''.26260$, and for J2233+4245 was $\alpha_{J2000.0} = 22^{\text{h}}33^{\text{m}}32^{\text{s}}.406507$ and $\delta_{J2000.0} = +42^{\circ}45'39''.92438$. Both positions were obtained from the GSFC 2009c.astro solution⁷.

We performed standard data reduction to the data from the three epochs. The process was basically analogous to the one described in Sect. 8.2.2.

⁷<http://gemini.gsfc.nasa.gov/solutions/>

8. Study of new gamma-ray binary candidates

Table 8.4: Orbital phase (absolute and relative to the periastron passage), synthesized beam size, and rms of the observations of project EM090.

Run	ϕ_{orb}	$\phi_{\text{orb}} - \phi_{\text{per}}$	HPBW _{size} [mas ²]	HPBW _{P.A.} [°]	rms [$\mu\text{Jy beam}^{-1}$]
EM090A	0.82	0.08	63.0×36.7	−43.2	21
EM090B	0.17	0.43	45.0×35.6	83.9	22
EM090C	0.38	0.64	15.3×13.2	−14.2	10

8.3.4 Results and discussion

We produced images of the three data sets with a natural weighting scheme to improve the sensitivity. The synthesized beam size (HPBW) and the rms noise of the images at the position of MWC 656 are quoted in Table 8.4. No radio source coincident with the position of MWC 656 was detected above $3\text{-}\sigma$ level. The proper motion of the MWC 656 measured by *Hipparcos* is $-2.8 \pm 0.9 \text{ mas yr}^{-1}$ in right ascension and $-3.2 \pm 0.9 \text{ mas yr}^{-1}$ in declination at epoch 1991.25. Therefore, it is not expected that the binary system is farther than $\sim 80 \text{ mas}$ from the *Hipparcos* position (used for the correlation). We explored an area up to 100 mas without any detection. We also explored larger areas up to a few arcseconds with a higher detection threshold of $5\text{-}\sigma$ without finding any significant source.

There are different reasons that could explain the non-detection of a radio counterpart with the current data. First, gamma-ray binaries usually display variable radio emission, and therefore AGL J2241+4454 is also probably a variable radio emitter. The non-detection could be justified if the observations were not conducted during the maximum of the radio light curve. Second, the radio flux density of the source may be lower than our uncertainties at $3\text{-}\sigma$ level. These two reasons are not mutually exclusive. Obviously, there is always the possibility that MWC 656 is in fact not a radio emitter at all, which would render the association of this Be star with the high-energy source AGL J2241+4454 improbable.

Another important consideration is that the VLBI observations may not be sensitive to the source if it is intrinsically large. The shorter baseline of the array, Ef-Wb, which are separated by 266 km , provide a uv distance of $\sim 1.5 \text{ k}\lambda$ at 1.6 GHz (19 cm wavelength). Using Equation 2.1 we can see that this corresponds to angular separations of about $\gtrsim 100\text{--}130 \text{ mas}$. If the source is intrinsically larger than this size it might be undetectable with the used interferometer. For a distance to the source of $\sim 2.6 \text{ kpc}$, this scale corresponds to $\sim 300 \text{ AU}$. However, all other gamma-ray binaries display radio emission more compact than these scales.

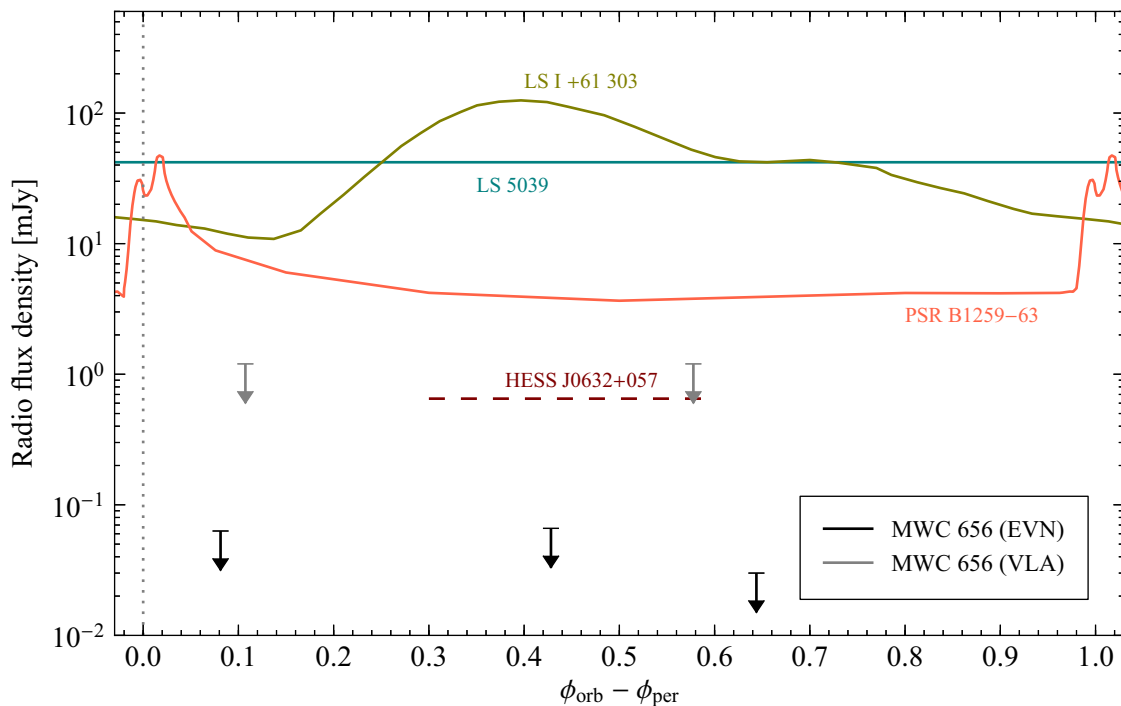


Figure 8.7: Radio emission at 1.6 GHz of gamma-ray binaries as a function of the post-periastron orbital phase. We show the upper limits on MWC 656 reported in this Chapter, and smooth light curves for other gamma-ray binaries (see text). The orbital periods of the sources are: 3.9 days for LS 5039, 26.5 days for LS I +61 303, 60.37 days for MWC 656, 321 days for HESS J0632+057, and 1237 days for PSR B1259–63.

Comparison with other gamma-ray binaries

In Fig. 8.7 we plot the light curves at 1.6 GHz of the known gamma-ray binaries with respect to the orbital phase after the periastron. For clarity, we plot for each source a smooth curve obtained by tracing the mean light curves reported in Ribó et al. (1999), Strickman et al. (1998), Johnston et al. (2005), and Skilton et al. (2009) for LS 5039, LS I +61 303, PSR B1259–63, and HESS J0632+057, respectively. We note that all flux densities in Fig. 8.7, except the upper limits from the EVN observations of MWC 656, were obtained with short-baseline interferometers with resolutions of the order of the arcsecond. LS 5039 displays a persistent and slightly variable ($\lesssim 30\%$) flux density at 1.6 GHz of about 40 mJy (Martí et al. 1998). LS I +61 303 displays the maximum around apastron, which occurs in this case at orbital phase 0.63 (0.4 post-periastron), although we note that the peak of the emission occurs periodically between orbital phases 0.45 and 0.95 (see Chapter 7). HESS J0632+057 has been detected with a flux density of ~ 0.7 mJy at 1.3 GHz (Skilton et al. 2009) close to apastron, approximately between orbital phases 0.3 and 0.6, although a detailed light curve has not been reported so far.

8. Study of new gamma-ray binary candidates

Finally, PSR B1259–63, with a significantly different timescale (the period is 1237 days), displays two radio outburst around periastron, and a minimum quiescent emission of ~ 4 mJy at 1.4 GHz (Johnston et al. 2005) from the pulsed emission, which is detected at all orbital phases except close to the periastron passage. MWC 656 has an orbital period between the one of LS I +61 303 and the one of HESS J0632+057, and therefore the expected maximum emission of this system should be at phase ~ 0.4 after periastron. However, we have a strict upper limit at post-periastron orbital phase 0.43 set by run EM090B. This suggests that, if the source displays transient radio emission, its maximum may not be close to the orbital phases inferred from the behaviour of LS I +61 303 and HESS J0632+057, or that it is displayed during short time intervals, or the source expands quickly and it is undetectable using VLBI.

We note that, even if the source does not display bright transient radio emission, it is expected that, if the binary system hosts a pulsar, pulsed radio emission were detectable. Free-free absorption is less important at apastron, and pulsed emission may not be absorbed far from the periastron, as in PSR B1259–63. However, it is difficult to estimate the free-free absorption in MWC 656, for which the eccentricity, the argument of the periastron, the inclination of the orbit, and the semimajor axis are not well constrained (Casares et al. 2012b). Consequently, the relative geometry along the orbit of the putative pulsar in MWC 656 is currently too uncertain, and the radio observations too scarce, to impose robust limits on the flux density/absorption of the putative pulsed emission of the source. We note that, apart from possible free-free absorption, it is also possible that the pulsar radio beams do not sweep through Earth’s line of sight (Lyne & Graham-Smith 2005).

The light curves shown in Fig. 8.7 describe very different timescales because the orbital periods are very different. Therefore, we also plot the light curves as a function of the days after periastron, as shown in Fig. 8.8. In this representation we see a more similar behaviour between the radio light curves of LS I +61 303 and PSR B1259–63. The low flux density variability of LS 5039 at arcsecond scales is probably caused by its short orbital period and relatively low eccentricity. On the other hand, the radio detections of HESS J0632+057 lie to the right of the plotted region, at more than 100 days after the periastron. This is difficult to understand if the trigger of the radio outburst is linked to the periastron passage, and the radio outburst may be related to other parameters, such as the separation between the compact object and the star, or the relative position of the circumstellar disc. In any case, no obvious relation appears in the current light curves. A better sampled light curve for HESS J0632+057, and a detection in radio of MWC 656 are needed to understand the radio outbursts in gamma-ray binaries.

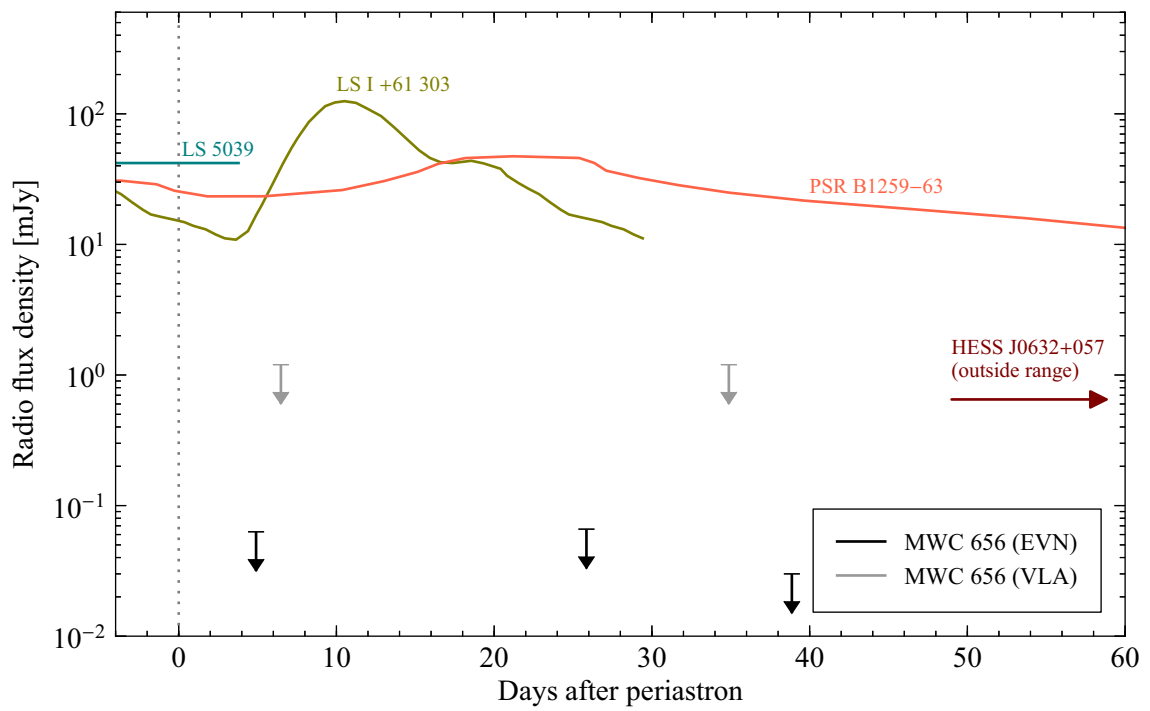


Figure 8.8: Same as in Fig. 8.7 but plotting against days after periastron. We note that the radio detections of HESS J0632+057 correspond to ~ 130 – 190 days after periastron.

9

Concluding remarks

9.1 Summary of the results

Gamma-ray binaries are extreme and unique objects in the Universe, from which a wide range of physical processes can be studied. These systems are characterised by a broadband SED dominated by HE photons with MeV–GeV energies, and show orbital modulation of the broadband emission. They display outflows of relativistic particles that produce synchrotron radio emission on projected distances of 1–100 AU. The principal aim of this thesis was to unveil the structure of the outflow of relativistic particles from these systems, which can be directly observed by means of very long baseline interferometry (VLBI) at radio wavelengths.

Before this thesis, only two of the three known gamma-ray binaries had been observed by means of VLBI, and the other three candidates had not been discovered (see Table 9.1 on the following page). Consequently, we followed two lines of research based on radio VLBI observations. On one hand, we conducted VLBI observational campaigns to study in depth the changes of the radio structures of the known gamma-ray binaries as a function of the orbital cycle. On the other hand, we conducted searches of the new gamma-ray binary candidates.

PSR B1259–63

We have discovered extended and variable radio structure from PSR B1259–63 that extends away from the binary system up to projected distances of 120 AU. This is the first observational evidence that young non-accreting pulsars orbiting massive stars can pro-

9. Concluding remarks

Table 9.1: Summary of the VLBI observations of the known gamma-ray binaries carried out in this thesis, and comparison with previous results.

Source	Previous works		This thesis	
	Observed	VLBI structure	Observed	VLBI structure
LS 5039	Yes	Non-variable	Yes	Periodic changes
1FGL J1018.6–5856	No	–	No	–
LS I +61 303	Yes	Periodic (?)	Yes	Periodic changes
AGL J2241+4454	No	–	Yes	Non-detected
HESS J0632+057	No	–	Yes	Variable
PSR B1259–63	No	–	Yes	Variable ^a

^a Preliminary VLBI images of the 2010 periastron passage of PSR B1259–63 suggest that its VLBI structure might vary periodically as well.

duce variable extended radio emission on AU scales. Since this is the only gamma-ray binary in which the presence of a pulsar has been confirmed, our results enable to test those models based on the interaction of a young non-accreting pulsar with the wind of a massive star in the context of the formation and evolution of radio structures.

LS 5039

LS 5039 is a fascinating binary system displaying one of the most stable periodic light curves at HE and VHE (apart from gamma-ray pulsars). The first VLBI image of LS 5039 (Paredes et al. 2000) led the authors to suggest that it was a new microquasar in the Galaxy. We observed the source and found that the morphology on AU scales changes on time scales similar to the orbital period. We found that a simple and shockless microquasar scenario is disfavoured by this result.

Based on this changing morphology, we aimed to characterise the radio morphological changes of LS 5039 and discriminate if they were either repeatable or erratic. We found that the structure of LS 5039 shows a periodic orbital modulation. We also found that this periodicity is stable on time scales of years. We modelled the basic properties of the outflow of relativistic particles of the source assuming the presence of a young non-accreting pulsar and found that it is possible to reproduce, in general, the observed structures and their orbital periodicity.

We obtained an accurate determination of the proper motion of LS 5039 by means of optical and interferometric radio observations. We derived the Galactic trajectory of the system and identified possible birth places for the system, which can be used to estimate its age. An accurate determination of the age is only possible if the distance to the source is better constrained, which will be done by the *Gaia* satellite in the next years. In parallel,

we also measured the proper motion of the isolated pulsar PSR J1825–1446 and obtained its Galactic space velocity.

LS I +61 303

We observed LS I +61 303 to cover an X-ray/gamma-ray outburst produced shortly before the apastron passage. We found extended and variable radio emission on scales of 5–10 AU, whose P.A. changes $\sim 130^\circ$ in ten days. The low frequency structure follows the behaviour of the structure at higher frequencies but on larger scales and with a time delay of more than one day. The observed morphology is compatible with the one found in observations conducted one year before at similar orbital phases, which suggests that the periodic orbital modulation of the source is stable on time scales of years, although we found significant differences in the morphology at particular orbital phases.

We obtained accurate astrometry at two radio frequencies and found the relative offsets between them. The outflow shows a frequency gradient along the direction of the extended emission. Furthermore, the core shift between frequencies shows a continuous change in the same sense of the relative astrometry. The behaviour is similar to the one expected from an outflow whose axis passes close to the line of sight of the observer.

HESS J0632+057

This gamma-ray binary candidate displayed an X-ray and gamma-ray outburst starting in January 2011. We performed e-VLBI observations that led to the discovery of compact radio emission unambiguously related to the Be star MWC 148, the proposed optical counterpart of HESS J0632+057, which is now known to be an eccentric binary system. Observations conducted 30 days after the first VLBI detection revealed faint extended radio emission with a size of 50–100 AU. Between the two observations the peak of the radio emission was displaced 20 AU, which is bigger than the orbit size. The source morphology, size, and peak displacement are similar to those found in the other gamma-ray binaries, supporting the gamma-ray binary nature of this source as well.

AGL J2241+4454

We conducted a VLBI campaign to search for the radio counterpart of the gamma-ray binary candidate AGL J2241+4454 based on its possible association with a binary system containing a Be star (MWC 656). However no compact radio emission was found coincident with the position of the star. Given the low upper limits obtained in three VLBI observations we conclude that the source may display transient radio emission lasting less than ~ 20 –30 days, or that the source displays a fast expanding outflow resolved by VLBI observations. A well sampled monitoring at different orbital phases will be needed to constrain the radio emission of this source. Our upper limits can provide constraints on the pulsed radio emission of the source, although a detailed analysis of the free-free absorption

9. Concluding remarks

during apastron should be conducted once the orbital elements of the binary system, as well as the properties of the stellar wind, are accurately determined.

1FGL J1018.6–5856 For completeness, a short comment on this new gamma-ray binary candidate. 1FGL J1018.6–5856 was discovered by searching for periodicities of *Fermi* sources, and shows intensity and spectral modulation at GeV energies with a 16.6-day period (Fermi LAT Collaboration et al. 2012b). Given the variability of the proposed X-ray and radio counterparts, and the spatial coincidence with an O6V((f)) star, these authors proposed this source as a new gamma-ray binary. The source has a variable flux density of 2–5 mJy as measured with ATCA¹, although no extended emission has been reported so far. The source was observed with the Australian LBA (PI: P. Edwards) a few weeks before the submission of this thesis, and therefore the results are not available yet.

9.2 Concluding remarks

Gamma-ray binaries are a relatively new population of binary systems with a very limited number of members, all of them showing the peak of the SED at MeV–GeV energies. It is important to establish common observational links between them in order to better understand the physical processes producing their broadband emission, as well as to define detailed criteria needed to identify new possible gamma-ray binaries. Before starting this thesis LS 5039 was known to display bipolar extended emission on AU scales, and LS I +61 303 was known to present variable radio structures showing orbital modulation. In this thesis we have explored the radio properties of gamma-ray binaries by means of VLBI observations on mas scales, which correspond to projected distances of a few AU at distances of a few kpc. After the studies presented in this thesis we have shown that:

- PSR B1259–63 displays extended and variable radio structures.
- The radio structure of LS 5039 is not persistent, but displays periodic orbital modulation, which is stable on time scales of years.
- A simple model for LS 5039 based on the interaction of the stellar wind with the wind of a young non-accreting pulsar can account for most of the orbital morphological changes of the source.
- The morphology of LS I +61 303 is confirmed to display orbital variability, which is stable on time scales of years, although it shows significant changes at certain orbital phases. Displacements of the peak of the emission are detected at a different rate for different frequencies. We found a changing frequency gradient along the structure of the source.

¹Australia Telescope Compact Array.

- The radio structure of HESS J0632+057 has been revealed and its association with the Be star MWC 148 has been set. A displacement of the peak of the emission larger than the orbit size was detected.
- No radio counterpart of AGL J2241+4454 has been found in the region around MWC 656. However, further exploration is needed to discard this association.

In this thesis we have revealed for the first time the radio structure of two gamma-ray binaries, and found periodic changes in the structure of other two (see Table 9.1). Based on these results, we have established the basic properties and behaviour of the radio emission of gamma-ray binaries on AU scales, and we have contributed to find characteristics that are common to all of them. These common traits can be useful to identify other possible candidates. The common properties of the radio emission of gamma-ray binaries derived from this thesis can be summarised in three points, which are model independent:

- Gamma-ray binaries display synchrotron radio emission that forms structures on AU scales.
- These radio structures show periodic orbital morphological variability, although erratic changes might occur.
- The position of the peak of the emission suffers displacements significantly larger than the size of the orbit.

These observational facts can be used to test the possible scenarios. By modelling the structure of the outflows it is possible to obtain physical parameters and reveal the nature of gamma-ray binaries.

Conclusion on the models

Our results show that the microquasar scenario is not favored for LS 5039. Also, we note that *bona fide* accreting microquasars do not fulfill the second property listed above. The periodic variability of the extended structure seen in some microquasars does not occur on orbital time scales.

On the other hand, the presence of a young non-accreting pulsar in PSR B1259–63 is clear, whereas for LS 5039 it is suggested by our modelling. Our results show that, among the five gamma-ray binaries studied in this thesis, four of them show very similar properties. Consequently, we expect that all binary systems showing gamma-ray emission and displaying the three VLBI observational properties quoted above contain a young non-accreting pulsar.



Orbital elements in binary systems and constraints to the mass of the compact object

A.1 Orbital elements in binary systems

The orbit of a binary system can be unambiguously defined by seven parameters, known as orbital elements, assuming that the orbit is unperturbed by external forces and that there is no internal dissipation. A description of the orbital elements can be found in Smart (1930) and Danby (1962). We need a plane of reference, which, in the case of binary systems is the plane of the sky, defined as the plane perpendicular to the line of sight to the observer. We can describe the orbit of the secondary star (hereafter component 2) with respect to the massive star (hereafter component 1), in which case the plane of the sky intersects the position of the massive star. Some of these parameters are plotted in the sketch of an arbitrary orbit shown in Fig. A.1. Two parameters are used to describe the shape and size of the ellipse:

- Eccentricity, e (0–1): defines how much elliptical the orbit is. $e = 0$ corresponds to a circle and $e = 1$ corresponds to a parabola.
- Semimajor axis, a (> 0): longest diameter of the ellipse divided by 2. This value corresponds to the relative ellipse (motion of one star with respect to the other). The absolute ellipse of each component has semimajor axis a_i , which is linked to the semimajor axis of the system by $a = a_1 + a_2$.

Three elements define the projection of the orbital plane (in which the ellipse is embedded) onto the plane of the sky:

A. Orbital elements in binary systems and constraints to the mass of the compact object

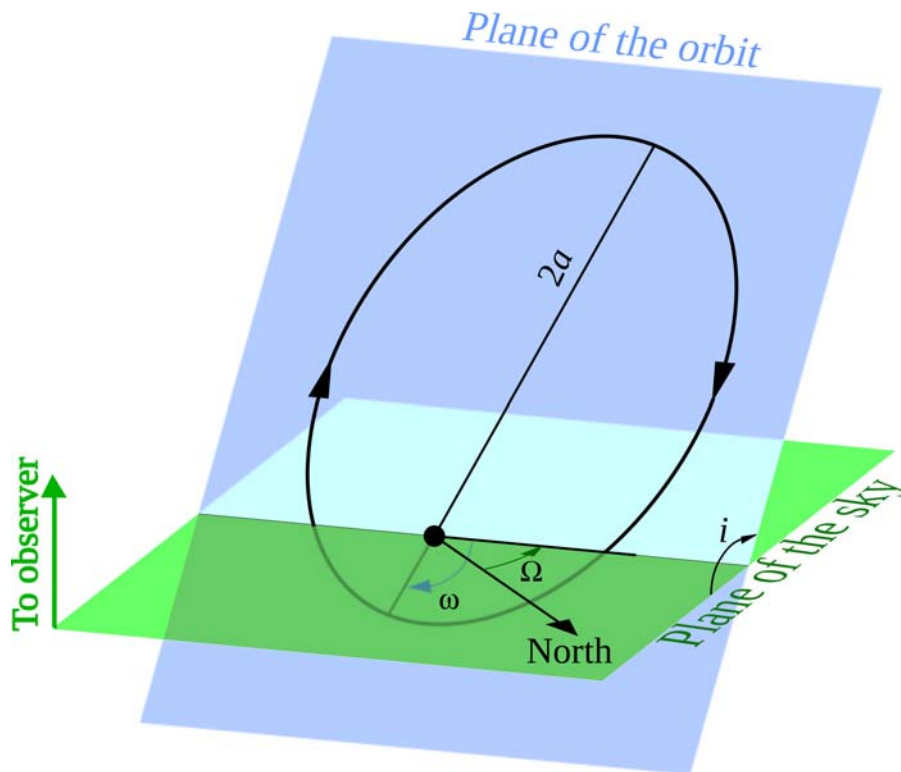


Figure A.1: Sketch of the angles involved in the characterisation of the orbit of a binary system. The orbital elements related to the orientation of the orbit in the sky are indicated. Adapted from https://commons.wikimedia.org/wiki/File:Orbital_elements.svg.

- Longitude of the ascending node, Ω (0 – 360°): is the position angle, measured from North to the East in the plane of the sky, of the ascending node of the orbit. An orbit has two nodes, defined in the line of nodes, which is the line intersecting the plane of the orbit with the plane of the sky. The ascending node is defined as the node from which the secondary star crosses behind the plane of the sky. A change in Ω represents a rotation of the orbit on the plane of the sky, around the line of sight of the observer.
- Inclination, i (0 – 180°): vertical tilt of the ellipse with respect to the plane of the sky. This is a rotation around the line of nodes. An orbit with an inclination of 90° is seen edge-on, and with an inclination of 0 or 180° is seen face on. Therefore, the inclination is also the angle between the line of sight and the direction perpendicular to the plane of the orbit. Orbits with $0^\circ < i < 90^\circ$ describe a counter-clockwise, or direct (prograde), rotation whereas inclinations $90^\circ < i < 180^\circ$ describe clockwise, or retrograde, rotation.
- Argument of periastron, ω (0 – 360°): angle from the ascending node to periastron

A.2. Degeneracy between the mass of the compact object and the orbit inclination

measured in the orbital plane. The two components of the system have their own argument of periastron w_i , and they differ by 180° , $\omega_1 = \omega_2 + 180^\circ$. For $180^\circ < \omega_2 < 360^\circ$ the secondary star is in front of the plane of the sky during the periastron passage (closer to the observer than the primary star), whereas for $0^\circ < \omega_2 < 180^\circ$ the secondary star is behind the plane of the sky during the periastron passage.

Finally, two elements characterise the timing properties of the orbit:

- Period, P_{orb} (> 0): duration of each orbital cycle.
- Time of periastron, T_0 : a reference time that relates the moment of the periastron passage¹ with a specific time (or epoch).

As an example of the effect of Ω and i on how the orbit is projected in the sky, we show in Fig. A.2 different projections of an orbit with $e = 0.5$.

The orbital elements of a binary system with a massive star and a compact object are usually determined from optical spectroscopic observations of the massive star, or, in case the compact object is a detectable pulsar, by pulsar timing analysis of its pulsed emission. These techniques alone cannot disentangle the ambiguity between the mass of the compact object and the orbit inclination (see below). Also, none of these techniques is sensitive to the direction of the longitude of the ascending node because this angle indicates the orientation of the projected orbit in the plane of the sky. The only way to obtain Ω is by means of direct imaging of the system.

A.2 Degeneracy between the mass of the compact object and the orbit inclination

The orbital elements of gamma-ray binaries can be obtained by means of radial velocity measurements. Optical spectroscopic observations provide the wavelength of a chemical element line shifted according to the Doppler effect induced by the projected velocity of the star in the direction of the line of sight from the observer. Current observations provide velocity shifts with an accuracy of a few km s^{-1} . With enough values obtained at different orbital phases, a radial velocity curve can be fitted to obtain the orbital elements. The orbital period, P_{orb} , and the epoch of the periastron passage, T_0 , can be determined either by the periodicity of the velocity curve or by other periodicities of the system (such as radio or X-ray outbursts). The fit also provides the radial velocity of the whole binary the system, γ , and the semi-amplitude of the radial velocity curve, K_1 (we remind that subindex 1 stands for the massive star), which are related to the orbit eccentricity, e , and the argument of periastron, ω . If only spectral lines of one star are observable, as is the case in gamma-ray binaries, it is not possible to disentangle the ambiguity between

¹In some binaries T_0 is not defined at periastron

A. Orbital elements in binary systems and constraints to the mass of the compact object

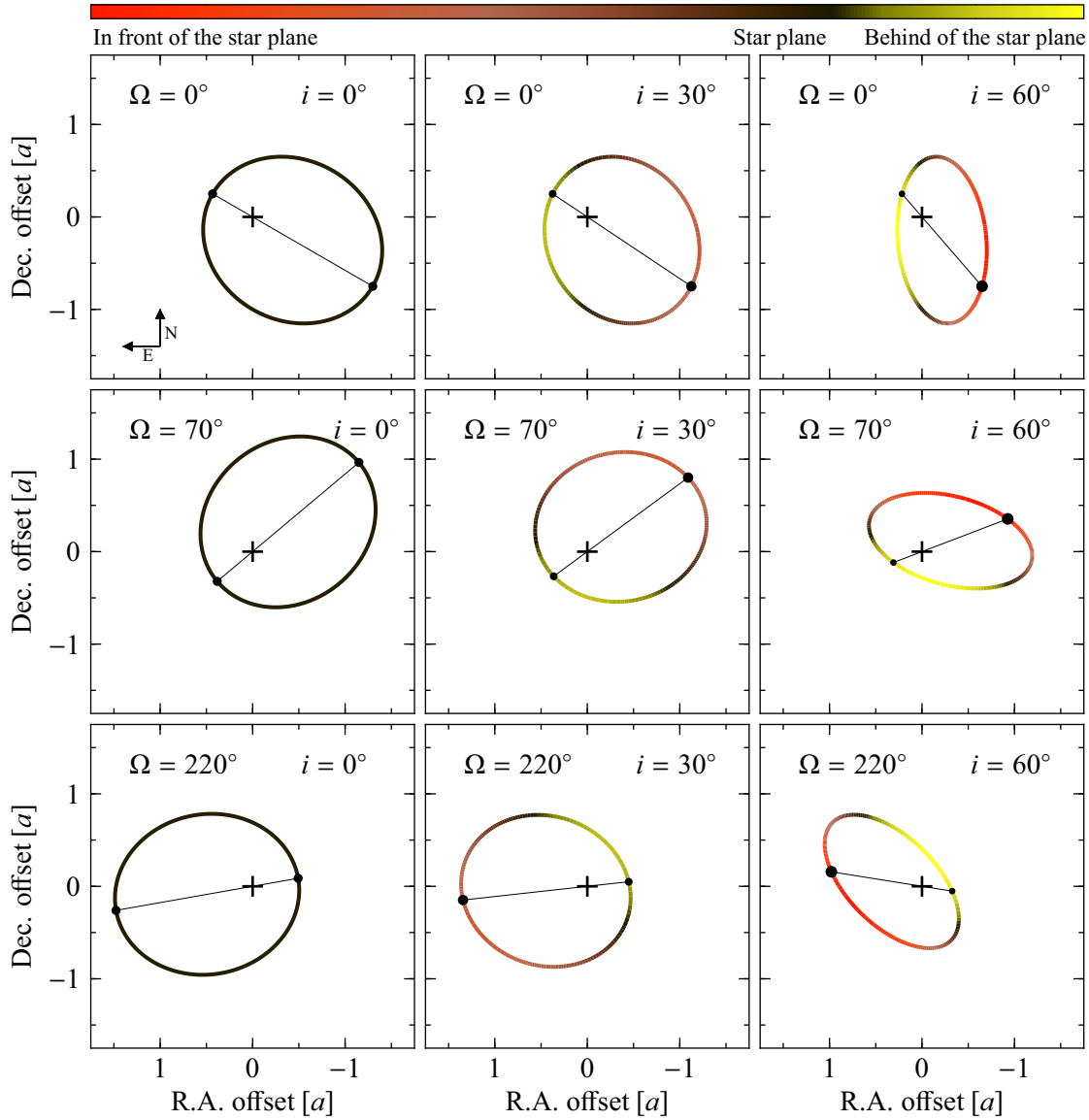


Figure A.2: Projections of an orbit with $e = 0.5$ and $\omega_2 = 60^\circ$ for different values of Ω and i . The small and large black circles are the positions of the compact object during periastron and apastron, respectively. The axes are in units of the semimajor axis of the orbit a . The angle Ω is the rotation around the axis perpendicular to the plane of the sky, whereas i is the tilt of the orbit.

the semimajor axis of the orbit, a , and its inclination from the plane of the sky, i . In particular, it is only possible to measure the quantity $a_1 \sin(i)$. It is convenient to work with the derived quantity $f(M_i)$, known as mass function, which has units of mass. The

A.2. Degeneracy between the mass of the compact object and the orbit inclination

mass function for the second star is

$$f(M_2) = \frac{M_2^3 \sin^3(i)}{(M_1 + M_2)^2} = \frac{M_2 \sin^3(i)}{\left(1 + \frac{M_2}{M_1}\right)^2}.$$

For the case when the primary star (1) is much more massive than the secondary (2), $M_2 \ll M_1$ implies that the ratio $\frac{M_2}{M_1} \rightarrow 0$. For this case the mass function represents an absolute lower limit to M_2 , which occurs for $i = 90^\circ$. Using the third Kepler law the mass function can be expressed as a function of two observable quantities:

$$f(M_2) = \frac{4\pi^2}{G} \frac{a_1 \sin i}{P_{\text{orb}}^2}.$$

In practice, the procedure to obtain the mass of the compact object is as follows. The spectroscopic observations provide the mass function of the compact object. The mass of the massive star is not measured, but estimated from its spectrophotometric properties. Normally, to first order, the spectral type is determined based on the optical spectra of the star, and its mass is inferred from the spectral type. Consequently, the mass of the massive star is not necessarily a measured value with Gaussian uncertainties, but a range of acceptable masses instead. Using the definition of the mass function above and the inferred mass of the massive star, there is still a degeneracy between the mass of the compact object (M_2) and the inclination of the system. None of these values can be obtained by optical spectroscopic observations of a single star. If the inclination can be determined by other means, then the mass of the compact object can be obtained:

$$M_2 = \frac{f(M_2)}{\sin^3(i)},$$

where we have assumed that $M_2 \ll M_1$.

B

Free-free absorption in LS I +61 303

In this appendix we explain how to determine the optimal orbital phase to conduct radio observations aimed to detect pulsations. We compute the free-free absorption along the orbit for LS I +61 303. These results have been published in Cañellas et al. (2012)¹.

Following Dubus (2006) we searched the orbital phases providing minimum absorption by computing the optical depth towards the compact object at different orbital phases and for different frequencies using the Rosseland mean opacity:

$$\tau \simeq 0.3 \left[\frac{\dot{M}_w}{10^{-8} M_\odot \text{ yr}^{-1}} \right]^2 \left[\frac{v_w}{2000 \text{ km s}^{-1}} \right]^{-2} \left[\frac{T}{10^4 \text{ K}} \right]^{-3/2} \left[\frac{\nu}{\text{GHz}} \right]^{-2} \int_{l_0}^{\infty} r^{-4} dl .$$

Distances are in astronomical units. We assumed a radial mass-loss rate of the Be star of $\dot{M}_w = 10^{-8} M_\odot \text{ yr}^{-1}$ (Howarth & Prinja 1989), a terminal wind speed of $v_{w,\infty} = 1750 \text{ km s}^{-1}$ (Hutchings 1979) and a β -law with $\beta = 0.8$ (Puls et al. 1996), and a temperature of $T = 28000 \text{ K}$ (Casares et al. 2005a). We note that this is an oversimplified model of the stellar wind because we do not consider the effect of the truncated circumstellar equatorial disc, or any difference between the wind polar and equatorial parameters (McSwain et al. 2011; Cañellas et al. 2012). We integrated along the line-of-sight path from the position of the compact object (l_0) up to the observer at ∞ . We have considered the orbital parameters in Casares et al. (2005a). Since we assumed that the compact object is a neutron star we used a mass for the compact object of $1.4 M_\odot$. A mass function of $0.0107 M_\odot$ implies an inclination of the orbit of $i = 65^\circ$, which is slightly outside but not

¹Cañellas, A., C. Joshi, B., M. Paredes, J., et al. 2012, A&A, 543, A122

B. Free-free absorption in LS I +61 303

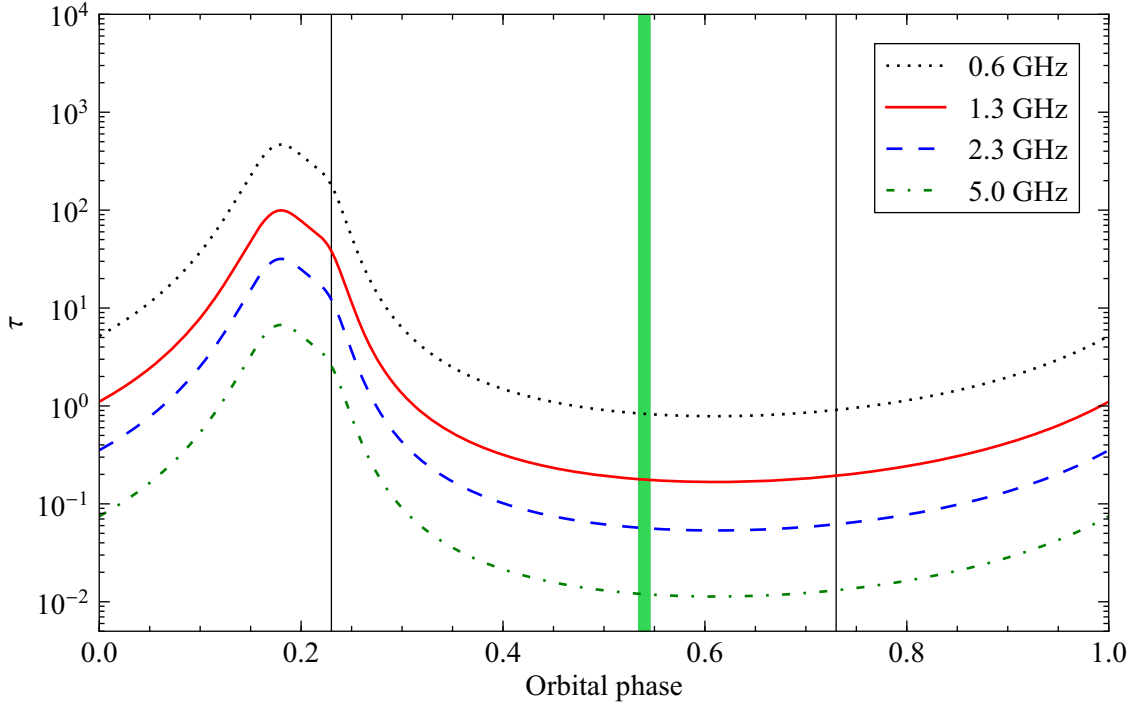


Figure B.1: Optical depth from the position of the compact object in LS I +61 303 for different orbital phases and for different frequencies. The vertical black lines indicate the orbital phase of the periastron (0.23) and the apastron (0.73). The observation phase range in Cañellas et al. (2012) is indicated by the vertical green stripe centred at orbital phase 0.54.

very far from the rough limit of 60° imposed by the lack of clear shell lines in Casares et al. (2005a). Note that these assumptions in the stellar wind and the choice of the orbital parameters plays an important role in the resulting absorption.

In Fig. B.1 we plot the optical depth as a function of the orbital phase. We indicate with a green line the orbital phase of the observation conducted with the GMRT, centred at orbital phase 0.54 (see Cañellas et al. 2012 for details). We can see that the absorption is not symmetric before and after the periastron and apastron passages. This is because the total path from the compact object to the observer is different when the compact object is in front and behind the plane of the sky, which depends on the orbital elements of the binary system (see Appendix A).

Using these opacities we estimated the absorbed pulsed flux density (S_ν) as a function of an hypothetical unabsorbed pulsed flux density at 1.3 GHz ($S_0 \equiv S_{1.3 \text{ GHz},0}$)

$$S_\nu = S_{\nu,0} e^{-\tau} = S_0 \left[\frac{\nu}{1.3 \text{ GHz}} \right]^\alpha e^{-\tau}, \quad (\text{B.1})$$

where 0 indicates unabsorbed values. We computed the expected flux density at different frequencies and different values of the spectral index (α , defined as $S \propto \nu^\alpha$). In Fig. B.2 we show the expected pulsed flux density at different frequencies for $\alpha = -1.5$ (a steep

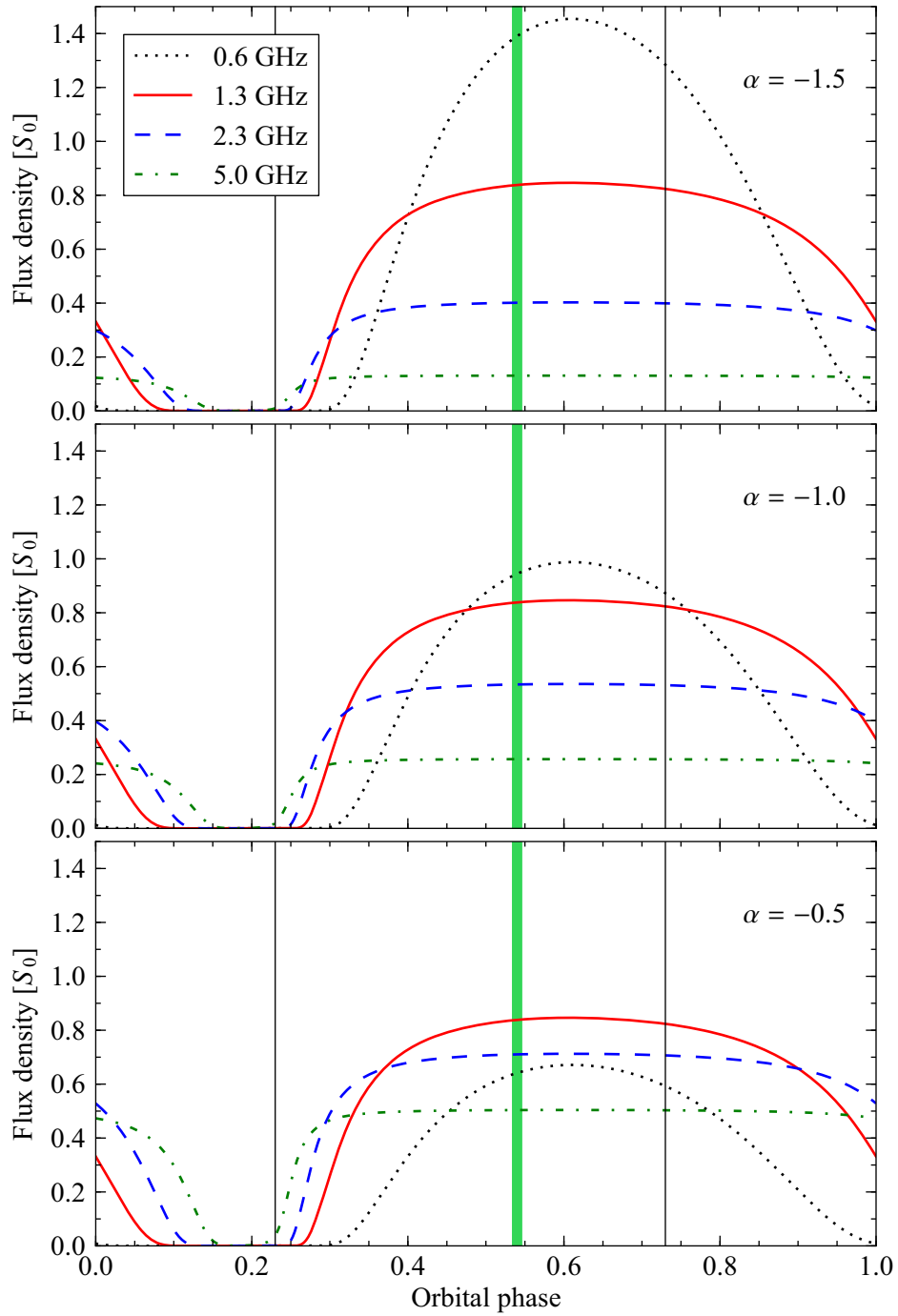


Figure B.2: Expected LS I +61 303 pulsed flux density along the orbit at different frequencies assuming that the intrinsic pulsed flux density at 1.3 GHz is S_0 and considering only free-free absorption effects. The periastron and apastron are indicated by the vertical black lines at phases 0.23 and 0.73, respectively. The observation phase range in Cañellas et al. (2012) is indicated by the vertical green stripe centred at orbital phase 0.54.

B. Free-free absorption in LS I +61 303

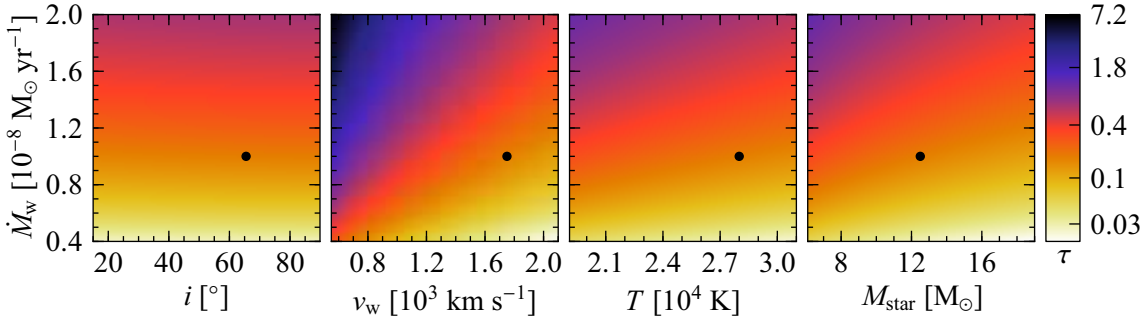


Figure B.3: Optical depth in logarithmic scale (colour bar) for different combinations of stellar parameters at orbital phase 0.54. The black circles mark the values adopted in this work. The dependence with the system inclination in the wide range $15\text{--}90^\circ$ (Casares et al. 2005a) is very low at this orbital phase, although it is strong around periastron.

spectrum), -1.0 (an intermediate value) and -0.5 (a very flat spectrum). $\alpha = -1.0$ can be considered a typical spectral index for pulsars.

For these simulations, the flux density variability of the pulsed emission at a given frequency is only caused by the change in the optical depth along the orbit. We concluded that the best orbital phase to try to detect pulsations in LS I +61 303 is ~ 0.6 . This orbital phase occurs approximately three days before the apastron passage. The lower flux densities would be received at $\sim 0.5\text{--}2$ GHz, assuming $\alpha = -1.0$. The highest observable flux density is expected to occur at orbital phase $\sim 0.6\text{--}0.7$, three days before apastron. The optimal frequency depends on the intrinsic spectral index of the unabsorbed emission. Higher frequencies are intrinsically very faint for a steep spectrum, although they are less absorbed, whereas lower frequencies can be severely absorbed, specially for orbital phases far from the optimal orbital phases. We found a good compromise by observing at 1.3 GHz.

In Fig. B.3 we plot the optical depth for a range of typical values of the stellar parameters for orbital phase 0.54. The ranges were selected to approximately cover the uncertainty range of each parameter. The inclination of the orbit is varely constrained between 15 and 90° (Casares et al. 2005a). The lower value plotted for the terminal wind velocity is 600 km s^{-1} , which is the estimated wind velocity at the equator in McSwain et al. (2011). The upper value is set to 2000 km s^{-1} , slightly above the value from (Hutchings 1979). The expected stellar temperature ranges from $21\,500 \text{ K}$ to $30\,000 \text{ K}$ (McSwain et al. 2011). Casares et al. (2005a) estimated the stellar mass to be between 10 and $15 M_\odot$. We can see that, under the conditions considered here, τ is about or below 1 at orbital phase 0.54. A higher opacity is expected for a slower stellar wind or for a less massive/hotter star.

References

- Abdo, A. A., Ackermann, M., Ajello, M., et al. 2010a, *Astrophysical Journal*, Supplement, 188, 405
- Abdo, A. A., Ackermann, M., Ajello, M., et al. 2010b, *Astrophysical Journal*, 723, 649
- Abdo, A. A., Ackermann, M., Ajello, M., et al. 2011, *Astrophysical Journal*, Letters, 736, L11
- Abdo, A. A., Ackermann, M., Ajello, M., et al. 2009a, *Astrophysical Journal*, Letters, 701, L123
- Abdo, A. A., Ackermann, M., Ajello, M., et al. 2009b, *Astrophysical Journal*, Letters, 706, L56
- Acciari, V. A., Aliu, E., Arlen, T., et al. 2011, *Astrophysical Journal*, 738, 3
- Acciari, V. A., Aliu, E., Arlen, T., et al. 2009a, *Astrophysical Journal*, 700, 1034
- Acciari, V. A., Aliu, E., Arlen, T., et al. 2009b, *Astrophysical Journal*, Letters, 698, L94
- Acciari, V. A., Beilicke, M., Blaylock, G., et al. 2008, *Astrophysical Journal*, 679, 1427
- Aharonian, F., Akhperjanian, A. G., Anton, G., et al. 2009, *Astronomy and Astrophysics*, 507, 389
- Aharonian, F., Akhperjanian, A. G., Aye, K.-M., et al. 2005a, *Science*, 309, 746
- Aharonian, F., Akhperjanian, A. G., Aye, K.-M., et al. 2005b, *Astronomy and Astrophysics*, 442, 1
- Aharonian, F., Akhperjanian, A. G., Bazer-Bachi, A. R., et al. 2006, *Astronomy and Astrophysics*, 460, 743
- Aharonian, F. A., Akhperjanian, A. G., Bazer-Bachi, A. R., et al. 2007, *Astronomy and Astrophysics*, 469, L1
- Albert, J., Aliu, E., Anderhub, H., et al. 2009, *Astrophysical Journal*, 693, 303
- Albert, J., Aliu, E., Anderhub, H., et al. 2006, *Science*, 312, 1771
- Albert, J., Aliu, E., Anderhub, H., et al. 2007, *Astrophysical Journal*, Letters, 665, L51
- Albert, J., Aliu, E., Anderhub, H., et al. 2008, *Astrophysical Journal*, 684, 1351
- Aleksić, J., Alvarez, E. A., Antonelli, L. A., et al. 2012a, *Astrophysical Journal*, Letters, 754, L10
- Aleksić, J., Alvarez, E. A., Antonelli, L. A., et al. 2011, *Astrophysical Journal*, Letters, 735, L5

REFERENCES

- Aleksić, J., Alvarez, E. A., Antonelli, L. A., et al. 2012b, *Astrophysical Journal*, 746, 80
- Aleksić, J., Antonelli, L. A., Antoranz, P., et al. 2010, *Astrophysical Journal*, 721, 843
- Anderhub, H., Antonelli, L. A., Antoranz, P., et al. 2009, *Astrophysical Journal, Letters*, 706, L27
- Aragona, C., McSwain, M. V., & De Becker, M. 2010, *Astrophysical Journal*, 724, 306
- Aragona, C., McSwain, M. V., Grundstrom, E. D., et al. 2009, *Astrophysical Journal*, 698, 514
- Avedisova, V. S. 2002, *Astronomy Reports*, 46, 193
- Barkov, M. V. & Khangulyan, D. V. 2012, *Monthly Notices of the RAS*, 421, 1351
- Bhattacharyya, S., Godambe, S., Bhatt, N., Mitra, A., & Choudhury, M. 2012, *Monthly Notices of the RAS*, 421, L1
- Blaauw, A. 1961, *Bulletin Astronomical Institute of the Netherlands*, 15, 265
- Blitz, L., Fich, M., & Stark, A. A. 1982, *Astrophysical Journal, Supplement*, 49, 183
- Blundell, K. M. & Bowler, M. G. 2004, *Astrophysical Journal, Letters*, 616, L159
- Bochow, A. 2011, PhD Thesis. Max-Planck-Institut für Kernphysik
- Bogovalov, S. V., Khangulyan, D., Koldoba, A. V., Ustyugova, G. V., & Aharonian, F. A. 2012, *Monthly Notices of the RAS*, 419, 3426
- Bogovalov, S. V., Khangulyan, D. V., Koldoba, A. V., Ustyugova, G. V., & Aharonian, F. A. 2008, *Monthly Notices of the RAS*, 387, 63
- Bongiorno, S. D., Falcone, A. D., Stroh, M., et al. 2011, *Astrophysical Journal, Letters*, 737, L11
- Bordas, P. 2009, PhD Thesis. University of Barcelona
- Bosch-Ramon, V. & Barkov, M. V. 2011, *Astronomy and Astrophysics*, 535, A20
- Bosch-Ramon, V., Barkov, M. V., Khangulyan, D., & Perucho, M. 2012, *Astronomy and Astrophysics*, 544, A59
- Bosch-Ramon, V. & Khangulyan, D. 2009, *International Journal of Modern Physics D*, 18, 347
- Bosch-Ramon, V. & Khangulyan, D. 2011, *Publications of the ASJ*, 63, 1023
- Bosch-Ramon, V., Khangulyan, D., & Aharonian, F. A. 2008, *Astronomy and Astrophysics*, 482, 397
- Bosch-Ramon, V., Motch, C., Ribó, M., et al. 2007, *Astronomy and Astrophysics*, 473, 545
- Bosch-Ramon, V., Paredes, J. M., Ribó, M., et al. 2005, *Astrophysical Journal*, 628, 388
- Bosch-Ramon, V., Romero, G. E., & Paredes, J. M. 2006, *Astronomy and Astrophysics*, 447, 263
- Brandt, N. & Podsiadlowski, P. 1995, *Monthly Notices of the RAS*, 274, 461
- Brinkmann, W., Yuan, W., & Siebert, J. 1997, *Astronomy and Astrophysics*, 319, 413

-
- Briskin, W. F., Benson, J. M., Beasley, A. J., et al. 2000, *Astrophysical Journal*, 541, 959
- Briskin, W. F., Benson, J. M., Goss, W. M., & Thorsett, S. E. 2002, *Astrophysical Journal*, 571, 906
- Briskin, W. F., Fruchter, A. S., Goss, W. M., Herrnstein, R. M., & Thorsett, S. E. 2003, *Astronomical Journal*, 126, 3090
- Brogan, C. L., Gelfand, J. D., Gaensler, B. M., Kassim, N. E., & Lazio, T. J. W. 2006, *Astrophysical Journal, Letters*, 639, L25
- Bulgarelli, A., Tavani, M., Chen, A. W., et al. 2012, *Astronomy and Astrophysics*, 538, A63
- Burke, B. F. & Graham-Smith, F. 2009, *An Introduction to Radio Astronomy*
- Cañellas, A., Joshi, B. C., Paredes, J. M., et al. 2012, *Astronomy and Astrophysics*, 543, A122
- Casares, J., Morales, J. C., Herrero, A., et al. 2012a, In preparation
- Casares, J., Ribas, I., Paredes, J. M., Martí, J., & Allende Prieto, C. 2005a, *Monthly Notices of the RAS*, 360, 1105
- Casares, J., Ribó, M., Ribas, I., et al. 2005b, *Monthly Notices of the RAS*, 364, 899
- Casares, J., Ribó, M., Ribas, I., et al. 2012b, *Monthly Notices of the RAS*, 2368
- Cerutti, B., Dubus, G., & Henri, G. 2008, *Astronomy and Astrophysics*, 488, 37
- Cerutti, B., Malzac, J., Dubus, G., & Henri, G. 2010, *Astronomy and Astrophysics*, 519, A81
- Chatterjee, S., Briskin, W. F., Vlemmings, W. H. T., et al. 2009, *Astrophysical Journal*, 698, 250
- Chatterjee, S., Vlemmings, W. H. T., Briskin, W. F., et al. 2005, *Astrophysical Journal, Letters*, 630, L61
- Chernyakova, M., Neronov, A., Aharonian, F., Uchiyama, Y., & Takahashi, T. 2009, *Monthly Notices of the RAS*, 397, 2123
- Chernyakova, M., Neronov, A., Lutovinov, A., Rodriguez, J., & Johnston, S. 2006, *Monthly Notices of the RAS*, 367, 1201
- Clark, J. S., Reig, P., Goodwin, S. P., et al. 2001, *Astronomy and Astrophysics*, 376, 476
- Clifton, T. R. & Lyne, A. G. 1986, *Nature*, 320, 43
- Clifton, T. R., Lyne, A. G., Jones, A. W., McKenna, J., & Ashworth, M. 1992, *Monthly Notices of the RAS*, 254, 177
- Cominsky, L., Roberts, M., & Johnston, S. 1994, *Astrophysical Journal*, 427, 978
- Condon, J., Darling, J., Kovalev, Y. Y., & Petrov, L. 2011, ArXiv: [1110.6252]
- Condon, J. J., Cotton, W. D., Greisen, E. W., et al. 1998, *Astronomical Journal*, 115, 1693
- Corbel, S., Dubus, G., Tomsick, J. A., et al. 2012, *Monthly Notices of the RAS*, 421, 2947
- Corbet, R. H. D., Cheung, C. C., Kerr, M., et al. 2011, *ATel*, 3221

REFERENCES

- Cordes, J. M. & Lazio, T. J. W. 2002, ArXiv Astrophysics e-prints
- Crowther, P. A., Hadfield, L. J., Clark, J. S., Negueruela, I., & Vacca, W. D. 2006, Monthly Notices of the RAS, 372, 1407
- Dambis, A. K., Mel'Nik, A. M., & Rastorguev, A. S. 2001, Astronomy Letters, 27, 58
- Danby, J. 1962, Fundamentals of celestial mechanics
- de Bruijne, J. H. J. 2012, Astrophysics and Space Science, 68
- Deller, A. T., Tingay, S. J., Bailes, M., & West, C. 2007, Publications of the ASP, 119, 318
- Dhawan, V., Mioduszewski, A., & Rupen, M. 2006, in VI Microquasar Workshop: Microquasars and Beyond
- Dhawan, V., Mirabel, I. F., Ribó, M., & Rodrigues, I. 2007, Astrophysical Journal, 668, 430
- Dubus, G. 2006, Astronomy and Astrophysics, 456, 801
- Dubus, G., Cerutti, B., & Henri, G. 2008, Astronomy and Astrophysics, 477, 691
- Dubus, G., Cerutti, B., & Henri, G. 2010, Astronomy and Astrophysics, 516, A18
- Durant, M., Kargaltsev, O., Pavlov, G. G., Chang, C., & Garmire, G. P. 2011, Astrophysical Journal, 735, 58
- Fabbiano, G. 2006, Annual Review of Astron and Astrophys, 44, 323
- Falcone, A., Bongiorno, S., Stroh, M., & Holder, J. 2011, ATel, 3152
- Faucher-Giguère, C.-A. & Kaspi, V. M. 2006, Astrophysical Journal, 643, 332
- Fender, R. 2006, Jets from X-ray binaries, ed. W. H. G. Lewin & M. van der Klis, 381–419
- Fender, R. P., Belloni, T. M., & Gallo, E. 2004, Monthly Notices of the RAS, 355, 1105
- Fermi LAT Collaboration, Abdo, A. A., Ackermann, M., et al. 2009, Science, 326, 1512
- Fermi LAT Collaboration, Ackermann, M., Ajello, M., et al. 2012a, Science, 335, 189
- Fermi LAT Collaboration, Ackermann, M., Ajello, M., et al. 2012b, Science, 335, 189
- Fey, A. L., Ma, C., Arias, E. F., et al. 2004, Astronomical Journal, 127, 3587
- Fey, A. L., Spangler, S. R., & Cordes, J. M. 1991, Astrophysical Journal, 372, 132
- Fomalont, E. B., Petrov, L., MacMillan, D. S., Gordon, D., & Ma, C. 2003, Astronomical Journal, 126, 2562
- Forbes, D. 2000, Astronomical Journal, 120, 2594
- Fragos, T., Willems, B., Kalogera, V., et al. 2009, Astrophysical Journal, 697, 1057
- Frail, D. A., Goss, W. M., & Whiteoak, J. B. Z. 1994, Astrophysical Journal, 437, 781
- Frail, D. A. & Hjellming, R. M. 1991, Astronomical Journal, 101, 2126
- Frail, D. A. & Scharringhausen, B. R. 1997, Astrophysical Journal, 480, 364
- Gaensler, B. M. & Frail, D. A. 2000, Nature, 406, 158
- Gaensler, B. M. & Johnston, S. 1995, Monthly Notices of the RAS, 275, L73
- Godambe, S., Bhattacharyya, S., Bhatt, N., & Choudhury, M. 2008, Monthly Notices of

- the RAS, 390, L43
- Gould, D. M. & Lyne, A. G. 1998, *Monthly Notices of the RAS*, 301, 235
- Green, D. A. 2009, *VizieR Online Data Catalog*, 7253, 0
- Gregory, P. C. 1999, *Astrophysical Journal*, 520, 361
- Gregory, P. C. 2002, *Astrophysical Journal*, 575, 427
- Gregory, P. C. & Taylor, A. R. 1978, *Nature*, 272, 704
- Grove, J. E., Tavani, M., Purcell, W. R., et al. 1995, *Astrophysical Journal, Letters*, 447, L113
- Grundstrom, E. D., Caballero-Nieves, S. M., Gies, D. R., et al. 2007, *Astrophysical Journal*, 656, 437
- Hadasch, D., Torres, D. F., Tanaka, T., et al. 2012, *Astrophysical Journal*, 749, 54
- Hales, C. A., Gaensler, B. M., Chatterjee, S., van der Swaluw, E., & Camilo, F. 2009, *Astrophysical Journal*, 706, 1316
- Hall, D. S. 1986, *Astrophysical Journal, Letters*, 309, L83
- Harrison, F. A., Ray, P. S., Leahy, D. A., Waltman, E. B., & Pooley, G. G. 2000, *Astrophysical Journal*, 528, 454
- Hermesen, W., Swanenburg, B. N., Bignami, G. F., et al. 1977, *Nature*, 269, 494
- H.E.S.S. Collaboration, Acero, F., Aharonian, F., et al. 2009, *Astronomy and Astrophysics*, 508, 1135
- Hill, A. B., Dubois, R., Torres, D. F., & Fermi LAT Collaboration. 2011, in *High-Energy Emission from Pulsars and their Systems*, ed. D. F. Torres & N. Rea, 498
- Hills, J. G. 1983, *Astrophysical Journal*, 267, 322
- Hinton, J. A. & Hofmann, W. 2009, *Annual Review of Astron and Astrophys*, 47, 523
- Hinton, J. A., Skilton, J. L., Funk, S., et al. 2009, *Astrophysical Journal, Letters*, 690, L101
- Hobbs, G., Lorimer, D. R., Lyne, A. G., & Kramer, M. 2005, *Monthly Notices of the RAS*, 360, 974
- Hobbs, G., Lyne, A. G., Kramer, M., Martin, C. E., & Jordan, C. 2004, *Monthly Notices of the RAS*, 353, 1311
- Høg, E., Fabricius, C., Makarov, V. V., et al. 2000, *Astronomy and Astrophysics*, 355, L27
- Högbom, J. A. 1974, *Astronomy and Astrophysics, Supplement*, 15, 417
- Howarth, I. D. & Prinja, R. K. 1989, *Astrophysical Journal, Supplement*, 69, 527
- Hughes, A. & Bailes, M. 1999, *Astrophysical Journal*, 522, 504
- Hutchings, J. B. 1979, *Publications of the ASP*, 91, 657
- Hutchings, J. B. & Crampton, D. 1981, *Publications of the ASP*, 93, 486
- Johnson, D. R. H. & Soderblom, D. R. 1987, *Astronomical Journal*, 93, 864
- Johnston, S., Ball, L., Wang, N., & Manchester, R. N. 2005, *Monthly Notices of the RAS*,

REFERENCES

- 358, 1069
- Johnston, S., Manchester, R. N., Lyne, A. G., et al. 1992, *Astrophysical Journal, Letters*, 387, L37
- Johnston, S., Manchester, R. N., Lyne, A. G., et al. 1996, *Monthly Notices of the RAS*, 279, 1026
- Johnston, S., Manchester, R. N., Lyne, A. G., Nicastro, L., & Spyromilio, J. 1994, *Monthly Notices of the RAS*, 268, 430
- Kennel, C. F. & Coroniti, F. V. 1984, *Astrophysical Journal*, 283, 710
- Khangulyan, D., Aharonian, F., & Bosch-Ramon, V. 2008, *Monthly Notices of the RAS*, 383, 467
- Khangulyan, D., Hnatic, S., Aharonian, F., & Bogovalov, S. 2007, *Monthly Notices of the RAS*, 380, 320
- Kijak, J., Gupta, Y., & Krzeszowski, K. 2007, *Astronomy and Astrophysics*, 462, 699
- Kim, C.-G., Kim, W.-T., & Ostriker, E. C. 2006, *Astrophysical Journal, Letters*, 649, L13
- Kirk, J. G., Ball, L., & Skjaeraasen, O. 1999, *Astroparticle Physics*, 10, 31
- Kishishita, T., Tanaka, T., Uchiyama, Y., & Takahashi, T. 2009, *Astrophysical Journal, Letters*, 697, L1
- Kniffen, D. A., Alberts, W. C. K., Bertsch, D. L., et al. 1997, *Astrophysical Journal*, 486, 126
- Kramer, M., Lyne, A. G., Hobbs, G., et al. 2003, *Astrophysical Journal, Letters*, 593, L31
- Kraus, J. D. 1973, *Radio astronomy*.
- Lamberts, A., Dubus, G., Lesur, G., & Fromang, S. 2012, *ArXiv e-prints* [1202.2060]
- Li, J., Torres, D. F., Zhang, S., et al. 2012, *Astrophysical Journal, Letters*, 744, L13
- Lockman, F. J. 1989, *Astrophysical Journal, Supplement*, 71, 469
- Loinard, L., Torres, R. M., Mioduszewski, A. J., et al. 2007, *Astrophysical Journal*, 671, 546
- Loktin, A. V. & Beshenov, G. V. 2003, *Astronomy Reports*, 47, 6
- Lorimer, D. R., Yates, J. A., Lyne, A. G., & Gould, D. M. 1995, *Monthly Notices of the RAS*, 273, 411
- Lucarelli, F., Verrecchia, F., Striani, E., et al. 2010, *The Astronomer's Telegram*, 2761, 1
- Lyne, A. G. & Graham-Smith, F. 2005, *Pulsar Astronomy*, ed. Lyne, A. G. & Graham-Smith, F.
- Lyne, A. G. & Lorimer, D. R. 1994, *Nature*, 369, 127
- Maíz-Apellániz, J. 2001, *Astronomical Journal*, 121, 2737
- Manchanda, R. K., Polcaro, V. F., Norci, L., et al. 1996, *Astronomy and Astrophysics*, 305, 457
- Manchester, R. N., Hobbs, G. B., Teoh, A., & Hobbs, M. 2005, *Astronomical Journal*,

- 129, 1993
- Manchester, R. N., Johnston, S., Lyne, A. G., et al. 1995, *Astrophysical Journal, Letters*, 445, L137
- Maraschi, L. & Treves, A. 1981, *Monthly Notices of the RAS*, 194, 1P
- Mariotti, M. 2011, *ATel*, 3161
- Marquardt, D. 1963, *SIAM J. Appl. Math.*, 11, 431
- Martí, J., Paredes, J. M., & Ribó, M. 1998, *Astronomy and Astrophysics*, 338, L71
- Martin, R. G., Tout, C. A., & Pringle, J. E. 2009, *Monthly Notices of the RAS*, 397, 1563
- Martocchia, A., Motch, C., & Negueruela, I. 2005, *Astronomy and Astrophysics*, 430, 245
- Massi, M., Paredes, J. M., Estalella, R., & Felli, M. 1993, *Astronomy and Astrophysics*, 269, 249
- Massi, M., Ribó, M., Paredes, J. M., et al. 2004, *Astronomy and Astrophysics*, 414, L1
- Massi, M., Ribó, M., Paredes, J. M., Peracaula, M., & Estalella, R. 2001, *Astronomy and Astrophysics*, 376, 217
- Massi, M., Ros, E., & Zimmermann, L. 2012, *Astronomy and Astrophysics*, 540, A142
- McCollum, B. 1993, in *Bulletin of the American Astronomical Society*, Vol. 25, *American Astronomical Society Meeting Abstracts*, 1321
- McSwain, M. V. & Gies, D. R. 2002, *Astrophysical Journal, Letters*, 568, L27
- McSwain, M. V., Gies, D. R., Huang, W., et al. 2004, *Astrophysical Journal*, 600, 927
- McSwain, M. V., Grundstrom, E. D., Gies, D. R., & Ray, P. S. 2010, *Astrophysical Journal*, 724, 379
- McSwain, M. V., Ray, P. S., Ransom, S. M., et al. 2011, *Astrophysical Journal*, 738, 105
- Melatos, A., Johnston, S., & Melrose, D. B. 1995, *Monthly Notices of the RAS*, 275, 381
- Mel'Nik, A. M. & Efremov, Y. N. 1995, *Astronomy Letters*, 21, 10
- Miller-Jones, J. C. A., Jonker, P. G., Nelemans, G., et al. 2009a, *Monthly Notices of the RAS*, 394, 1440
- Miller-Jones, J. C. A., Sakari, C. M., Dhawan, V., et al. 2009b, in *8th International e-VLBI Workshop*
- Mirabel, I. F. 2006, *Science*, 312, 1759
- Mirabel, I. F., Dhawan, V., Mignani, R. P., Rodrigues, I., & Guglielmetti, F. 2001, *Nature*, 413, 139
- Mirabel, I. F., Mignani, R., Rodrigues, I., et al. 2002, *Astronomy and Astrophysics*, 395, 595
- Mirabel, I. F. & Rodrigues, I. 2003, *Science*, 300, 1119
- Mirabel, I. F., Rodrigues, I., & Liu, Q. Z. 2004, *Astronomy and Astrophysics*, 422, L29
- Mirabel, I. F. & Rodríguez, L. F. 1994, *Nature*, 371, 46
- Mirabel, I. F. & Rodríguez, L. F. 1999, *Annual Review of Astron and Astrophys*, 37, 409

REFERENCES

- Moldón, J., Johnston, S., Ribó, M., Paredes, J. M., & Deller, A. T. 2011a, *Astrophysical Journal, Letters*, 732, L10
- Moldón, J., Ribó, M., & Paredes, J. M. 2011b, *The Astronomer's Telegram*, 3180, 1
- Moldón, J., Ribó, M., & Paredes, J. M. 2011c, *Astronomy and Astrophysics*, 533, L7
- Moldón, J., Ribó, M., & Paredes, J. M. 2011d, in *High-Energy Emission from Pulsars and their Systems*, ed. D. F. Torres & N. Rea, 1–2
- Moldón, J., Ribó, M., & Paredes, J. M. 2012a, *Astronomy and Astrophysics* (in press)
- Moldón, J., Ribó, M., Paredes, J. M., et al. 2012b, *Astronomy and Astrophysics*, 543, A26
- Monet, D. G. 1998, in *Bulletin of the American Astronomical Society*, Vol. 30, American Astronomical Society Meeting Abstracts, 120
- Monet, D. G., Levine, S. E., Canzian, B., et al. 2003, *Astronomical Journal*, 125, 984
- Moran, J. M. & Dhawan, V. 1995, in *Astronomical Society of the Pacific Conference Series*, Vol. 82, *Very Long Baseline Interferometry and the VLBA*, ed. J. A. Zensus, P. J. Diamond, & P. J. Napier, 161
- Mukherjee, R. 2011, in *High Energy Phenomena in Relativistic Outflows III*, ed. J. M. Paredes, M. Ribó, M., F. A. Aharonian, G. E. Romero
- Napoli, V. J., McSwain, M. V., Boyer, A. N. M., & Roettenbacher, R. M. 2011, *Publications of the ASP*, 123, 1262
- Negueruela, I., Ribó, M., Herrero, A., et al. 2011, *Astrophysical Journal, Letters*, 732, L11
- Okazaki, A. T., Nagataki, S., Naito, T., et al. 2011, *Publications of the ASJ*, 63, 893
- Okazaki, A. T., Romero, G. E., & Owocki, S. P. 2008, in *Proceedings of the 7th INTEGRAL Workshop*
- Ong, R. A. 2011, *ATel.* #3153
- Pacholczyk, A. G. 1970, *Radio astrophysics. Nonthermal processes in galactic and extragalactic sources*
- Pandey, M., Rao, A. P., Ishwara-Chandra, C. H., Durouchoux, P., & Manchanda, R. K. 2007, *Astronomy and Astrophysics*, 463, 567
- Paredes, J. M. 1987, PhD thesis, University of Barcelona, (1987)
- Paredes, J. M. 2011, *ArXiv e-prints* [1101.4843]
- Paredes, J. M., Bosch-Ramon, V., & Romero, G. E. 2006, *Astronomy and Astrophysics*, 451, 259
- Paredes, J. M., Martí, J., Peracaula, M., & Ribo, M. 1997, *Astronomy and Astrophysics*, 320, L25
- Paredes, J. M., Martí, J., Ribó, M., & Massi, M. 2000, *Science*, 288, 2340
- Paredes, J. M., Massi, M., Estalella, R., & Peracaula, M. 1998, *Astronomy and Astrophysics*, 335, 539
- Paredes, J. M., Ribó, M., Bosch-Ramon, V., et al. 2007, *Astrophysical Journal, Letters*, 664, L39

-
- Paredes, J. M., Ribó, M., Ros, E., Martí, J., & Massi, M. 2002, *Astronomy and Astrophysics*, 393, L99
- Pavlov, G. G., Chang, C., & Kargaltsev, O. 2011a, *Astrophysical Journal*, 730, 2
- Pavlov, G. G., Misanovic, Z., Kargaltsev, O., & Garmire, G. P. 2011b, *ATel.* #3228
- Peracaula, M., Gabuzda, D. C., & Taylor, A. R. 1998, *Astronomy and Astrophysics*, 330, 612
- Pradel, N., Charlot, P., & Lestrade, J.-F. 2006, *Astronomy and Astrophysics*, 452, 1099
- Puls, J., Kudritzki, R.-P., Herrero, A., et al. 1996, *Astronomy and Astrophysics*, 305, 171
- Rea, N., Torres, D. F., Caliendo, G. A., et al. 2011, *Monthly Notices of the RAS*, 416, 1514
- Reed, B. C. 2000, *Astronomical Journal*, 120, 314
- Reed, B. C. 2003, *Astronomical Journal*, 125, 2531
- Reich, W., Fuerst, E., Reich, P., & Reif, K. 1990, *Astronomy and Astrophysics, Supplement*, 85, 633
- Reich, W., Fuerst, E., Reich, P., Sofue, Y., & Handa, T. 1986, *Astronomy and Astrophysics*, 155, 185
- Reid, M. J. 1993, *Annual Review of Astron and Astrophys*, 31, 345
- Reid, M. J. & Brunthaler, A. 2004, *Astrophysical Journal*, 616, 872
- Reid, M. J., McClintock, J. E., Narayan, R., et al. 2011, *Astrophysical Journal*, 742, 83
- Reig, P., Ribó, M., Paredes, J. M., & Martí, J. 2003, *Astronomy and Astrophysics*, 405, 285
- Remillard, R. A. & McClintock, J. E. 2006, *Annual Review of Astron and Astrophys*, 44, 49
- Ribó, M., Paredes, J. M., Moldón, J., Martí, J., & Massi, M. 2008, *Astronomy and Astrophysics*, 481, 17
- Ribó, M., Paredes, J. M., Romero, G. E., et al. 2002a, *Astronomy and Astrophysics*, 384, 954
- Ribó, M., Paredes, J. M., Romero, G. E., et al. 2002b, *Astronomy and Astrophysics*, 384, 954
- Ribó, M., Reig, P., Martí, J., & Paredes, J. M. 1999, *Astronomy and Astrophysics*, 347, 518
- Rodgers, A. W., Campbell, C. T., & Whiteoak, J. B. 1960, *Monthly Notices of the RAS*, 121, 103
- Romero, G. E., Okazaki, A. T., Orellana, M., & Owocki, S. P. 2007, *Astronomy and Astrophysics*, 474, 15
- Romero, G. E., Torres, D. F., Kaufman Bernadó, M. M., & Mirabel, I. F. 2003, *Astronomy and Astrophysics*, 410, L1
- Sabatini, S., Tavani, M., Striani, E., et al. 2010, *Astrophysical Journal, Letters*, 712, L10

REFERENCES

- Sarty, G. E., Szalai, T., Kiss, L. L., et al. 2011, *Monthly Notices of the RAS*, 411, 1293
- Schönrich, R., Binney, J., & Dehnen, W. 2010, *Monthly Notices of the RAS*, 403, 1829
- Sharpless, S. 1959, *Astrophysical Journal*, Supplement, 4, 257
- Shepherd, M. C. 1997, in *Astronomical Society of the Pacific Conference Series*, Vol. 125, *Astron. Data Anal. Software Syst. VI*, ed. G. Hunt & H. Payne, 77
- Sidoli, L., Pellizzoni, A., Vercellone, S., et al. 2006, *Astronomy and Astrophysics*, 459, 901
- Sierpowska-Bartosik, A. & Torres, D. F. 2007, *Astrophysical Journal*, Letters, 671, L145
- Sierpowska-Bartosik, A. & Torres, D. F. 2008, *Astroparticle Physics*, 30, 239
- Skilton, J. L., Pandey-Pommier, M., Hinton, J. A., et al. 2009, *Monthly Notices of the RAS*, 399, 317
- Skrutskie, M. F., Cutri, R. M., Stiening, R., et al. 2006, *Astronomical Journal*, 131, 1163
- Smart, W. M. 1930, *Monthly Notices of the RAS*, 90, 534
- Sokolovsky, K. V., Kovalev, Y. Y., Pushkarev, A. B., Mimica, P., & Perucho, M. 2011, *Astronomy and Astrophysics*, 535, A24
- Stephenson, C. B. & Sanduleak, N. 1971, *Publications of the Warner & Swasey Observatory*, 1, 1
- Stone, R. C. 1982, *Astronomical Journal*, 87, 90
- Strickman, M. S., Tavani, M., Coe, M. J., et al. 1998, *Astrophysical Journal*, 497, 419
- Sun, X. H., Reich, P., Reich, W., et al. 2011, *Astronomy and Astrophysics*, 536, A83
- Szostek, A. & Dubus, G. 2011, *Monthly Notices of the RAS*, 411, 193
- Takahashi, T., Kishishita, T., Uchiyama, Y., et al. 2009, *Astrophysical Journal*, 697, 592
- Takata, J., Okazaki, A. T., Nagataki, S., et al. 2012, *Astrophysical Journal*, 750, 70
- Takata, J. & Taam, R. E. 2009, *Astrophysical Journal*, 702, 100
- Tam, P. H. T., Huang, R. H. H., Takata, J., et al. 2011, *Astrophysical Journal*, Letters, 736, L10
- Tasker, N. J., Condon, J. J., Wright, A. E., & Griffith, M. R. 1994, *Astronomical Journal*, 107, 2115
- Tauris, T. M., Fender, R. P., van den Heuvel, E. P. J., Johnston, H. M., & Wu, K. 1999, *Monthly Notices of the RAS*, 310, 1165
- Tavani, M. & Arons, J. 1997, *Astrophysical Journal*, 477, 439
- Tavani, M., Bulgarelli, A., Piano, G., et al. 2009, *Nature*, 462, 620
- Tavani, M., Grove, J. E., Purcell, W., et al. 1996, *Astronomy and Astrophysics*, Supplement, 120, C221
- Taylor, G. B., Carilli, C. L., & Perley, R. A., eds. 1999, *Astronomical Society of the Pacific Conference Series*, Vol. 180, *Synthesis Imaging in Radio Astronomy II*
- Tetzlaff, N., Neuhäuser, R., Hohle, M. M., & Maciejewski, G. 2010, *Monthly Notices of the RAS*, 402, 2369

-
- Thompson, A. R., Moran, J. M., & Swenson, G. W. 1986, *Interferometry and synthesis in radio astronomy*. New York, Wiley-Interscience
- Torra, J., Fernández, D., & Figueras, F. 2000, *Astronomy and Astrophysics*, 359, 82
- Torres, D. F. & Rea, N., eds. 2011, *High-Energy Emission from Pulsars and their Systems*
- Tudose, V., Fender, R. P., Garrett, M. A., et al. 2007, *Monthly Notices of the RAS*, 375, L11
- Uchiyama, Y., Tanaka, T., Takahashi, T., Mori, K., & Nakazawa, K. 2009, *Astrophysical Journal*, 698, 911
- van den Heuvel, E. P. J., Portegies Zwart, S. F., Bhattacharya, D., & Kaper, L. 2000, *Astronomy and Astrophysics*, 364, 563
- Vercellone, S., Chen, A. W., Giuliani, A., et al. 2008, *Astrophysical Journal, Letters*, 676, L13
- Vink, J. S., de Koter, A., & Lamers, H. J. G. L. M. 2000, *Astronomy and Astrophysics*, 362, 295
- Von Hoensbroech, A. 1998, *Mem. Societa Astronomica Italiana*, 69, 1055
- Walker, R. C. 1999, in *Astronomical Society of the Pacific Conference Series*, Vol. 180, *Synthesis Imaging in Radio Astronomy II*, ed. G. B. Taylor, C. L. Carilli, & R. A. Perley, 433
- Wang, C., Lai, D., & Han, J. L. 2006, *Astrophysical Journal*, 639, 1007
- Wang, N., Johnston, S., & Manchester, R. N. 2004, *Monthly Notices of the RAS*, 351, 599
- Wex, N., Johnston, S., Manchester, R. N., et al. 1998, *Monthly Notices of the RAS*, 298, 997
- Willems, B., Henninger, M., Levin, T., et al. 2005, *Astrophysical Journal*, 625, 324
- Williams, S. J., Gies, D. R., Matson, R. A., et al. 2010, *Astrophysical Journal, Letters*, 723, L93
- Zabalza, V., Bosch-Ramon, V., & Paredes, J. M. 2011, *Astrophysical Journal*, 743, 7
- Zacharias, N., Finch, C., Girard, T., et al. 2009, *VizieR Online Data Catalog*, 1315, 0
- Zacharias, N., Finch, C., Girard, T., et al. 2010, *Astronomical Journal*, 139, 2184
- Zacharias, N., Urban, S. E., Zacharias, M. I., et al. 2000, *Astronomical Journal*, 120, 2131
- Zacharias, N., Zacharias, M. I., & de Vegt, C. 1999, *Astronomical Journal*, 117, 2895
- Zamanov, R. K., Martí, J., Paredes, J. M., et al. 1999, *Astronomy and Astrophysics*, 351, 543
- Zdziarski, A. A., Neronov, A., & Chernyakova, M. 2010, *Monthly Notices of the RAS*, 403, 1873
- Zdziarski, A. A., Sikora, M., Dubus, G., et al. 2012, *Monthly Notices of the RAS*, 421, 2956



UNIVERSITAT DE BARCELONA

